Measurement and Modelling of Light Scattering by Small to Medium Size Parameter Airborne Particles

by

David Samuel McCall

Submitted to the University of Hertfordshire in partial fulfilment of the requirements of the degree of PhD

2010

Supervisor: Dr. E. Hesse

Contents

Abstract 4

Acknowledgements 5

Chapter 1 - Introduction 7

Chapter 2 - The Study of Light and an introduction to Light Scattering theory. 9

2.1 - The Study of Light 9

2.1.1 - Conflicting Theories 9

2.1.2 - An Electromagnetic Phenomenon 10

2.1.3 - Wave Particle Duality and Quantum Physics 10

2.2 – Properties of Light 11

2.2.1 - Polarization 11

2.2.2 - The Stokes Parameters 13

2.2.3 - Mueller Matrices 14

2.2.4 - The Phase Function 16

2.2.5 - Asymmetry Parameter 17

2.2.6 - Degree of Linear Polarization 17

Chapter 3 - Geometric Optics 19

3.1 - The Ray Approximation 19

3.1.1 - Light Propagation through changing media. 19

3.1.2 - Snell's Law 19

3.1.3 - The Fresnel Equations 21

3.2 – Important Light Scattering considerations 22

3.2.1 - Scattering Cross Sections 22

3.2.2 - Size Parameter 23

Chapter 4 - Scattering by Small Particles 25

4.1 - Computational Approaches 25

4.1.1 - Mie Theory 25

4.1.2 - SVM – Separation of Variables Method 25

4.1.3 - T-Matrix 26

4.1.4 - DDA - Discrete Dipole Approximation 26

4.1.5 - FDTD - Finite Difference Time Domain 26

4.1.6 - GO - Geometric Optics....27
Chapter 5 – Experimental Set-up and Method for Measuring Scattering Properties of Saharan Dust Particles..29
5.1 - The Electrodynamic Balance (EDB)....29
5.1.1 - Modelling of the Particle Trajectory....30
5.1.2 - Large-Angle Scattering Measurements....33
5.1.3 - Low-Angle Scattering Measurements....34
5.1.4 - Extrapolation of Direct Forward Scattering Intensity....34
Chapter 6 - Modelling Rough Surfaces using Stochastically Generated Meshes....37
6.1 - Gaussian Random Particles....37
6.2 - Determining the Projected Area of a Complex Particle....39
6.3 - Non-spherical Particles....41
Chapter 7 - Improving the efficiency of Geometric Optics Ray Tracing using Spatial Subdivision. 43
7.1 - Increasing Facetation....43
7.1.1 - Comparison of GO calculations for Faceted Spheres with Mie Theory and GO for analytic spheres. 44
7.2 - Implementation....47
7.2.1 - Implementation of Spatial Subdivision....47
7.2.2 - Implementation in GO....50
7.3 - Results....51
7.3.1 - Performance Increase due to Spatial Subdivision....51
7.3.2 - Optimizing the Distribution of the Bounding Boxes. 53
7.4 - Conclusions....54
Chapter 8 - Properties of Saharan Dust Particles....56
8.1 - Scanning Electron Microscopy....56
8.1.1 – The Mineral Dust Sample....56
8.1.2 – Refractive Index....56
8.1.3 – Surface Roughness....57
Chapter 9 - Levitation & Scattering Experiments....60
9.1 - Case Study 1:....60
9.1.1 – Levitation and Scattering Measurements....60
9.1.2 - Modelling the Particle....65
9.1.3 – RTDF and GO calculations....65

9.1.4 - RMS Comparison of phase functions 75
9.1.5 - Asymmetry Parameter 76
9.2 – Case Study 2: 78
9.2.1 – Levitation and Scattering Experiments 78
9.2.2 – Modelling the Particle 81
9.2.3 – RTDF and GO calculations 82
9.2.4 - RMS Comparison of phase functions 91
9.2.5 – Asymmetry Parameter 92
9.3 – Case Study 3 93
9.3.1 – Levitation and Scattering Experiments 93
9.3.2 – Modelling the Particle 95
9.3.3 – RTDF and GO Calculations 96
9.3.4 – RMS Comparison of phase functions 105
9.3.5 – Asymmetry Parameter 106
9.4 – Case Study 4 107
9.4.1 – Levitation and Scattering Experiments 107
9.4.2 – Modelling the Particle 109
9.4.3 – RTDF and GO calculations 110
9.4.4 – RMS Comparison of phase functions 119
9.4.5 – Asymmetry Parameter 120
Chapter 10 – Summary and Outlook 121
Bibliography 125

Abstract

An investigation into the light scattering properties of Saharan dust grains is presented. An electrodynamic trap has been used to levitate single dust particles. By adjusting the trap parameters, partial randomisation of the particle orientation has been introduced. While levitated, the particles were illuminated by a laser, and a rotating half-wave retarder enabled selection of vertically or horizontally polarized incident light. A laser diffractometer and linear photodiode array have been used to measure intensity at scattering angles between 0.5° and 177°. Combining these measurements with Fraunhofer diffraction as calculated for a range of appropriately-sized apertures allows the calculation of the phase function and degree of linear polarization.

The phase functions and degree of linear polarisation for four case study particles are presented - the phase functions are found to be featureless across most of the scattering region, with none of the halo features or rainbow peaks associated with regularly shaped particles such as hexagonal columns or spheres.

Particle models comprised of large numbers of facets have been constructed to resemble the levitated particles. Utilizing Gaussian random sphere methods, increasing levels of roughness have been added to the surfaces of these models. A Geometric Optics model and a related model, Ray Tracing with Diffraction on Facets, have been modified to calculate scattering on these particle reconstructions. Scattering calculations were performed on each of these reconstructions using a range of refractive indices and two rotation regimes – one where the orientations of the reconstructed particle were limited to match those observed when the particle was levitated, and one where the orientation was not limited.

Qualitative comparisons are performed on the phase functions and degree of linear polarization, where it is observed that the addition of roughness to the modelled spheroids causes the computed phase functions to increasingly resemble those from the levitated particles. Limiting the orientation of the particles does not affect the scattering noticeably. The addition of a very small absorption coefficient does not change the comparisons considerably. As the absorption coefficient is increased, however, the quality of the comparisons decreases rapidly in all cases but one.

The phase functions are quantitatively compared using RMS errors, and further comparison is performed using the asymmetry parameter.

Acknowledgements

I am eternally grateful to the following people for their assistance throughout this project:

The supervisory team:

Dr. Evelyn Hesse (Principal Supervisor)

Dr. Zbigniew Ulanowski

Prof. Paul Kaye

The following people, for helpful discussions and advice:

Ken Henman (for assistance with the SEM)

Dr. Chris Stopford

Dr. John Atkinson

Dr. Jim Collett

Dr. Richard Greenaway

Dr. Warren Stanley

My partner Rachel and my family.

This project was supported by the Natural Environment Research Council.

Chapter 1 - Introduction

The importance of airborne particulates to the Earth-Atmosphere radiation balance is well established. Aerosols such as Ice crystals (e.g. those found in Cirrus clouds) [1] and Saharan Dust Particles [2] have direct effects on the world's energy budget by scattering and absorbing solar radiation.

Weather prediction models and climate models rely on data that is as realistic as possible, so it is important that the radiative effects of atmospheric aerosols are well understood. The radiative properties of Cirrus ice have been studied in some depth [1], but the level of influence of atmospheric dust on global energy cycles is unclear, in large part due to the uncertainties regarding the optical properties of the dust particles. It is even unclear whether the global net radiative forcing due to atmospheric dust is positive or negative [3]. Average forcing due to infrared radiation [4] has been measured to be positive, while average forcing due to solar radiation has been measured to be negative – large dust particles have been noted to cause localised heating due to absorption. The effect of dust also differs over different surfaces – a radiative transfer model has indicated that Saharan dust will cause a warming over desert environments, but a cooling over water.

At least 50% of the atmospheric dust worldwide can be traced back to the Saharan desert [5], and estimates of the amount of atmospheric dust originating from northern Africa range from 260×10^6 to 1500×10^6 tons per year [6]. The dust is transported from the desert by wind, and can travel many hundreds or thousands of kilometres from the Saharan region over the Atlantic Ocean – larger amounts of dust are emitted in the period between March and September than for the remaining 6 months of the year [3].

Here, an Electrodynamic Balance (EDB) [7] is used to levitate single Saharan dust grains, to enable scattering experiments to be performed. The particle is illuminated by a laser, and a Laser Diffractometer [8] and Linear Photodiode Array [9] are used to measure the scattered flux at scattering angles from 0.5º to 177º. The direct forward scattering is approximated by Fraunhofer diffraction on a range of randomly oriented (in the plane perpendicular to the incident beam) ellipses corresponding to the average cross-section of the particle as it rotates in the trap [10]. With the range of scattering data measured in the experiment, we can calculate the asymmetry parameter, scattering phase function and degree of linear polarization.

Prior to levitation, the Saharan dust grains to be levitated are examined using optical microscopy, in order to obtain size and shape information. Some particles from the dust sample used were also examined by electron microscopy, and small scale surface structure was noted. This information is used when modelling scattering by the particles.

Currently, computational limitations mean that atmospheric dust particles are difficult to model accurately. It has been shown that simplifying the shape to simple spheres and spheroids results in large errors in measurement [11] [12]. There are various analytical methods available for computing scattering by irregular particles, but very few of these methods can take into account detailed particle geometry. Those that can are limited to smaller particles, due to the computational requirements of these methods [13].

Geometric Optics (GO) is an approximate technique used to compute scattering by particles not suitable for computation by exact methods. GO provides rapid computation, and is flexible in terms of the particle

geometries that can be considered. Although pure GO is primarily applicable to large size parameter particles, there have been improvements made which allow GO to bridge the gap between small to large size parameter particles. Ray Tracing with Diffraction on Facets (RTDF) [14] [15] [16] shows marked improvement over GO for intermediate size parameter particles. Creating particle geometries for use with the RTDF model is relatively simple, being a matter of creating a closed polyhedron. However, particles such as Saharan dust grains require so many polygons to be accurately represented that the RTDF model becomes inefficient, and can take weeks to return results.

In order that RTDF may be used efficiently, a spatial subdivision regime has been designed and implemented. This reduces computation time drastically, and enables computation of scattering for complex particles comprised of many thousands of facets in a very reasonable time.

The results of the scattering measurements (phase function, asymmetry parameter and degree of linear polarization) for several Saharan dust grains are presented and unique scattering characteristics are discussed. Scattering properties of levitated dust grains are compared with scattering properties of simulated dust particles as calculated by RTDF and GO, and the values of RTDF and GO as suitable modelling tools for calculating the properties of airborne Saharan dust are investigated.

Chapter 2 - The Study of Light and an introduction to Light Scattering theory.

2.1 - The Study of Light

2.1.1 - Conflicting Theories

Through the ages, our understanding of the nature of light has undergone many evolutionary steps. In approximately 1000AD Alhazen built on the long held knowledge that light propagates in a straight line and can be reflected, by postulating that light rays were streams of particles consisting purely of energy – this view was held for several centuries, even so far as Isaac Newton, who published his own Corpuscular Theory of Light in the latter half of the 17th century. While this theory could explain the reflection of light accurately, it was unable to explain refraction correctly. Newton also worked on a wave theory of light, but generally gravitated towards his corpuscular theory in his later years. During the same period, Robert Hooke and then Christiaan Huygens developed their own wave theories, Huygens theory being particularly accurate – he was able to derive the laws of reflection and refraction, and was able to show that light slowed down upon entering a denser medium. However, he limited his idea of a light wave to that of a longitudinal wave, rather like a mechanical wave – a major downfall of this concept was that a mechanical wave requires a medium through which to pass. Also hypothesized by Newton, a 'Luminiferous Aether' was assumed to be an invisible and ubiquitous medium which would allow for the propagation of light. It would be late in the 19th century before the experiments of Michelson & Morley would indicate that the aether did not exist.

Unfortunately, during most of the 18th century, advances in the wave theory of light were not given the credence due to them, owing to the esteem in which Newton was held. It was Thomas Young who can be credited with reviving the wave theory of light, by demonstrating that light emanating from two sources shows evidence of interference, only possible if light has the properties of a wave.

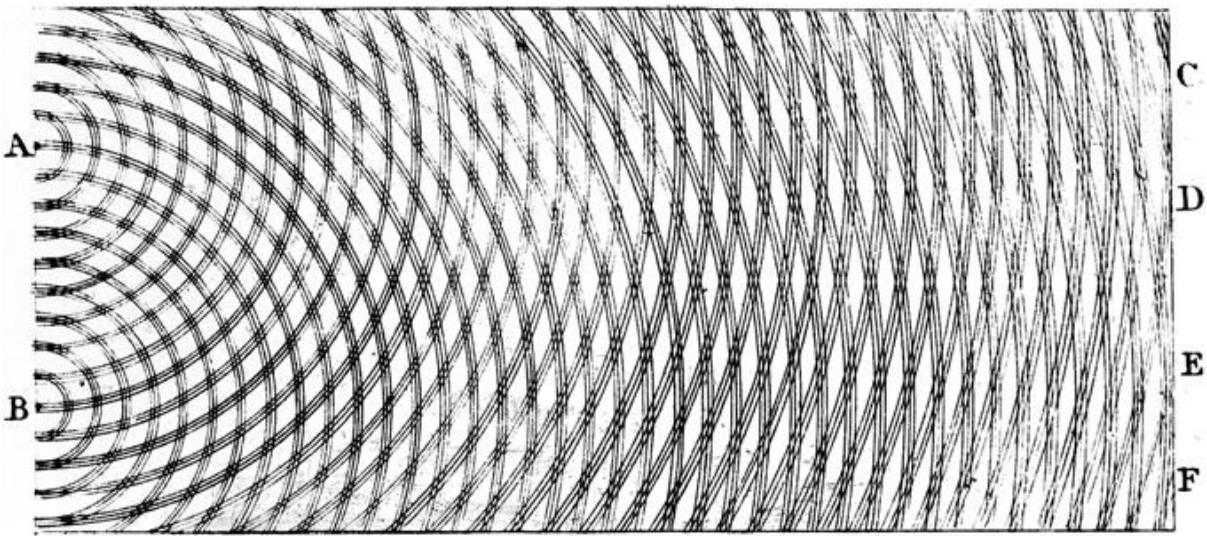

Figure 2-1 - Thomas Young's sketch showing how the propagation of wave fronts from two sources could produce interference. This is a key experiment in the development of the wave theory of light.

His so-called 'Double-slit experiment' (also known as Young's experiment) consists of a coherent light source illuminating an obstruction in which two parallel slits are cut. The light passing through these slits is then incident on a screen. Thomas Young's famous sketch showing how the wave fronts propagate from the two slits is shown in **Figure 2-1**.

2.1.2 - An Electromagnetic Phenomenon

In the mid 19th century, Michael Faraday discovered that the plane of polarization of linearly polarized light could be changed in the presence of a magnetic field, an effect known as Faraday rotation. It was this observation that led Faraday to relate the phenomenon of light to electromagnetism, and to postulate that light was an electromagnetic vibration. Not long after, James Clark Maxwell was able to take all of the combined knowledge on electromagnetism and formulate a single set of equations describing all electromagnetic phenomena. He was able to show, theoretically, that an electromagnetic field could propagate as a transverse wave. Upon deriving the speed of this wave, Maxwell found that the speed was the same as the speed of light, thus demonstrating that light was "*an electromagnetic disturbance in the form of waves*." This effectively ended the consideration of Newton's corpuscular theory as a valid explanation of light.

2.1.3 - Wave Particle Duality and Quantum Physics

The wave theory as described by Maxwell, while successfully explaining a huge number of phenomena that had hitherto been poorly understood, did not account for all the phenomena associated with light. The observation that the speed of light was consistent in all frames of reference was in direct contradiction with intuition and all known laws of motion. With his special theory of relativity, Einstein linked space and time, and provided us with his famous mass energy equivalence formula:

$$E = mc^2 \tag{2.1}$$

Where E is the energy contained in the object, m is the mass of the object and c is the speed of light. In 1900, Max Planck introduced the first tentative steps of what was to become known as Quantum Mechanics. He postulated that the energy emitted through electromagnetic radiation was not continuous, but rather was emitted in discrete packets, or 'quanta' of energy. The energy of each quantum was related to its frequency via a constant h, known as Planck's constant. For electromagnetic radiation with a frequency f, the energy contained in each quantum would be:

$$E = hf \tag{2.2}$$

The photoelectric effect, whereby a light shining on a surface causes electrons to be ejected from that surface, was also resolved by Albert Einstein in 1905. He resurrected the particle theory of light, and was able to explain the effect by postulating that light consisted of individual photons. It was known that the energy of the electrons ejected from the metal surface was not dependent on the intensity of the light incident on it, but rather the frequency of the light. Building on the work performed by Max Planck, Einstein proposed a new theory governing light, whereby light was transmitted via means of individual packets, known as photons. However, he proposed that photons could take on the characteristics of both waves and particles simultaneously, a body of work for which he would win the Nobel Prize in 1921.

Each photon emitted by a source exhibits the properties of both a wave and a particle. The photons interact in a similar fashion to particles, and yet have a frequency, like a wave. Louis De Broglie showed in 1924 that the dual wave-particle nature of photons could also be extended to electrons – this gave a complete solution to the photoelectric effect. Just a few years later, he showed that this could be applied to all subatomic particles – photons, neutrons, etc., all exhibit the same particle and wave properties.

2.2 – Properties of Light

2.2.1 - Polarization

The polarization of a wave describes the orientation of the oscillations of a wave in the plane that is perpendicular to its direction of propagation. An electromagnetic wave is comprised of two orthogonal oscillating waves - an electric field and a magnetic field. The polarization of the electromagnetic wave is conventionally defined by the path the electric field vector follows over one full oscillatory period. Consider the electric field vector as composed of two orthogonal waves, travelling in the positive z-direction. One wave oscillates in the x-plane, and the other in the y-plane.

$$\vec{E}_x(z,t) = A_x \cos(kz - \omega t) \tag{2.3}$$

$$\vec{E}_y(z,t) = A_y \cos(kz - \omega t + \varepsilon) \tag{2.4}$$

Where A is the amplitude of the wave, k is the wavenumber, ω is the angular frequency, t is the time, and ε is the phase difference between the waves. When these waves are superimposed, the result is

$$\vec{E}_{res}(z,t) = \vec{E}_x(z,t) + \vec{E}_y(z,t) \tag{2.5}$$

The polarization state of this resulting wave depends on the phase difference ε and the amplitude of the x and y components of the wave. If there is no x component (A_x=0) then the light is vertically polarized. Conversely, if there is no y component (A_y=0) then the light is horizontally polarized.

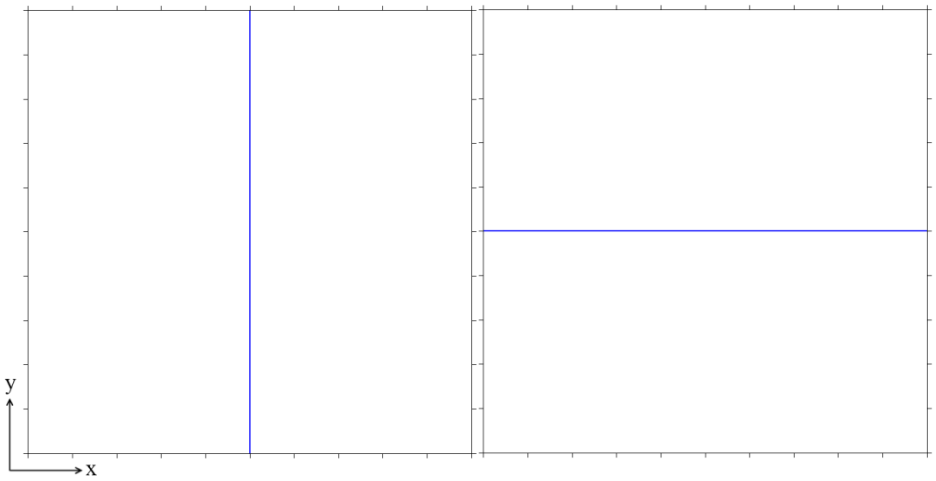

Figure 2-2 – Vertically and horizontally polarized waves. For the vertically polarized wave, the amplitude of the x-component of the wave is 0. For the horizontal polarization, the amplitude of the y-component of the wave is 0.

If A_x=A_y, and ε is equal to any integer multiple of π, then the waves can be said to be linearly polarized at 45°. For ε=0,2π,4π,6π... the polarization is 45°. For ε=π,3π,5π... the angle is -45°.

$$\vec{E}_{res}(z,t) = \left(A_x + A_y\right)\cos(kz - \omega t)\,, \varepsilon = 0, \pi, 2\pi, 4\pi \ldots \tag{2.6}$$

$$\vec{E}_{res}(z,t) = -\left(A_x + A_y\right)\cos(kz - \omega t)\,, \varepsilon = \pi, 3\pi, 5\pi \ldots \tag{2.7}$$

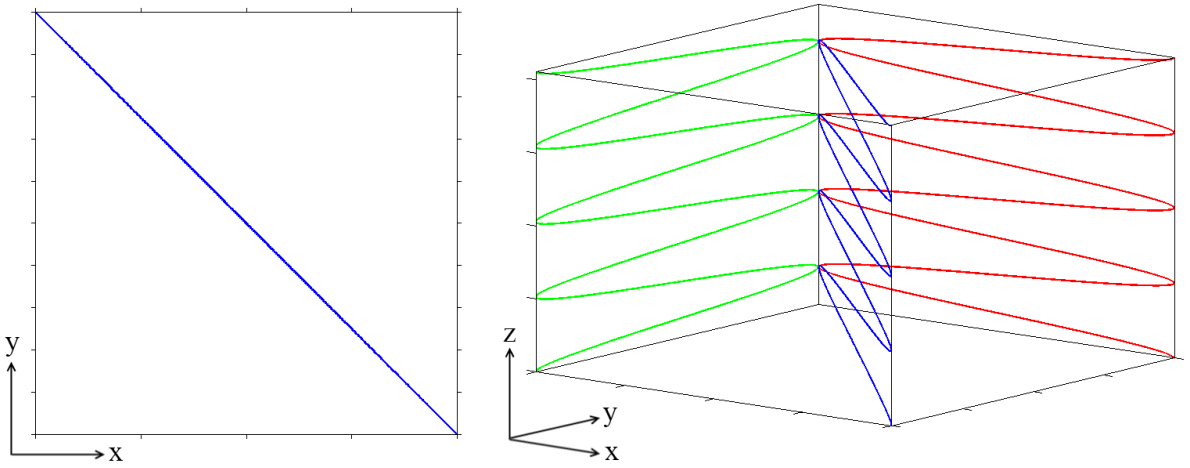

Figure 2-3 – Linear polarization at -45° of a transverse wave comprised of two waves that are out of phase by an odd integer multiple of π and have equal amplitudes. As the wave propagates, its electric field vector describes a straight line in the *x-y* plane. On the right, the two wave components and the resulting wave can be seen (Resulting wave is shown in blue).

This is a state known as linear or plane polarisation. As the wave propagates, its oscillations are confined to a single plane. Viewed in the *x-y* plane, the resulting field vector describes a line. The gradient of this line is defined by the relative amplitudes of the two waves. This can be seen in **Figure 2-2** and **Figure 2-3**

When ε is equal to an odd integer multiple of $\frac{\pi}{2}$ and the wave amplitudes are equal, the phase difference is such that the resulting wave is circularly polarized. This can be seen in **Figure 2-4**.

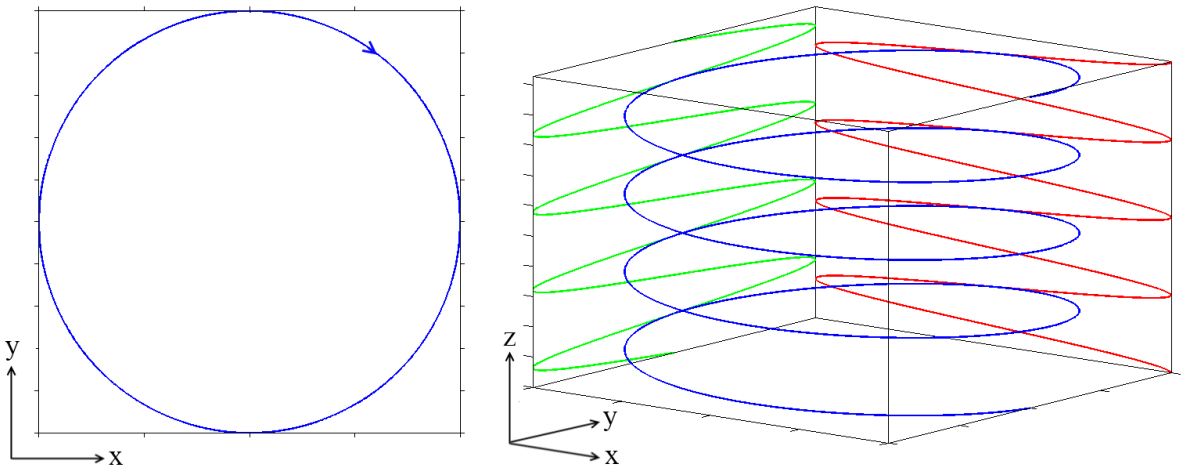

Figure 2-4 – Circular polarization of a transverse wave. The phase difference between the two waves is $\frac{\pi}{2}$ and the wave amplitudes are equal. As can be seen on the left, the electric field vector rotates in the *x-y* plane as the wave propagates in the *z* direction. On the right, the two component waves and the resulting wave can be seen. The direction of propagation of the wave is in the positive *z*-direction – therefore, this wave exhibits right-handed polarization.

Another important state of polarization is known as elliptical polarization. This can occur as a result of several factors. It occurs when the phase difference is not 0 or an odd multiple of $\frac{\pi}{2}$ – in this case, the wave amplitudes can be identical or different, and the polarization will be elliptical. It can also occur when the phase difference is a multiple of $\frac{\pi}{2}$, but the wave amplitudes are not equal. The path described by the tip of the electric field vector in the *x-y* plane is an ellipse, as seen in **Figure 2-5**.

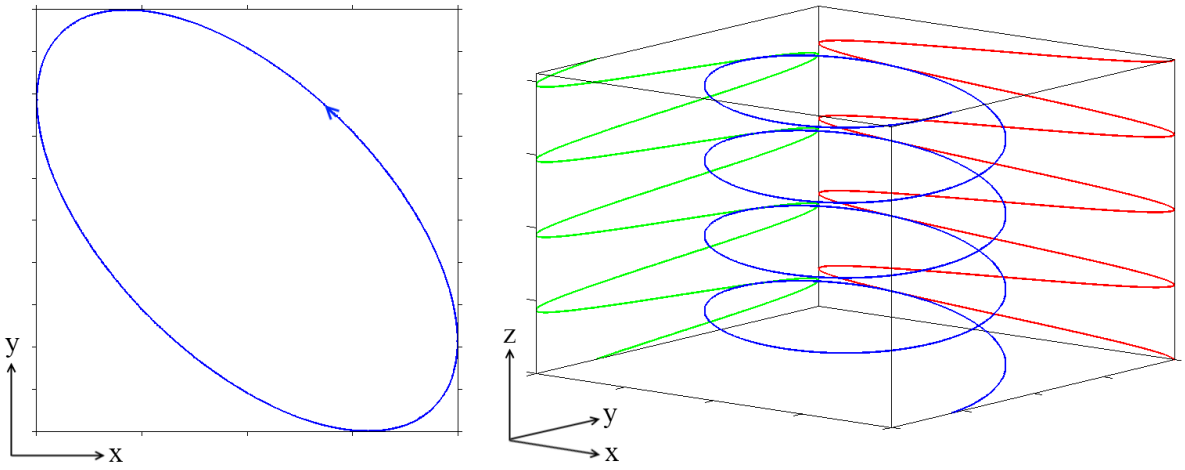

Figure 2-5 – Elliptical polarization caused by a phase difference of -125°. The two component waves are of equal amplitude. The wave is travelling in the positive z-direction, and exhibits left-handed polarization.

Elliptical polarization is the most general description of the polarization state of a wave – all other states are special cases of this state.

When considering circular and elliptical polarization, we also consider whether the wave is left or right circularly polarized. The convention adopted by physicists is to point the thumb of the left or right hand towards the source of the wave, in the opposite direction to the wave's propagation. If the curl of the fingers of the left hand matches the direction of rotation of the electric field vector, then the field is left polarized – likewise, if the curl of the fingers of the right hand matches the rotation of the electric vector, then the wave is right polarized. This can be applied to both circular and elliptical polarizations.

2.2.2 - The Stokes Parameters

The equation of an ellipse can be produced from equations (2.3) and (2.4)

$$\left(\frac{\vec{E}_x(z,t)}{A_x}\right)^2 + \left(\frac{\vec{E}_y(z,t)}{A_y}\right)^2 - 2\frac{\vec{E}_x(z,t)}{A_x}\frac{\vec{E}_y(z,t)}{A_y}\cos\varepsilon = \sin^2\varepsilon \tag{2.8}$$

By time averaging (2.8) we can produce the Stokes parameters

$$\left(A_x^2 + A_y^2\right)^2 = \left(A_x^2 - A_y^2\right)^2 + \left(2A_xA_y\cos\varepsilon\right)^2 + \left(2A_xA_y\sin\varepsilon\right)^2 \tag{2.9}$$

$$S_0^2 = S_1^2 + S_2^2 + S_3^2 \tag{2.10}$$

These four parameters are very often written in the form of a vector.

$$\mathbf{S} = \begin{bmatrix} S_0 \\ S_1 \\ S_2 \\ S_3 \end{bmatrix} = \begin{bmatrix} I \\ Q \\ U \\ V \end{bmatrix} = \begin{bmatrix} A_x^2 + A_y^2 \\ A_x^2 - A_y^2 \\ 2A_xA_y \cos\varepsilon \\ 2A_xA_y \sin\varepsilon \end{bmatrix} \tag{2.11}$$

The first parameter I is the irradiance of the beam – the second parameter indicates the level of linear polarization of the beam in the vertical and horizontal plane. If the beam is vertically polarized, then the value of Q is -1; if horizontally polarized, Q=1. U describes the level of 45° polarization. If the beam is polarized at 45°, then U=1; if at -45°, U=-1. The final parameter V indicates the level of circular polarization. For a right circularly polarized beam, V=1; for left circularly polarized, V=-1.

Some common polarization states as described by the Stokes vector are shown below. I_0 is the intensity, and is often normalised to 1.

Linear horizontally polarised: $I_0 \begin{bmatrix} 1 \\ 1 \\ 0 \\ 0 \end{bmatrix}$

Linear vertically polarised: $I_0 \begin{bmatrix} 1 \\ -1 \\ 0 \\ 0 \end{bmatrix}$

Linearly polarised at +45°: $I_0 \begin{bmatrix} 1 \\ 0 \\ 1 \\ 0 \end{bmatrix}$

Right circularly polarised: $I_0 \begin{bmatrix} 1 \\ 0 \\ 0 \\ 1 \end{bmatrix}$

Left elliptically polarised, ε=-125°: $I_0 \begin{bmatrix} 1 \\ 0 \\ -0.8192 \\ -0.5736 \end{bmatrix}$

2.2.3 - Mueller Matrices

If an incoming electromagnetic wave is described by a Stokes Vector, an optical system with which it interacts is described by a Mueller matrix M. When a Stokes vector $\boldsymbol{S}$ describing an incident wave is multiplied by a Mueller matrix, the resulting vector is the transmitted Stokes vector $\boldsymbol{S'}$ for that interaction.

$$\boldsymbol{S'} = M\boldsymbol{S} \tag{2.12}$$

Each Matrix consists of 16 elements, and represents the action of an optical component on the polarisation state of the incident light. The Mueller matrix for a half-wave retarder plate [17], such as that used in the Laser Diffractometer [8] (described in a later chapter) is:

$$\begin{bmatrix} 1 & 0 & 0 & 0 \\ 0 & 1 & 0 & 0 \\ 0 & 0 & -1 & 0 \\ 0 & 0 & 0 & 1 \end{bmatrix} \tag{2.13}$$

These are a useful tool when dealing with Geometric Optics, as the polarisation state of each light ray must be accurately calculated as it passes through the object. The GO code by Macke [18], and hence RTDF, make use of Stokes vectors and Mueller matrices for ray interactions with flat polygonal crystal facets. For each interaction, 3 Mueller matrices are multiplied together to produce a final Mueller matrix. This Matrix is then applied to the Stokes vector of the incident light. The first Matrix transforms the incident Stokes vector to the point where the interaction will occur. To maintain the polarisation state of the incident ray, this can be set to an identity Matrix, an approach used in RTDF. A Stokes vector is defined relative to a plane, and for GO calculations this is usually the scattering plane. For each interaction, the Stokes vector is rotated into a new reference plane. This rotation is applied using a rotation matrix $R(\alpha)$, where the rotation angle is anti-clockwise when looking along the direction of propagation. After the rotation of the incident vector, a 4x4 Matrix F describing the Fresnel coefficients [19] is applied. Multiplying the incident Mueller matrix by the Rotation matrix and then the Fresnel matrix will produce the Mueller Matrix for the interaction. The rotation matrix and Fresnel matrix for reflected and transmitted light are shown below. The vectors describing the reflected and transmitted light have been resolved into parallel (||) and perpendicular (⊥) components with respect to the plane of incidence: $r_{\parallel}$ and $r_{\perp}$ are the respective amplitude reflection coefficients, and $t_{\parallel}$ and $t_{\perp}$ are the amplitude transmission coefficients.

$$R(\alpha) = \begin{bmatrix} 1 & 0 & 0 & 0 \\ 0 & \cos 2\alpha & \sin 2\alpha & 0 \\ 0 & -\sin 2\alpha & \cos 2\alpha & 0 \\ 0 & 0 & 0 & 1 \end{bmatrix} \tag{2.14}$$

$$F_{reflection} = \frac{1}{2}\begin{bmatrix} r_{\parallel}r_{\parallel}^* + r_{\perp}r_{\perp}^* & r_{\parallel}r_{\parallel}^* - r_{\perp}r_{\perp}^* & 0 & 0 \\ r_{\parallel}r_{\parallel}^* - r_{\perp}r_{\perp}^* & r_{\parallel}r_{\parallel}^* + r_{\perp}r_{\perp}^* & 0 & 0 \\ 0 & 0 & 2Re(r_{\parallel}r_{\perp}^*) & 2Im(r_{\parallel}r_{\perp}^*) \\ 0 & 0 & -2Im(r_{\parallel}r_{\perp}^*) & 2Re(r_{\parallel}r_{\perp}^*) \end{bmatrix} \tag{2.15}$$

$$F_{transmission} = \frac{1}{2}\begin{bmatrix} t_{\parallel}t_{\parallel}^* + t_{\perp}t_{\perp}^* & t_{\parallel}t_{\parallel}^* - t_{\perp}t_{\perp}^* & 0 & 0 \\ t_{\parallel}t_{\parallel}^* - t_{\perp}t_{\perp}^* & t_{\parallel}t_{\parallel}^* + t_{\perp}t_{\perp}^* & 0 & 0 \\ 0 & 0 & 2Re(t_{\parallel}t_{\perp}^*) & 2Im(t_{\parallel}t_{\perp}^*) \\ 0 & 0 & -2Im(t_{\parallel}t_{\perp}^*) & 2Re(t_{\parallel}t_{\perp}^*) \end{bmatrix} \tag{2.16}$$

Given a 4x4 identity matrix I, the Mueller matrices for reflected and transmitted light are:

$$M_{reflected} = F_r R(\alpha) I \tag{2.17}$$

$$M_{transmitted} = F_t R(\alpha) I \tag{2.18}$$

As we can calculate the Mueller matrix for a given interaction, it stands to reason that it would be possible to compute a matrix for a full scattering event. Such a matrix is called the Scattering matrix (also known as the

phase matrix). The elements of the scattering matrix describe a scattering event in terms of intensity and polarization.

$$\begin{bmatrix} P_{11} & P_{12} & P_{13} & P_{14} \\ P_{21} & P_{22} & P_{23} & P_{24} \\ P_{31} & P_{32} & P_{33} & P_{34} \\ P_{41} & P_{42} & P_{43} & P_{44} \end{bmatrix} \tag{2.19}$$

The sixteen elements of the scattering matrix are, in general, nonzero. However, let us consider a single particle that is undergoing random rotation – for each orientation of the particle, a new scattering matrix is formed. The final scattering matrix for light incident on this randomly oriented particle is simply the sum of the individual matrices, and symmetry relations cause several of the terms to become zero [19]. Some other substitutions can also be made, as shown in (2.20).

$$\begin{bmatrix} P_{11} & P_{12} & 0 & 0 \\ P_{12} & P_{22} & 0 & 0 \\ 0 & 0 & P_{33} & P_{34} \\ 0 & 0 & -P_{34} & P_{44} \end{bmatrix} \tag{2.20}$$

Throughout this thesis, two of the terms in this matrix are of particular importance: p_{11}, known as the *Phase Function*, and p_{12}, which is used to derive a term known as the *degree of linear polarization*.

2.2.4 - The Phase Function

The phase function is the most important scattering result used throughout this thesis. It defines the intensity of the scattered light as a function of the polar angle θ and the azimuthal angle φ, and it is standard practise to normalise the function over all space, using the relation shown in (2.21).

$$\frac{1}{4}\int_{4\pi} P_{11}(\theta,\varphi)d\Omega = \frac{1}{4\pi}\int_0^{2\pi}\int_0^{\pi} P_{11}(\theta,\varphi)\sin(\theta)d\theta d\varphi = 1 \tag{2.21}$$

However, when the phase function is referred to throughout this thesis, the azimuthally-averaged phase function will be used. By integrating over φ between 0 and 2π, the phase function becomes a function of θ between 0 and π only. The normalisation condition now becomes

$$\frac{1}{2}\int_0^{\pi} P_{11}(\theta)\sin(\theta)d\theta = 1 \tag{2.22}$$

In **Figure 2-6**, the phase function for a non-absorbing sphere of radius 5μm with incident light of wavelength λ=0.5145μm is shown. Due to the high dynamic range of intensity of the scattered light, when a phase function is presented in graphical format the ordinate is given in logarithmic (base 10) format.

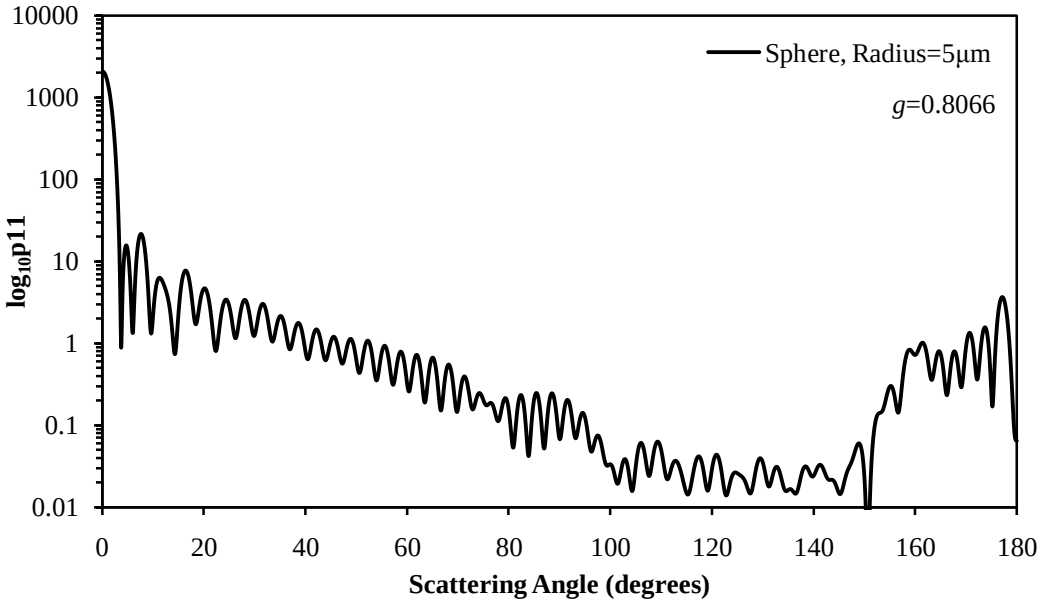

Figure 2-6 – The azimuthally averaged phase function as calculated using Mie Theory for a sphere of radius 5μm and refractive index 1.55 + 0i. The incident light is of wavelength λ=0.5145μm.

2.2.5 - Asymmetry Parameter

A parameter derived from the phase function indicates the degree to which a phase function scatters either in the forward ($0°<\theta<90°$) or backward ($90°<\theta<180°$) direction. It is defined by

$$g = \frac{1}{2}\int_0^{\pi} P_{11}(\theta)\sin(\theta)\cos(\theta)d\theta \tag{2.23}$$

The addition of the $\cos(\theta)$ causes forward scattering to contribute positively to the asymmetry parameter, while backward scattering will decrease it. For the phase function in **Figure 2-6**, the asymmetry parameter has been calculated to be g = 0.8066.

2.2.6 - Degree of Linear Polarization

The *degree of polarisation* for light with Stokes Parameters *I,Q,U* & *V* is given by the ratio

$$p = \frac{\sqrt{Q^2 + U^2 + V^2}}{I} \tag{2.24}$$

This can be separated into two parts, namely the degree of linear polarisation and degree of circular polarisation.

$$p_{linear} = \frac{\sqrt{Q^2 + U^2}}{I} \tag{2.25}$$

$$p_{circular} = \frac{V}{I} \tag{2.26}$$

The Stokes Parameters for unpolarized incident light are given by

$$\mathbf{S_i} = I_0 \begin{bmatrix} 1 \\ 0 \\ 0 \\ 0 \end{bmatrix} = \begin{bmatrix} I_0 \\ 0 \\ 0 \\ 0 \end{bmatrix} \tag{2.27}$$

When we apply the scattering matrix (2.19), the scattered Stokes Parameters are given by

$$\mathbf{S_s} = \begin{bmatrix} P_{11}I_0 \\ P_{21}I_0 \\ P_{31}I_0 \\ P_{41}I_0 \end{bmatrix} \tag{2.28}$$

Utilizing the simplified scattering matrix resulting from the application of symmetry relations (2.20) for a randomly aligned particle, $P_{31} = 0$, $P_{41} = 0$ and $P_{12} = P_{21}$. Therefore, we can now define the degree of linear polarisation for unpolarised incident light as

$$p_{linear} = -\frac{P_{12}}{P_{11}} \tag{2.29}$$

Figure 2-7 shows the degree of linear polarisation as calculated using Mie Theory for a sphere of radius 5μm with incident light of wavelength λ=0.5145μm.

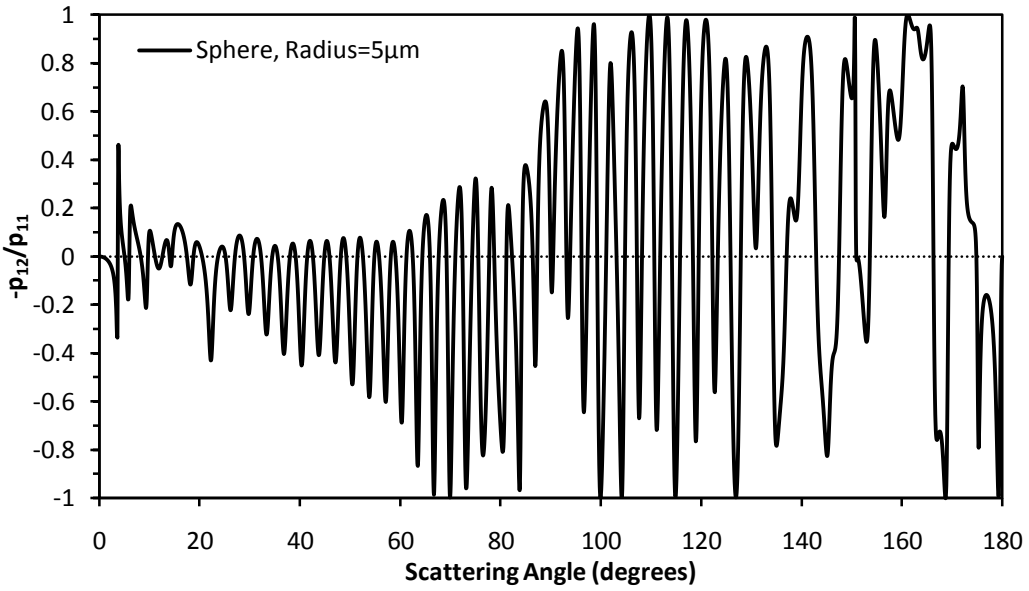

Figure 2-7 – The degree of linear polarisation as calculated using Mie Theory for a sphere of radius 5μm and refractive index 1.55 + 0i. The incident light is of wavelength λ=0.5145μm

The degree of linear polarisation indicates how much the light is vertically or horizontally polarised with respect to a horizontal reference plane (+ve = horizontally polarised, -ve = vertically polarised).

Chapter 3 - Geometric Optics

3.1 - The Ray Approximation

Viewed at a distance comparable to the wavelength of the radiation, the wave fronts (surfaces of constant phase) emitted by a point source are spherical and propagate with radial symmetry away from the source. When viewed at a distance much larger than the wavelength of the emitted waves, the wave fronts can be considered to be planar. The waves can be considered to be propagating in a direction perpendicular to the wave front. When a line is drawn parallel to this direction of propagation we can regard this as a light ray – these are very convenient to use when considering the path which light will take.

3.1.1 - Light Propagation through changing media.

The propagation speed of light in a vacuum is a well known constant, having a value of 299,792,458 meters per second (often simplified as 300,000,000 meters per second). The first calculations to determine the speed of light were performed in the 17th century, and the value we now know as c was not finalised until 1975. The speed of light in a vacuum is related to both the permittivity of free space ε_0, and the permeability of free space μ_0, by the equation

$$c = \frac{1}{\sqrt{\varepsilon_0 \mu_0}} \tag{3.1}$$

When a wave traverses through any medium (that is not a vacuum) its velocity is reduced. The *refractive index* of a medium is a measure of how the velocity of a wave is reduced relative to its velocity in a vacuum. It takes the form $n = n_r + in_i$, where the imaginary component describes the absorption of light by the material through which it is travelling. In cases where the imaginary component is very small, such as water at visible wavelengths, it is often omitted completely, and the refractive index becomes $n = n_r$. The GO and RTDF models described and used later in this thesis allow for a complex refractive index to be considered, and model the absorption of light accordingly.

For radiation travelling through a medium of refractive index n, its phase velocity v is given by

$$v = \frac{c}{n} \tag{3.2}$$

The refractive index of water at room temperature is approximately 1.333. Electromagnetic radiation passing through water will therefore have a phase velocity of approximately $0.75c$.

3.1.2 - Snell's Law

When a wave passes through a boundary between two media of differing refractive index, the direction of propagation of the wave is altered. Depending on the angle of incidence of the wave and refractive indices of the media, the wave will either be totally reflected off the boundary, or part of the amplitude of the wave will be refracted through the interface and part will be reflected. The equation describing the relationship between the

angle of incidence, transmission angle and the refractive indices of each of the media is known as **Snell's Law** (also known as Descartes' law, or the Snell-Descartes' law). The law states that the ratio of the sine of the incident angle to that of the transmitted angle is the same as the ratio of the refractive index of the transmitted medium to that of the incident medium.

$$n_1 \sin\theta_1 = n_2 \sin\theta_2 \tag{3.3}$$

It is this law that describes why a straight object standing in water will appear to be bent at the boundary between air and water. **Figure 3-1** demonstrates how a ray incident on an air-water boundary is partially reflected through the boundary, and partially reflected back. The **Fresnel equations** describe the relative amplitudes of the reflected and transmitted waves, and will be covered in the next section.

As has been described above, when a wave is incident on a boundary between two media, the wave is transmitted at an angle depending on the incident angle of the wave and the ratio of the refractive indices of the two media. A further important concept which arises is that of the **Critical Angle**. When the refractive index of the incident medium is larger than that of the medium into which the ray is transmitted, there will be a maximum angle at which transmission of the wave will occur. Any light incident at an angle equal to or greater than the critical angle will

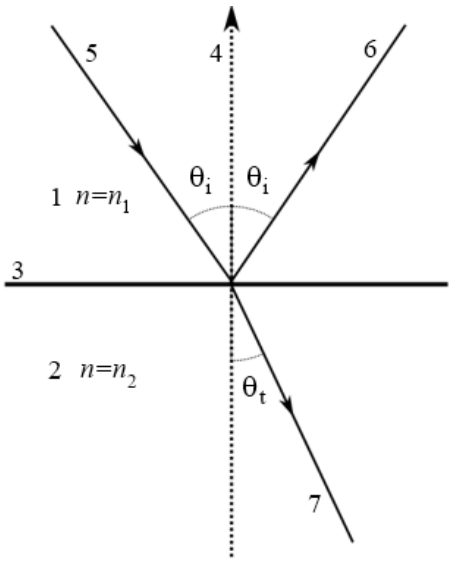

Figure 3-1 - A diagram showing a ray of light incident on a boundary between two media of differing refractive index. The labelled components of the diagram are: 1: Medium 1 – In this case air, with a refractive index of approximately 1. 2: Medium 2 – In this case water, with a refractive index of approximately 1.333. 3: The boundary between the two media. 4: The normal to the boundary. 5: The incident ray, incident on the boundary at an angle $\boldsymbol{\theta_i = 35°}$ to the normal. 6: Reflected ray, leaving the boundary at angle $\boldsymbol{\theta_i}$ to the normal, and remaining inside medium 1. 7: The transmitted ray, which refracts through the boundary layer and travels through medium 2. It is transmitted at angle $\boldsymbol{\theta_t = 25.49°}$ to the normal.

undergo **Total Internal Reflection**. By setting the transmitted angle to 90° and applying the above equation, it is a simple matter to determine a formula for the critical incident angle.

$$\theta_{crit} = \sin^{-1}\frac{n_2}{n_1} \tag{3.4}$$

For a ray in water incident on a water/air boundary, an incident angle greater than approximately 48.61° will result in 100% of the amplitude of the ray being reflected back into the water.

3.1.3 - The Fresnel Equations

The Fresnel Equations describe the relationship between the amplitudes of the reflected and transmitted waves at a boundary. The laws can be stated in terms of incident and transmitted angles, and there are separate cases for light polarized perpendicular to (⊥) and parallel (||) to the plane of incidence.

$$r_{\parallel} = \frac{\tan(\theta_i - \theta_t)}{\tan(\theta_i + \theta_t)} \tag{3.5}$$

$$r_{\perp} = -\frac{\sin(\theta_i - \theta_t)}{\sin(\theta_i + \theta_t)} \tag{3.6}$$

$$t_{\parallel} = \frac{2\sin\theta_t \cos\theta_i}{\sin(\theta_i + \theta_t)\cos(\theta_i - \theta_t)} \tag{3.7}$$

$$t_{\perp} = \frac{2\sin\theta_t \cos\theta_i}{\sin(\theta_i + \theta_t)} \tag{3.8}$$

These equations describe the fractional amplitudes for the reflected and transmitted waves. In order to give the intensities for the waves, the above values must be squared. How the reflected and transmitted intensities for a wave incident on an air/water boundary vary according to incident angle are shown in **Figure 3-2** & **Figure** 3-3.

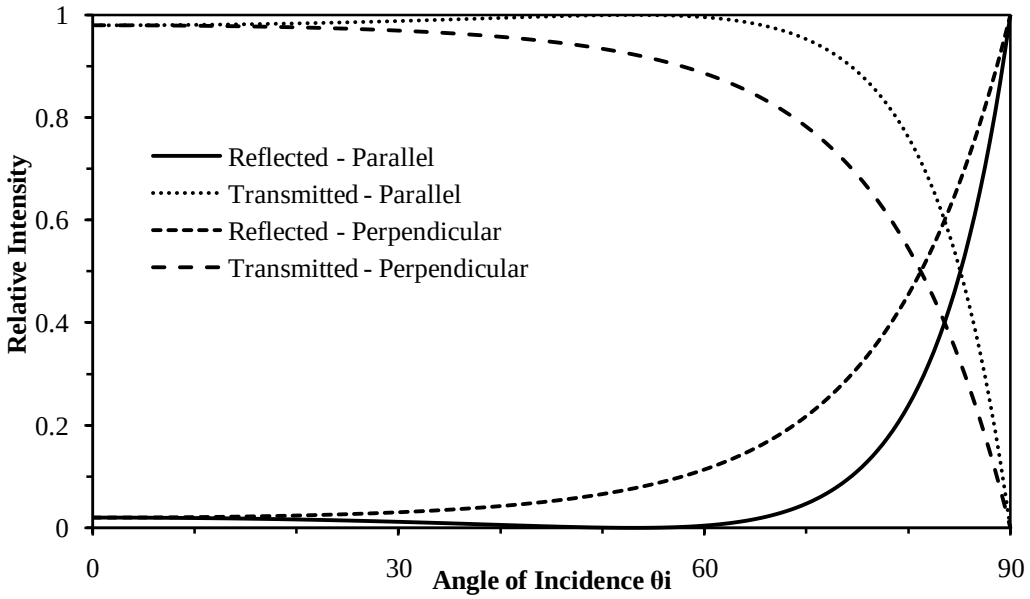

Figure 3-2 – Relative intensities of the reflected and transmitted components for rays in air (n=1) incident on water (n=1.33). Parallel and perpendicular polarizations are shown.

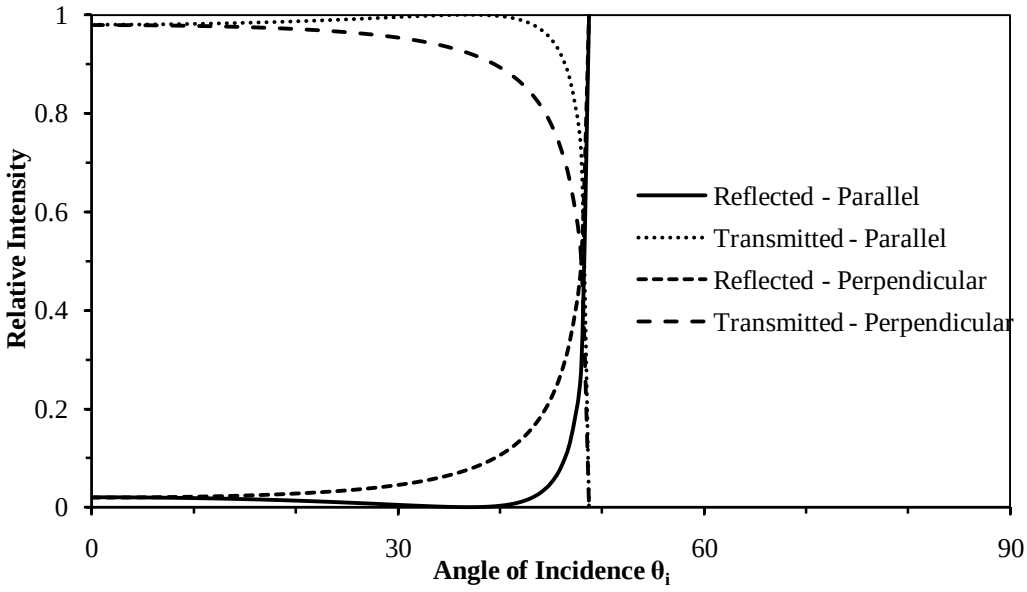

Figure 3-3 – Relative Intensities for reflected and transmitted rays in water (*n*=1.33) incident on a boundary with air (*n*=1). The critical angle for this interaction is ~48.75°. When the incident angle is equal to or greater than the critical angle, no part of the ray amplitude is transmitted - total internal reflection takes place.

3.2 – Important Light Scattering considerations

3.2.1 - Scattering Cross Sections

Scattering cross sections are used in a number of areas of physics – when used in condensed matter physics, the *photoionisation cross section* states the probability of the ionisation due to the emission of an electron. Here, however, they are used to describe the removal of flux from an incident beam due to the presence of a scatterer. Two of the most important values are known as the scattering cross-section (C_{sca}) and the absorption cross-section (C_{abs}). These values describe the removal of energy from the incident beam due to scattering and absorption, respectively. The total amount of flux removed from the beam is known as the extinction cross-section (C_{ext}), and is simply the sum of the scattering and absorption cross-sections.

$$(C_{ext}) = (C_{sca}) + (C_{abs}) \tag{3.9}$$

When considering cross sections in the GO code by Macke [18] and RTDF [15], two cross sections must be considered –the final scattering results are a result of both projected area diffraction and geometric ray tracing, and a cross section for each component is calculated. The ray tracing component C_{ray} is defined by

$$C_{ray} = A_{proj}\frac{E_{out}}{E_{in}} \tag{3.10}$$

where A_{proj} is the average projected area of the particle, and E_{in} and E_{out} denote the amount of energy entering and leaving the particle due to ray-tracing. The diffraction component C_{diff} denotes the amount of scattering of the incident beam as a result of diffraction. When these are taken into account, the phase function for a GO with projected area diffraction calculation is given by

$$P(\theta) = \frac{C_{ray}P_{ray} + C_{diff}P_{diff}}{C_{diff} + C_{ray}} \tag{3.11}$$

where P_{ray} and P_{diff} are the ray tracing and diffraction phase functions.

3.2.2 - Size Parameter

An important quantity in light scattering is the size of the scatterer compared to the wavelength of the incident light. This is a dimensionless value known as the **Size Parameter**, often denoted by X_s, and for a sphere is given by

$$X_s = \frac{2\pi r}{\lambda} \tag{3.12}$$

where r is the radius of the sphere, and λ is the wavelength of the incident light. This thesis is primarily concerned with particles that can be considered prolate or oblate spheroids, and the above equation cannot be used. In this thesis two methods are used to calculate the size parameter of a spheroid – the first is equal-volume-sphere, where the volume of the spheroid is calculated and the radius for a sphere of equal volume is used to calculate the size parameter. The volume V_{sphere} of a sphere of radius r is given

$$V_{sphere} = \frac{4}{3}\pi r^3 \tag{3.13}$$

The volume $V_{spheroid}$ of a spheroid with axes a, b, where $b = \varepsilon a$ and ε is the aspect ratio, is given by

$$V_{spheroid} = \frac{4}{3}\pi a^2 b \tag{3.14}$$

By setting the two volumes equal, solving for r and then substituting into the size parameter equation, the equal-volume-sphere size parameter for a spheroid is given by

$$X_{spheroid} = \frac{2\pi\sqrt[3]{a^2 b}}{\lambda} \tag{3.15}$$

This method is identical for prolate and oblate spheroids. The second method used is equal-surface-area-sphere, where the surface area of the spheroid is calculated, and the radius for a sphere of equal surface area is used to calculate the size parameter. The surface area for a sphere is given by

$$A_{sphere} = 4\pi r^2 \tag{3.16}$$

The surface area calculations for prolate and oblate spheroids differ – the surface area for a prolate spheroid where $a>b$ is given by

$$A_{prolate} = 2\pi\left(a^2 + \frac{ab\alpha}{\sin\alpha}\right) \tag{3.17}$$

where

$$\alpha = \cos^{-1}\left(\frac{a}{b}\right) \tag{3.18}$$

By setting the two surface area values equal, solving for *r* and then substituting into the size parameter equation, the equal-surface-area-sphere size parameter for a prolate spheroid is given by

$$X_{prolate} = \frac{\sqrt{2}\pi}{\lambda}\sqrt{\left(a^2 + \frac{ab\alpha}{\sin(\alpha)}\right)} \tag{3.19}$$

For an oblate spheroid with $b>a$, the surface area is given by

$$A_{oblate} = 2\pi\left[a^2 + \frac{b^2}{\sin(\beta)}\ln\left(\frac{1+\sin(\beta)}{\cos(\beta)}\right)\right] \tag{3.20}$$

where

$$\beta = \cos^{-1}\left(\frac{b}{a}\right) \tag{3.21}$$

Therefore, the equal-surface-area-sphere size parameter for an oblate spheroid is given by

$$X_{oblate} = \frac{\sqrt{2}\pi}{\lambda}\sqrt{\left[a^2 + \frac{b^2}{\sin(\beta)}\ln\left(\frac{1+\sin(\beta)}{\cos(\beta)}\right)\right]} \tag{3.22}$$

Chapter 4 - Scattering by Small Particles

The scattering, absorption and emission of electromagnetic radiation by small particles is omnipresent, and is central to many science and engineering disciplines. Light scattering phenomena can be observed in rainbows, glories, haloes, white clouds and blue skies that are the direct result of sunlight incident on gas molecules and particles suspended in the Earth's atmosphere [20].

Electromagnetic radiation will propagate in a vacuum with no change in its intensity or polarization state. However, a small particle introduced to the beam will absorb and reradiate the energy in a manner specific to the geometry and composition of the particle. All matter is composed of protons and electrons – illumination of matter by an electromagnetic wave sets these electric charges into oscillatory motion according to the electric field of the incident wave [21]. The excited protons and electrons may transfer this energy into other forms (such as heat) or they may reradiate the energy. It is this secondary radiation that is considered the scattering of energy by the particle.

In order that the scattered electric field at any point in space for a given system can be known, it is necessary to generate solutions for the electromagnetic wave equations for that system. For simple homogeneous particles, this can be performed relatively easily. In 1908, Gustav Mie, in an effort to understand the scattering exhibited by gold particles suspended in water, developed and published solutions for the scattering of electromagnetic radiation by spherical particles. Mie was not the first to construct a solution to the problem of scattering by a sphere (it was most likely Lorenz), but his results are the most well-known.

4.1 - Computational Approaches

4.1.1 - Mie Theory

Mie theory derives a three-dimensional wave equation for electromagnetic radiation. When appropriate boundary conditions are enforced at the surface of a sphere, the result is a separable partial differential equation. This equation can be solved by summation of an infinite series of orthogonal products, the details of which can be found in most texts on Light Scattering, such as [22]. Many FORTRAN codes are available, notably the code developed by Michael Mishchenko [23] [24]. In this thesis, where Mie results have been computed, this code has been used.

4.1.2 - SVM – Separation of Variables Method

While Mie theory offers a perfect solution to the problem of computing light scattering from a sphere, it is only useful as a first order approximation of scattering by non-spherical particles. In theory, if it is possible to formulate a coordinate system that coincides with a particle surface, then it is possible to apply a separation of variables method. Solutions have been obtained for homogeneous arbitrary spheroids and infinite cylinders [25], but it is generally not possible to define a coordinate system that coincides with the surface of a hexagonal column. In most cases, this means that it is not possible to use this method for studying cirrus ice. On the basis of a formulation of SVM for infinitely extended hexagonal cylinders [26], an approximation for finitely extended hexagonal columns has been derived. This has shown a moderate amount of success [27], but is

limited to intermediate size parameter columns of large aspect ratio ($L/2r \geq 3$). This method is currently (and is likely to remain) unsuitable for calculating scattering by Saharan dust particles, due to their lack of symmetry and random surface features (as shown in Chapter 8).

A number of methods have been developed for calculating scattering on arbitrarily shaped particles – some of these are detailed below.

4.1.3 - T-Matrix

The T-Matrix method [28] [29] is a largely exact technique for calculating scattering properties on non-spherical particles. The incident and scattered fields are expanded into vector spherical wave functions, and are related by the use of a Transformation Matrix (T-Matrix). This transformation Matrix is only dependent on the properties of the scatterer, and once calculated allows any scattering characteristics of the scatterer to be determined. The T-Matrix method is particularly suited to particle shapes with axial symmetry and smaller size parameter, but has been applied to hexagonal columns of size parameter approximately twenty [30]. While the method is theoretically applicable to any size and geometry of particle, the computational demands become intractable as the size and complexity of the particle increase. As computational power increases and implementations of T-matrix become capable of dealing with ever larger and more complex particles, this is likely to become the favoured method for computation of light scattering characteristics.

4.1.4 - DDA - Discrete Dipole Approximation

The Discrete Dipole Approximation (DDA) [31] is a numerical method for calculating scattering. The particle is divided up into an array of polarisable points. When an electromagnetic wave is incident on the points, each point is excited according to the incident wave and the scattered wave from all the other points. The entire scattered field for the particle can be calculated by considering the electromagnetic field due to each point. DDA is capable of dealing with any particle geometry, but the computation time needed to gain convergence for very large numbers of polarisable points means that the method is generally applied to smaller size parameters. An overview of the DDA method and discussion on the accuracy of different implementations can be found in [32].

4.1.5 - FDTD - Finite Difference Time Domain

The Finite Difference Time Domain (FDTD) method is another numerical method for calculating scattering that allows for complex particle shapes to be modelled. The method was introduced by Yee [33] and involves splitting the particle up into cubic regions known as Yee Cells. The electromagnetic variations at each cell are iterated in time steps according to the influence of an electromagnetic plane wave. The electromagnetic state of each cell becomes stable after a sufficient number of time steps. The FDTD method is a versatile method, but is, like many numerical methods, limited due to computational restraints. Each Yee Cell must be of sufficiently small size to allow the electromagnetic interactions to be calculated accurately (size << wavelength of incident light), and also small enough to model all the features of the particle. It is also important to avoid 'staircasing,' where the Yee Cells produce roughness on the surface of the particle. The effect can be seen to have a large effect on very small particles, where the roughness produced by the cells is not insignificant when compared to

the size of the particle [34]. The volume encompassing the particle must also be divided into Yee Cells, and this leads to very large computational domains. Due to these computational demands, scattering properties for particles of size parameter approximately forty can be calculated when the refractive index is close to one. For particles of higher refractive index, the largest size parameter which can be calculated is approximately twenty.

4.1.6 - GO - Geometric Optics

The term Geometric Optics refers to the approach whereby the path of a ray is traced as it is incident on a scatterer. The application of Snell's law allows us to determine the path of the ray and subsequent refracted and reflected rays through the scatterer, and applying the Fresnel equations allows us to determine the intensity of these sub rays. For scattering by a particle, a Monte Carlo approach can be taken, where a bundle of unpolarized and parallel rays are given random starting points. The path for each ray through the scatter is calculated, and the rays leaving the scatterer are collected into angular bins. Knowing the intensity and polarization state of each outgoing ray allows the scattering properties of the particle to be obtained.

The pure ray tracing method is very flexible, as it can be applied to almost any shape of particle, and allows for very rapid computation. Pure ray tracing results are size-independent, and various approaches have been taken to add size dependence to the results. Classical Geometric Optics (GO) is the method whereby pure ray tracing results are combined with the diffraction pattern for the projected area of the object being considered. Although diffraction is not considered in the ray tracing part of the results, the addition of the projected area diffraction enables accurate calculation of scattering properties for large size parameter, randomly oriented, non-spherical particles. For spheres, accurate results when compared with Mie Scattering can be obtained for particles of size parameter >600 [35]. For particles with greater asymmetry, such as spheroids, accurate results with analytic techniques can be found for size parameters of approximately 60.

Improvements to the basic GO method have enabled accurate scattering computation for smaller size parameters. The Improved Geometric Optics method (IGO) [36] is a hybrid technique where ray tracing results are combined with a rigorous treatment of the transformation of the electromagnetic field from the near field to the far field. When applied to ice crystals, this method gives results comparable to FDTD calculations for size parameters of approximately 20. While being a very versatile technique, it is very computationally expensive and the code is not publicly available.

Another improvement to the GO method, and the technique primarily used within this thesis, is Ray Tracing with Diffraction on Facets (RTDF) [15]. Used for computing scattering on polyhedrons, this technique treats each facet of a particle as an aperture. During normal ray tracing calculations, the path a ray will take is determined by the angle of incidence of the ray and the refractive indices of the incident and transmitted media. With RTDF, the ray path is adjusted according to the far-field deflection angle that an energy flow line flowing through a slit would experience. When modelled in 2D, this path adjustment is determined by the size of the slit, the ray distance from the edges of the slit, and the wavelength of the incident light. Extended to 3D, this deflection is modelled using two deflections according to the 2D case.

RTDF offers the flexibility and computational efficiency commonly associated with GO. The addition of an improved diffraction formula produced vast improvements over GO for small size-parameter hexagonal

columns when compared to SVM [16]. The further addition of the capacity to calculate scattering on curved surfaces produced excellent results for scattering on circular cylinders when compared to T-Matrix calculations [37].

Chapter 5 – Experimental Set-up and Method for Measuring Scattering Properties of Saharan Dust Particles.

5.1 - The Electrodynamic Balance (EDB)

The electrodynamic balance was previously developed to facilitate the study of single microscopic particles. A single microparticle can be charged, injected into the trap and then levitated. The levitated particle can then be illuminated by laser light, and its scattering properties measured.

The electrodynamic balance (EDB) [7] used in the experiments reported here is of the double ring double disc type. It consists of two truncated copper cones acting as ac-electrodes, and two indium tin oxide (ITO) coated glass plates with metallic cylindrical extensions acting as dc-electrodes. The upper glass plate has a circular aperture approximately 1.5mm in diameter. A fine tungsten needle is located above the upper dc-electrode, and can be moved in 3 dimensions by use of a micromanipulator. **Figure 5-1** shows the arrangement of these components.

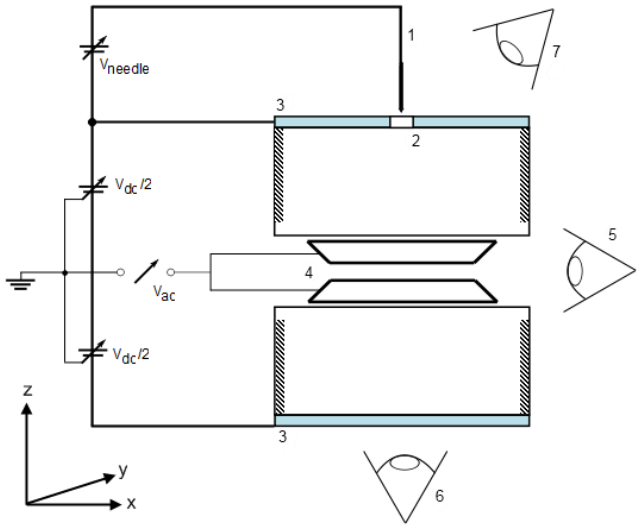

Figure 5-1 - A cross-section representation of the EDB. The labelled components are: 1: Tungsten Needle. 2: Aperture in upper dc-electrode. 3: Coated Glass plates, acting as dc-electrodes. 4: Two truncated hollow cones, acting as ac-electrodes. 5: Horizontal camera with long working distance objective. 6: Vertical camera with long working distance objective. 7: Microscope.

The particles are placed onto small pieces of glass coverslip, which are then placed on the upper dc-electrode. Using the micromanipulator and viewing the top of the upper dc-electrode through the microscope, the tungsten needle is manoeuvred so that it picks up the particle. The needle tip with the particle attached is then placed in the centre of the aperture. The glass plates have a dc-voltage applied to them, and the truncated copper cones have an ac-voltage applied to them. Initially, the upper dc-electrode is positive with regards to the lower dc-electrode. This is to accelerate the particle (after a positive charge has been applied) into the trap. For a silica sphere of radius ~5μm, a suitable ac-voltage would be 1000V at 250Hz, and the dc-voltage would be 24V. The tungsten needle has a large (with regards to the upper dc-electrode) positive voltage applied to it. A larger positive voltage (>800V) will enable the particle to obtain a larger charge, and will be more stable when it is

trapped. After some experimentation, it has been determined that using a short pulse (~20ms duration) as the supply voltage for the needle gives a higher chance of successfully trapping the particle than steadily increasing the voltage. This is because, in the non-pulsed mode, the particle may launch at a lower than optimal voltage, and may not be stable within the trap.

5.1.1 - Modelling of the Particle Trajectory

When the particle is launched, it is subjected to the combined forces of the ac field, aerodynamic drag and gravity:

$$m\frac{\mathrm{d}^2\mathbf{r}}{\mathrm{d}t^2} = q\mathbf{E}(\mathbf{r},t) + mg\mathbf{e}_z + \mathbf{F}_D \tag{5.1}$$

Where m is the particle mass, q is the particle charge and $\mathbf{r}$ is the particle's position. $\mathbf{E}(\mathbf{r},t)$ is the electric field distribution due to the applied ac and dc voltages, g the acceleration due to gravity, $\mathbf{e}_z$ the unit vector pointing directly downwards.

$\mathbf{E}_{\mathrm{ac}}(\mathbf{r},t)$ is the electric field distribution along the vertical axis throughout the centre of the trap due to the ac-potential. Given a known potential $V_{ac}(x=0,y=0,z)$ the electric field can be numerically calculated for this region. The peak electric potential for an applied ac voltage of 1000V throughout the trap is shown in **Figure 5-2.**

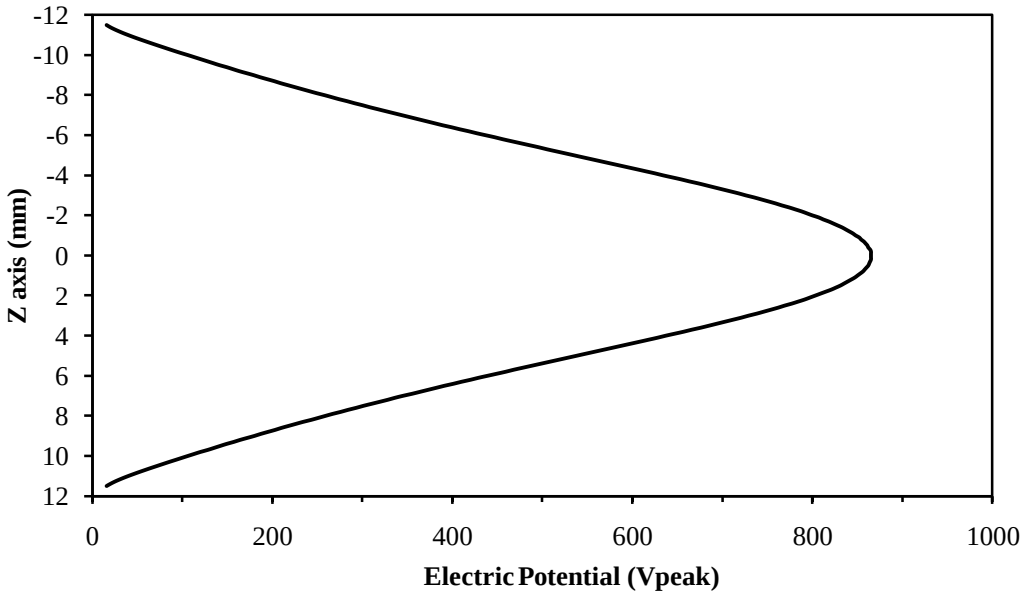

Figure 5-2 - The peak ac-potential along the vertical axis at the centre of the trap. The potential is shown varying across a range of -11.5mm to 11.5mm. This potential is due to an applied voltage of amplitude 1000V

The electric field at a point is equal to the negative gradient of the electric potential V due to the applied ac and dc voltages.

$$\mathbf{E} = -\nabla V \tag{5.2}$$

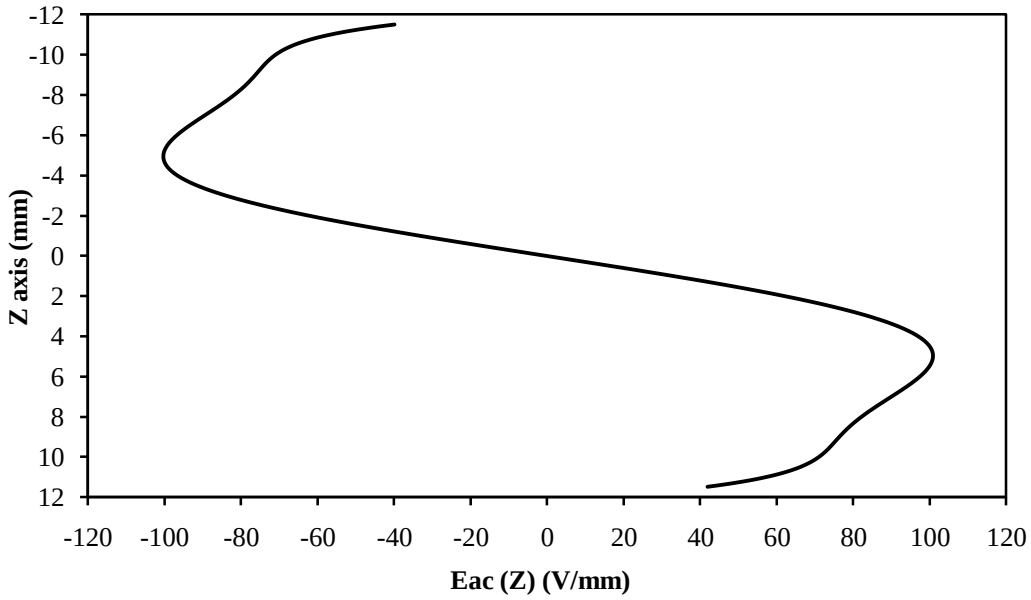

Figure 5-3 – The ac field amplitude along the vertical axis of the trap.

Figure 5-3 shows the ac field amplitude corresponding to the ac-potential along the vertical axis of the trap shown in **Figure 5-1**.

For launching we consider only the *z*-component of the electric field along the vertical symmetry axis of the trap, where the *x* and *y* components of the field are zero. Therefore the field at any given point is:

$$\mathbf{E}_z = -\frac{\delta V}{\delta z} \tag{5.3}$$

$\mathbf{F}_D$ is the aerodynamic drag force. The force is parallel but directly opposite to the direction of motion. It is defined by:

$$\mathrm{F}_{\boldsymbol{D}} = -\frac{1}{2} D A \rho_m \left(\frac{d\mathbf{r}}{dt}\right)\left|\frac{d\mathbf{r}}{dt}\right| \tag{5.4}$$

D is the drag coefficient, A is the projected area of the particle, ρ_m is the density of the medium, and $\frac{d\mathbf{r}}{dt}$ is the velocity of the particle. For low Reynolds numbers *Re*, the drag coefficient D can be approximated as:

$$D = \frac{24}{Re} \tag{5.5}$$

where

$$Re = \left|\frac{d\mathbf{r}}{dt}\right| \frac{l_c \rho_m}{\mu}, \tag{5.6}$$

l_c is the characteristic length of the particle, and μ is the viscosity of the surrounding medium [7]. By solving the equation of motion (Eqn. 5.1), making use of Eqns. 5.2 - 5.6, we can plot the trajectory that the particle will follow after injection. This trajectory modelling is then used to optimise launching parameters for using the EDB.

Figure 5-4 shows the calculated vertical displacement with time for a particle injected into the trap. The figure is for a silica sphere of radius 5μm, density 2700kgm^{-3} and charge 10fC. The viscosity of air is assumed to be 1.8x10^{-5}kgm^{-1}s^{-1} at room temperature. Here, the particle is successfully trapped.

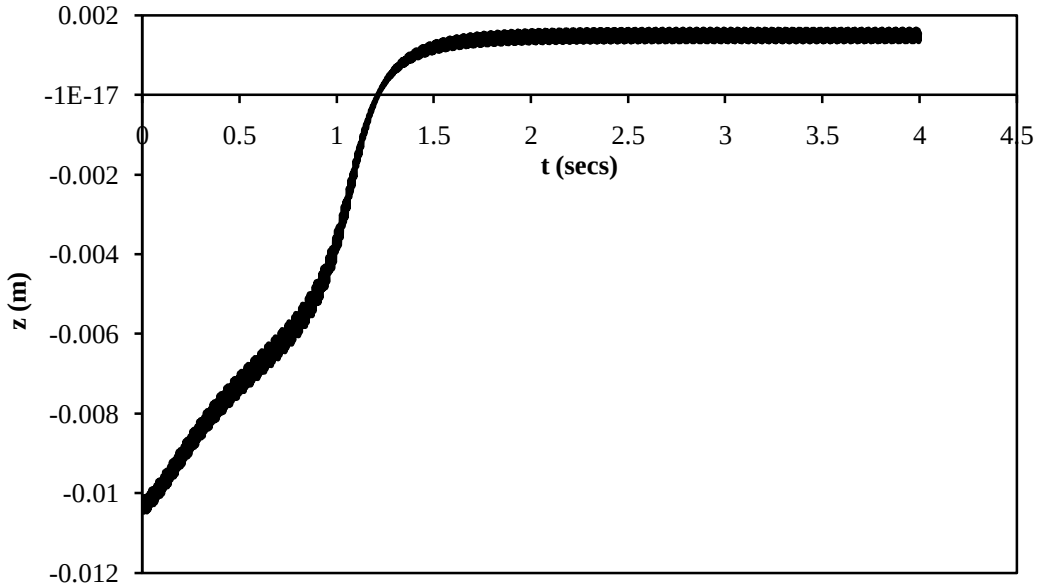

Figure 5-4 - The launch trajectory for a silica sphere of radius 5μm. In this calculation, the ac amplitude is 1000V, the ac frequency is 200Hz, the ejection voltage is 120V and the dc voltage is -6V. The particle enters the trapping region and is accelerated towards the centre of the trap. As the particle passes the centre of the trap however, it is rapidly slowed, and reaches equilibrium approximately 2 seconds after injection. The z axis is inverted. The width of the trajectory is due to the particle oscillating at a very high frequency.

Figure 5-5 demonstrates what happens when the trap parameters are set incorrectly, for the particle in question. Using the same parameters as in **Figure 5-4** but with a particle of radius 6μm is insufficient to successfully trap the particle. The increased mass of the sphere causes it to pass straight through the trap.

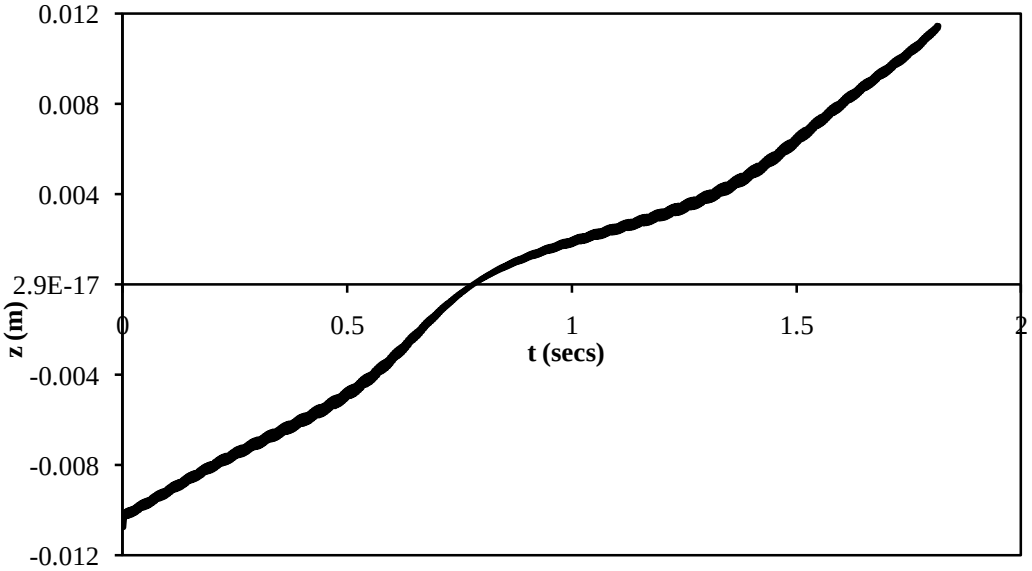

Figure 5-5 – The launch trajectory for a silica sphere of radius 6 μm. Using the same trap parameters as in **Figure 5-4**, the particle is too heavy to be trapped, and passes through the trap.

When the particle is observed to enter the field of view of the horizontal camera, the polarity of the dc-voltages is reversed. This causes the upper dc-electrode (now negative) to pull the particle upwards, and the lower electrode (now negative) to repel the particle. The dc-voltage is then adjusted so that gravity is exactly compensated for by the dc-field and the particle is moved to the centre of the trap, which is the most stable area.

When the particle is located in the trap centre, it is then possible to begin scattering experiments. The particle is illuminated by laser light of wavelength 514.5nm, and the light scattered by the particle is incident on a Laser Diffractometer (LD) [8] and a Linear Photodiode array (LPA) [9]. A plan view of the arrangement of these components can be seen in **Figure 5-6**.

5.1.2 - Large-Angle Scattering Measurements

The Laser Diffractometer enables measurement of scattered flux from scattering angles 3º to 177º. As can be seen in **Figure 5-6**, the light scattered by the levitated particle is incident on an array of optical fibres arranged at 1 degree intervals in a semicircle around the EDB. The optical fibres pass the collected light to a photomultiplier, where it is transformed into an electrical signal and then amplified. In order that the system can differentiate between the fibres, the ends of the fibres are arranged in a circle in front of the photomultiplier. A disc with a single eccentric aperture rotates in between the ends of the fibres and the photomultiplier, and allows light from only one fibre at a time to pass through. The disc normally rotates at 20Hz, giving scattering measurements between 3º and 177º every 50ms.

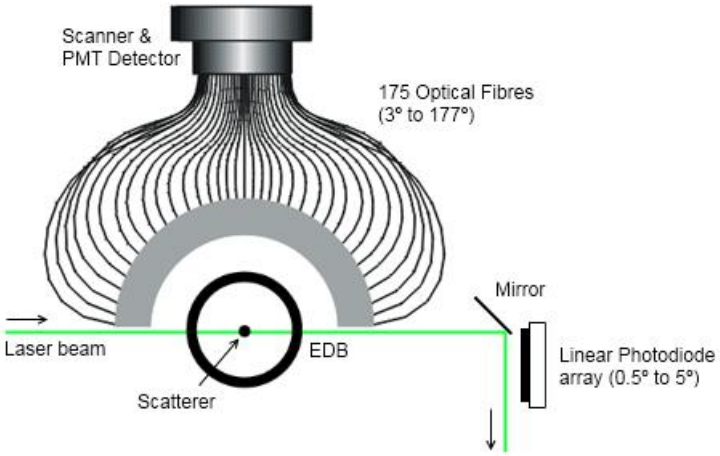

Figure 5-6 – Plan view of the arrangement of components for measuring light scattering from single levitated particles.

The diffractometer only gives a linear signal within a specific range of light intensity. The voltage supplied to the photomultiplier must be adjusted so that the signal peaks are below the upper limit for signal linearity, and the signal lows are above the lower limit for signal linearity. As the dynamic range of a scattering phase function is very large, this entails taking and then combining multiple readings. A typical approach would be to sample the small-angle scattering and large-angle scattering separately. For the small-angle scattering, a measurement would involve ensuring that the photomultiplier voltage results in scattering readings between 3º and 10º within the linearity limits. The large-angle scattering would involve a similar approach, but for scattering angles between 8º and 177º. The overlap in angle readings will allow combining the two signals into

a full scattering measurement. For particles where the scattering has a very large dynamic range or has halo features, more than two readings may be required.

For a full set of data to be obtained from the LD, at least 8 measurements are taken. A half-wave polarization retarder is in place between the laser aperture and the trap, and can be rotated to produce either vertically or horizontally polarized light. Readings are taken for vertical and horizontal polarizations of the incident light for a set of photomultiplier gains, as described above. For each measurement, a corresponding background reading is also taken (the particle is moved out of the beam by altering the EDB DC voltage), which allows background subtraction.

5.1.3 - Low-Angle Scattering Measurements

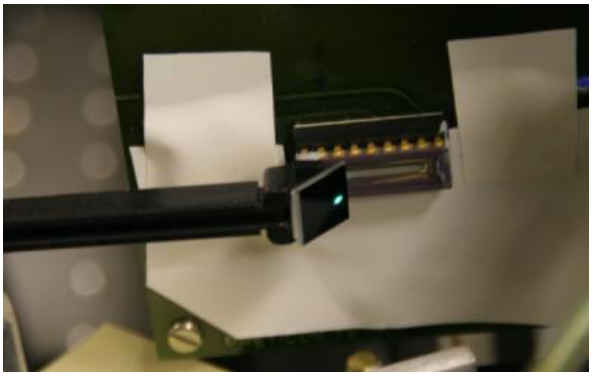

Figure 5-7 - Linear Photodiode Array used to capture small angle scattering data. The laser can be seen impacting on the mirror.

The Linear Photodiode Array (LPA) shown in **Figure 5-6** & **Figure 5-7** enables scattering measurements between 0.5º and 5º. Measurements are recorded by 512 elements, separated in this arrangement by a scattering angle of 0.01061º. The Array is a 16-bit device, and so can record 65,536 discrete intensity values. An attenuating filter is placed between the laser aperture and rotating polarizer in order that the scattered intensity will not cause the array to saturate. However, even with the filter in place, the laser beam would cause the array to saturate. To avoid this, a mirror is placed so as to deflect the beam and protect the array from direct illumination. The detectable scattering range is therefore between 0.5º and 5º.

5.1.4 - Extrapolation of Direct Forward Scattering Intensity

When the Laser Diffractometer and Linear Photodiode Array measurements are complete, we can proceed with computing the full scattering measurement. With the combined LD and Linear Photodiode Array data, we have scattering data between 0.5º and 177º. However, the forward scattering peak is at 0º, and much of the high intensity scattering is contained in the region between 0º and 0.5º. Scattering at such low angles is dominated by diffraction, and is largely independent of particle shape. Therefore, this data can be extrapolated by considering a diffraction pattern of an aperture corresponding to the average cross-section of the particle as 'seen' by the laser beam. For spherical, or close to spherical particles, a randomly spinning particle will have a circular or almost circular projected cross section, and we can extrapolate the small angle scattering data using Lorenz-Mie theory. However, for highly aspherical particles, an approach needs to be found that will consider the changing cross-section that the particle defines as it rotates. A suitable solution is to consider Fraunhofer

diffraction on a series of randomly oriented elliptical apertures [9]. Analytic solutions for diffraction on a fixed elliptical aperture have been determined [10]. For a small angle approximation, the diffracted intensity for an ellipse as a function of scattering angle θ can be written:

$$I(\theta) = \left(\frac{2\pi ab}{k}\right)^2 \int_0^{2\pi} \left(\frac{J_1(k\beta)}{\beta}\right)^2 d\varphi \tag{5.7}$$

Where a and b are the semi-axes of the ellipse, J_1 is the Bessel function of the first kind, k is the wavenumber, φ is the azimuthal angle and

$$\beta = \sqrt{(a\theta\cos\varphi)^2 + (b\theta\sin\varphi)^2} \tag{5.8}$$

In order that the orientation is randomized, the integration is carried out over the azimuthal angle φ. **Figure 5-8** shows intensity as a function of scattering angle for a range of ellipses.

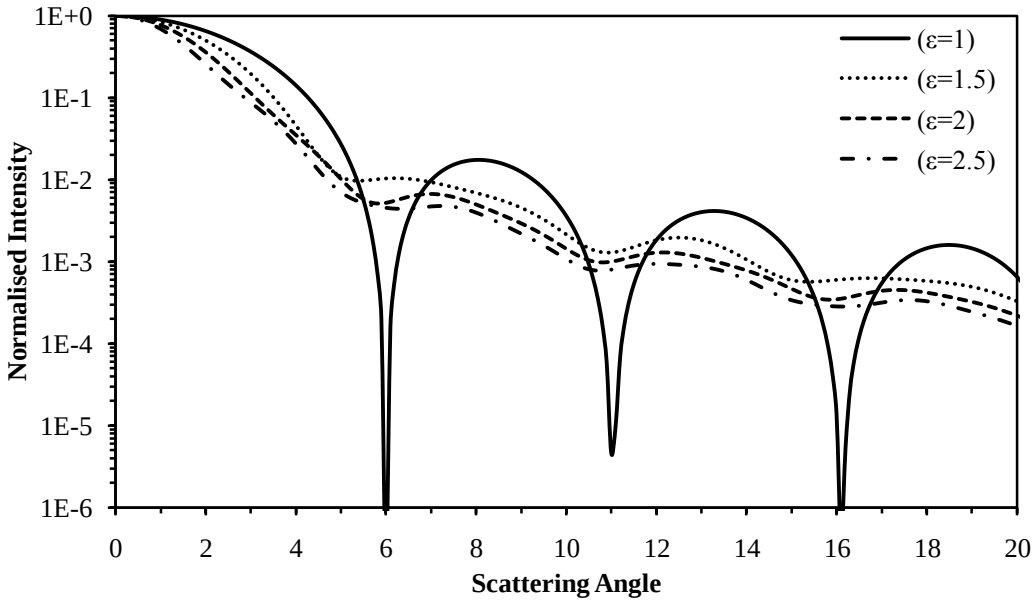

Figure 5-8 – A plot of intensity as function of scattering angle for a randomly oriented ellipse. The ellipses have semi-axes *a* and *b*, where *b* = *a*eps*. In the above, *a* = 3μm and the incoming radiation is of wavelength 514.5nm.

When projected onto a 2-D plane, the diffraction pattern for a circle forms an intensity pattern consisting of concentric circles known as an Airy pattern. Utilising **equations 7 & 8**, it is possible to compute the diffraction patterns for elliptical apertures; a range of these are shown in **Figure 5-9**.

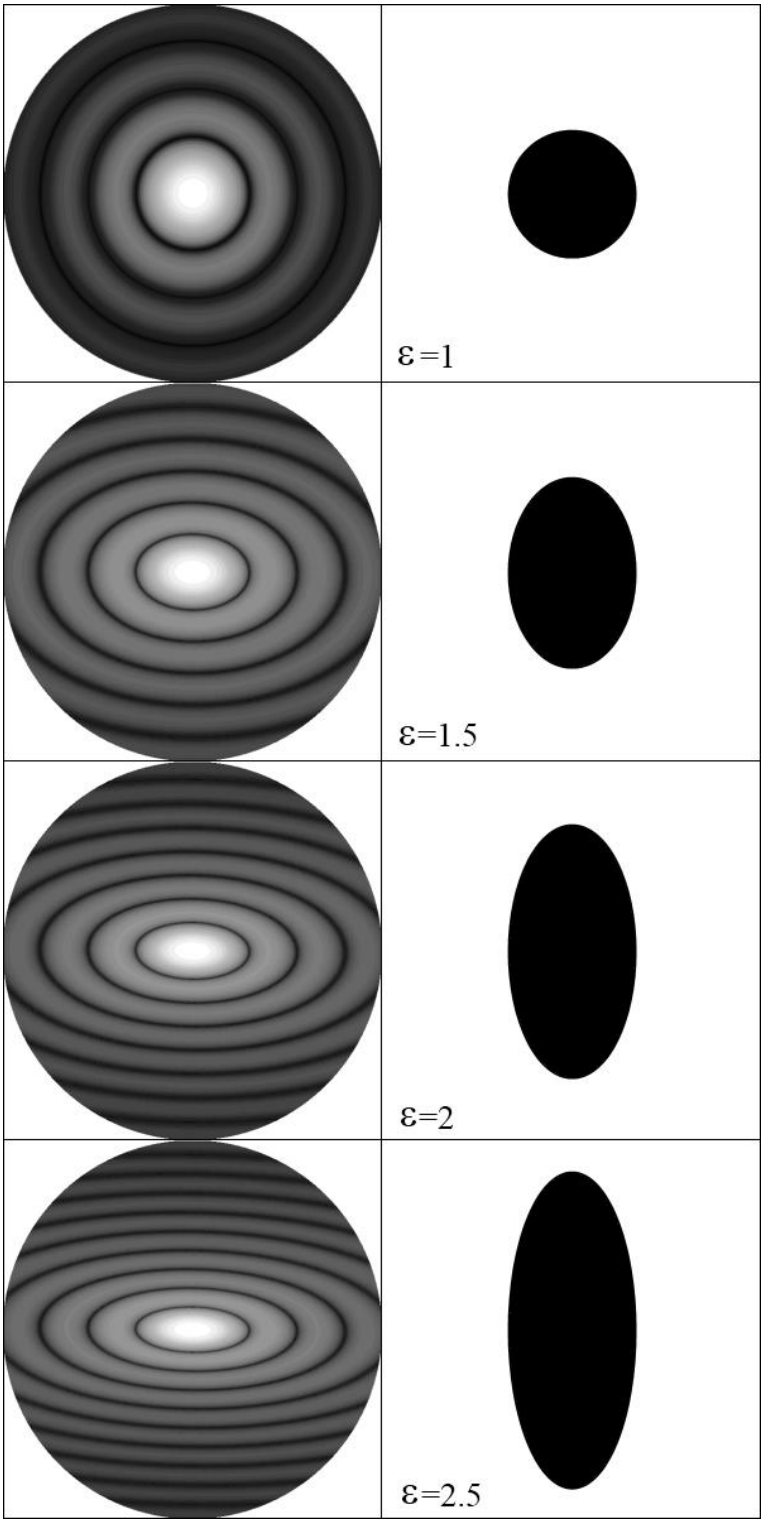

Figure 5-9 – The diffraction patterns caused by a range of apertures of changing aspect ratio. The diffraction patterns are shown for angles up to 20 degrees. For an aspect ratio of 1, an Airy pattern is produced. As the aspect ratio is increased, the diffraction patterns become more elliptical in nature. For these patterns, the semi-minor axis of each aperture was 3 microns, and the wavelength of the incident light was 514.5 nm.

Chapter 6 - Modelling Rough Surfaces using Stochastically Generated Meshes

6.1 - Gaussian Random Particles

As we will see in Chapter 8, dust particles are highly irregular in shape, and the surfaces are rough and can be considered fractal in nature. A possible method of modelling scattering by these particles is to create a suitable particle mesh using a Gaussian Random sphere (GRS) [38] and then apply a Ray Tracing technique, in this case RTDF. A sphere is described using a radius, extending from a specific fixed point. In the GRS approach, the radius of the sphere is varied according to multivariate lognormal statistics. By adjusting the correlation angle Γ and the standard deviation σ associated with the generation of the sphere, the shape of the sphere can be distorted significantly. Code written by K. Muinonen and T. Nousiainen has been made publicly available, and has been used to produce the following distorted spheres.

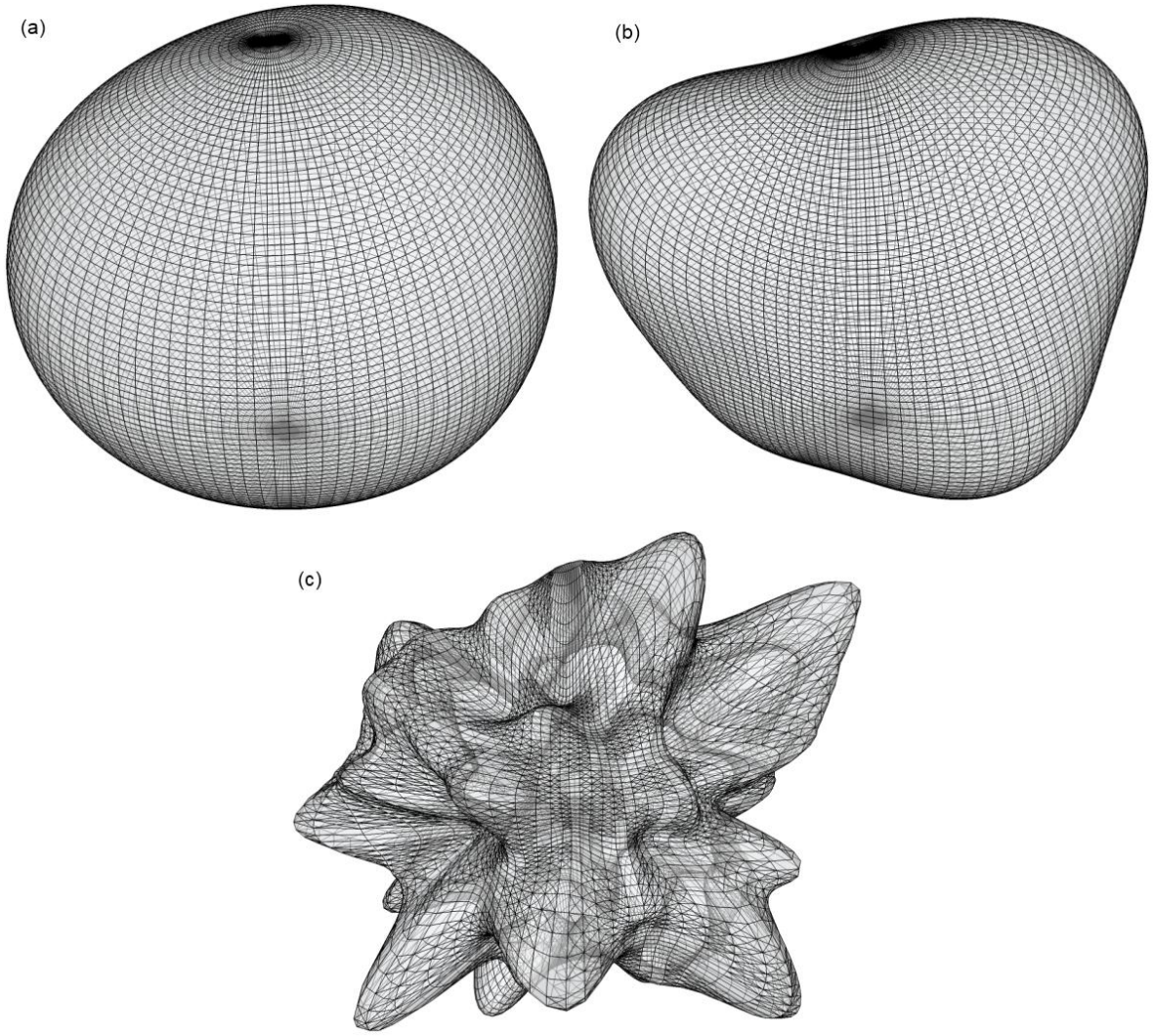

Figure 6-1 - 3 Gaussian Random particles as produced by the Muinonen & Nousiainen code. Here, the standard deviation across all three particles is 0.2. Particle (a) has correlation angle $\Gamma = 90°$. Particle (b) has $\Gamma = 45°$. Particle (c) has $\Gamma = 10°$.

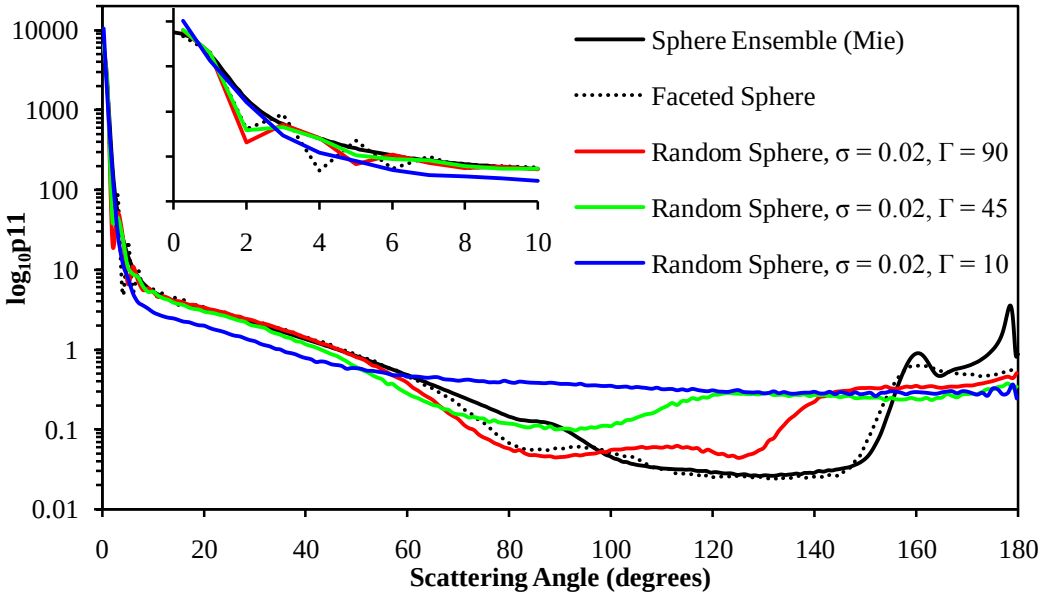

Figure 6-2 – Phase functions for the Gaussian Random spheres shown in **Figure 6-1**, compared with Mie theory for an ensemble of spheres and a faceted sphere. The faceted sphere and Gaussian sphere phase functions were calculated using RTDF. The spheres were of size parameter X_s=100, the refractive index was 1.5+0i.

It can be seen in **Figure 6-1** that the lower the correlation angle, the more deformed the particle becomes. This deformation also affects the scattering properties of the particle significantly, as shown in **Figure 6-2**. As the sphere becomes more distorted, the phase function changes significantly – the peaks and troughs associated with scattering from a sphere are gradually smoothed out as the particle becomes less spherical.

The correlation angle defines the angular range over which the statistical variation must apply. For very large correlation angles, the statistical radial variation is applied over a large angular range, and therefore the sphere is only slightly distorted, as in **Figure 6-1(a)**. For small correlation angles, the radial variation is applied over a small angular range, and therefore the sphere becomes highly distorted, as seen in **Figure 6-1 (c)**. In utilising this code, there are limits as to the lowest correlation angle that can be used – correlation angles below 3.5° will cause the program to crash. While this low correlation angle combined with a small standard deviation will produce a particle with apparent surface roughness, the small-scale structure seemingly representative of the dust particles shown in Chapter 8 is not present. It is reasonable to assume that a smaller correlation angle would produce a much better approximation, and to achieve this, the Gaussian Sphere code was modified – instead of using Double Precision arithmetic, it now uses Quadruple Precision arithmetic. The correlation angle can now be lowered to approximately 0.6°; by using a suitably low standard deviation and a large enough number of facets, the particle appears to have very small scale surface roughness. Examples of Gaussian Random Spheres generated using very small correlation angles are shown in **Figure 6-3**.

The original Ray Tracing code written by A. Macke, and hence RTDF, can in theory be applied to particles such as these. However, the models were written primarily to calculate scattering on simple faceted objects, such as the hexagonal ice columns commonly found in Cirrus clouds. The number of facets to be considered, even for a fairly complex aggregate of hexagonal columns, would typically be under 100. In order that enough of the small scale surface detail is replicated, the dust particles would commonly be comprised of more than 30,000 facets. The time taken for RTDF calculations depend on the number of facets being considered, with the

execution time increasing according to the square of the number of facets. I have implemented a spatial subdivision routine within RTDF, in order that the execution time for these complex particles remains realistic. Full details of this routine can be found in Chapter 7.

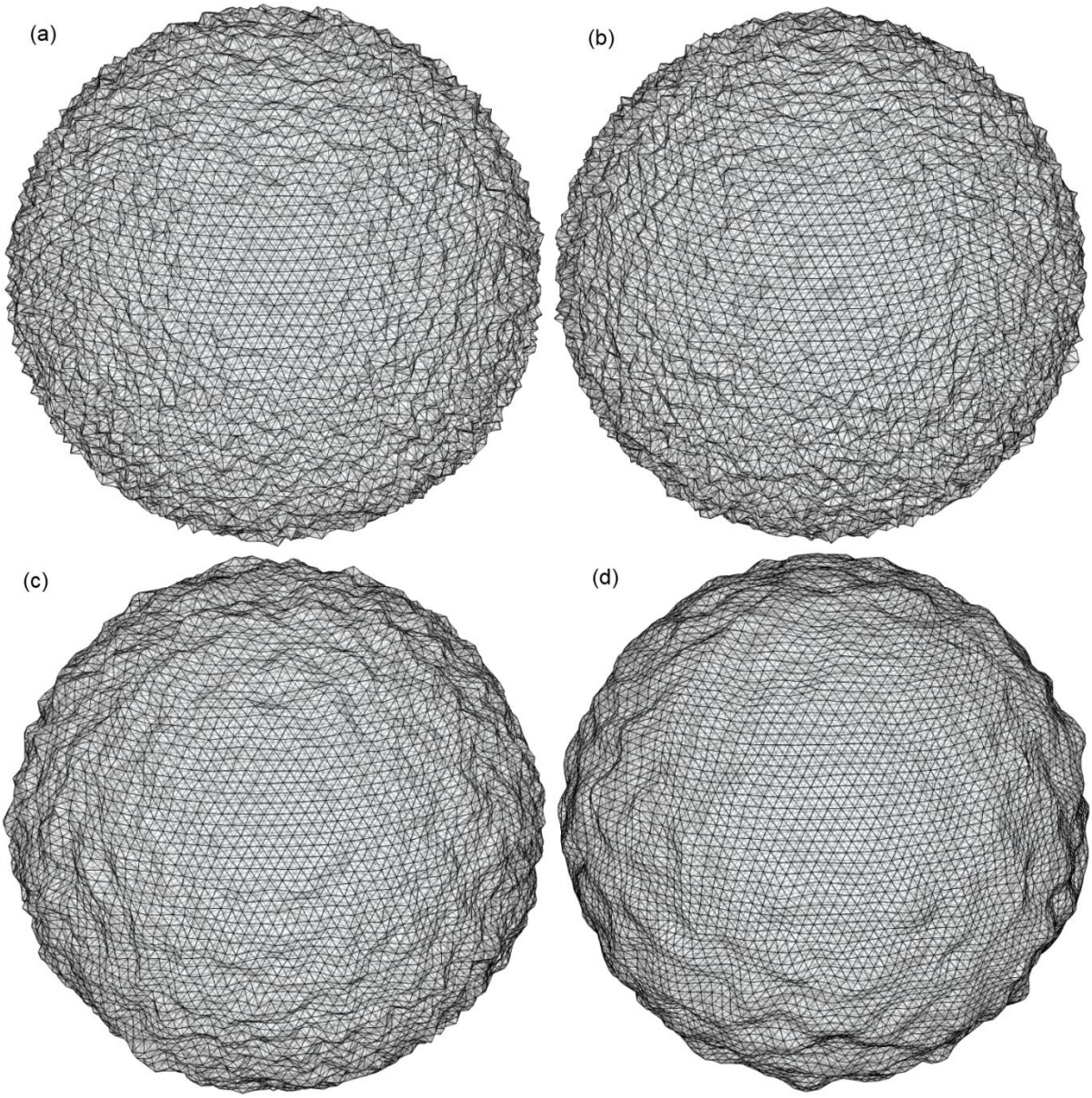

Figure 6-3 – Gaussian Random spheres generated using small correlation angles Γ. All spheres use a standard deviation of 0.015. (a) Γ=0.6° (b) Γ=1.0° (c) Γ=2.0° (d) Γ=3.0°

6.2 - Determining the Projected Area of a Complex Particle

The RTDF model combines Geometric Optics Ray Tracing with projected area diffraction. The projected area is calculated by finding the contour of the 2-D shape the particle projects in the Z-direction. For particles with a very complex contour, however, the contour finding routines within RTDF were insufficient, and would cause the model to cease execution. I have implemented a new method of finding the contour of a complex particle.

When viewing the particle from the orientation of the beam, all facets that are not facing 'upwards' into the beam are eliminated. The remaining facets are then separated into four 'quadrants,' where the quadrants span the angular range from 0-90°, 90-180°, 180-270°, 270-360°. This demarcation is performed to reduce the number of calculations that will be performed later.

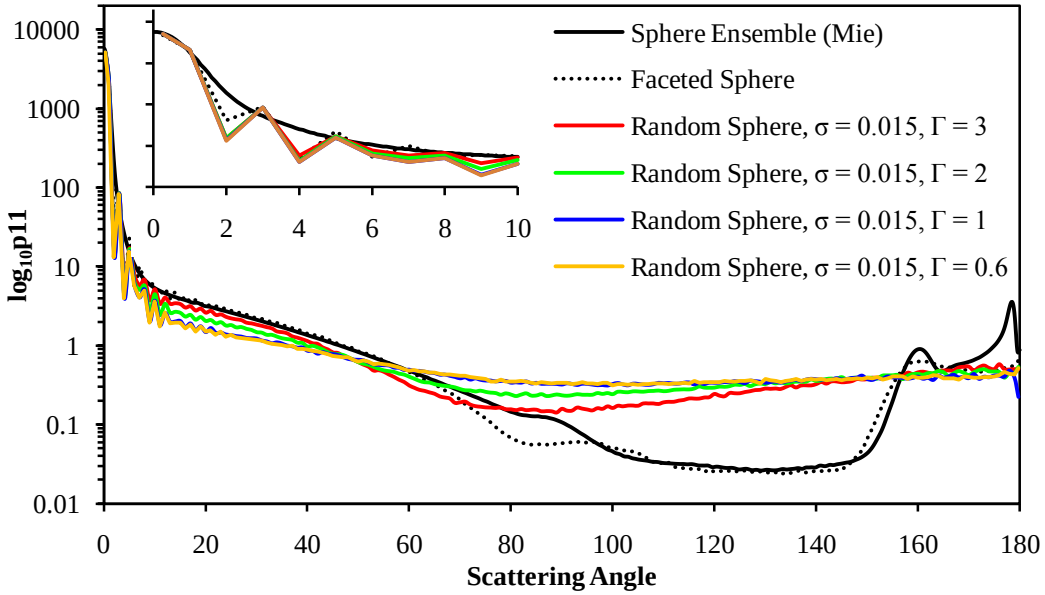

Figure 6-4 – Phase functions for the faceted spheres shown in **Figure 6-3**. Also shown for comparison are phase functions for an ensemble of spheres as calculated using Mie Theory, and for a faceted sphere. The calculations for the faceted spheres were performed using RTDF. All spheres were of size parameter X_s=100, and the refractive index was 1.5 + 0i.

A series of 2-D vectors are created with origins at (x=0, y=0). Each vector has direction components

$$x = \sin\theta, y = \cos\theta$$

where θ is the angle between the vector and the y-axis, and this angle increases from 0° to 360°. The number of separate angles in this range is determined before execution. Each vector is tested for an intersection with every facet within the current quadrant. The intersection point furthest from the origin for each vector is recorded. Using this method, a contour defining the outer edges of the projected shape of the polygon is created. More complex particles would need a larger number of angles to be tested to give an accurate contour. The scattering calculations are averaged over several thousand orientations of the particle, so it is appropriate to consider the projected area of each orientation as an ellipse. Upon calculation of the contour, the major and minor axes of the ellipse are calculated, and these are used to calculate the azimuthally-averaged angular intensity due to diffraction for that orientation. The equations for calculating diffraction due to an elliptical aperture [10], as seen previously in Chapter 5, are again used.

Figure 6-4 shows the phase functions for the spheres shown in **Figure 6-3** compared with phase functions for an ensemble of spheres calculated using Mie Theory and a faceted sphere. The calculations for the faceted spheres were performed using RTDF. The spheres were of size parameter X_s=100, and the refractive index was 1.5 + 0i. As in **Figure 6-2**, it can be seen that the addition of roughness to the particles changes their scattering properties considerably. As the roughness increases, the phase functions exhibit higher side scattering than the spheres, and lose the rainbow peak completely.

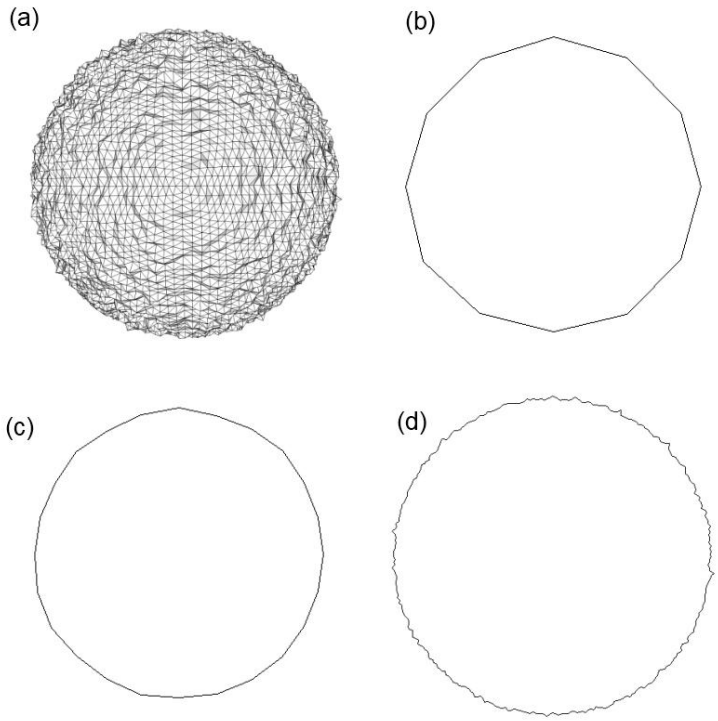

Figure 6-5 – A comparison of different angular step sizes used when calculating the projected contour of a complex particle. (a) – The particle as 'seen' by the incident radiation. (b) – A contour created using an angular step of 30°. (c) – A contour created using an angular step of 15°. (d) A contour created using an angular step of 1°.

Typically, using an angular step of 1° is sufficient to render the contour of a complex particle accurately. **Figure 6-5** shows the contour for a complex particle, calculated using decreasing angular steps. It can be seen that the accuracy of the contour representation increases as smaller angular steps are used. This method can also be used for simpler particles, such as hexagonal columns or droxtals. In order to maintain the efficiency of RTDF for dealing with these particles, it is prudent to increase the angular step size.

6.3 - Non-spherical Particles

As the Saharan Dust particles that will be analysed are largely non-spherical, a program was written that takes the file containing a polygonal mesh, and will stretch it in any or all of the three major axes. This can be used to recreate the approximate dimensions and aspect ratio of a particle we wish to model. Examples of these modified particles are shown in **Figure 6-6.**

This approach does not take into account more irregular particle shapes, however. It also does not account for any flat, facet-like features on the surface of a particle, an example of which is shown in Case Study 2 in Chapter 9.

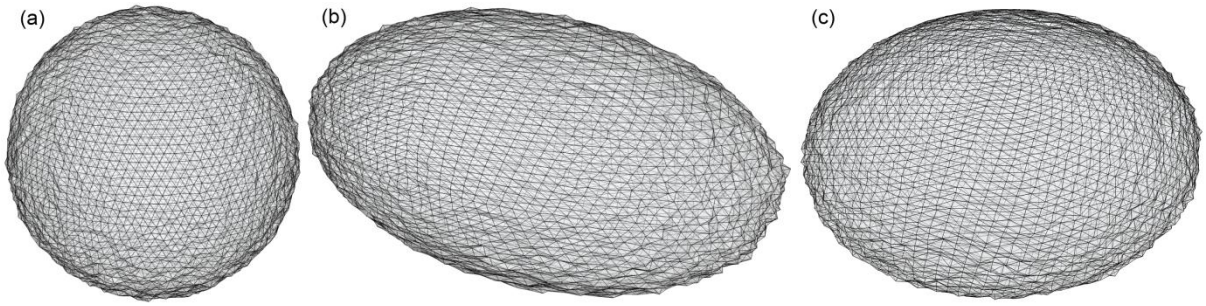

Figure 6-6 – A Gaussian random sphere which has been distorted in order to form two different spheroids. (a) – A standard sphere. (b) – A prolate spheroid, of aspect ratio ε=1.5. (c) – An oblate spheroid, of aspect ratio ε=3.0.

Chapter 7 - Improving the efficiency of Geometric Optics Ray Tracing using Spatial Subdivision.

Ray Tracing is the basis for a number of Geometric Optics (GO) light scattering models – The path and intensity of a light ray through an object is calculated using Snell's law and Fresnel's equations. This technique can be applied to any object that can be defined analytically, but can also be applied to any closed polyhedron – this gives the technique a wide range of applicability. Many GO implementations exist, but here we consider the model created by Andreas Macke et al. [18].

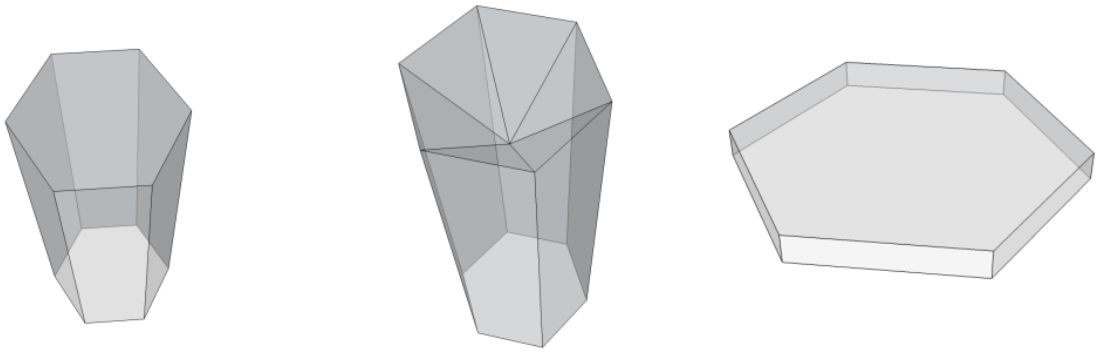

Figure 7-1 - An example of the crystal geometries which can be treated within the GO model **[18]**. (Left to Right) – A hexagonal column, a hexagonal column with an indented basal facet, a hexagonal plate.

7.1 - Increasing Facetation

An attractive feature of GO is its computational efficiency, and the fact that the efficiency is size-independent for a given shape and number of facets. The GO code by Macke et al. might typically take less than a minute to calculate scattering by a hexagonal column such as that seen in **Figure 7-1**. This execution time increases rapidly, however, for increased numbers of facets. In order to approximate smooth surfaces of objects such as cylinders, spheres and spheroids, many more facets must be used, and the execution time increases accordingly. Some faceted spheres can be seen in **Figure 7-2**.

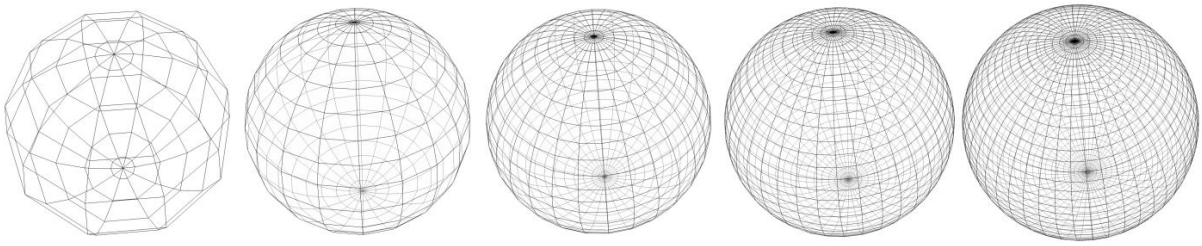

Figure 7-2 - Spheres comprised of (Left to Right) 128, 392, 968, 1800 and 3200 facets.

7.1.1 - Comparison of GO calculations for Faceted Spheres with Mie Theory and GO for analytic spheres.

For spheres, a marked improvement in the calculated scattering when compared with Mie theory is noted for increased facetation. As the number of facets increases, the scattering pattern of the faceted sphere approaches that of a smooth sphere. As GO results do not include interference effects, a fairer comparison with Mie theory involves integrating over a size distribution of spheres [39] which has the effect of smoothing out the maxima and minima associated with interference. Here, a gamma distribution [23] is used.

The gamma distribution is given by:

$$n(r) = kr^{(1-3b)/b} exp\left(-\frac{r}{ab}\right) \tag{7.1}$$

where r is the sphere radius, and a and b are the shape and scale parameters of the gamma distribution, respectively. The constant k is chosen for each size distribution so that the size distribution satisfies the normalisation condition:

$$\int_{r_{min}}^{r_{max}} n(r)dr = 1 \tag{7.2}$$

The average area of geometric projection per particle is given by:

$$\langle G \rangle = \int_{r_{min}}^{r_{max}} n(r)\pi r^2 dr \tag{7.3}$$

The effective radius and effective variance of a size distribution are given by:

$$r_{eff} = \frac{1}{\langle G \rangle}\int_{r_{min}}^{r_{max}} n(r)\pi r^3 dr \tag{7.4}$$

$$v_{eff} = \frac{1}{\langle G \rangle r_{eff}^2}\int_{r_{min}}^{r_{max}} n(r)\left(r - r_{eff}\right)^2 \pi r^2 dr \tag{7.5}$$

For the gamma distribution with $r_{min} = 0$ and $r_{max} = \infty$, the values of a and b correspond to the values for r_{eff} and v_{eff}, respectively.

The phase function as calculated by Mie Theory shown in **Figure 7-3** was generated using a gamma distribution with the following values:

$$r_{min} = 0$$

$$r_{max} = 800$$

$$a = 100$$

$$b = 0.1$$

where r_{min}, r_{max} and a are given in terms of size parameter.

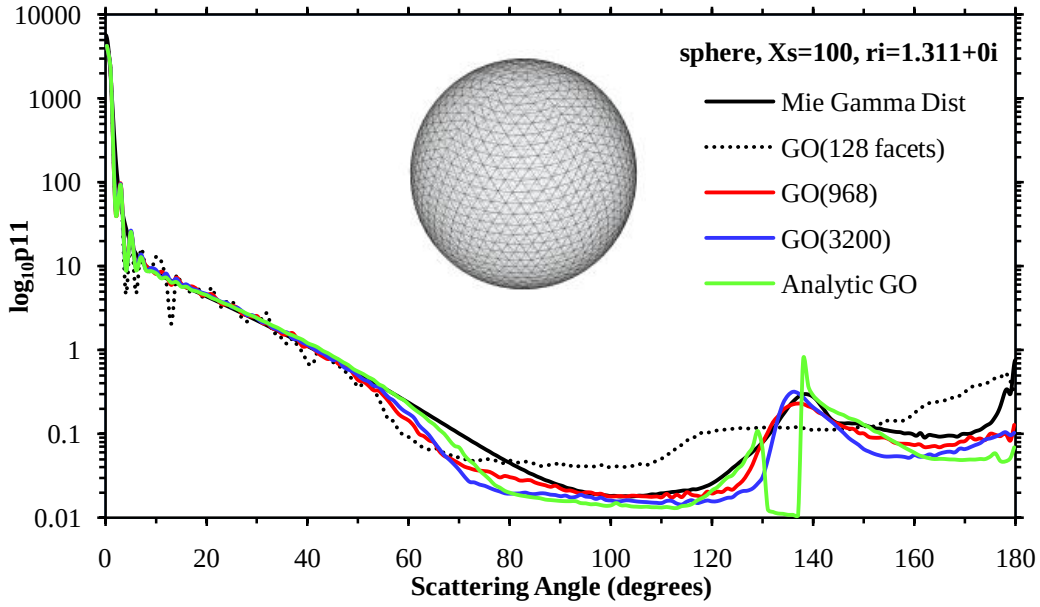

Figure 7-3 - Comparison between phase functions for a size distribution of spheres calculated by Mie theory, GO scattering by faceted spheres and by an analytically defined sphere. The GO faceted spheres were comprised of 128, 392, 968, 1800 and 3200 facets. All spheres were of size parameter 100, and the refractive index was 1.311+0i.

Also shown is a phase function calculated (labelled 'Analytic GO') using an alternative Geometric Optics model for computing scattering on analytically defined spheres and spheroids. [40]. We can see that the GO scattering by faceted spheres approximation improves as the number of facets in each sphere is increased. While this increased facetation approaches the GO solution for an analytic sphere, the time taken to calculate scattering increases sharply according to the number of polygons. This is due to the algorithm used to identify which polygon has been intersected by a light ray. A 2-Dimensional representation of rays intersecting with a polygon is shown in **Figure 7-4**. In this figure, all reflected rays are ignored – only refracted rays are shown. A black circle marks a point at which calculations are performed to determine which segment of the polygon the ray will intersect with. At each of these points, every segment that makes up the polygon has to be tested against the position and vector of the ray. For Ray 1, 6 calculations are required. Ray 2 intersects with the hexagon four times, so a total of 5 * 6 = 30 calculations are needed. For these eight rays, a total of 6 + 30 + 18 + 18 + 18 + 18 + 18 + 6 = 132 calculations are performed. For more complex shapes, this number can rapidly increase. The number of calculations needed increases dramatically as the number of lines in a polygon increases. Whenever reflected rays are introduced, the number of calculations increases further.

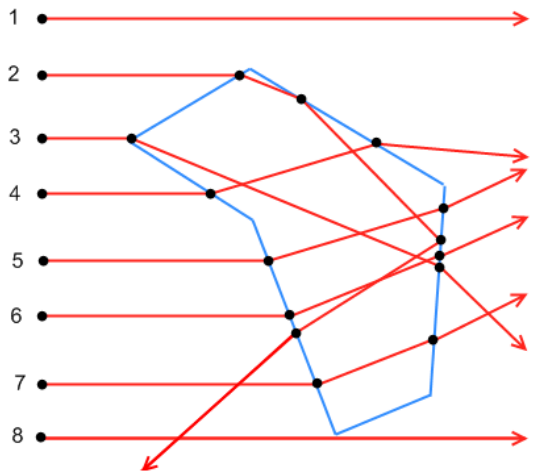

Figure 7-4 - A 2-D representation of rays intersecting with a polygon. Black circles indicate where intersection calculations have to be performed. Only refracted rays are shown.

In **Figure 7-5**, we can see how the time taken for calculation of scattering using GO increases as the number of facets is increased. The geometries used are faceted approximations of spheres, and range from very simple (8 facets) to very complex (3200 facets). GO scattering on a sphere with 3200 facets takes approximately 930 minutes - 15½ hours to complete. If we wanted more accuracy, the time taken would increase approximately according to the square of the number of facets. The data indicates that the time taken for calculations increases approximately quadratically with the number of facets - for a sphere of 5000 facets, calculation time would be of the order of 2200 minutes (over 36 hours).

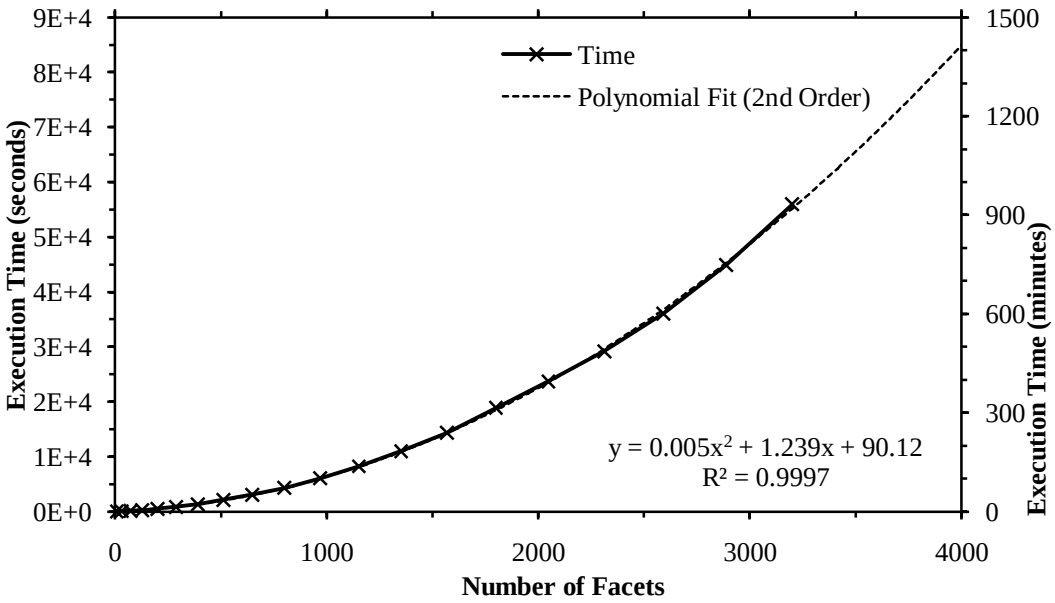

Figure 7-5 - Times taken for GO calculations for randomly-oriented increasingly faceted spheres. Times are shown in both minutes and seconds. A trend line has been added and extrapolated to show the likely time taken for spheres comprised of up to 4000 facets. The trend line equation calculates time in seconds.

In order to reduce this calculation time, a spatial subdivision regime [41] can be used. This is an approach commonly used in computer graphics applications in order to optimize rendering time [42]. In a standard ray-tracing approach, every ray that enters a 'scene' to be rendered would have to be tested against every object

within the scene, to see if an intersection is found. With a spatial subdivision scheme, groups of objects are placed within bounding boxes, which can be perfect cubes or cuboids. Instead of testing a ray for an intersection within an object, the ray is tested for an intersection with a bounding box. If an intersection is found, the ray is then tested against every object contained within the bounding box. This reduces the number of calculations needed, and a carefully arranged set of bounding boxes can dramatically decrease rendering time for a complex set of objects.

7.2 - Implementation

7.2.1 - Implementation of Spatial Subdivision

In *n*-dimensional space, a plane of dimension *n*-1 will split that space into two subspaces. By defining one of these subspaces as being *above* the plane and the other as being *below* the plane, any single point in the *n*-dimensional space can be defined by its location relative to the plane. **Figure 7-6** shows how points can be defined as being either above or below a dividing plane.

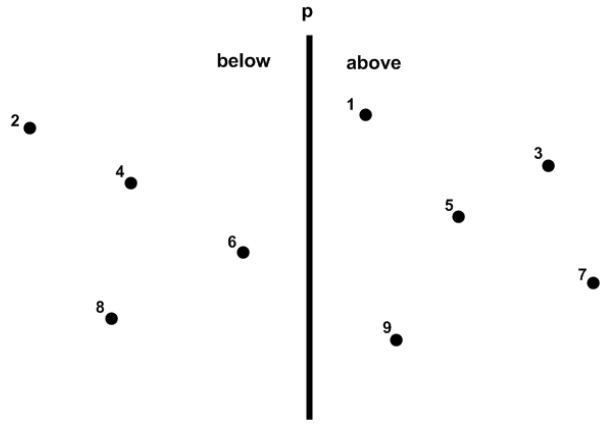

Figure 7-6 - A 2-Dimensional space split into two subspaces by a 1-dimensional plane **p**. Points 1, 3, 5, 7 & 9 are all above the plane, while points 2, 4, 6 & 8 are all below it.

In order to automate this procedure computationally, we can define a normal to the plane. We can then define a vector for every point we want to determine the position of. This vector should point towards the plane. By taking a dot-product of the plane normal and each of these vectors in turn, we can determine on which side of the plane the point lies. In **Figure 7-7**, we can see a polygon with six points that intersects a plane p. Each of the points in the polygon has a vector $\vec{v}_n$ pointing towards the plane. The dot product $\vec{v} \cdot \vec{n}$ will be positive for all points below the plane, and negative for all points above it.

By adding more planes parallel to the already present plane, we can define the location of a point with more accuracy. By adding planes perpendicular to these planes, we can start to build up a grid structure, and the location of points can be defined as coordinates within this grid. This can be seen in **Figure 7-8**, where the polygon seen in **Figure 7-7** has been further segmented by a total of ten planes. Five planes are parallel and infinitely long in the *y*-direction, and five are parallel and infinitely long in the *x*-direction.

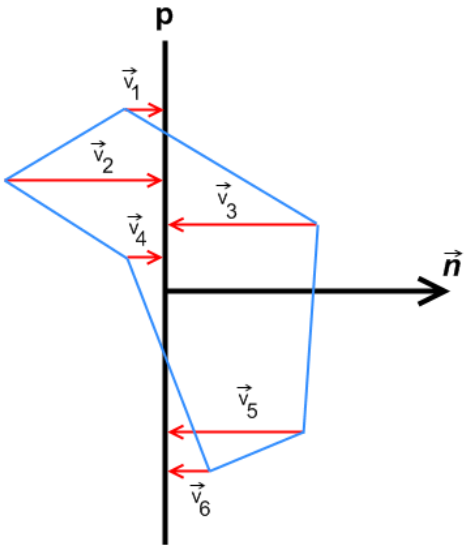

Figure 7-7 - A dividing plane p with normal $\vec{n}$. Each of the points in the polygon has vector $\overrightarrow{v_n}$ pointing towards the plane. By taking a dot product of the vector for each point and the plane normal, we can determine which side of the plane it lies on.

The planes divide the 2-D space into rectangular 'boxes.' The distribution of line segments throughout the boxes only needs to be calculated once, and this is performed before ray-tracing takes place. A ray traversing the boxes should only be tested for intersection with segments of the polygon that are contained in the box where the ray is currently located. If the ray does not intersect a polygon segment within that particular box, it can move to the next box and test for an intersection with all the segments contained in it.

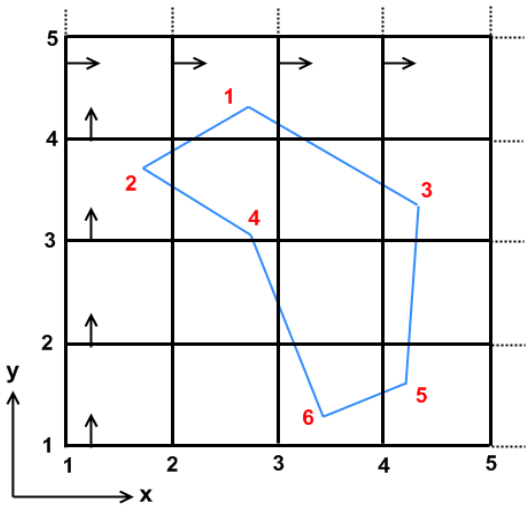

Figure 7-8 - A polygon segmented by 10 planes. This gives a total of 16 'cells.' The points 1-6 can be located according to their cell coordinates. E.g. point 1 is located in cell (2,4).

The ray traversal procedure is very simple. The ray can be located at a box coordinate (*x*,*y*). As all the planes perpendicular to the *x*-axis are parallel to each other, the ray vector can be tested against the normal of any of these planes. If the dot product of the ray vector and the normal is positive, then the ray is travelling positively in the *x*-direction. The same procedure is performed for all planes perpendicular to the *y*-axis. Then the

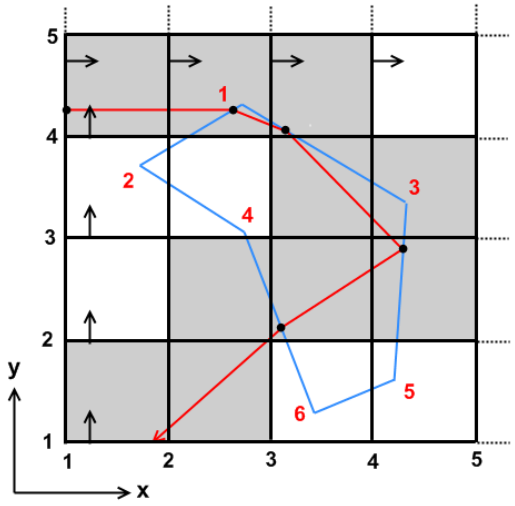

Figure 7-9 - A ray passing through a subdivided 2-D space containing a polygon. The grey boxes indicate a cell through which the ray passes.

distance between the current ray position and the prospective *x* and *y* plane is tested. The shortest distance indicates the plane that is intersected first, and the new ray location in box coordinates is known.

In **Figure 7-9**, a ray passing through a segmented 2-D space containing a polygon is shown. The grey boxes indicate the path of the ray in box coordinates. In each of the boxes, the ray must be tested for intersections against any segments of the polygon present (either partially or completely) within that box. In **Table 7-1**, the path that the ray takes in terms of box coordinates is shown. It can be easily seen that the ray path as shown in **Figure 7-9** now requires a total of only 14 intersection calculations. In **Figure 7-4** it was shown that a total of thirty calculations were needed for this single ray. While it is true that calculating intersections with the bounding planes do add some overhead, these calculations are computationally simpler, and, for complex polyhedrons, fewer in number than the polygon segment calculations.

Cell	# Segments	Segment Names
(1,4)	0	
(2,4)	2*	2-1, 1-3
(3,4)	1*	1-3
(3,3)	1	1-3
(4,3)	2	1-3,3-5
(4,2)	1*	3-5
(3,2)	1*	6-4
(2,2)	1	6-4
(2,1)	0	
(1,1)	0	
Total	14	

Table 7-1 - Cell locations, number of intersections and names of segments for the ray path shown in **Figure 7-9**. Where the number of segments is marked with a star, the ray has hit a segment within that cell and a recalculation after intersection is required. Therefore, the number of segments in that cell must be counted twice.

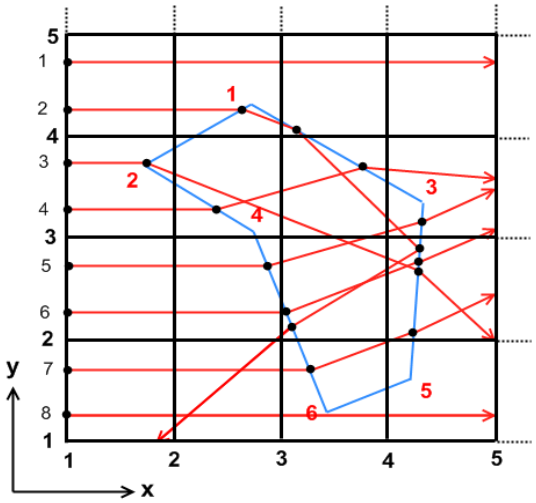

Figure 7-10 - Eight rays passing through a subdivided space and intersecting with a polygon. Rays are numbered 1-8, from top to bottom.

In **Figure 7-10**, the ray paths originally shown in **Figure 7-4** are replicated, with the addition of dividing planes. Whereas previously the total number of intersection calculations that had to be performed was 132, the new total is less than half that, at 61. **Table 7-2** shows us that each ray requires significantly fewer intersection calculations.

Ray number	Intersection Tests (no subdivision)	Intersection Tests (with subdivision)
1	6	3
2	30	14
3	18	10
4	18	10
5	18	8
6	18	7
7	18	8
8	6	4
Total	132	64

Table 7-2 – The number of intersection tests for each ray whenever no subdivision is used, and then when spatial subdivision is used.

7.2.2 - Implementation in GO

The subdivision regime described above has been extended to 3-D and implemented into the GO code [18]. A program has been written to prepare the bounding boxes for the polyhedron to be computed. This program gives the user the option to choose the number of boxes they would like to divide the polyhedron into. The user can define the number of boxes along the *x*, *y* and *z* axes independently, and choose how they are distributed. The program then creates a data file – this contains references to each of the boxes present in the 3-D space, and the number of facets contained within each. A facet can be present in one or more boxes. This initial program is efficient – A polyhedron consisting of 115,200 facets with the space subdivided into 1 million boxes can be

analysed in approximately 2 minutes. When the data file is written, the GO program can be executed. **Figure 7-11** shows a sphere of 3200 facets in a space that has been subdivided into 1000 boxes.

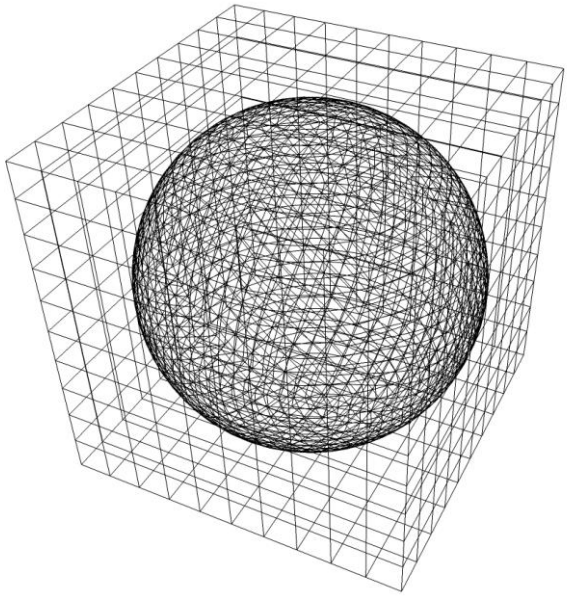

Figure 7-11 - A sphere comprised of 3200 facets in a space subdivided into 1000 cells. There are 10 cells along each of the *x*, *y* and *z* axes.

7.3 - Results

7.3.1 - Performance Increase due to Spatial Subdivision

The GO program was executed multiple times using different numbers of dividing planes. The number of boxes along each of the *x*, *y* and *z* axes was incremented from 1 to 10 (giving a total number of boxes ranging between 1 and 1000). Spheres with a range of facets numbering between 8 and 3200 were used.

As the GO program uses Monte Carlo methods, measurement of the time required for analysis of a given sphere will vary from one run to the next. Therefore, calculations for each sphere were performed ten times, and the time presented below is an average of these execution times. The following options were set within the GO program –

- Number of orientations of the model particle – 10000
- Incident rays per orientation – 100
- Maximum number of ray reflections and transmissions – 10
- Maximum number of total internal reflections – 100

The computer used was a Linux workstation, equipped with dual quad-core Intel Xeon CPUs running at 3.16GHz. The GO program is not multi-threaded; neither does it make use of parallel processing. The amount of RAM used varies according to the complexity of the polyhedron for which computation is taking place, and the number of bounding boxes used. In the following examples, the amount of RAM used did not rise above 350MB.

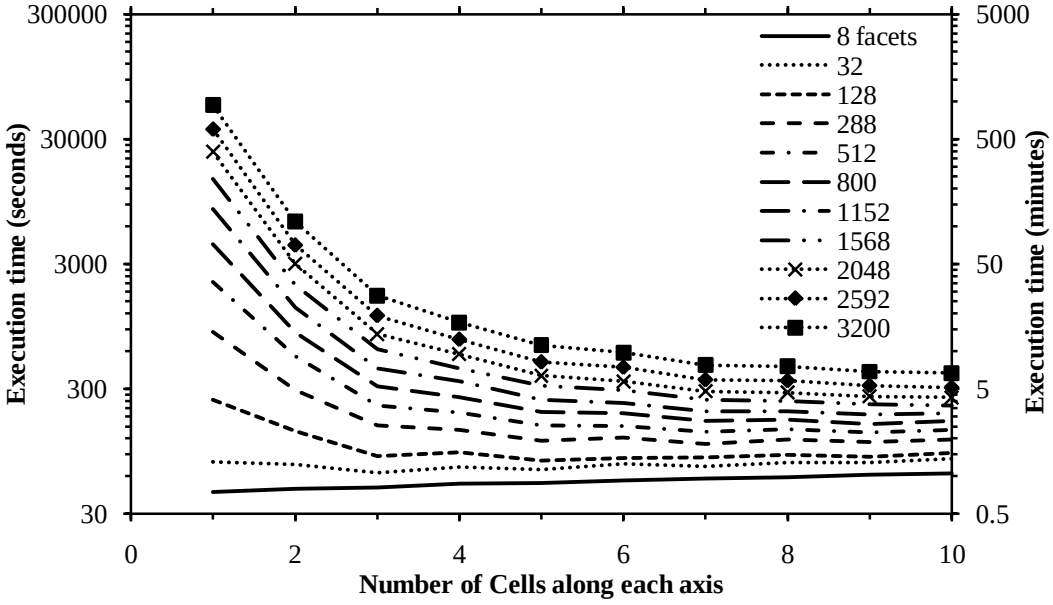

Figure 7-12 - Computation time for faceted spheres with different numbers of bounding boxes.

Figure 7-12 shows how the time needed for computation of a faceted sphere decreases as the number of boxes in the 3-D space is increased. With one box in each direction, the time taken for computation of a sphere comprised of 3200 facets is approximately 932 minutes. This corresponds to the original GO program, with no spatial subdivision included. However, as the number of boxes is increased, computation time drops dramatically. Having 2 boxes in each axial direction (a total of $2^3 = 8$ boxes) decreases the time required to 108 minutes – less than $1/8^{th}$ of the original time. The shortest time taken was observed whenever $10^3 = 1000$ boxes were used. The calculation time was reduced to 6.693 minutes – $1/139^{th}$ of the original time taken.

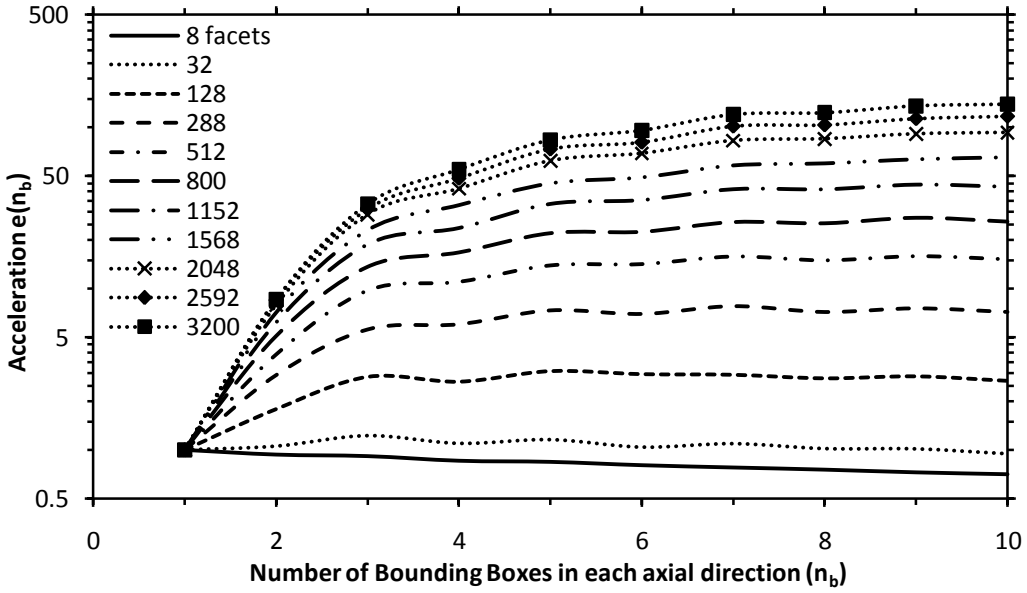

Figure 7-13 - Change in acceleration of GO calculations for faceted spheres when increasing numbers of bounding boxes are used. The total number of cells $\boldsymbol{n_c} = \boldsymbol{n_b^3}$, where $\boldsymbol{n_b}$ is the number of boxes along each axis. The acceleration $\boldsymbol{e(n_c)}$ is calculated by dividing the time taken for calculation by the original GO code by the time taken for calculation with changing values of $\boldsymbol{n_c}$. The calculations are shown for particles comprised of 8 facets up to 3200 facets.

Figure 7-13 shows how the acceleration ($e = e(n_c)$, where n_c is the number of boxes - defined as the time taken for calculations using the original GO code divided by the time taken for calculation using n_c boxes) changes for a faceted sphere as the number of boxes is increased. The acceleration changes for 10 spheres with increasing numbers of facets are shown. The computational overhead due to the bounding boxes implementation will scale according to the number of boxes; however, 1 box adds such low overhead that the acceleration is approximately 1. It can be seen that the overhead of introducing boxes causes the time taken for GO calculations for very low numbers of facets to actually increase. Moreover, calculations for particles with large numbers of facets respond positively to the introduction of bounding boxes, and the acceleration increases rapidly.

7.3.2 - Optimizing the Distribution of the Bounding Boxes.

In **Figure 7-12**, we can see that the execution times for spheres with large numbers of facets drop considerably as bounding boxes are added. However, the gain in acceleration is offset to some degree by the computational overhead of the bounding boxes. In certain cases, such as very low numbers of facets or very large numbers of boxes, this overhead can be significant, and may remove any benefits. Therefore, it is important to use a number and distribution of bounding boxes that will allow for the maximum reduction in execution time. The spheres considered so far have an axially-symmetric distribution of facets, and so it is prudent to use a similar distribution with the bounding boxes. For shapes which are not spatially evenly distributed, a different approach must be taken. **Figure 7-14** shows a cylinder (**Figure 7-14 (a)**) and two different bounding box distributions. The side facets of the cylinder extend along the *z*-axis, and so dividing these up as in **Figure 7-14 (b)** will only create

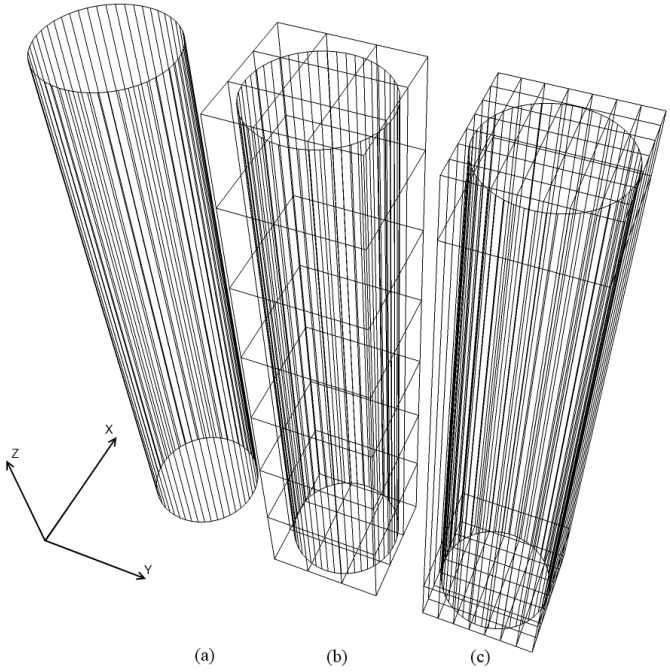

Figure 7-14 - From left to right: (a) - A faceted cylinder, (b) - the cylinder with an inefficient distribution of bounding planes, and (c) - the cylinder with an efficient distribution of bounding planes.

unnecessary work for the program. A more efficient approach is to use rectangular cuboids and to vary their size and distribution so that adjacent boxes containing the same facets are avoided, as in **Figure 7-14 (c)**. This will allow for a reduction in ray intersection calculations.

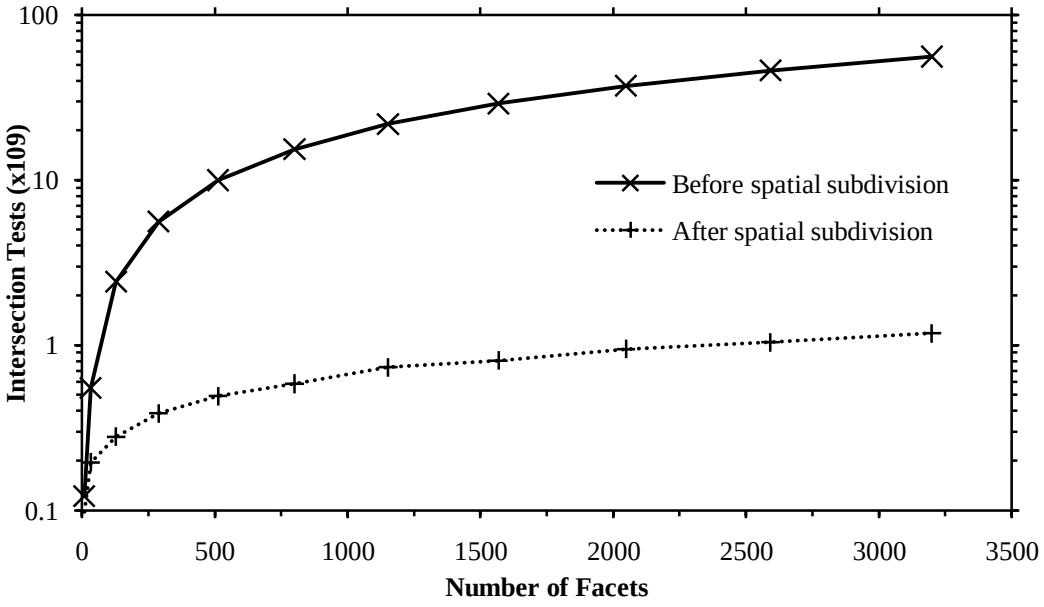

Figure 7-15 - The total number of intersection tests required for randomly oriented faceted spheres. Calculation times before and after the application of spatial subdivision are shown.

Figure 7-15 shows how the number of intersection tests for faceted spheres change as a result of spatial subdivision. As the number of facets is increased, the disparity between the number of intersection tests performed before and after spatial subdivision also increases. For a sphere of 3200 facets, the number of intersection tests before the addition of spatial subdivision is over 47 times the number of tests after spatial subdivision has been added. **Figure 7-16** shows that the increase in computation time with the number of facets is now linear when the number of facets is greater than 500. The expected computation time for a sphere of 5000 facets is now approximately 435 seconds (~7 ¼ minutes). Before the addition of spatial subdivision, the expected computation time for a sphere of 5000 facets was approximately 2200 minutes – spatial subdivision has reduced the expected computation time to less than 1/300th of the original GO program.

7.4 - Conclusions

It has been shown that the time taken for a GO calculation without spatial subdivision increases approximately quadratically according to the number of facets. A method of reducing the execution time for GO calculation of an object with a large number of facets has been developed and implemented. When applied to complex polyhedrons of more than 100 facets, the spatial subdivision technique developed here has been shown to reliably decrease the time required for computation. It has been shown that the relationship between the time taken and the number of facets is now approximately linear when the number of facets is more than 500. The predicted calculation time for a sphere comprised of 5000 facets has been reduced from 36 hours to under 7.5 minutes. This reduction in computation time comes at no cost to the accuracy of the calculations.

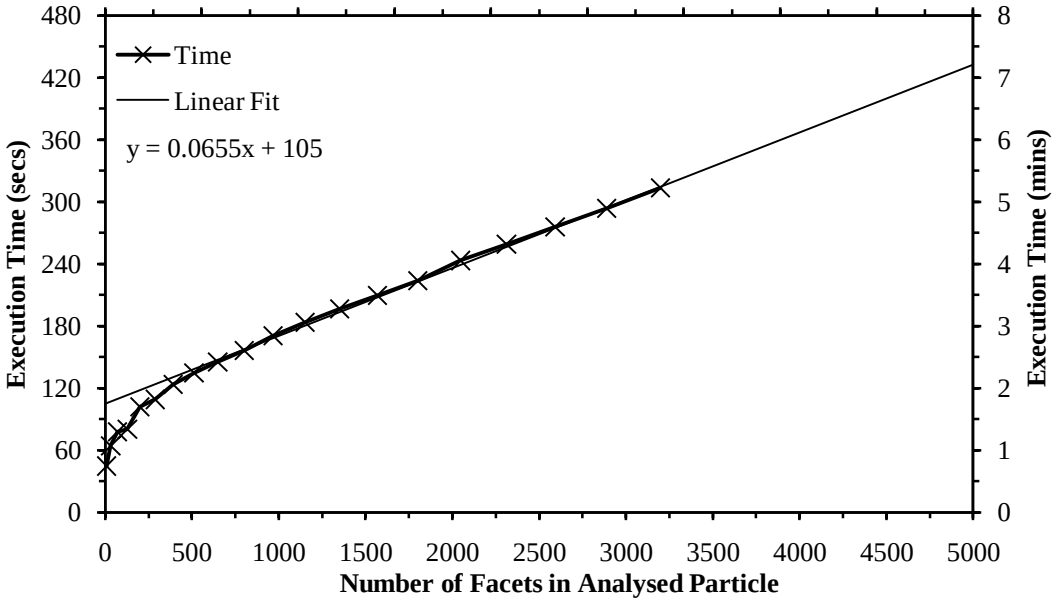

Figure 7-16 - Times taken for GO calculations of randomly-oriented increasingly faceted spheres are shown. Times are shown in both minutes and seconds. Here, spatial subdivision was used for each of the spheres. A trend line has been added where the number of facets > 500 and extended to show the likely time taken for spheres comprised of up to 5000 facets. The trend line equation calculates time in seconds.

This method is applicable to any Ray Tracing technique where ray-polygon intersections are calculated. It has been implemented into RTDF, which is based on the GO model created by A. Macke [18] and used throughout this chapter.

Chapter 8 - Properties of Saharan Dust Particles

8.1 - Scanning Electron Microscopy

8.1.1 – The Mineral Dust Sample

The dust sample used throughout this thesis was sourced from a Hamada in south-east Morocco (29.84957° N, 6.01508° W) in May 2006 as part of the SAMUM project [43]. The sample was sieved to contain dust particles of size 20-75µm. The mineralogy of the sample was semi-quantified using X-ray Diffraction, and the method of Reference Intensity Ratios. It was reported to contain quartz, albite, calcite, microcline, hematite and the clay minerals chlorite and kaolinite – quartz, microcline and chlorite are predominant [44].

8.1.2 – Refractive Index

As part of the Saharan Mineral Dust Experiment (SAMUM) the refractive index of the dust was determined from airborne measurements of particle size distributions and aerosol absorption coefficients [43]. Three different visible wavelengths were used, being blue (467nm), green(530nm) and red (660nm). The real part of the refractive index demonstrated only slight variance, with values between 1.55 and 1.56 at all wavelengths. The imaginary component of the refractive index demonstrated slightly more sensitivity to the wavelength of the incoming light – at 450nm the imaginary component varied between 3.1×10^{-3} and 5.2×10^{-3}. At 700nm the values ranged between 0.2×10^{-3} and 2.5×10^{-3}.

When viewed under an optical microscope prior to levitation, a reasonable idea of the shape and proportions of the particle can be obtained. However, very small scale surface structures will have a large impact on the scattering properties of an individual particle. In order that the scattering properties of the particles could be well understood, particles were chosen from the sample at random, and viewed under a Scanning Electron Microscope (SEM). In doing this, a clearer picture of small surface structure and overall particle morphology could be obtained.

A JEOL JCM-5700 SEM was used for all electron micrographs shown here, unless otherwise stated. A typical approach when performing electron microscopy on a sample is to apply a very thin (<100 nm) conductive coating – typically gold or carbon is used. This allows the sample to dissipate any built up charge to earth, via the stage on which the sample is mounted. Without this dissipation of charge, the particle could be seen to suddenly 'jump' when under high magnification. A primary goal when using the SEM was to analyse a particle, and then recover that particle and perform scattering measurements on it. To this end, we did not wish to coat the particles with a conducting layer, as this would alter the scattering characteristics. To achieve this, a practice called Environmental Microscopy was used. Instead of a very high vacuum within the electron microscopy chamber – standard practice when using a coated particle – a lower vacuum was used. Air was allowed inside the chamber, and the charge that built up on the particle due to the electron beam could dissipate into the air. However, it was discovered that the process of evacuating and then re-ventilating the chamber caused the particles to be displaced from their positions on the microscopy stage. Therefore, it was extremely difficult to recover a particle after examination, and it was decided that the Electron Microscopy would be used to obtain a

general impression of the surface characteristics of the particle sample. When performing scattering experiments, size and shape information of the individual levitated particle taken from an optical microscope would be used for particle reconstruction.

8.1.3 – Surface Roughness

Initially, images of a grouping of dust particles were taken – this is shown in **Figure 8-1**. It can be seen in the image that the larger particles have smaller particles attached to them. During the levitation experiments, it is likely that some of these smaller particles will become detached from the larger particles. It can also be seen from this image that the larger particles have an angular appearance, and at this scale, appear to have almost planar surfaces. **Figure 8-2** demonstrates that the particle surfaces are not planar, and demonstrate a considerable amount of surface roughness. In **Figure 8-3** & **Figure** 8-4 it is obvious that surface roughness is common to all the particles examined. It can be seen, however, that the level of surface roughness in the sample can change considerably - **Figure 8-4** shows three particles, with differing surface textures.

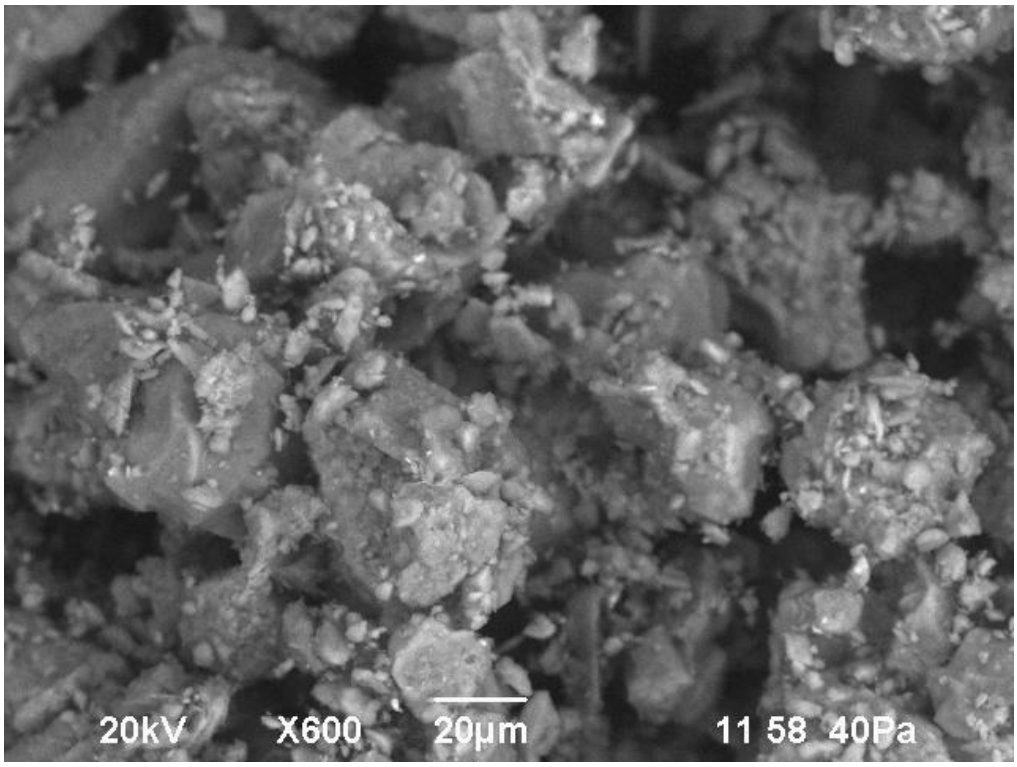

Figure 8-1 – An SEM image of a grouping of dust particles. We can see that the larger particles have smaller particles attached to their surfaces.

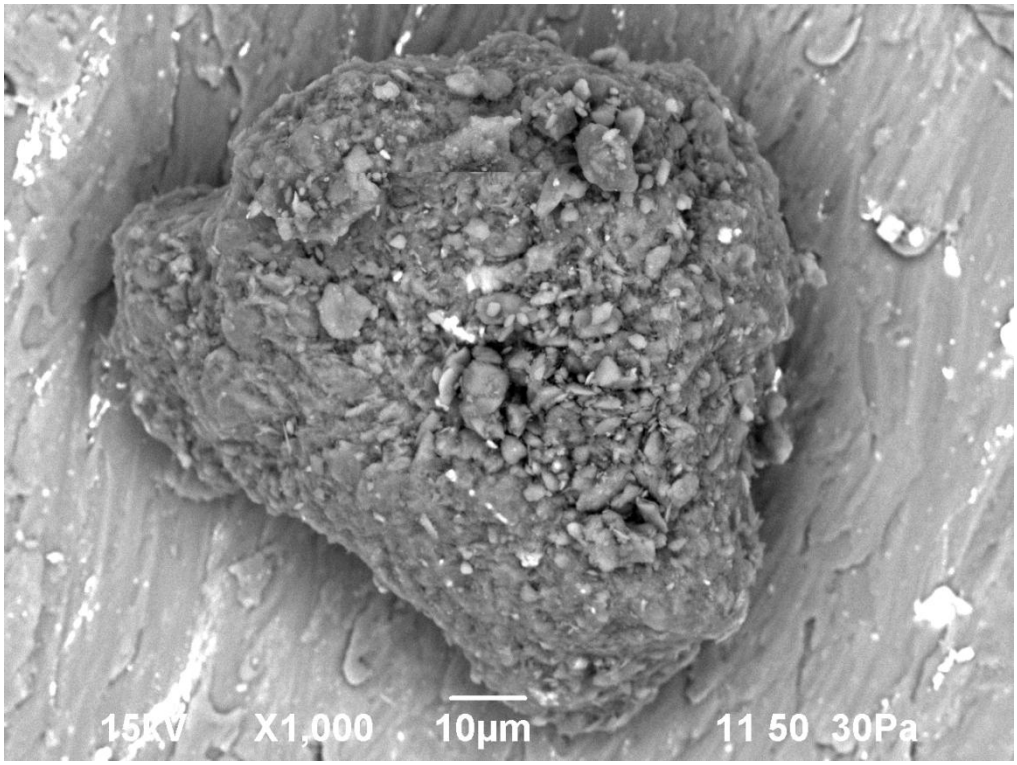

Figure 8-2 – An SEM image of a single dust particle. There are smaller particles attached to the surface of the particle. It can be clearly seen that the surface of the particle is not planar and demonstrates roughness, even at this magnification.

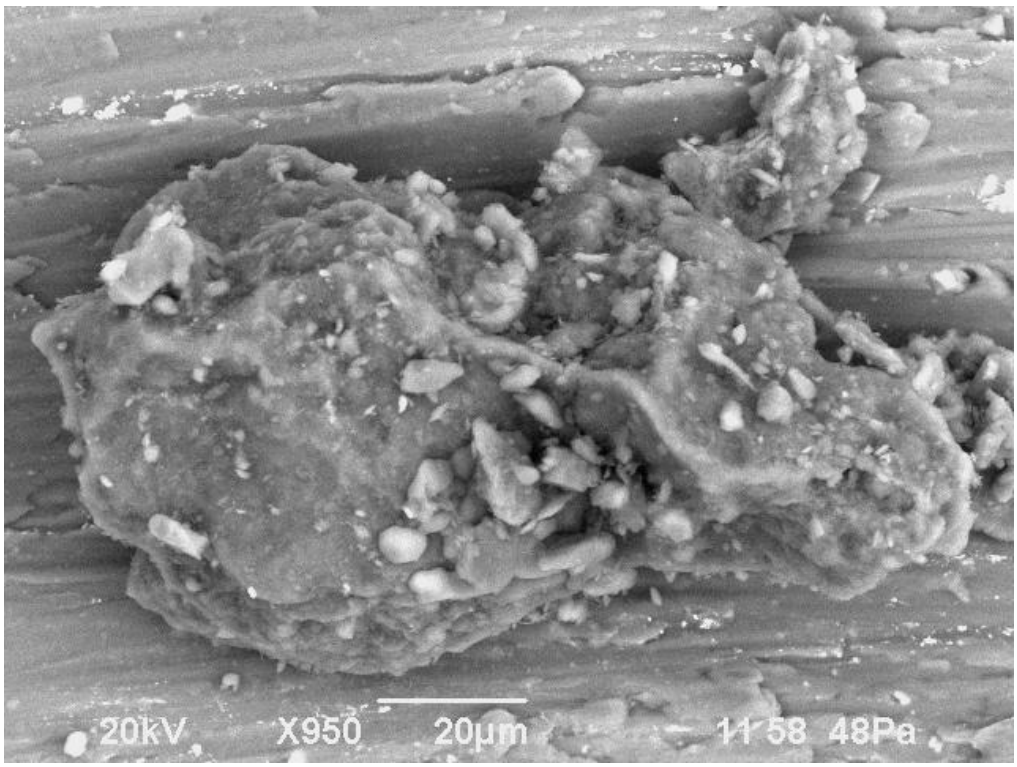

Figure 8-3 – Another particle demonstrating surface roughness, but of a lesser degree than the previous particle.

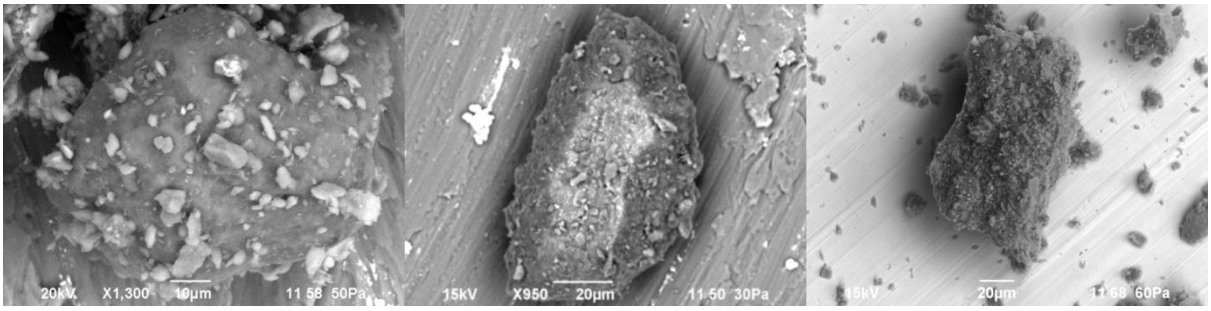

Figure 8-4 – A series of particles showing increasing levels of surface roughness from left to right.

All the particles differ quite considerably in the details of their shape. Some of the particles are very much like oblate spheroids, while others are elongated and are reminiscent of prolate spheroids. It appears, however, that the elongated particles do not have extreme aspect ratios: the particles above have an aspect ratio lower than three. When these particles are modelled for RTDF calculations, this will be an important factor.

Chapter 9 - Levitation & Scattering Experiments

9.1 - Case Study 1:

9.1.1 – Levitation and Scattering Measurements

In order to measure the scattering properties of the dust particles, the Electrodynamic Balance (EDB), Laser Diffractometer (LD) and Linear Photodiode Array (LPA) as described in Chapter 5 were used. Before levitation, each particle was imaged in multiple orientations using an optical transmission microscope. Using these images, the particle dimensions and overall morphology can be established. In **Figure 9-1-1** a Saharan dust particle is shown. It is an irregularly shaped particle with a maximum dimension of 28.5µm. **Figure 9-1-1 (a)** shows the particle in such an orientation that its short axis is 19.5µm. In **Figure 9-1-1 (b)** the short axis of the particle is 22.5µm. To calculate an approximate size parameter, we consider the particle as a prolate spheroid. Using the measurements taken, the particle has an Equal-Surface-Area-Sphere size parameter of between 137 and 149, and an Equal-Volume-Sphere size parameter of between 135 and 148. The incident light is of wavelength λ=0.5145µm.

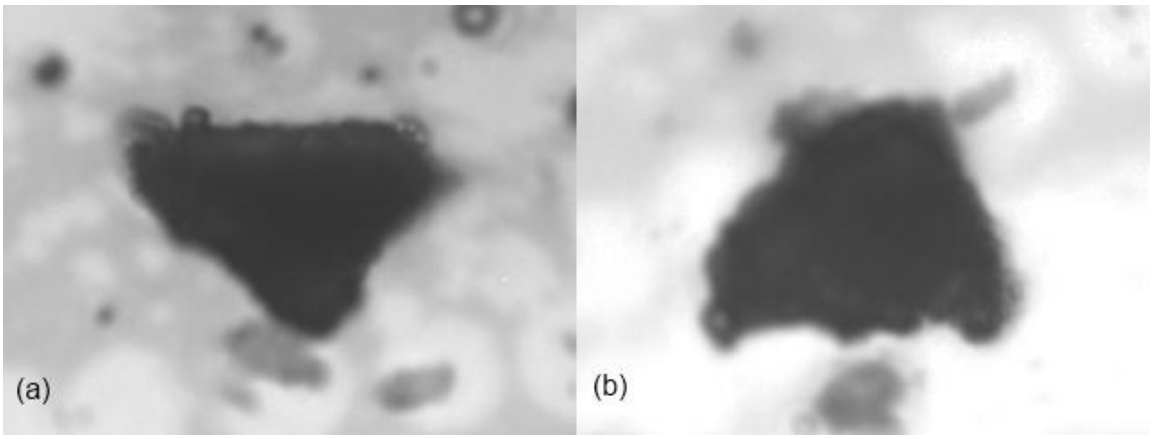

Figure 9-1-1 - A pre-levitation optical transmission microscopy image of a single Saharan Dust particle. In image (b) the particle has been rotated about 90° along its long axis (the long axis is horizontal here). The approximate particle dimensions are (a) 28.6µm x 19.5µm, (b) 28.6µm x 22.5µm. The approximate size parameter is between 137 and 149 (Surface Area) and 135 and 148 (Volume).

The particle in **Figure 9-1-1** was imaged, and then transferred to the EDB for levitation. The following EDB parameters were used:

DC Voltage – 24V (at injection), 6.1V (at centre of trap).

AC Voltage – 1000V @ 230Hz.

Injection Voltage – 800V pulse (50ns input pulse)

The particle was trapped successfully with the long axis vertical, and was observed to be undergoing a regular oscillatory motion, performing a full rotation about the vertical axis at approximately 0.5Hz. By increasing the AC Voltage to 1150V and decreasing the AC frequency to 180Hz, the frequency of rotation was increased to approximately 1Hz. **Figure 9-1-2** shows the motion of the particle when viewed from above. The reading

shown in **Figure 9-1-3** was taken using the Laser Diffractometer – as described in Chapter 5, both vertical and horizontal polarizations of the incident light were used, and multiple readings were

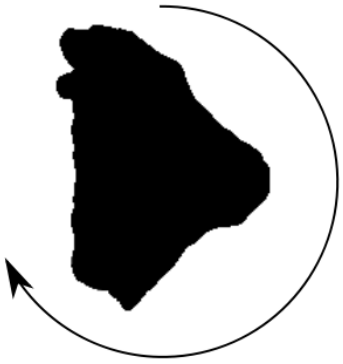

Figure 9-1-2 – The particle was trapped with the long axis in the horizontal plane. Full rotation about the vertical axis was observed.

taken incorporating background readings and high/low photomultiplier gains. The dynamic range of the gathered data was such that only two photomultiplier gains were needed. The Laser Diffractometer only measures angles to 177°, so angles 178° - 180° are given the same value as 177°. This is suitable due to the low dynamic range in this scattering region.

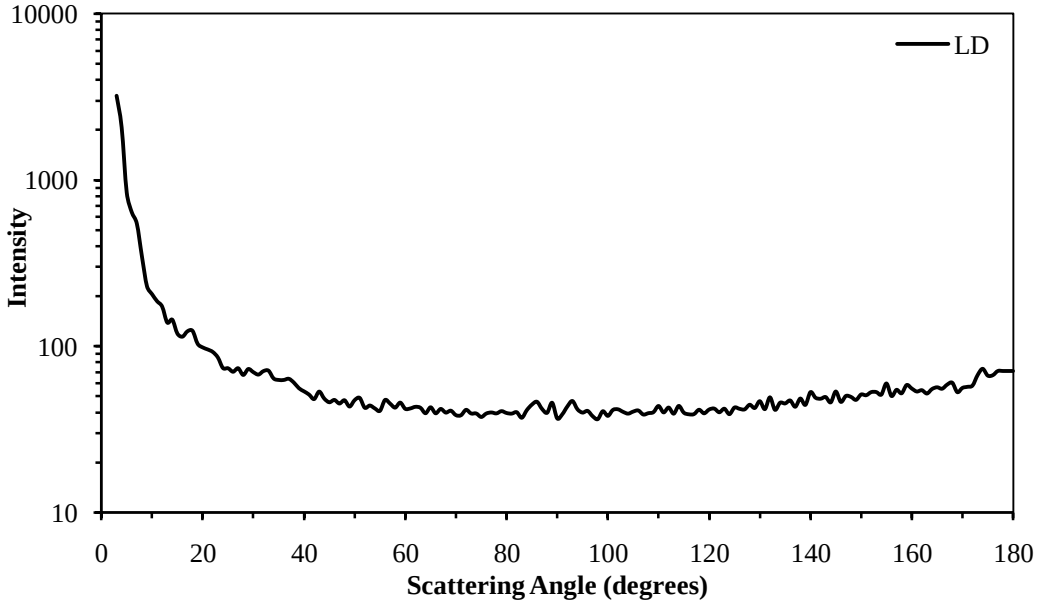

Figure 9-1-3 – The angular scattering intensity as recorded using the Laser Diffractometer for the particle in **Figure 9-1-1.** Readings were taken for vertically polarized light and for horizontally polarized light. The above is an average of those readings. Data is shown for scattering angles from 3° to 177°.

It can already be clearly seen that the scattering properties for this dust particle deviate enormously from that of a sphere. The scattering is nearly constant in the 60° - 180° region, and the interference effects and scattering peaks associated with regular particles are absent. The forward scattering intensity for the region between scattering angles 0.58° and 3.5° is shown in **Figure 9-1-4**. It can be seen that the peaks and troughs indicative of diffraction by a near-circular aperture are present. As the particle is strongly aspherical, if its rotation in the trap were completely random there would be either smaller peaks and troughs, or none at all. Therefore, this

may be an effect of the particle rotation being non-random. For a complete phase function, it is necessary to extrapolate the very small angle scattering data – in this case between 0° and 0.6°. To do this, the current small angle data

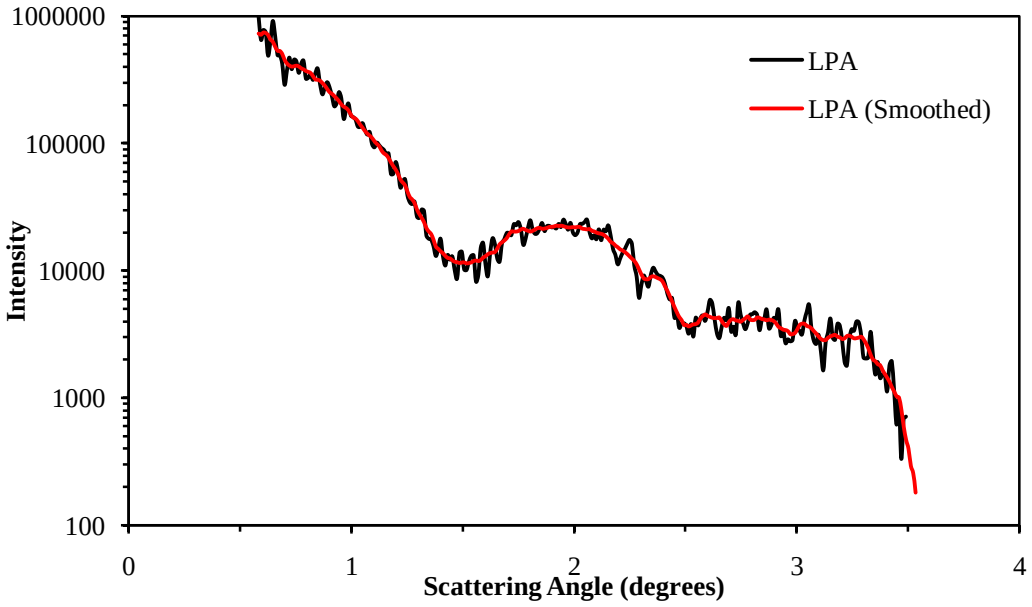

Figure 9-1-4 – Forward scattering intensity as measured using a Linear Photodiode Array for the particle shown in **Figure 9-1-1**. The vertical and horizontal polarization readings have been averaged and then been smoothed by interpolation.

is compared with 3 small angle computations - scattering for a sphere of similar size parameter, scattering for a gamma distribution of spheres [23] and the forward diffraction intensity for an ensemble of elliptical apertures.

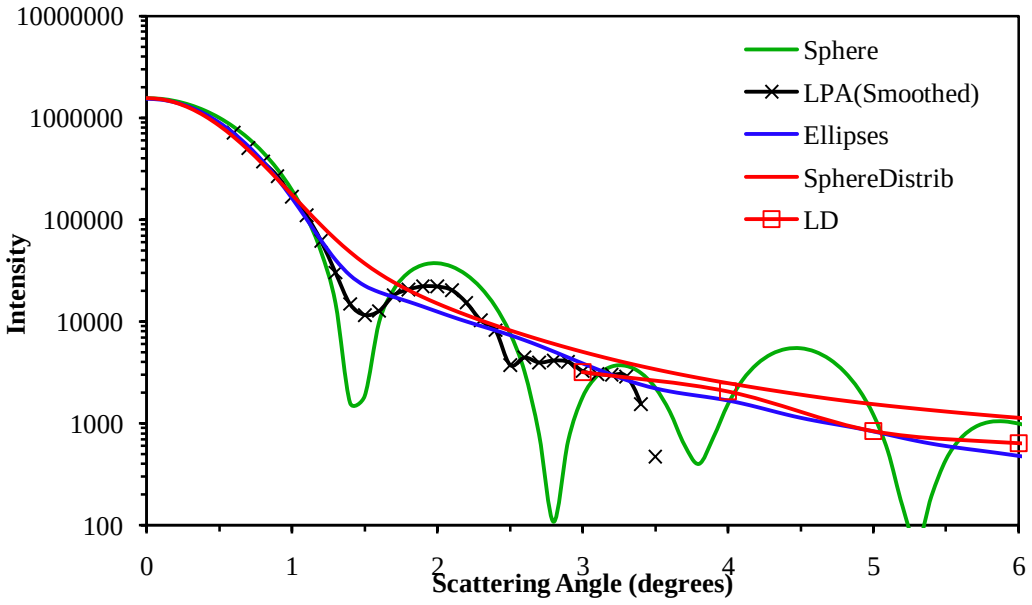

Figure 9-1-5 – The small angle scattering data for the particle shown in **Figure 9-1-1** compared with a single sphere (X_s=146), a gamma distribution of spheres (X_s=146, shape parameter a=146, scale parameter b=0.1, r_{min}=0 and r_{max}=800, all values given in terms of size parameter), and diffraction on a range of randomly oriented ellipses. Given the limited rotation of the particle and the close to 1 aspect ratio, the calculation was performed using a minimum radius of 8µm, a maximum radius of 14.3µm, an aspect ratio of 1.2727 and the wavelength of the incident light λ=0.5145µm. 20 values across this range were used. The data from the laser diffractometer is also shown between 3° and 6°. For the spheres, a refractive index of 1.55 + 0.001i was used.

Figure 9-1-5 shows how the scattering data recorded from the Linear Photodiode Array compares to scattering for spheres and diffraction on a range of elliptical apertures.

In the region 0.6° to 2.4°, excellent agreement between the LPA measured results and the diffraction on a range of ellipses is obtained. The angular position of the intensity peaks and troughs for the single sphere coincide well with the LPA data also, but there is a very large difference in the dynamic range of the two results. The gamma distribution of spheres is frequently used for results where interference effects have been averaged out – if the particle orientation in the trap had been successfully randomized, it is likely that this would have been the best approximation to the scattering data, as the peaks and troughs would have been removed.

The full phase function is calculated by placing the above results together, and then integrating over the full angular range, as described in Chapter 5. The resulting phase function is shown in **Figure 9-1-6**. Also shown for comparison is the phase function for a gamma distribution of spheres. The dust particle exhibits similarly strong forward scattering, but otherwise deviates strongly from Mie theory. This is especially noticeable between 70° and 160°, where the measured scattering intensity is much higher. As was noticed previously, between 20° and 180°, the measured intensity demonstrates very low variation, and is almost constant. None of the intensity peaks or specular reflections that would be anticipated from particles with spherical symmetry or with planar surfaces are present. This is a strong indicator that the surface of the particle is irregular. The degree of linear polarization for the particle is shown in **Figure 9-1-7**, and takes on the form of a bell curve as a function of scattering angle. The peak of the bell curve is 0.16. Both the phase function and DLP show agreement with readings found for scattering by meteoritic dust grains [45]. The asymmetry parameter for this particle has been calculated as approximately 0.59.

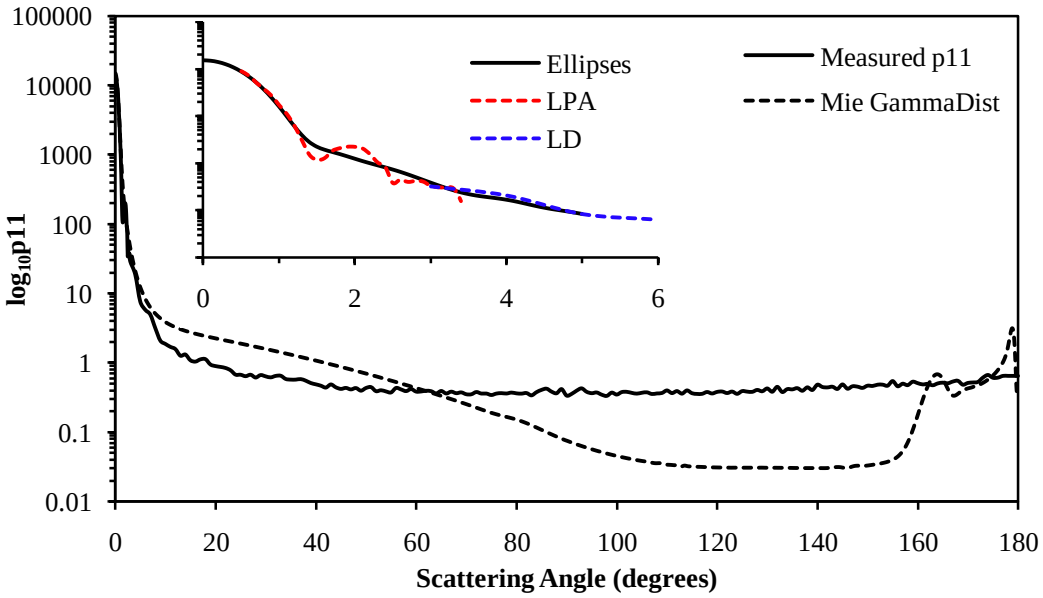

Figure 9-1-6 – The full phase function for the particle shown in **Figure 9-1-1**. The phase function for a gamma distribution of spheres is also shown for comparison. Inset: The small angle scattering data, showing how the 3 readings are joined together. The refractive index used in the sphere distribution calculations is 1.55 + 0.001i.

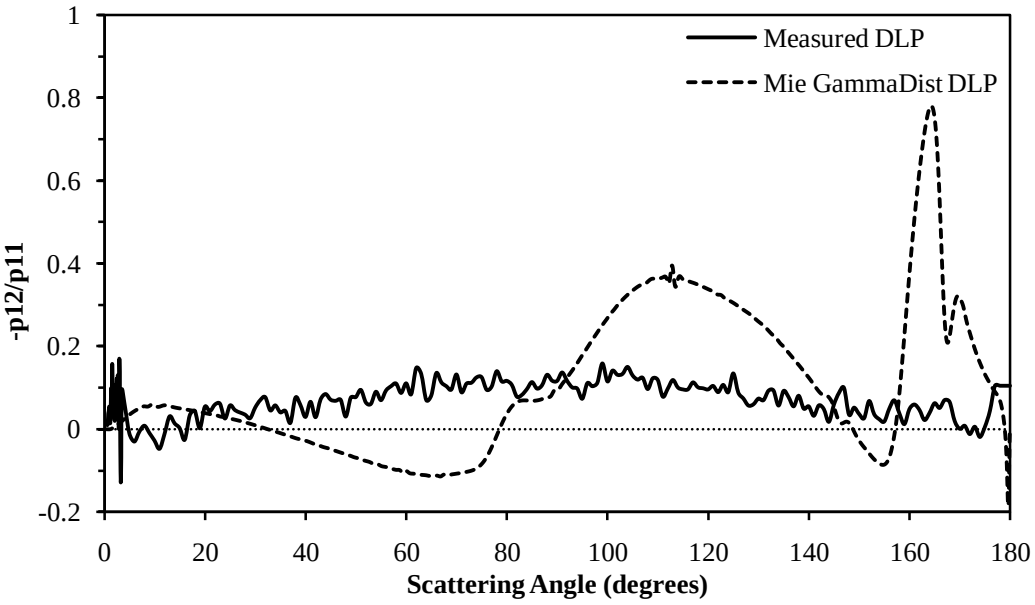

Figure 9-1-7 – The degree of linear polarization for the particle shown in **Figure 9-1-1**. Also shown for comparison is the DLP for a gamma distribution of spheres.

9.1.2 - Modelling the Particle

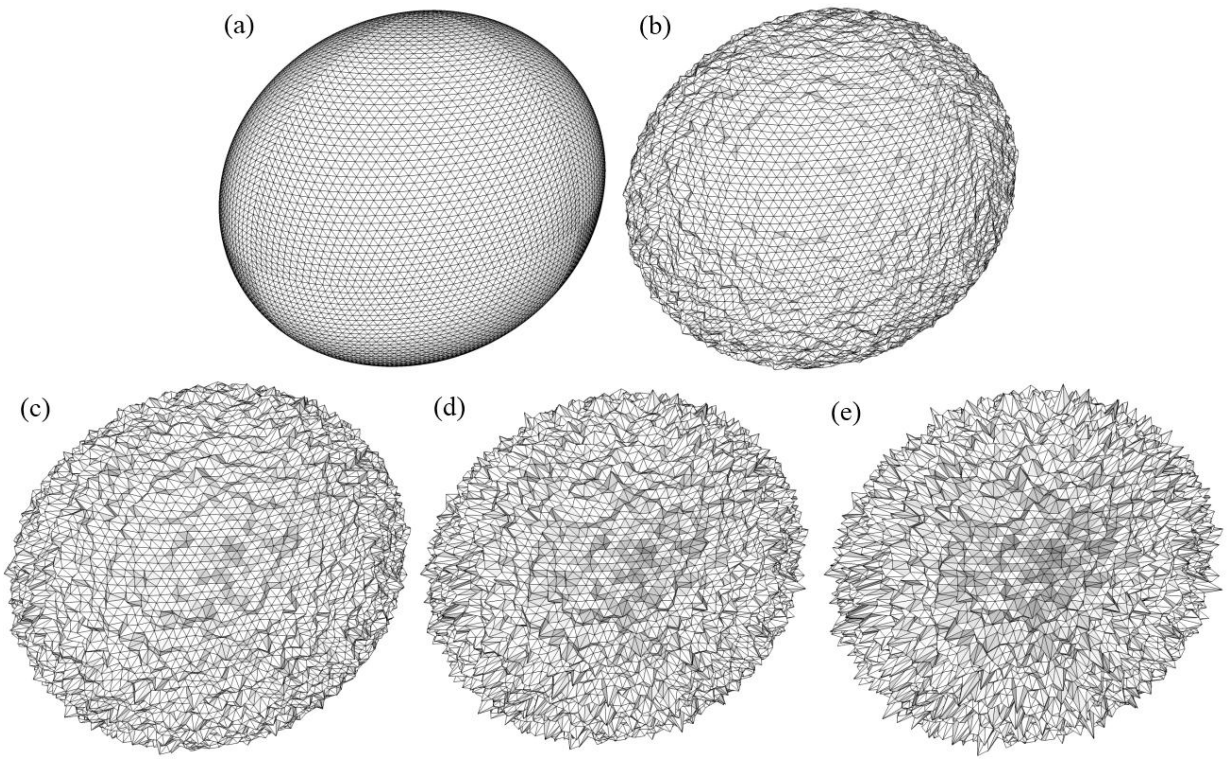

Figure 9-1-8 – Polygonal mesh approximations of the particle shown in **Figure 9-1-1**. All the figures are composed of 20,000 facets. Particle (a) is a perfect prolate spheroid, of aspect ratio ε=0.787. Particles (a) – (d) have surfaces generated using Gaussian Random statistics **[38]** and a correlation angle of 1°. The standard deviation σ for each particle is (a) σ=0.0, (b) σ=0.01, (c) σ=0.02, (d) σ=0.03, (e) σ=0.04.

Due to the very complex nature of the particle, it was unsuitable for exact reconstruction using a polygonal mesh. Therefore, the particle was considered as a prolate spheroid with aspect ratio ε=0.787 and equal-volume-sphere size parameter 146, and polygonal meshes were constructed according to these parameters. These meshes were then distorted according to the Gaussian statistics [38] discussed in Chapter 6. Using a correlation angle of 1°, and a standard deviation ranging from 0.01 to 0.04, the polygonal meshes shown in **Figure 9-1-8** were generated.

9.1.3 – RTDF and GO calculations

Scattering calculations for each of the particles presented in **Figure 9-1-8** were carried out using the RTDF [15], [16] and GO [18] model. As the particle was not completely randomly oriented in the beam, the rotation of the particle within the models was also limited. In order to simulate the long axis of the particle lying in the horizontal plane parallel to the direction of the beam propagation, the alpha Euler angle was set to α=90°. To simulate the freedom of rotation of the particle about the vertical axis perpendicular to the direction of the beam propagation, the beta Euler angle was given freedom of the angular range, $0° \leq \beta \leq 360°$. The gamma Euler angle was restricted so that the long axis of the particle could only deviate a small amount from the horizontal plane, $-5° \leq \gamma \leq 5°$. To determine the effect of the particle rotation on scattering, further calculations were performed, this time with completely random rotation allowed.

It is important to note how the scattering data is binned in the RTDF and GO models. For all calculations shown here, the 1° - 179° region is binned at 1° intervals, and bins have been added at 0.25° and 179.75°. They collect all rays exiting between 0.0° and 0.5°, and 179.5° and 180°, respectively. However, at very low angles diffraction is dominant, and is calculated exactly using the equations presented in Chapter 5. It is unlikely that finer binning of the ray-tracing part of RTDF and GO in the near forward direction would have any noticeable effect on the phase functions calculations.

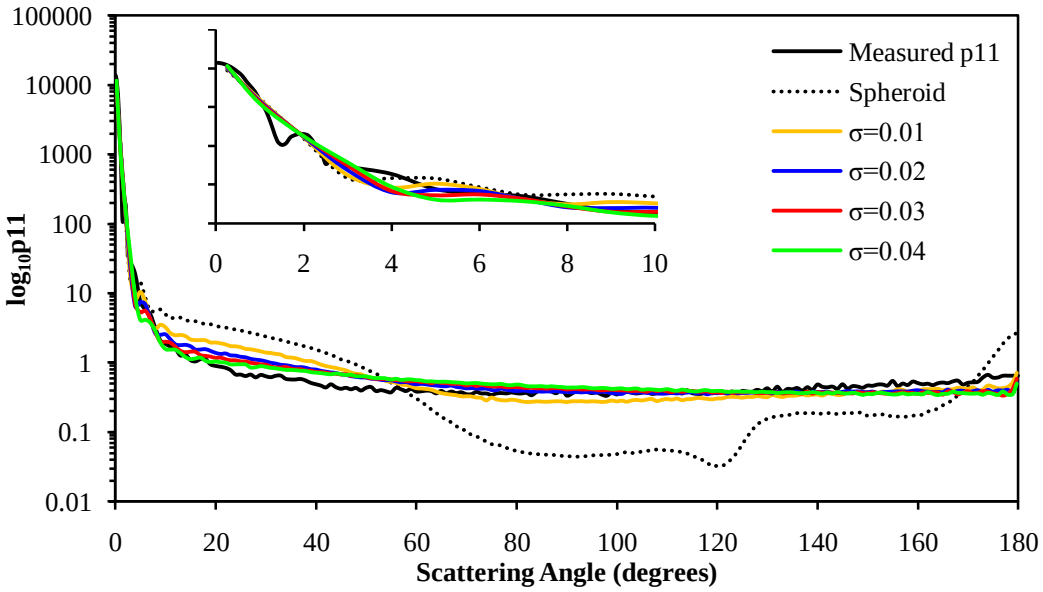

Figure 9-1-9 - The scattering phase functions as calculated using RTDF for a range of modelled particles compared with the measured phase function for particle 1. The modelled particles are those shown in **Figure 9-1-8**, and the refractive index used for these calculations is 1.55 + 0i. In these calculations, the orientation of the particle was limited as described in the text.

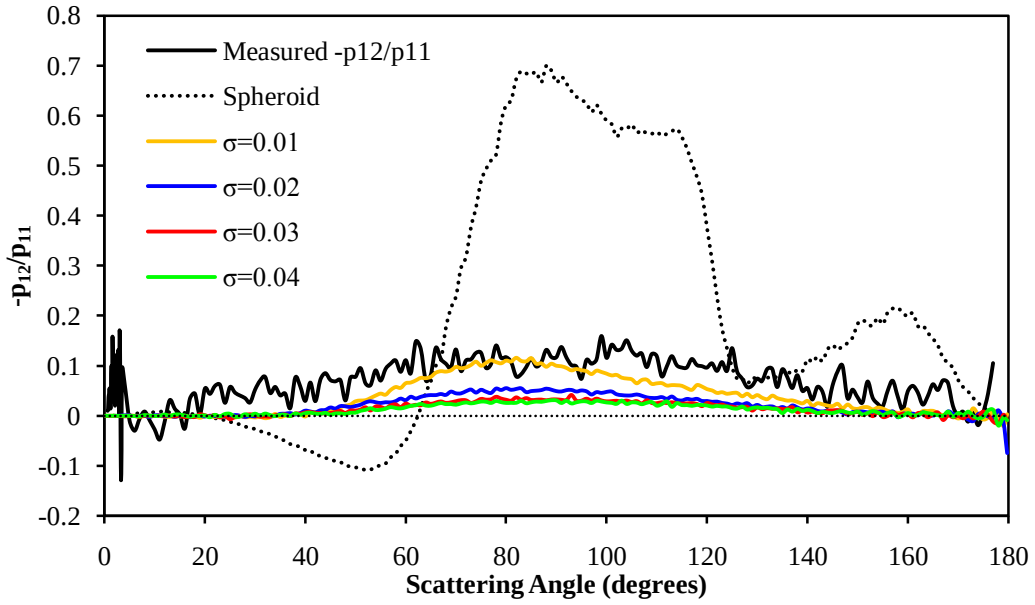

Figure 9-1-10 – As in **Figure 9-1-9** for the Degree of Linear Polarisation.

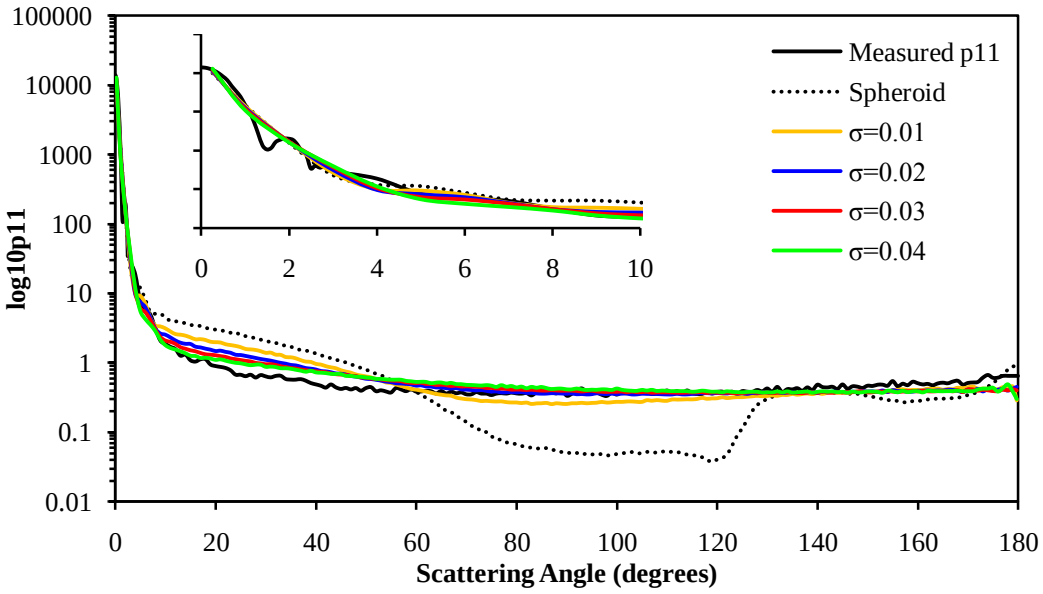

Figure 9-1-11 – As **Figure 9-1-9**. In these calculations, the particle was free to rotate randomly.

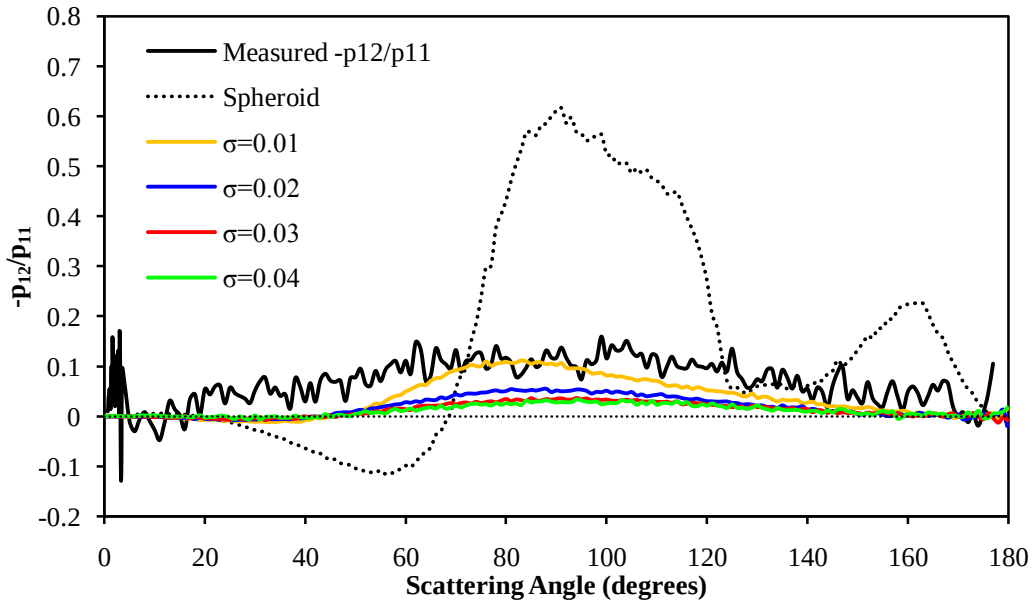

Figure 9-1-12 – As in **Figure 9-1-11** for the Degree of Linear Polarisation.

Figure 9-1-9 – 9-1-12 show RTDF calculations using a refractive index of 1.55 + 0i. It is immediately apparent that adding surface roughness to the modelled particles improves the comparison with the measured results, particularly in the mid-scattering range. As σ is increased, the modelled approximation improves significantly between 8° and 60°. Above 60°, higher values of σ demonstrate the same homogeneity that the measured results show, with a relatively flat phase function.

The DLP results also indicate that the rough surface particles are an improvement over smooth spheroids. The results take on the form of a flattened bell curve, and the peaks decrease as σ is increased. The measured DLP is larger across most of the angular range than the modelled particles.

For both sets of results, it is noticeable that limiting the orientation of the particles does not have a significant effect.

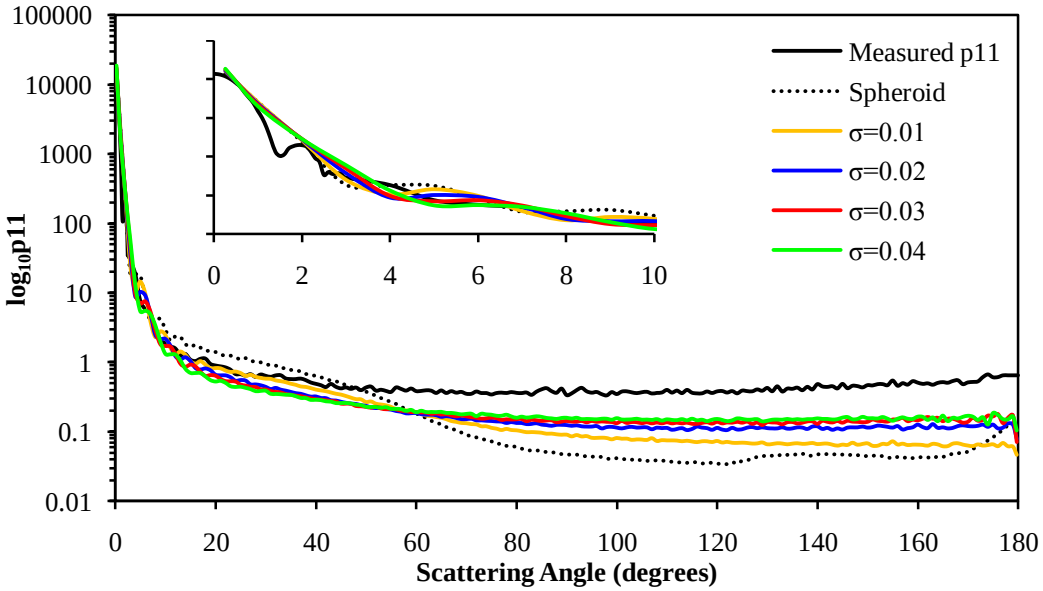

Figure 9-1-13 - As in **Figure 9-1-9** but with a refractive index of 1.55 + 0.003i.

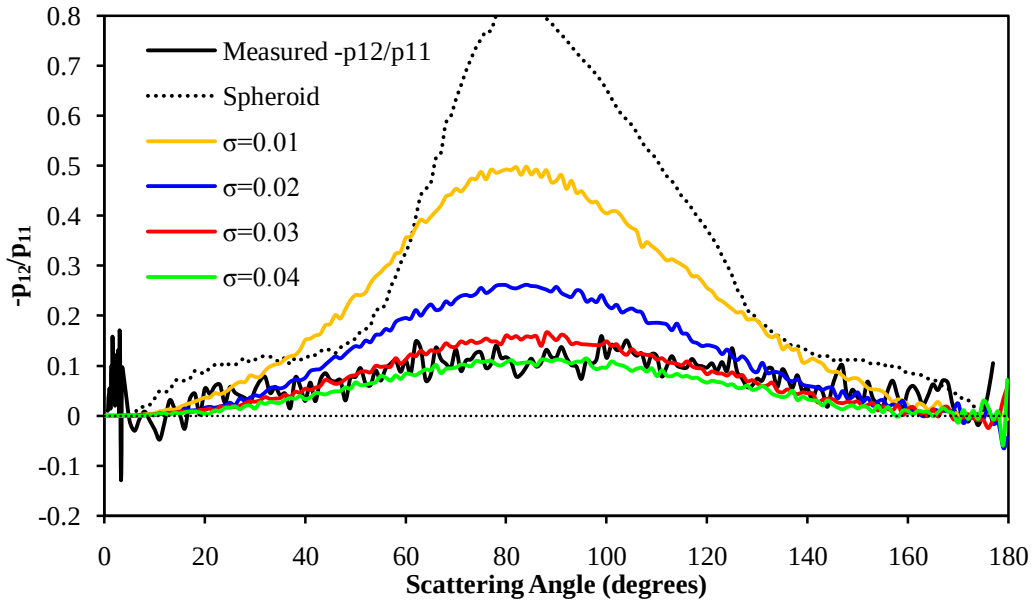

Figure 9-1-14 – As in **Figure 9-1-13** for the Degree of Linear Polarisation.

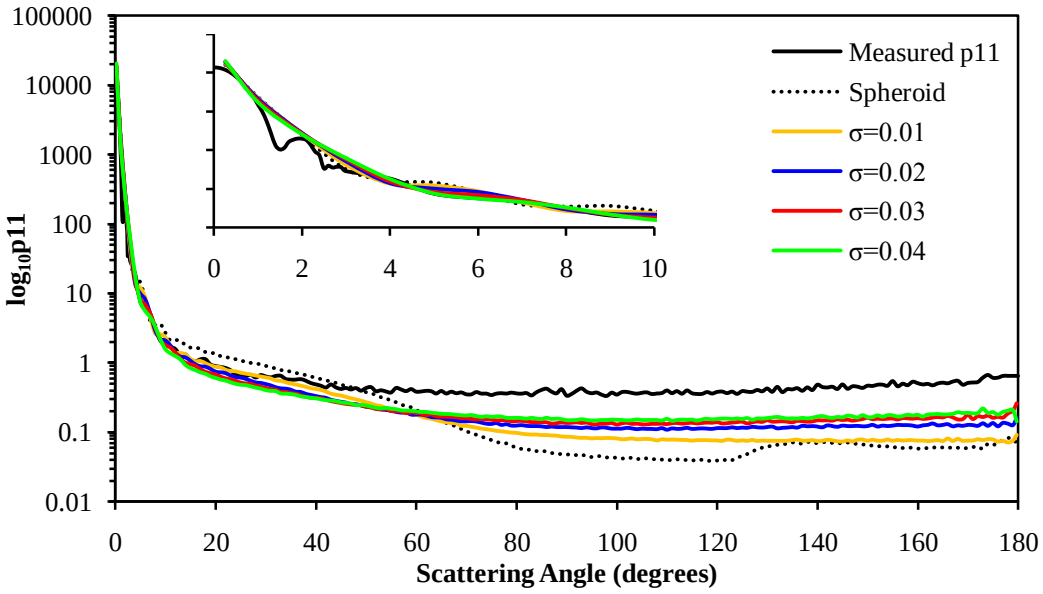

Figure 9-1-15 - As in **Figure 9-1-11Error! Reference source not found.** but with a refractive index of 1.55 + 0.003i.

Figure 9-1-16 – As in **Figure 9-1-15** for the Degree of Linear Polarisation.

Figure 9-1-13 – Figure 9-1-16 show RTDF calculations using a refractive index of 1.55 + 0.003i. The phase function comparison above 30° deviates from the measured results considerably, although larger values of σ show moderately better agreement. The calculated results are considerably lower than the measured results for mid-high scattering angles.

Conversely, the DLP results improve considerably on those with no absorption. As σ increases, the calculated results approach the measured results.

Again, limiting the orientation of the particle does not have a large effect on either the phase function or the DLP.

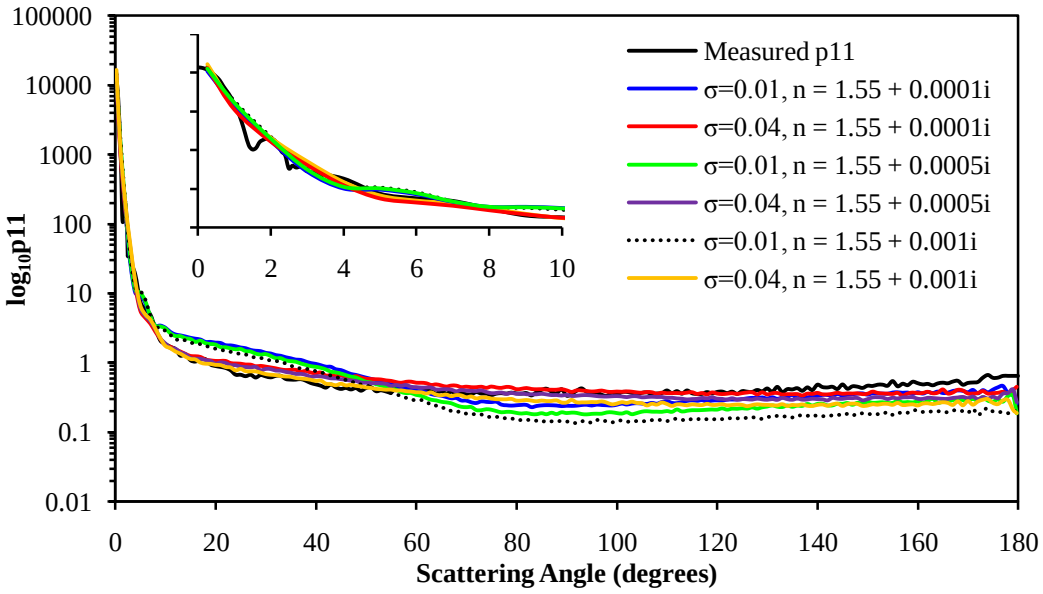

Figure 9-1-17 - The scattering phase functions as calculated using RTDF for a range of modelled particles compared with the measured phase function for particle 1. The modelled particles are those shown in **Figure 9-1-8**. The complex component of the refractive index was varied, and two values of σ were used. Here, the particle was free to orient randomly.

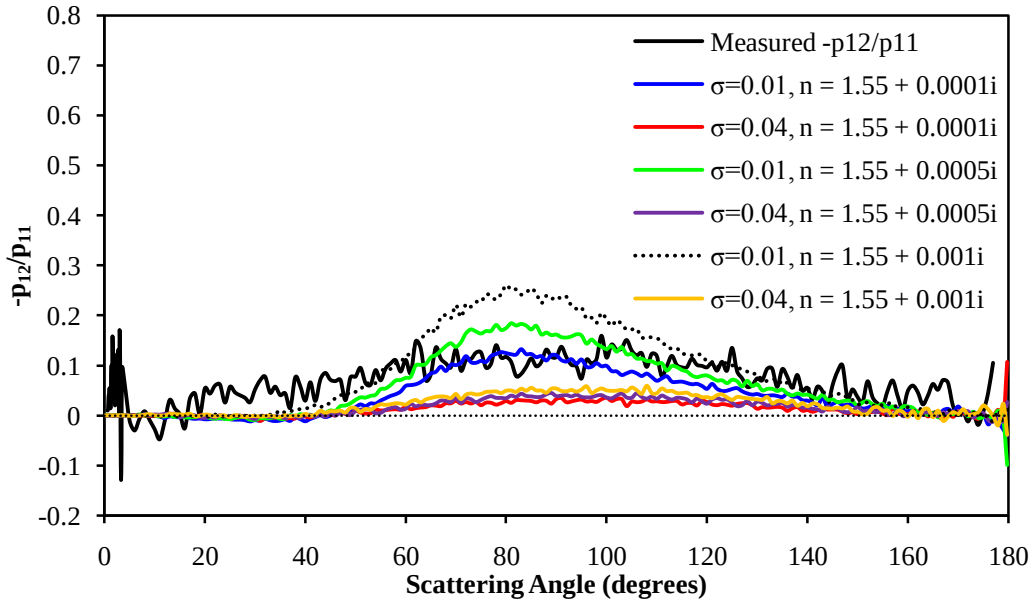

Figure 9-1-18 – As in **Figure 9-1-17** for the Degree of Linear Polarisation.

Figure 9-1-17 – 9-1-18 show RTDF calculations for a range of surface roughness values and a range of absorption components. We can see that the agreement in the forward scattering region is improved for computations where σ=0.04. Between approximately 10° and 50°, computations where σ=0.01 diverge from the measured phase function; above this, the computed phase functions are lower than the measured phase function. Higher values of σ give improved agreement across the entire angular range. In the forward scattering region, higher absorption gives improved agreement, while in the backscattering region, lower absorption is better.

Higher values of σ show a much lower DLP than was measured for the particle. Decreasing σ gives increased agreement in the side scattering region. As σ was increased, the computed DLP decreased in the side scattering region below that measured for the levitated particle.

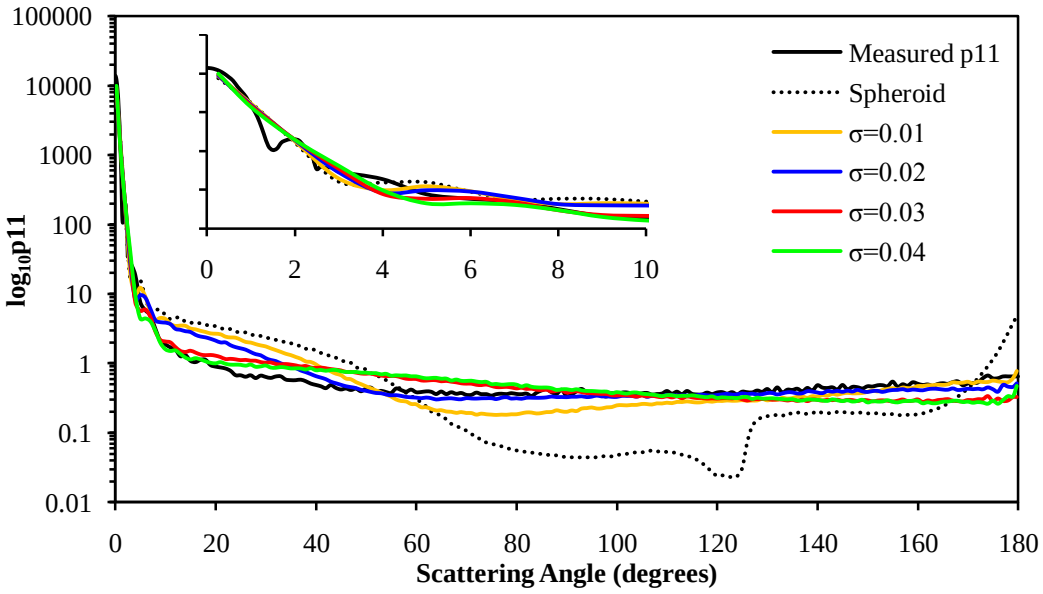

Figure 9-1-19 - The scattering phase functions as calculated using GO for a range of modelled particles compared with the measured phase function for particle 1. The modelled particles are those shown in **Figure 9-1-8**, and the refractive index used for these calculations is 1.55 + 0i. In these calculations, the orientation of the particle was limited as described in the text.

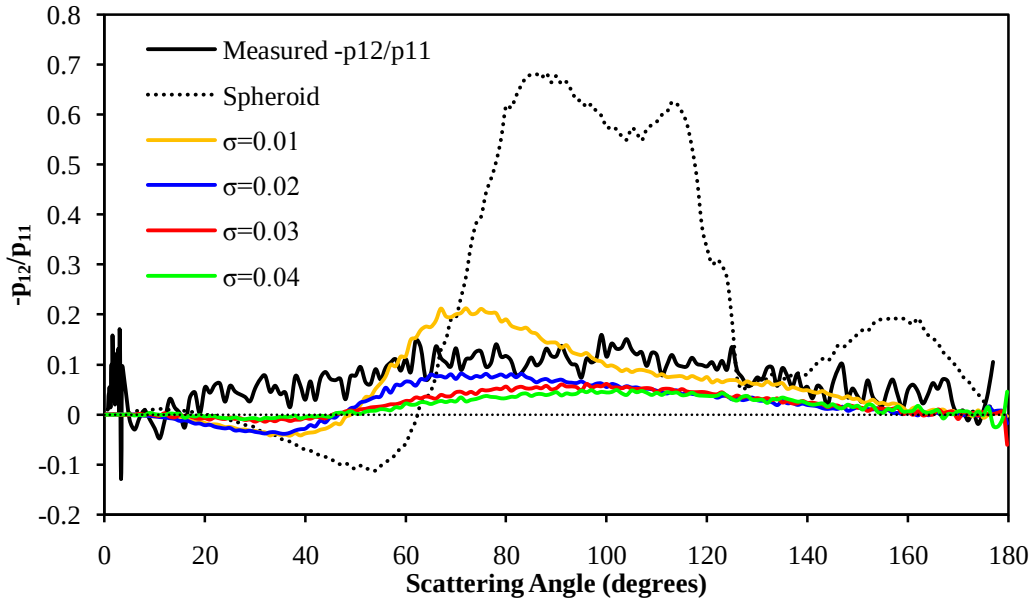

Figure 9-1-20 – As in **Figure 9-1-19** for the Degree of Linear Polarisation.

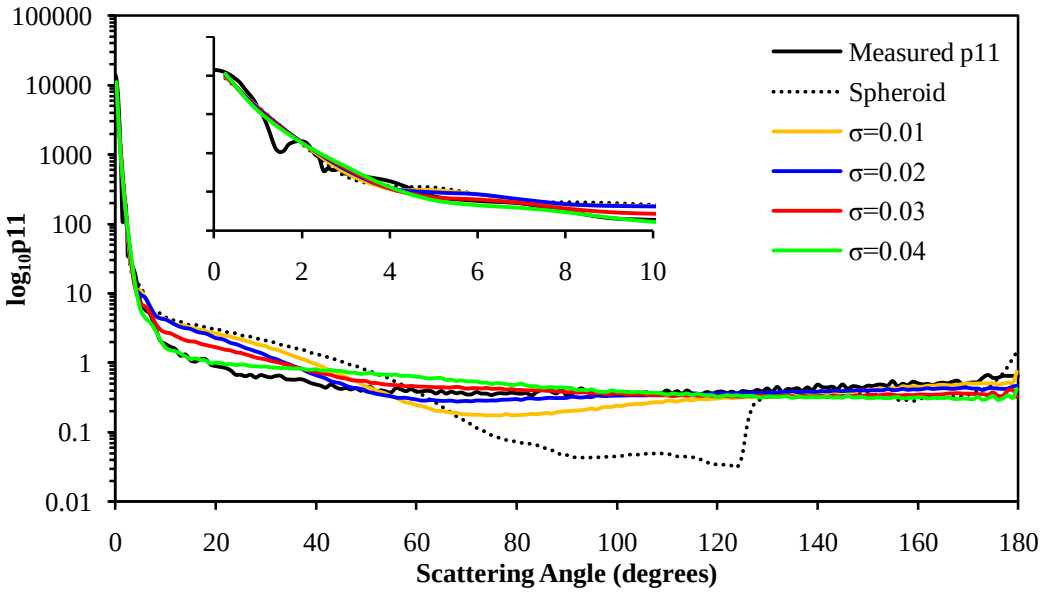

Figure 9-1-21 – As in **Figure 9-1-19** but the particle was free to rotate randomly.

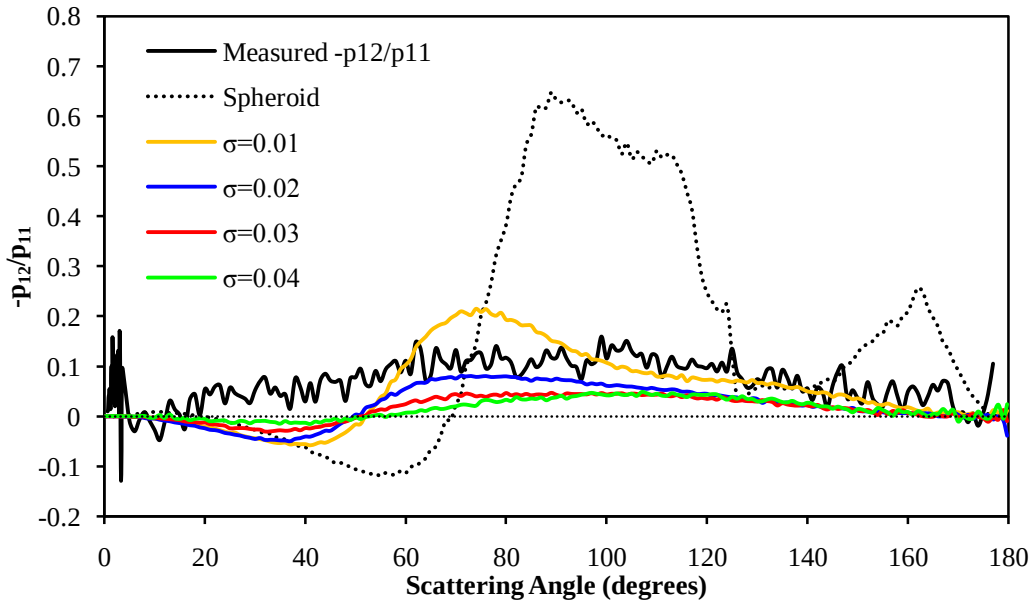

Figure 9-1-22 – As in **Figure 9-1-20** for the Degree of Linear Polarisation.

Figure 9-1-19 – 9-1-22 show GO calculations using a refractive index of 1.55 + 0i. . Again, as in the RTDF results, the small angle scattering regions compares well. For σ=0.01 or 0.02, there is a significant disparity in the phase functions between 8° and ~120°. Between 8° and 50°, the calculated phase functions are higher than the measured, and between 50° and 120°, the calculated phase functions are lower than the measured. As σ is increased, the comparison does improve. When σ=0.04, the phase functions fits well until 20°, and then again at angles >100°.

The DLP results differ considerably from RTDF. There is a dip in the DLP for all values of σ, although this is less pronounced as σ is increased. The flattened bell curve shape of the measured DLP is not replicated well by any of the calculations.

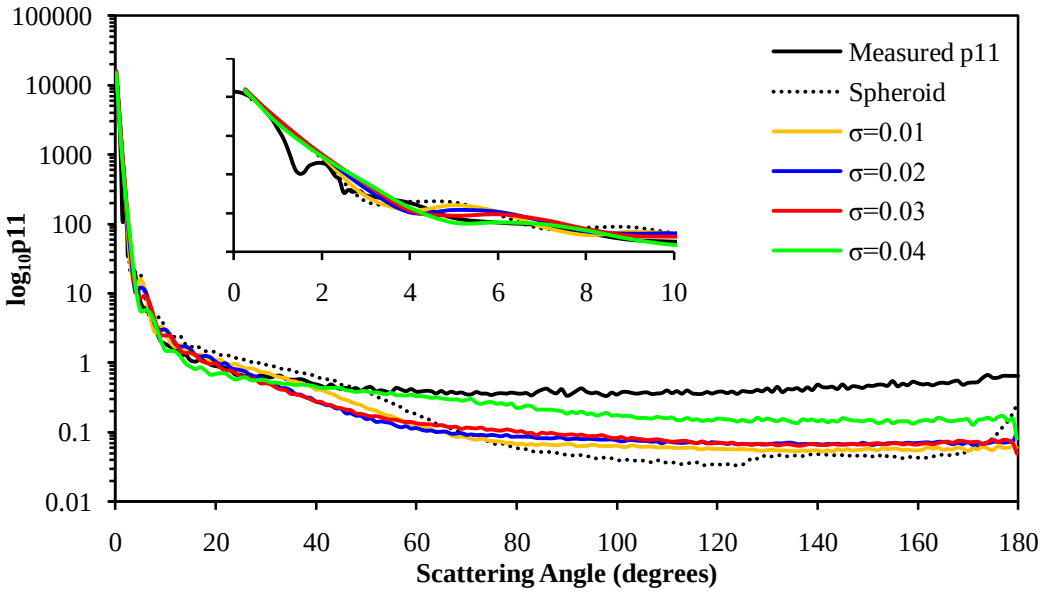

Figure 9-1-23 - As in **Figure 9-1-19** but with a refractive index of 1.55 + 0.003i.

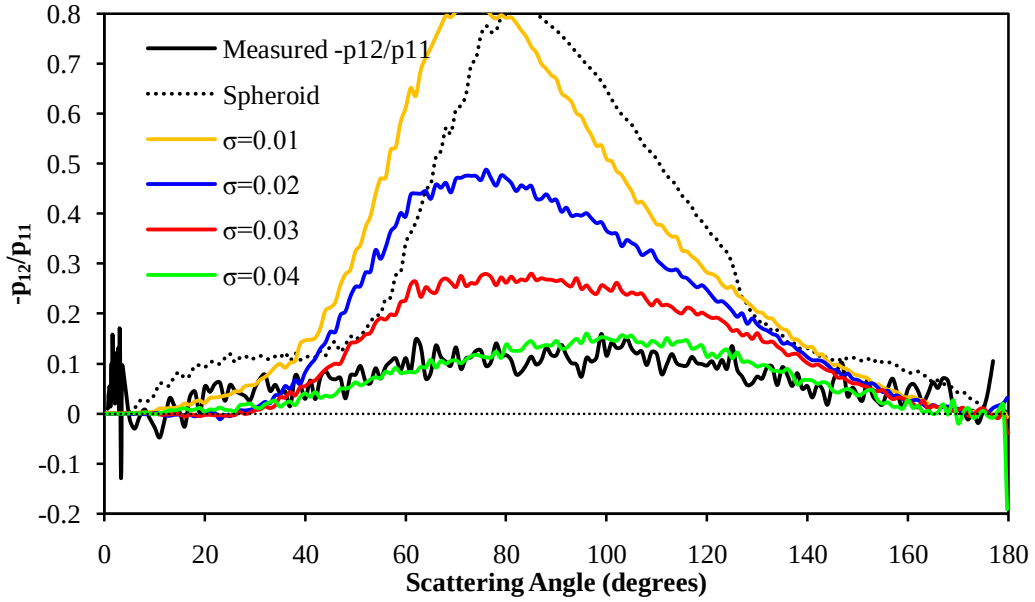

Figure 9-1-24 – As in **Figure 9-1-23** for the Degree of Linear Polarisation.

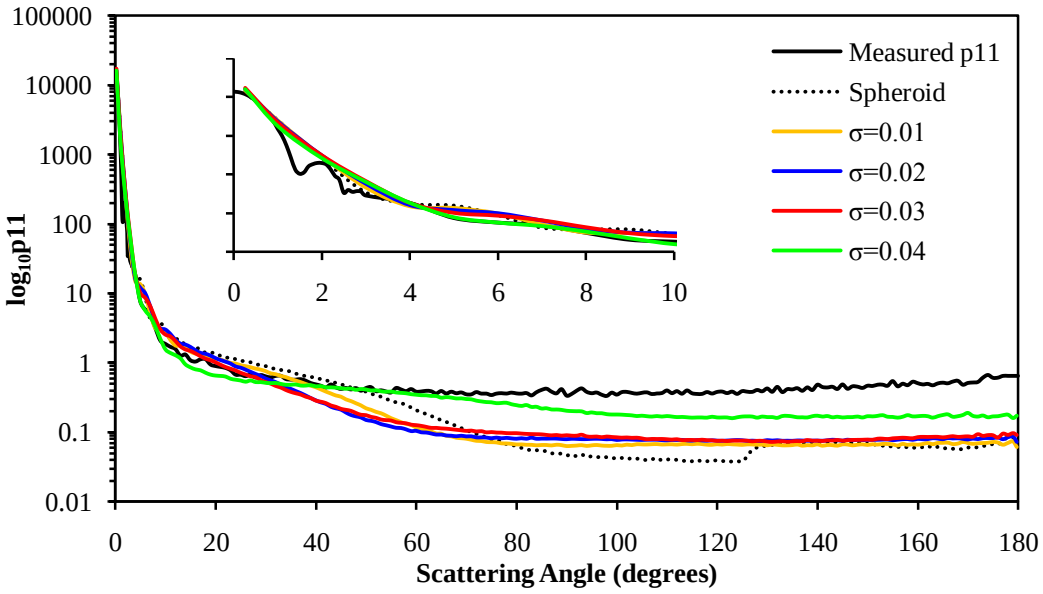

Figure 9-1-25 As in **Figure 9-1-21** with a refractive index of 1.55 + 0.003i.

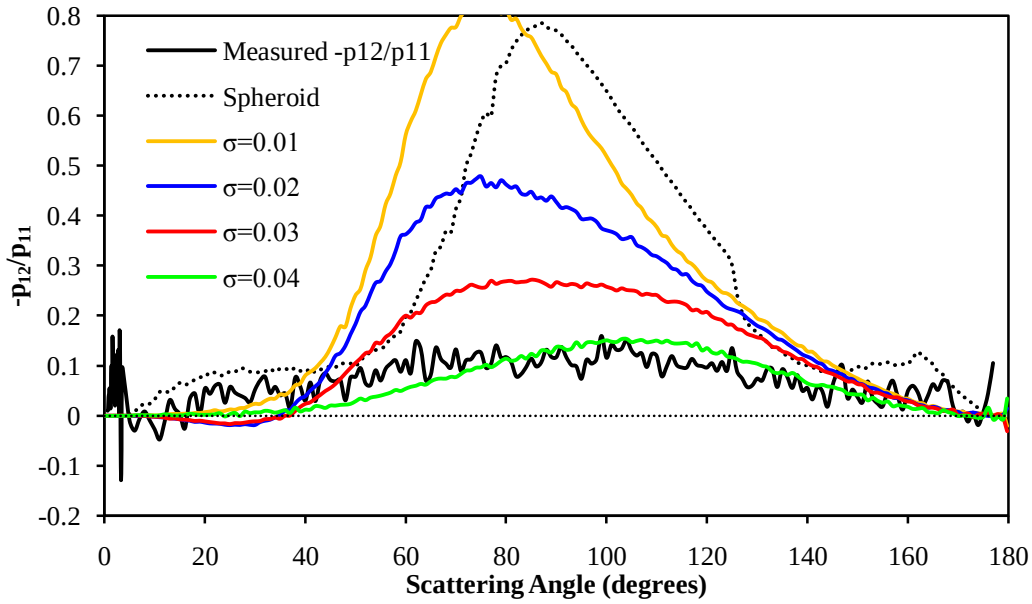

Figure 9-1-26 – As in **Figure 9-1-25** for the Degree of Linear Polarisation.

Figure 9-1-23 – 9-1-26 show GO calculations using a refractive index of 1.55 + 0.003i. The measured phase function is replicated well at small angles for all non-zero values of σ. However, small values of sigma demonstrate much lower side scattering than was measured. When σ=0.04, the phase function compares well between 0° and 60°, but for angles above 60°, it too is much lower than the measured results.

The DLP results are similar to those calculated by RTDF. At the highest value of σ, they compare very favourably with the measured results. There is a noticeable change in the shape of the DLP between orientation limited and random orientation calculations. On this occasion, the orientation limited results compare more favourably than the random orientation.

9.1.4 - RMS Comparison of phase functions

When comparing two phase functions quantitatively, steps must be taken to ensure that the comparison is meaningful. The scattering data from the RTDF/GO calculations and the measurements for the levitated particle is binned at 1-degree intervals. A linear comparison of the angular values of two phase functions is going to be heavily weighted towards the small angle region, where the majority of the scattered intensity is located. This small angle region is heavily dependent on diffraction, which for a randomly oriented particle is dependent more on size than on shape. In order to gain a more accurate idea of how the particle shape influences scattering, an RMS subtraction of the base 10 logarithm of the phase function values is performed. This will provide us with a scalar value which can be compared with other RMS subtractions in order to quantitatively evaluate the goodness of fit between two phase functions.

The RMS 'error' value E_{rms} is given by

$$E_{rms} = \sqrt{\frac{1}{181}\sum_{\theta=0}^{180}(\log_{10}(p_1(\theta)) - \log_{10}(p_2(\theta)))^2} \tag{9.1}$$

Where p_1 is the phase function for the levitated particle and p_2 is the phase function as calculated using GO or RTDF. Higher values of E_{rms} indicate increased variance between the measured and computed results across the angular range. A value of 0 would indicate complete conformity across the entire range.

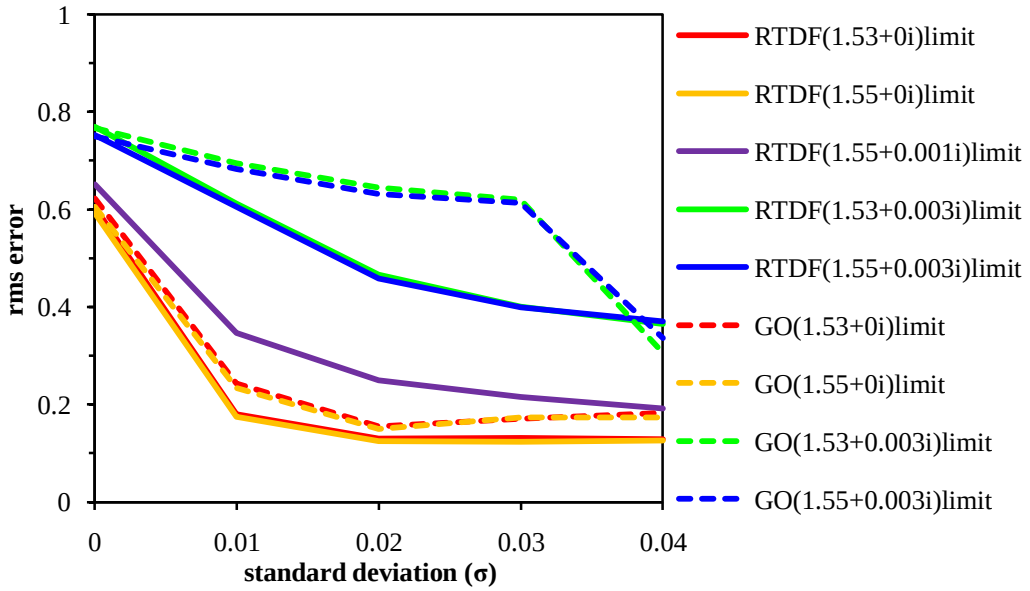

Figure 9-1-27 – RMS errors comparison for the measured results with respect to computations for a range of standard deviations. For these calculations, the particle orientation was limited as described in the text.

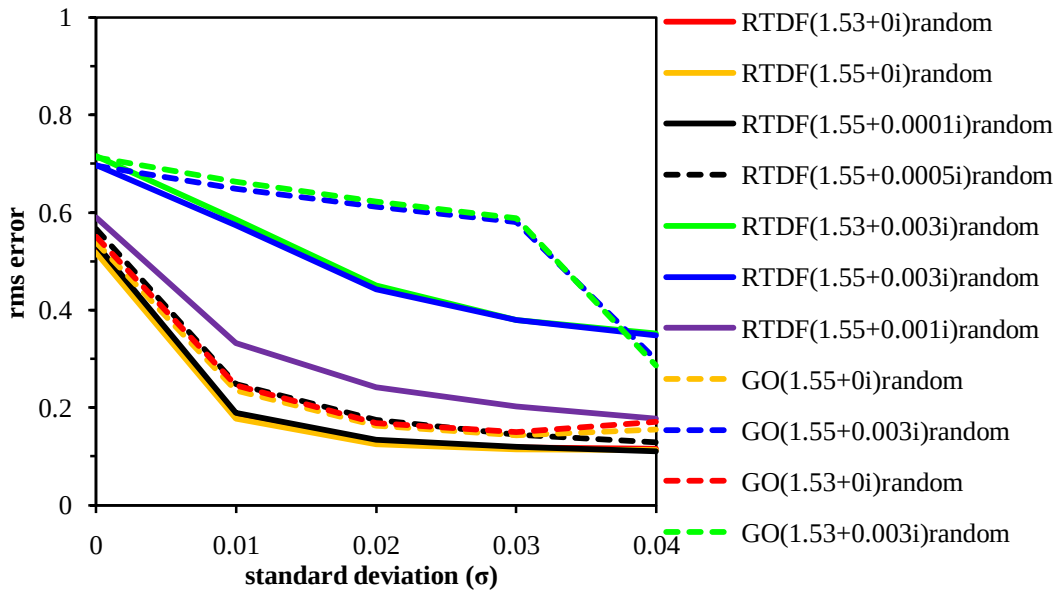

Figure 9-1-28 – As in **Figure 9-1-27** but the particle was allowed to orient freely.

The RMS error values are shown in **Figure 9-1-27** and **Figure 9-1-28**. The addition of absorption generally increases the size of the error, except in a very few GO cases. In general, it is clear that as σ increases, the comparison improves, except in the case for non-absorbing GO calculations, where the error value increases for higher values of σ. As mentioned previously, limiting the orientation of the particles does not seem to have a considerable effect on the calculations.

9.1.5 - Asymmetry Parameter

The asymmetry parameter is also used here for quantitative comparison. The asymmetry parameter for the levitated particle is 0.593, as calculated from the measured phase function.

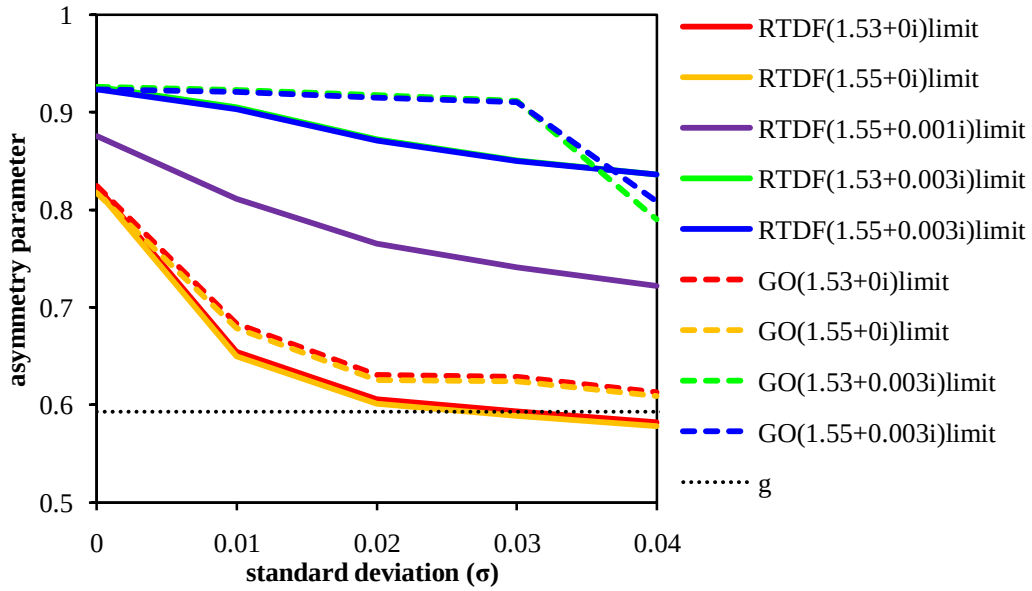

Figure 9-1-29 – Comparison of calculated asymmetry parameters with that of the levitated particle (g). Here, the particle orientation was limited as described in the text.

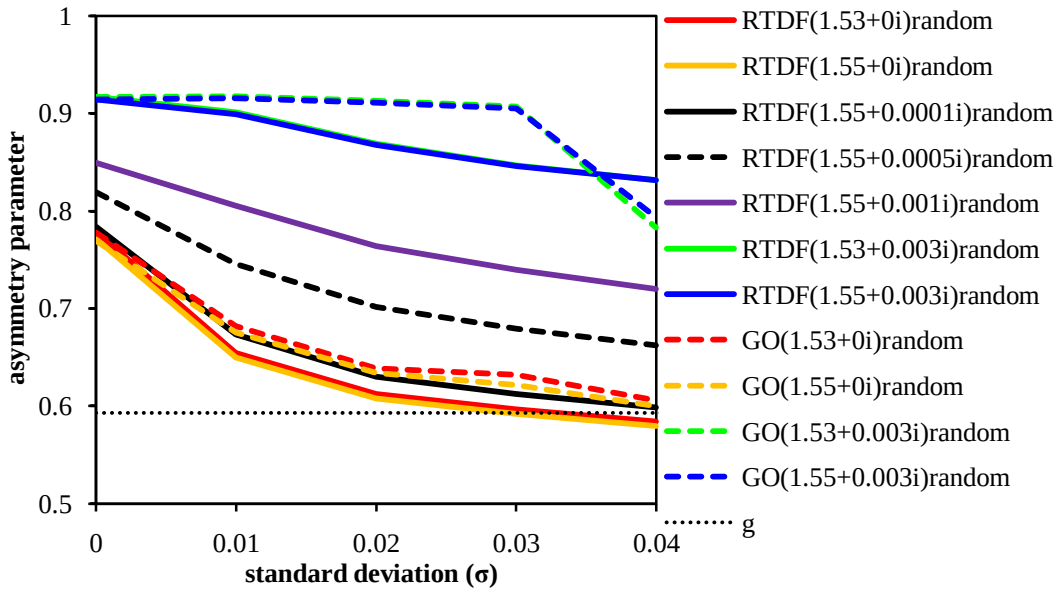

Figure 9-1-30 – As in **Figure 9-1-29** but the particle was allowed to orient freely.

Figure 9-1-29 and **Figure 9-1-30** show that as the roughness of the modelled particle surface increases, the asymmetry parameter decreases. For non-absorbing or lightly-absorbing particles, higher values of σ demonstrate reasonable agreement with the measured result. This is the same for both limited orientation and randomly oriented particles.

9.2 – Case Study 2:

9.2.1 – Levitation and Scattering Experiments

A much larger dust particle was analysed while levitated in the EDB. This particle, when levitated, underwent only a small amount of rotation, and was held almost steady in the trap. A video was taken throughout the scattering measurement which shows the narrow range of motion of the particle. **Figure 9-2-1** shows transmission microscopy images of the particle, which appears strongly reminiscent of a prolate spheroid. The size parameter is in the range 278-282 (equal surface area size parameter) or 269-274 (equal volume size parameter).

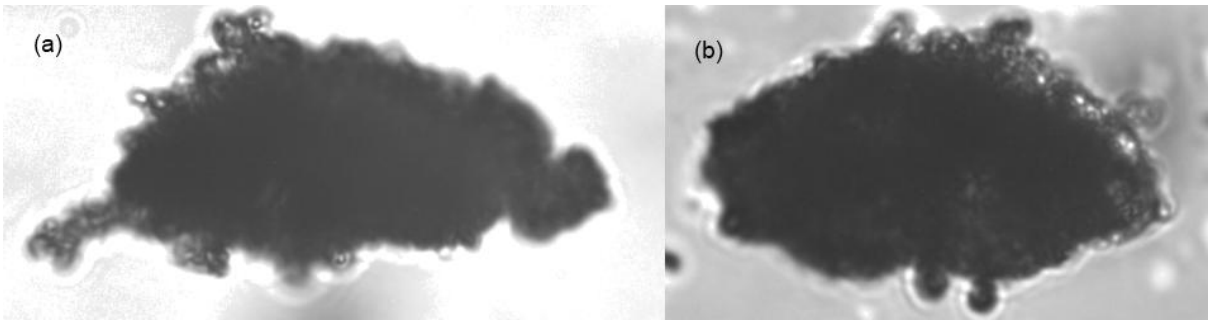

Figure 9-2-1 - Transmission Microscopy image of the dust particle. In (b) the particle has been rotated 90° about the long axis – it is also tilted slightly towards the lens, and so this image is foreshortened. The approximate particle dimensions are: (a) 67.5µm x 35.7µm, (b) 66.8µm x 36.9µm. The approximate size parameter is between 278 and 282 (Surface Area) or 269 and 274 (Volume).

Figure 9-2-2 shows the particle when levitated in the EDB, as viewed from a camera facing vertically upwards into the trapping region. **Figure 9-2-2(a)** shows the particle when externally illuminated (no laser illumination). **Figure 9-2-2(b)** shows the particle illuminated only by the laser. We can see that the particle as shown in **Figure 9-2-2(a)** corresponds to the particle orientation in **Figure 9-2-1(a)**. Therefore, the cross-section of the particle that the laser beam will 'see' corresponds to **Figure 9-2-1(b)**, allowing for slight rotation about the vertical axis. By considering the particle as a prolate spheroid and the angle of incidence of the laser beam, we can calculate the projected area of the particle in the beam. This information is necessary for extrapolating the direct forward scattering information from a range of ellipses.

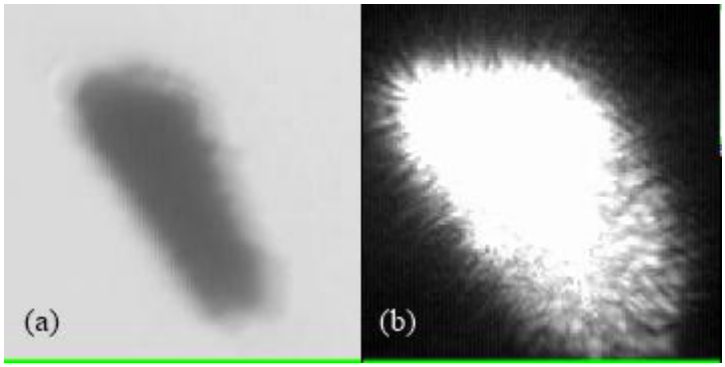

Figure 9-2-2 - Images of the particle levitated in the EDB taken by a vertically facing camera. (a) Shows the particle when externally illuminated (no laser illumination). (b) Shows the particle when illuminated by the laser.

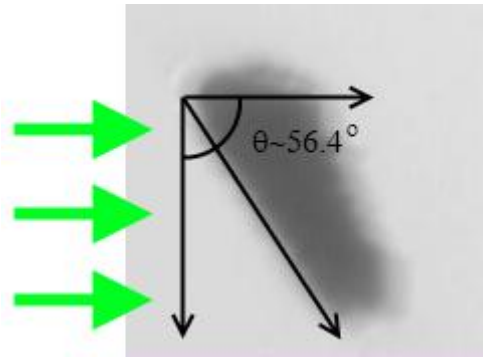

Figure 9-2-3 – The relative orientation of the particle and the incident laser beam. The angle between the long axis of the particle and the angle of propagation of the laser beam is shown.

During the scattering experiments, the particle was largely stable in the orientation shown in **Figure 9-2-2**. Small rotational movements were observed, primarily as a result of the motion of air – due to both motion in the room and convection currents. The angle θ was observed to change, with a maximum of θ~75° and a minimum of θ~25°. These movements were infrequent and short however, and the preferred orientation was as shown. By considering the particle as a prolate spheroid with semi-major axis = 33.4μm and semi-minor axis = 18.5μm, we can calculate the projected area of the particle at any given angle. For the angle given above (θ~56.4°), the projected area of the particle is 1722.867μm^2. As the semi-minor axis of 18.5μm will not change, the projected area corresponds to an ellipse with semi-major axis 29.64μm and aspect ratio 1.602. For the maximum rotation θ~75°, the projected area is 1895.58μm^2 and corresponds to an ellipse with semi-major axis 32.62 μm and aspect ratio 1.76. For the minimum rotation θ~25°, the projected area is 1273.82μm^2, and corresponds to an ellipse with semi-major axis 21.92μm and an aspect ratio 1.18.

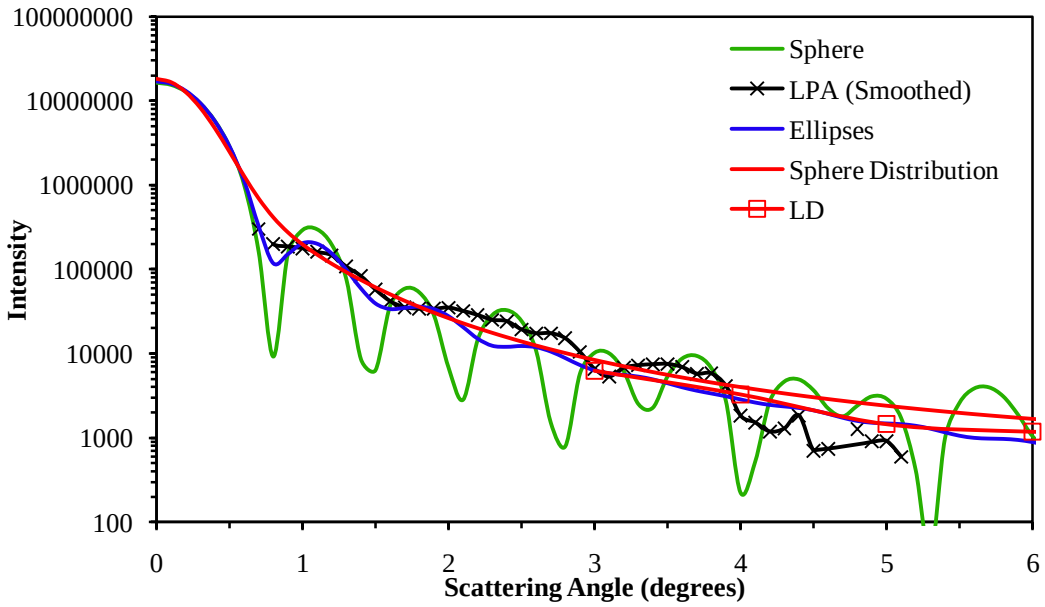

Figure 9-2-4 - Small angle scattering data and fitting patterns for the particle shown in **Figure 9-2-1**. The sphere data for comparison was generated using a single sphere (X_s=276) and a gamma distribution of spheres (X_s=276, shape parameter a=276, scale parameter b=0.1, r_{min}=0 and r_{max}=800, all values except b given in terms of size parameter). With the particle range of motion being very limited, a narrow size range of elliptical apertures was used. The minimum radius was 18.5μm, the maximum radius was 22μm, the aspect ratio was 1.602 and the wavelength of the incoming light λ=0.5145μm. For the spheres a refractive index of 1.55+0.001i was used.

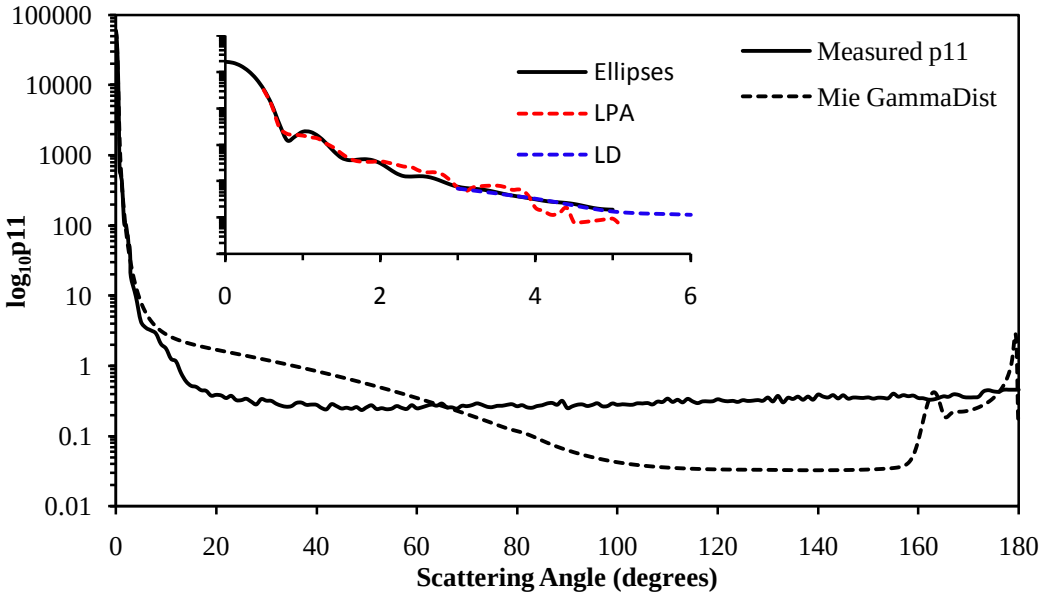

Figure 9-2-5 - The full scattering phase function for the particle shown in **Figure 9-2-1**. For comparison, a phase function for a gamma distribution of spheres is shown. Inset: Small angle scattering data, showing how the data from the ellipses, Linear Photodiode Array and Laser Diffractometer fit together.

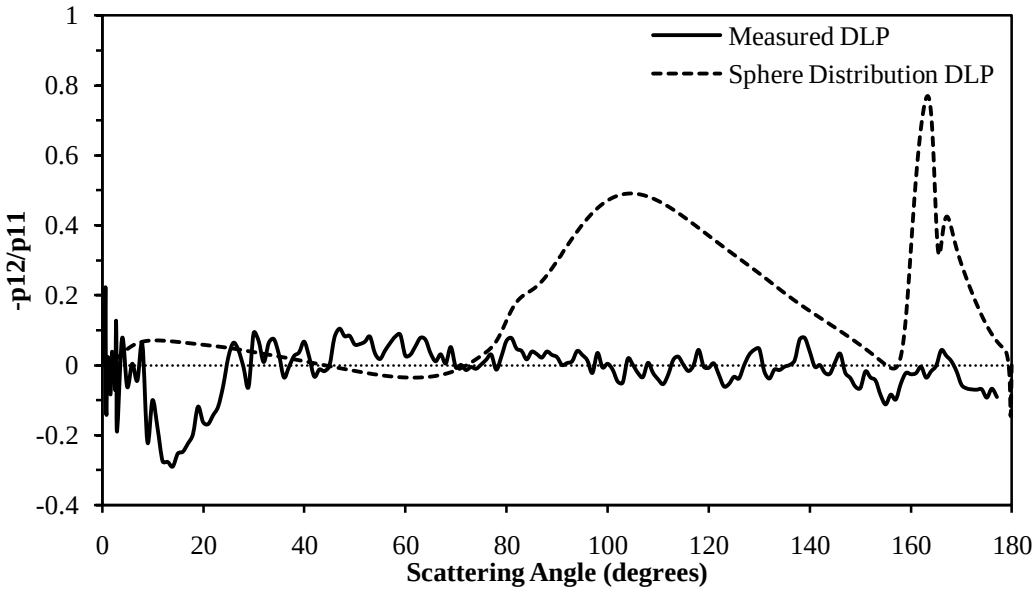

Figure 9-2-6 - The degree of linear polarization for the particle shown in **Figure 9-2-1**. Also shown for comparison is the DLP for a gamma distribution of spheres.

The measured phase function again demonstrates a relatively constant scattered intensity, with few features at scattering angles above 40 degrees. In the forward scattering region, there is a halo-like inflection, appearing as a 'step' at approximately 10 degrees. This is attributable to the non-random motion of the particle during the levitation experiment. Any flat, facet like features on the surface will cause a mode of scattering resulting in a peak. The degree of linear polarisation for the particle also demonstrates this, with a strong negative polarisation peak in the pertinent region. The DLP, aside from this peak, is very low for the entirety for the phase function. This indicates that the surface morphology is inhomogeneous, with few regular features. The asymmetry parameter for the particle has been calculated as 0.682.

9.2.2 – Modelling the Particle

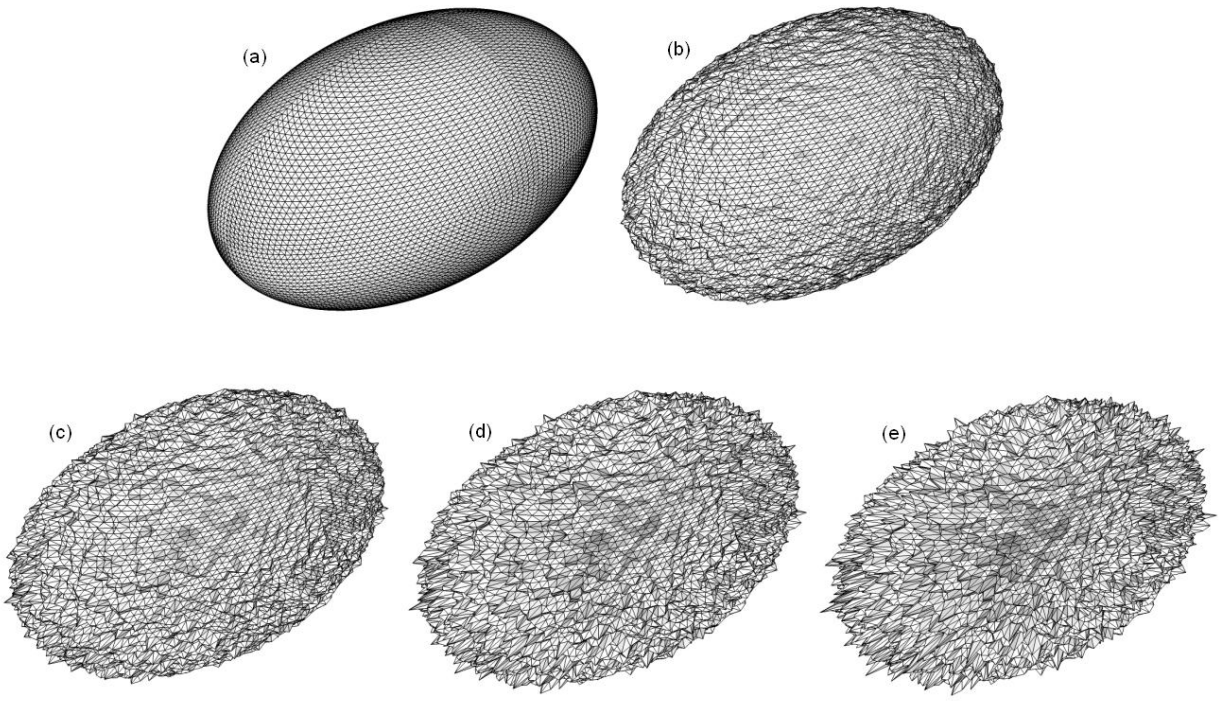

Figure 9-2-7 - Polygonal mesh approximations of the particle shown in Figure 9-29. All the figures are composed of 20,000 facets. Particle (a) is a perfect prolate spheroid, of aspect ratio ε=0.541. Particles (a) – (d) have surfaces generated using Gaussian Random statistics **[38]** and a correlation angle of 1°. The standard deviation σ for each particle is (a) σ=0.0, (b) σ=0.01, (c) σ=0.02, (d) σ=0.03, (e) σ=0.04.

Again, the particle is modelled as a prolate spheroid. The modelled equal-volume-sphere size parameter is 276 and the aspect ratio is 0.541. Utilising the Gaussian random particle regime as described in Chapter 6, particles of increasing roughness were created.

9.2.3 – RTDF and GO calculations

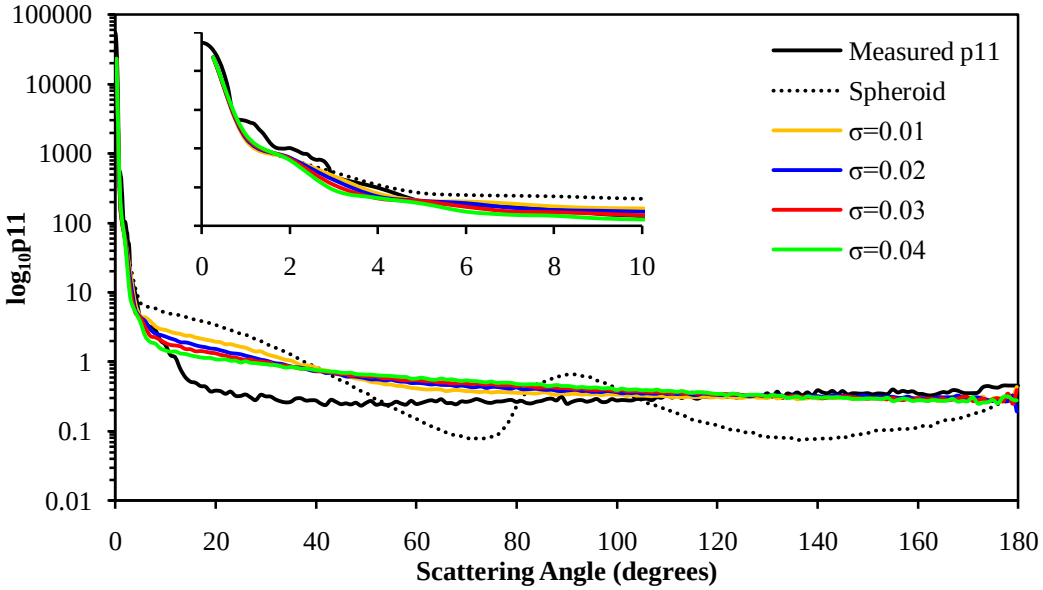

Figure 9-2-8 - The scattering phase functions as calculated using RTDF for a range of modelled particles compared with the measured phase function for particle 2. The modelled particles are those shown in **Figure 9-2-7**, and the refractive index used for these calculations is 1.55 + 0i. In these calculations, the orientation of the particle was limited as described in the text.

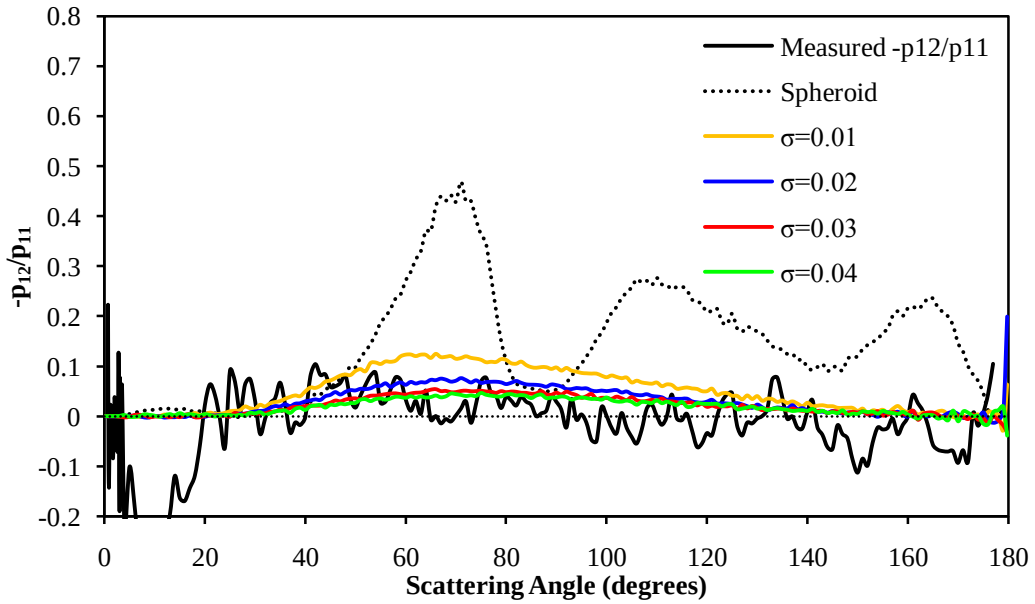

Figure 9-2-9 – As in **Figure 9-2-8** for the Degree of Linear Polarisation.

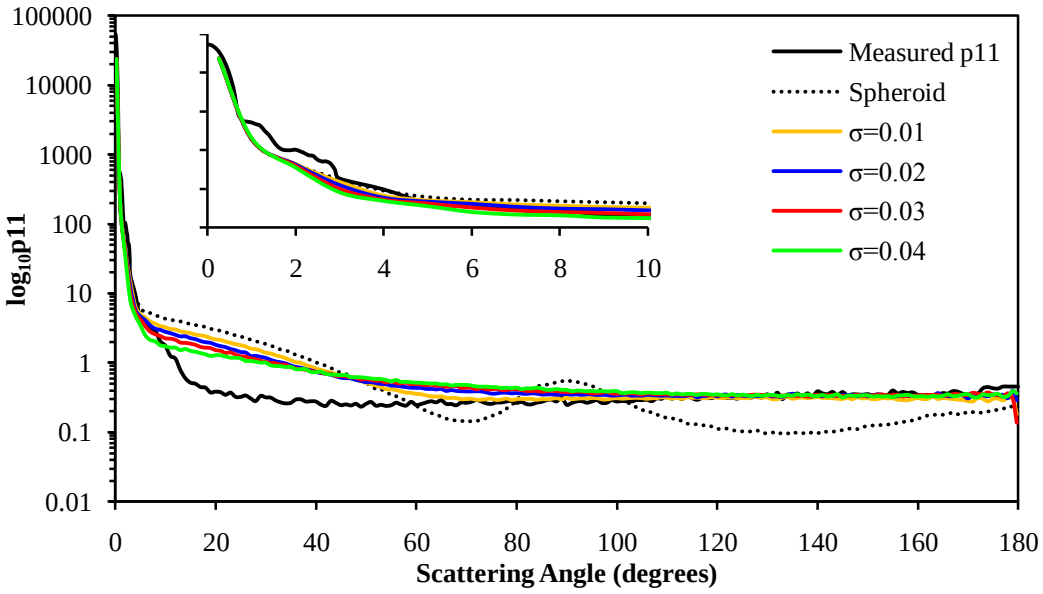

Figure 9-2-10 – As in **Figure 9-2-8** but the particle was free to rotate randomly.

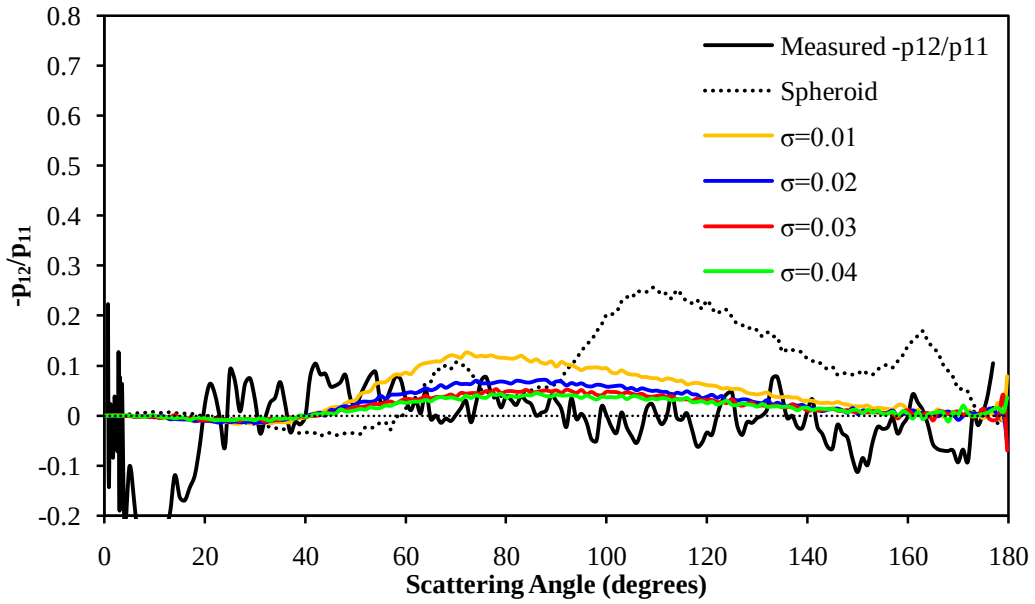

Figure 9-2-11 – As in **Figure 9-2-10** for the Degree of Linear Polarisation.

Figure 9-2-8 – 9-2-11 show RTDF calculations using a refractive index of 1.55 + 0i. The calculations show agreement in the forward scattering region from 0° to 5°, and the backscattering region above 90°. Due to the approximation of the particle by a spheroid, the 10° halo inflection is not well represented. For angles between 10° and 60°, all of the calculated results are higher than the measured results.

The calculated DLP results resemble a skewed bell curve – this is in contrast to the measured results, which are relatively uniform, excepting the depolarisation peak attributable to the halo peak. Both the measured and calculated DLP results are very low.

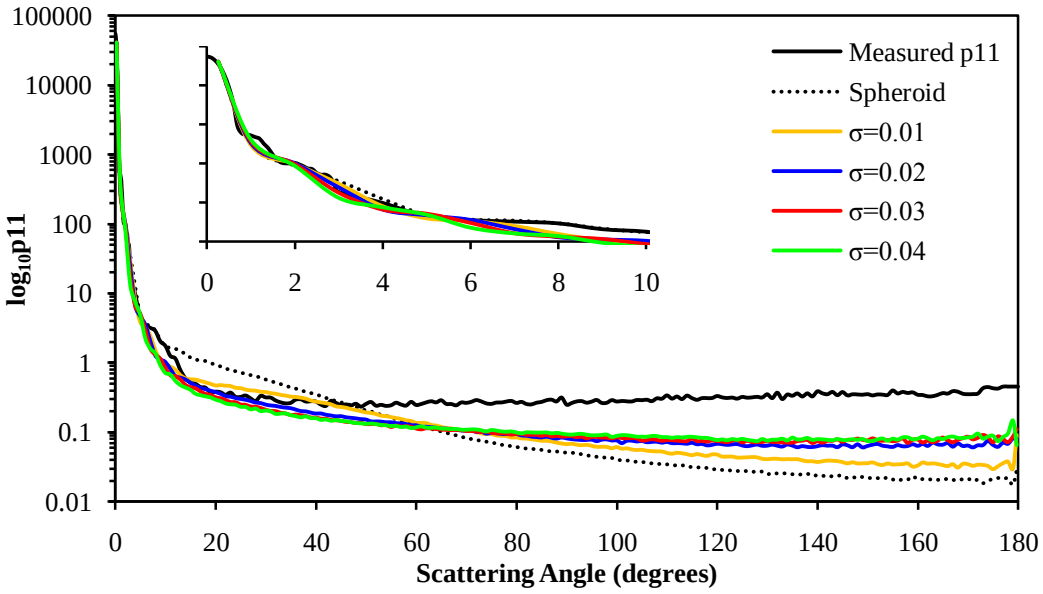

Figure 9-2-12 - As in **Figure 9-2-8** for refractive index 1.55 + 0.003i

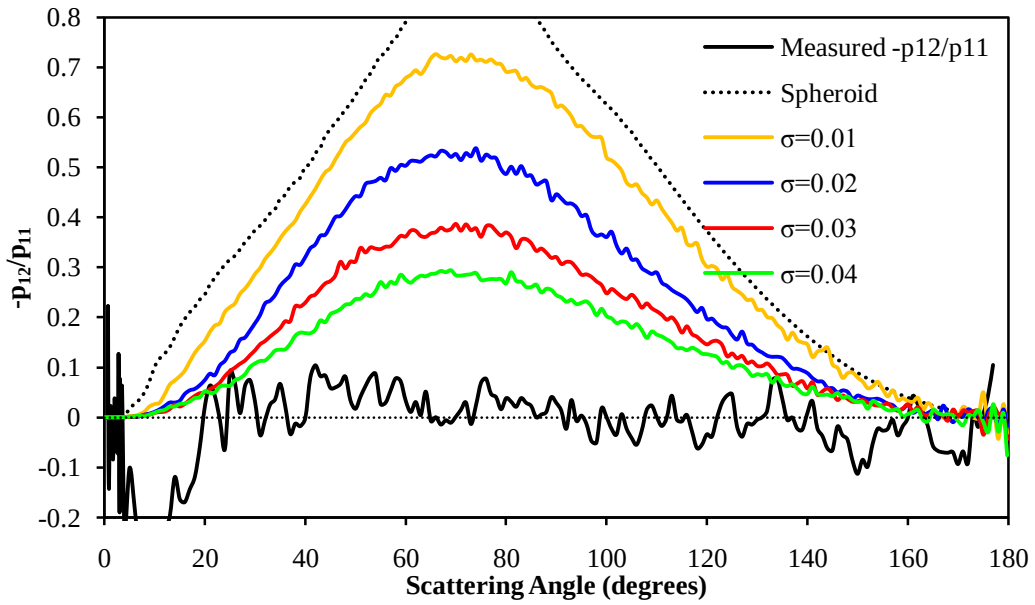

Figure 9-2-13 – As in **Figure 9-2-12** for the Degree of Linear Polarisation.

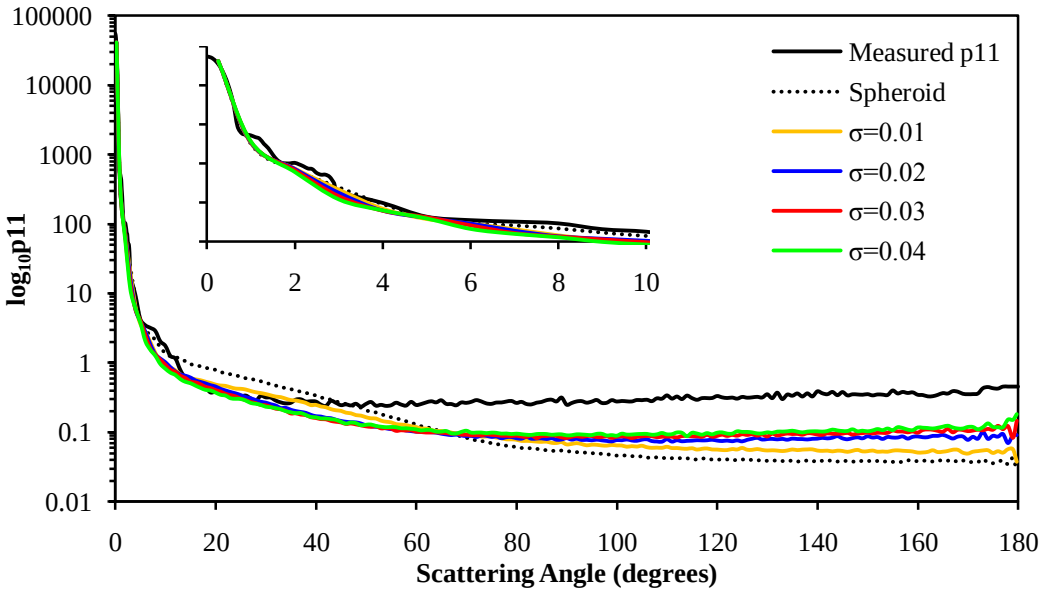

Figure 9-2-14 – As in **Figure 9-2-10** for refractive index 1.55 + 0.003i.

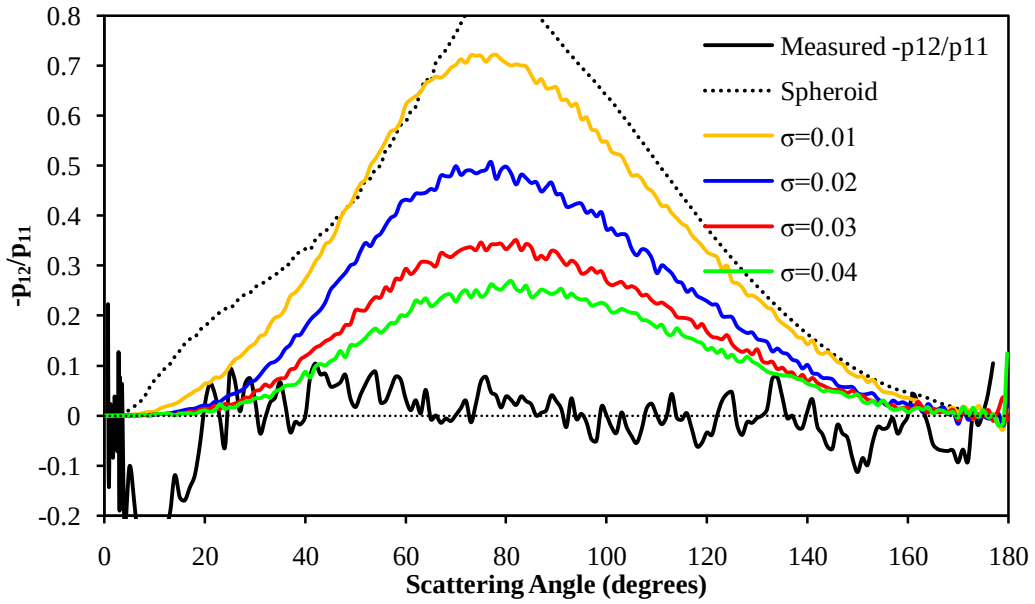

Figure 9-2-15 – As in **Figure 9-2-14** for the Degree of Linear Polarisation.

Figure 9-2-12 – 9-1-15 show RTDF calculations using a refractive index of 1.55 + 0.003i. The calculations show agreement in the forward scattering region from 0° to ~35°, but above that are much lower than the measured results. All the calculations show a similar lack of features.

The calculated DLP results again resemble a skewed bell curve, but here the results are much higher than the measured results.

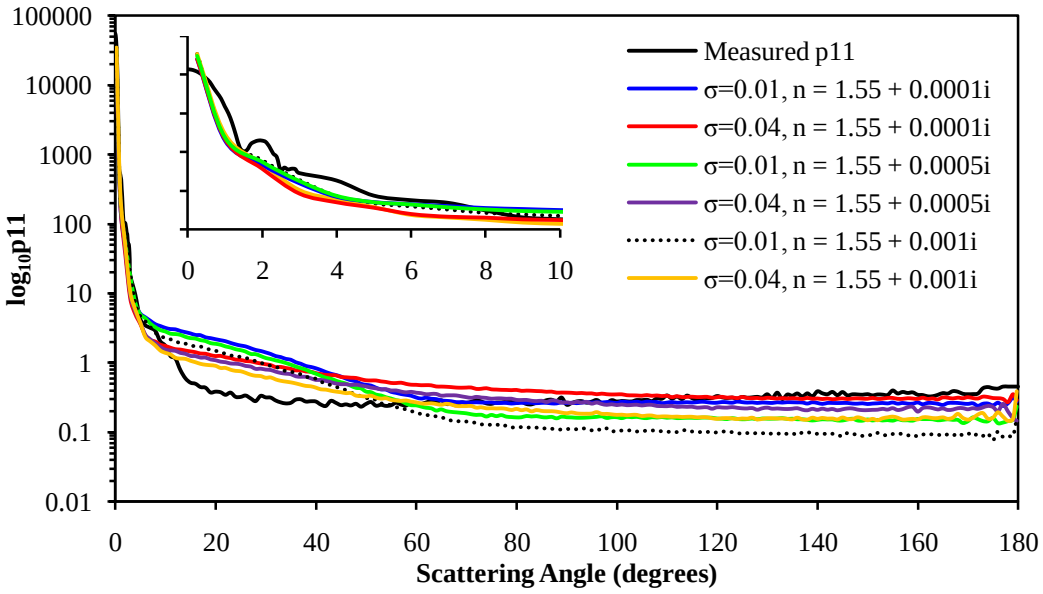

Figure 9-2-16 – The scattering phase functions as calculated using RTDF for a range of modelled particles compared with the measured phase function for particle 2. The modelled particles are those shown in **Figure 9-2-7**. The complex component of the refractive index was varied, and two values of σ were used. Here, the particle was free to orient randomly.

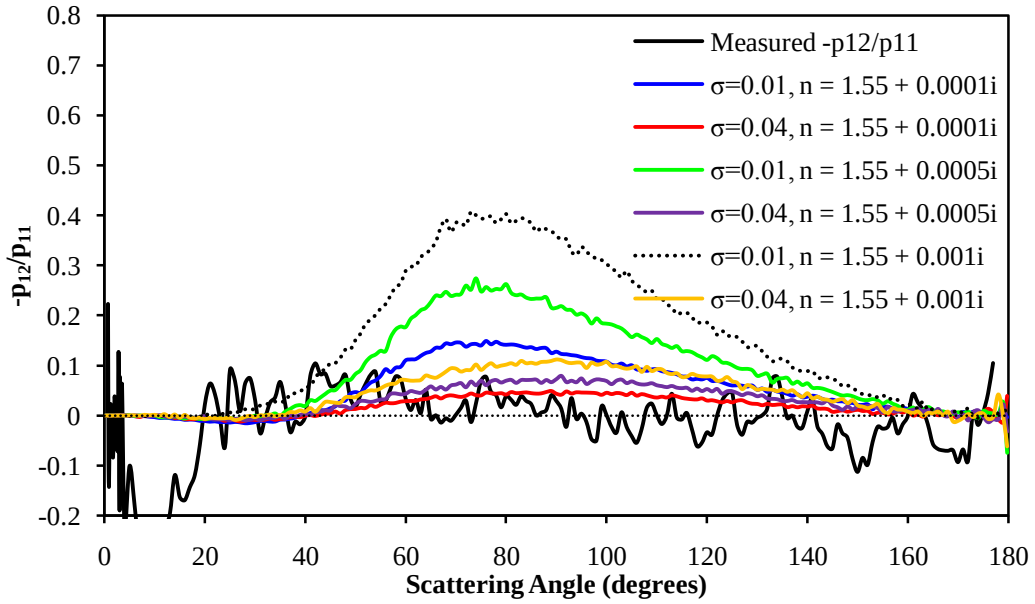

Figure 9-2-17 - As in **Figure 9-2-16** for the Degree of Linear Polarisation

Figure 9-2-16 and **9-2-17** show RTDF calculations for a range of surface roughness values and absorption components. As with previous RTDF calculations, the halo-like feature in the forward scattering region is not represented, due to the shape of the modelled particle. All the phase functions show reasonable agreement with the measured results between 0° and approximately 10°. At angles above this, they are considerably higher in intensity. The computed results with high values of σ have steadily decreasing phase functions from 10° to the back scattering region. They are higher than the measured phase function until approximately 120° (n = 1.55 + 0.0001i), 90° (n = 1.55 + 0.005i), 60° (n = 1.55 + 0.001i). Low values of σ have a pronounced 'dip' at approximately 60°, a less pronounced feature than is seen on smooth spheroids. The computed intensity is lower than the measured particle for all scattering angles above 60°.

The computed DLP results again do not replicate the halo-like feature in the forward scattering region. The measured results are fairly low across the entire angular range, whereas the computed results all show a peak in the side scattering region. Computations with a low value of σ have a relatively high DLP peak at approximately 75°, with the largest absorption components showing the highest peak.

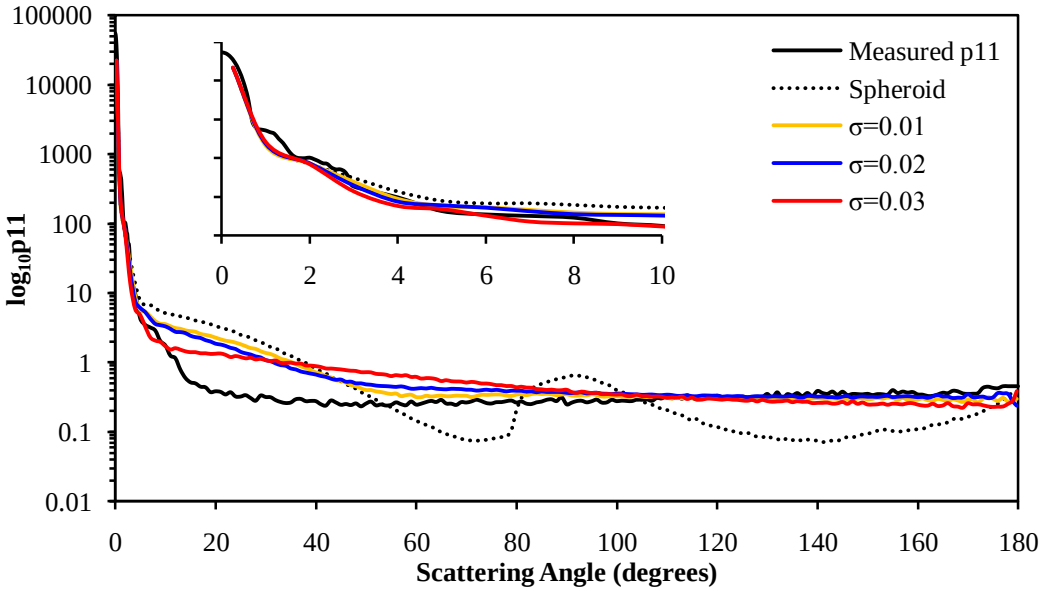

Figure 9-2-18 - The scattering phase functions as calculated using GO for a range of modelled particles compared with the measured phase function for particle 2. The modelled particles are those shown in **Figure 9-2-7**, and the refractive index used for these calculations is 1.55 + 0i. In these calculations, the particle orientation was limited as described in the text.

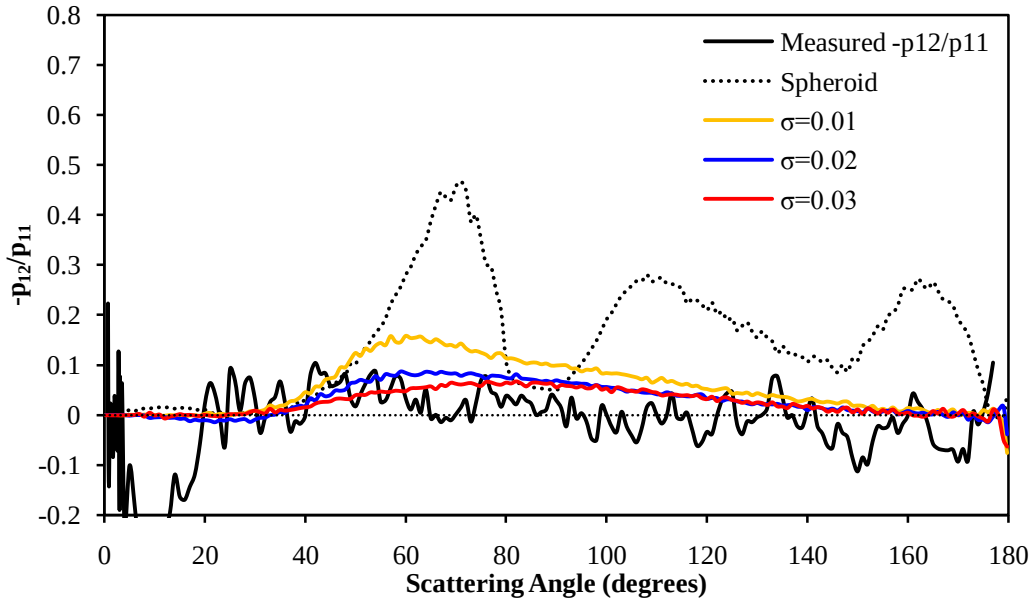

Figure 9-2-19 – As in **Figure 9-2-18** for the Degree of Linear Polarisation.

The Ray Tracing results are incomplete due to a known issue with the Ray Tracing code. For polygonal meshes with very small facets at small angles to each other, the program can become stuck in a loop. This situation is more likely to arise with larger values of sigma.

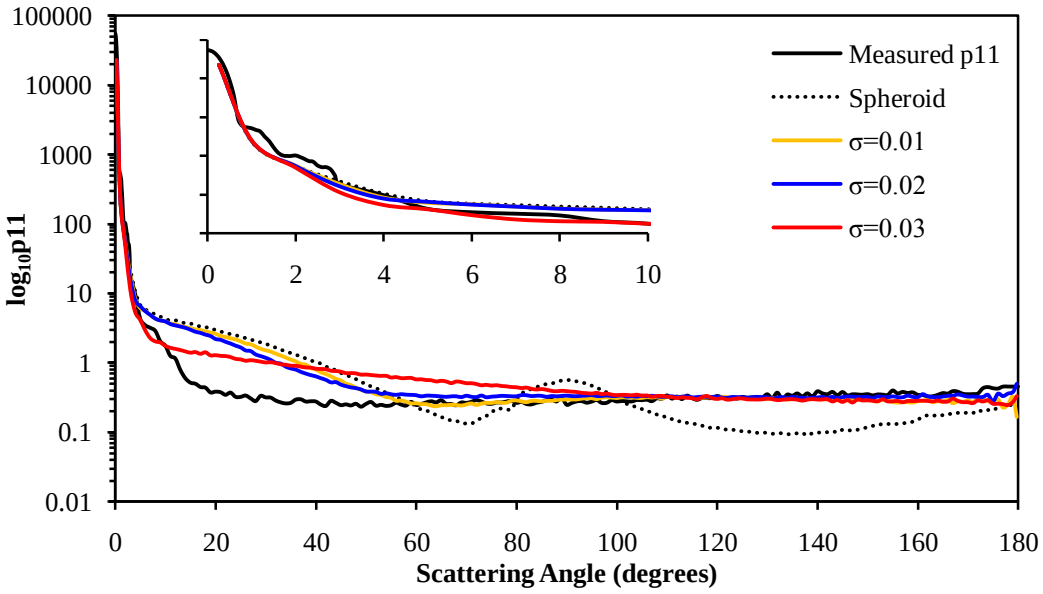

Figure 9-2-20 – As in **Figure 9-2-18** but the particle was free to rotate randomly.

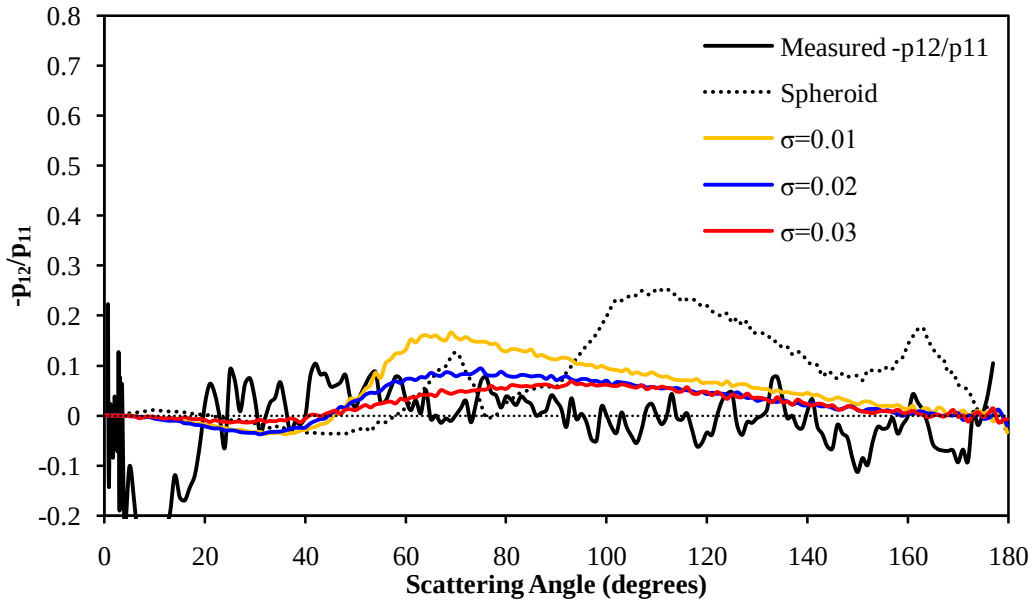

Figure 9-2-21 – As in **Figure 9-2-20** for the Degree of Linear Polarisation.

Figure 9-2-18 – 9-2-21 show GO calculations using a refractive index of 1.55 + 0i. The GO results are similar to RTDF in that they demonstrate agreement with the measured phase function in the forward scattering and back scattering regions. The RTDF calculations show slightly better agreement in the backscattering region above 120 degrees.

The DLP results also resemble a skewed bell curve, but with a small negative peak at approximately 35°.

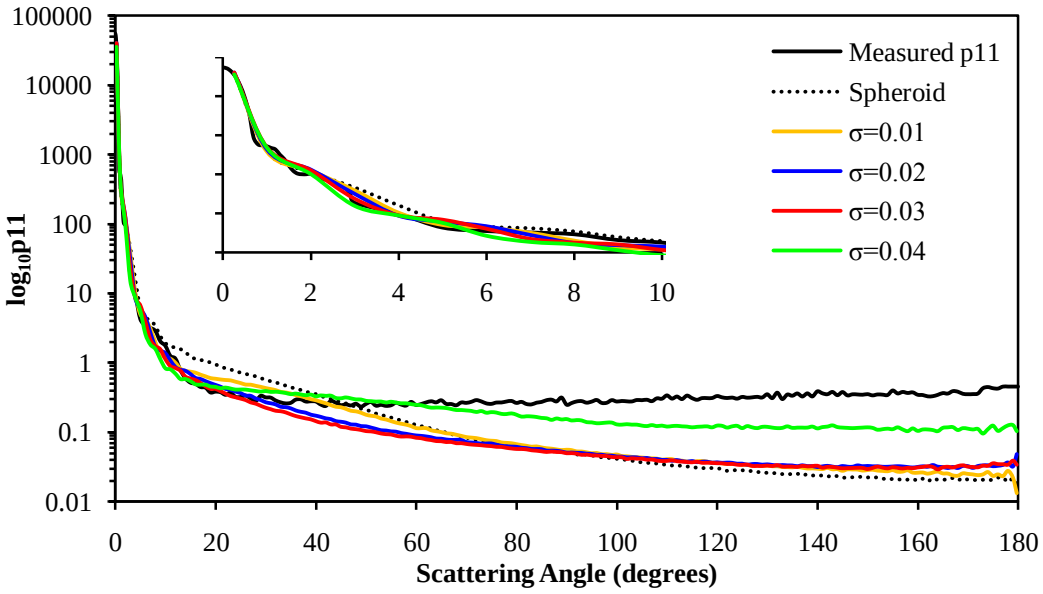

Figure 9-2-22 – As in **Figure 9-2-18** for refractive index 1.55 + 0.003i.

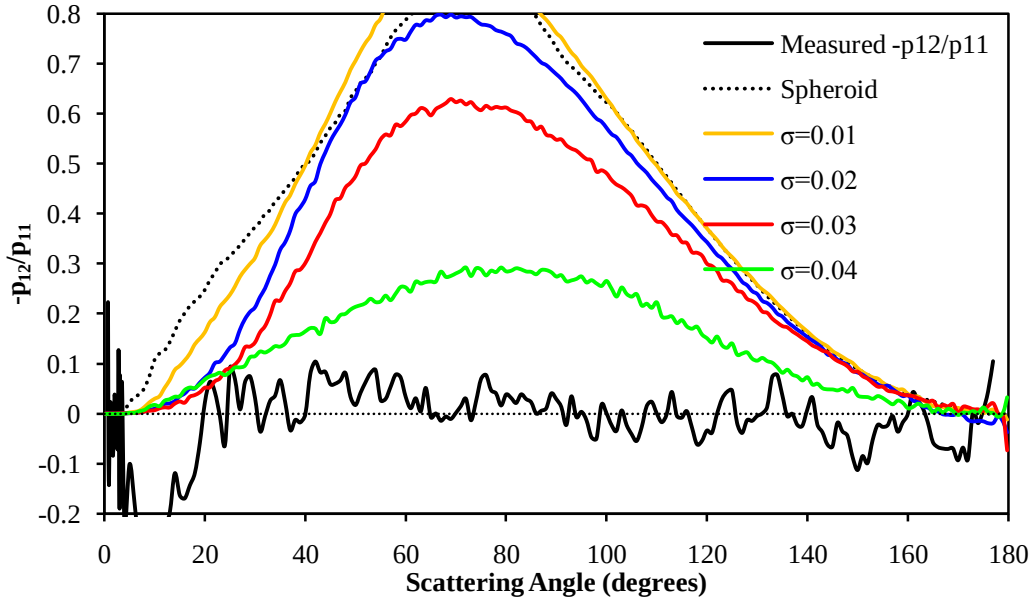

Figure 9-2-23 – As in **Figure 9-2-22** for the Degree of Linear Polarisation.

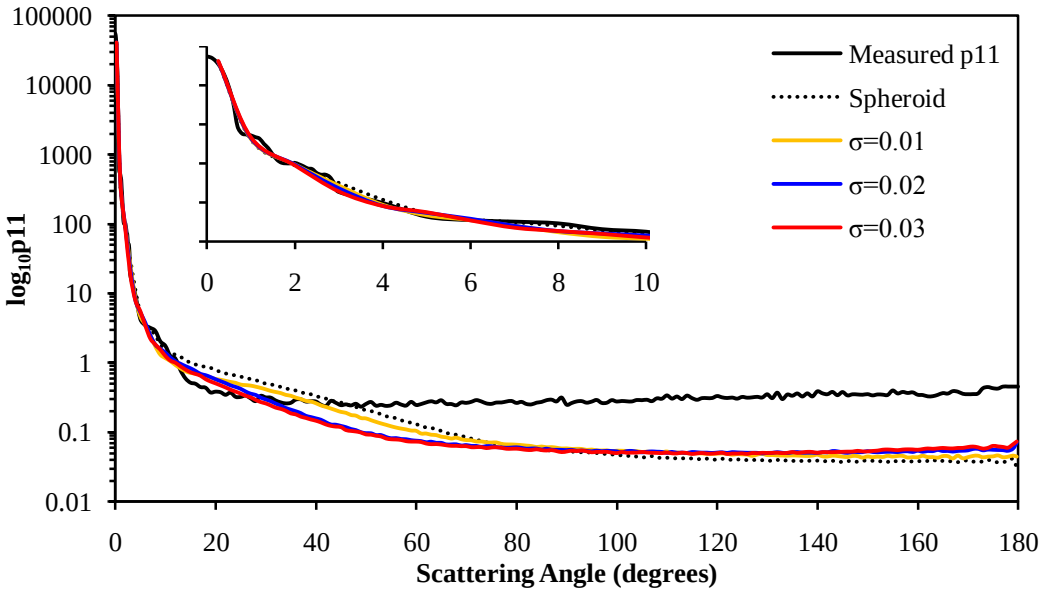

Figure 9-2-24 – As in **Figure 9-2-20** for refractive index 1.55 + 0.003i.

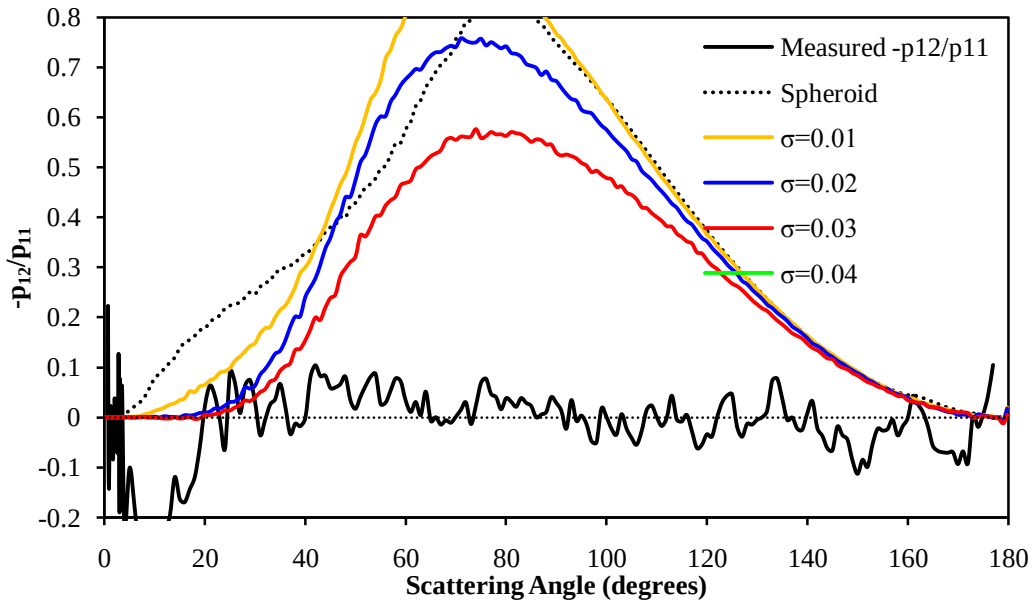

Figure 9-2-25 – As in **Figure 9-2-24** for the Degree of Linear Polarisation.

Figure 9-2-22 – 9-2-25 show GO calculations using a refractive index of 1.55 + 0.003i. Similarly to RTDF, there is good agreement between 0° and 35°, and then poor agreement at higher scattering angles. At higher angles, the calculated results are much lower than the measured results.

The DLP results again resemble a skewed bell curve. They are much higher than the calculated DLP for much of the range of scattering angles.

9.2.4 - RMS Comparison of phase functions

The RMS errors for the phase functions of the modelled particles are presented as described in **9.1.4**.

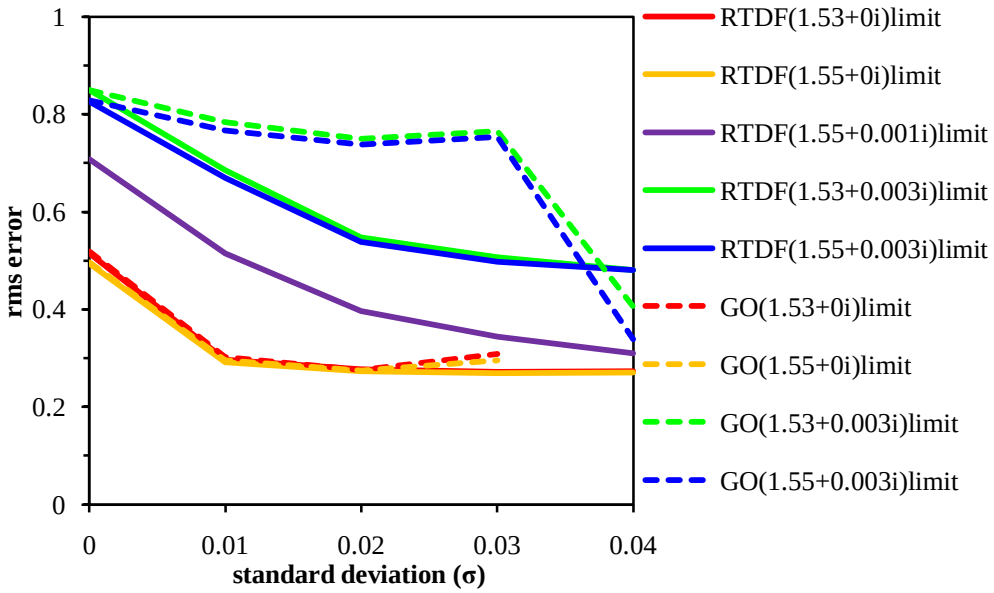

Figure 9-2-26 – RMS errors comparison. For these calculations, the particle orientation was limited as described in the text.

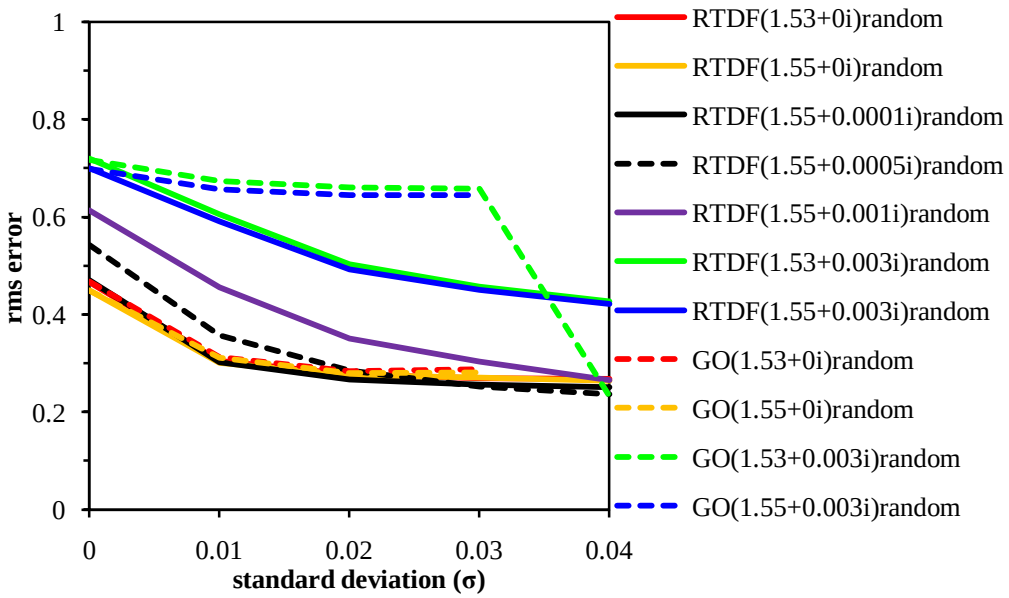

Figure 9-2-27 – RMS errors comparison. For these calculations, the particles were allowed to orient randomly.

The figures show a trend towards a lower RMS difference as the standard deviation of the modelled particle is increased. In general, this applies to both RTDF and GO calculations, except for the case of GO with σ=0.04. Here, the lowest RMS difference is seen at a sigma value of 0.02, with an increase thereafter. Calculations for non-absorbing or lightly absorbing particles show smaller errors than absorbing particles. Allowing the particles to orient randomly gives a slightly lower error than for limited orientations.

9.2.5 – Asymmetry Parameter

The asymmetry parameter for the levitated particle is 0.682, as calculated from the measured phase function.

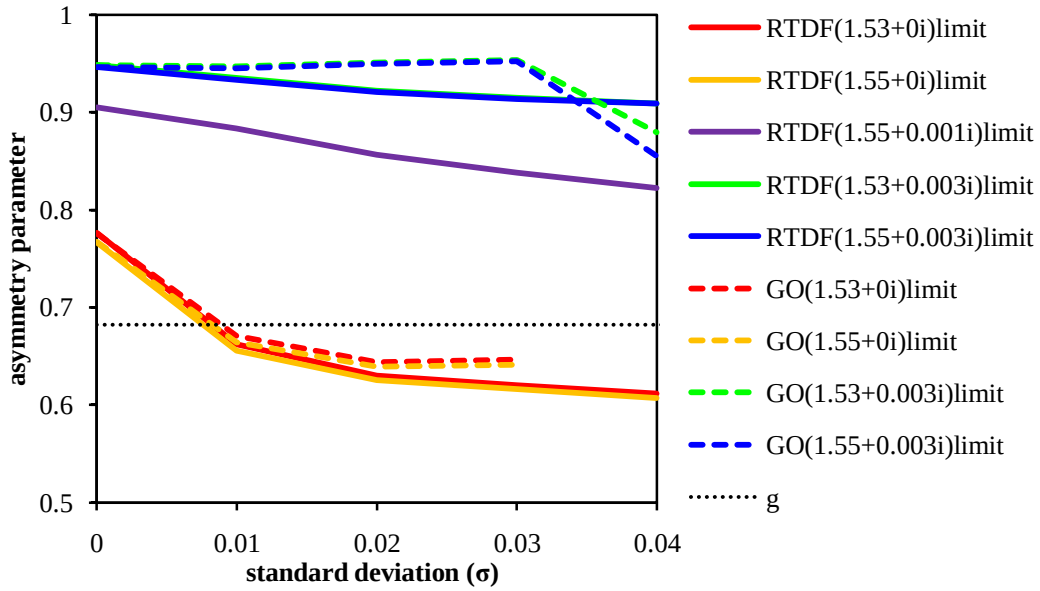

Figure 9-2-28 - Comparison of calculated asymmetry parameters with that of the levitated particle (g). Here, the particle orientation was limited as described in the text.

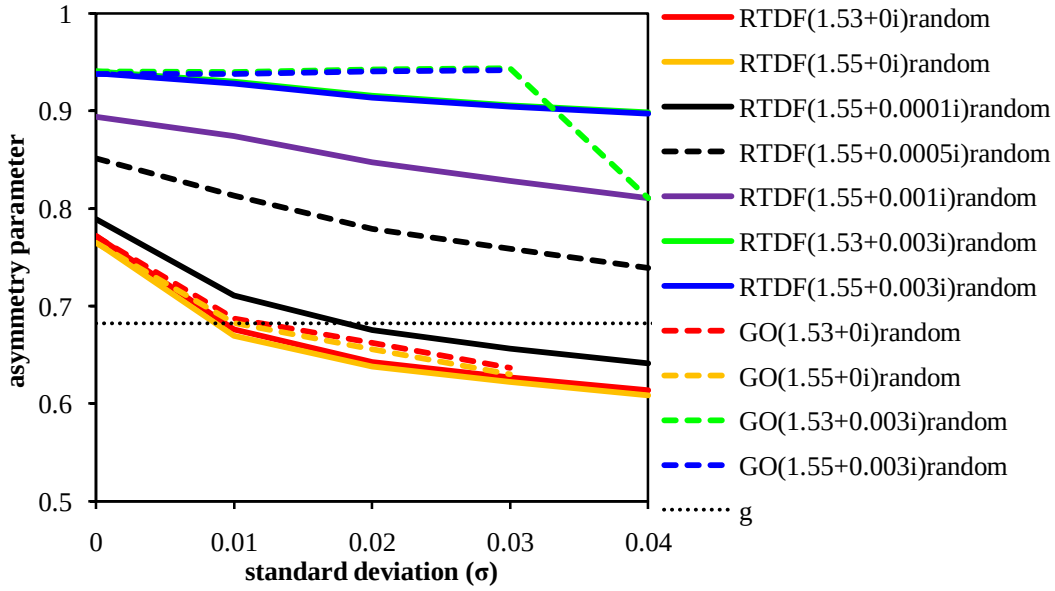

Figure 9-2-29 - Comparison of calculated asymmetry parameters with that of the levitated particle (g). Here, the particles were allowed to orient randomly.

Figure 9-2-28 and **Figure 9-2-29** again show that as the roughness of the modelled particle surface increases, the asymmetry parameter decreases. The figures show that calculations without an absorption component or having a very small absorption component approximate the asymmetry parameter very well for both RTDF and GO at low values of σ. As the standard deviation for the particle model increases above 0.01 (non-absorbing), or 0.02 (n = 1.55 + 0.0001i), the agreement decreases.

9.3 – Case Study 3

9.3.1 – Levitation and Scattering Experiments

Dust particle 3 is an elongated particle with an approximate aspect ratio of 2. The size parameter is in the range 144 – 160 (equal surface area sphere) or 138 – 155 (equal volume sphere).

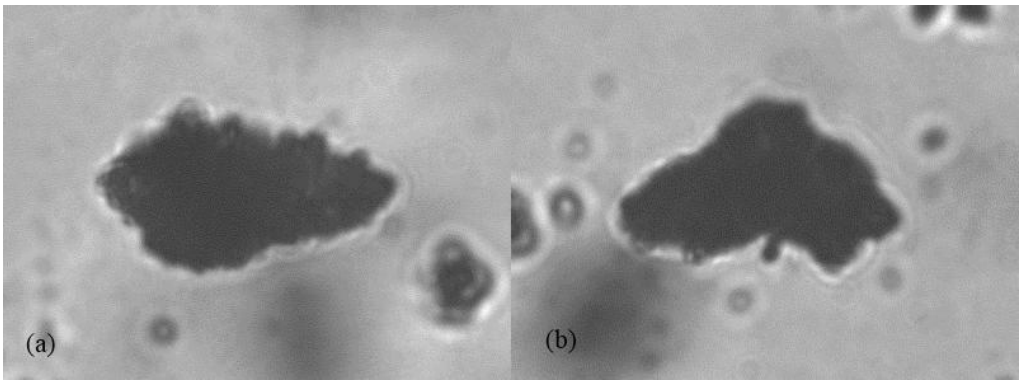

Figure 9-3-1 – Transmission Microscopy image of particle 3. Image (b) shows the particle in (a) after a rotation of 90° about the long axis, assuming the long axis to be parallel to the horizontal. The particle dimensions are: (a) 37.5µm x 21µm, (b) 37.5µm x 17.6µm.

When this particle was levitated, it was oriented vertically in the trap and was tilting rapidly about its midpoint. While undergoing this motion, the particle was also rotating rapidly in the trap, undergoing approximately 3 full rotations per second.

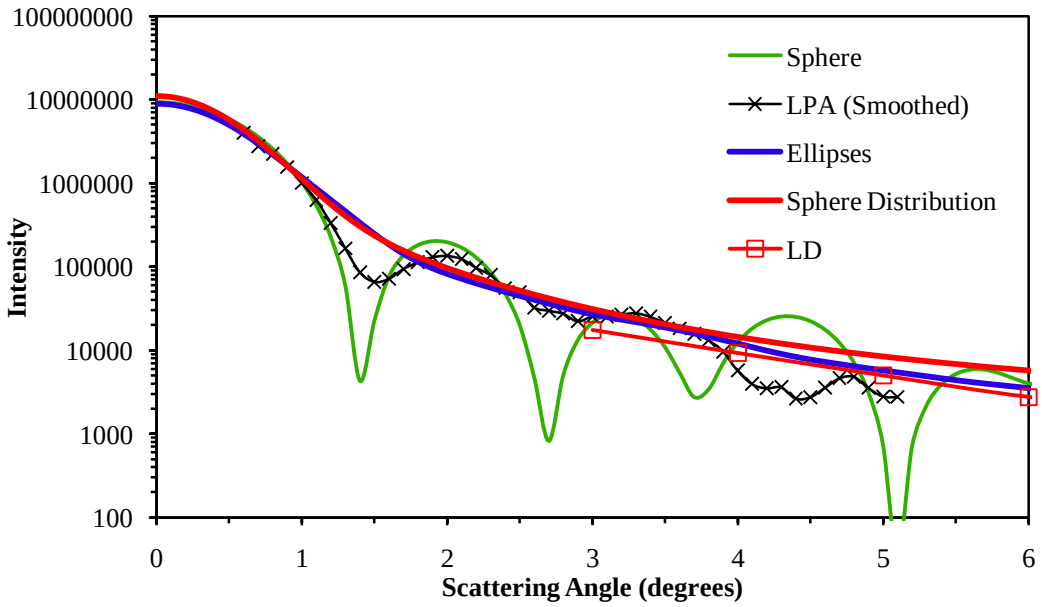

Figure 9-3-2 – Small angles scattering data and fitting patterns for the particle shown in **Figure 9-3-1**. The sphere data for comparison was generated using a single sphere (X_s = 150) and a gamma distribution of spheres (X_s = 150, shape parameter a=150, scale parameter b=0.1, r_{min}=0 and r_{max}=800, all values except b given in terms of size parameter). For the spheres a refractive index of 1.55 + 0.001i was used. For the ellipses, a minimum radius of 6 µm, a maximum radius of 11 µm and an aspect ratio of 2 was used.

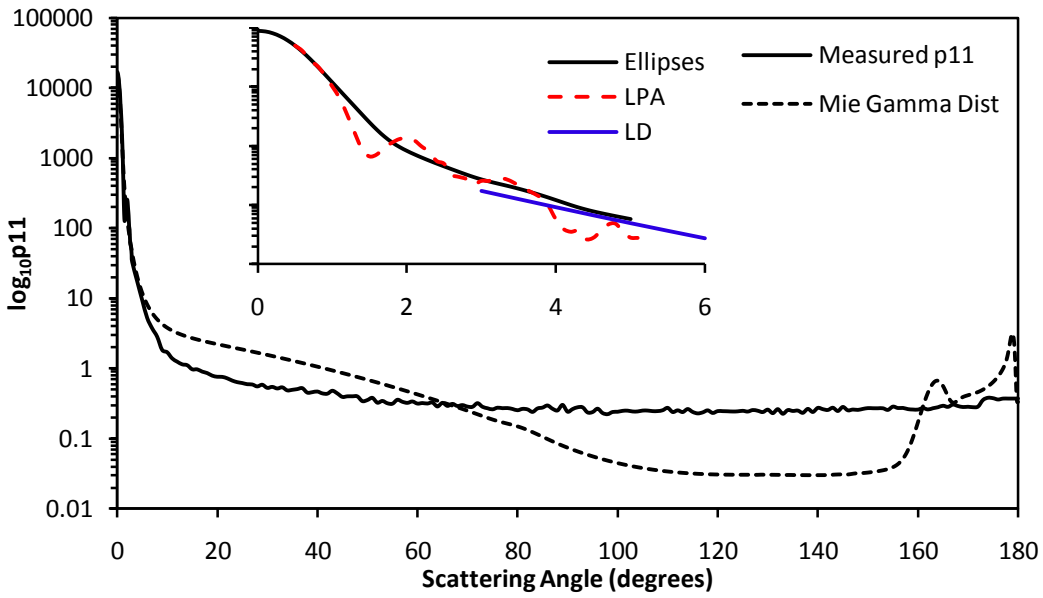

Figure 9-3-3 - The full scattering phase function for the particle shown in **Figure 9-3-1**. For comparison, a phase function for a gamma distribution of spheres is shown. Inset: Small angle scattering data, showing how the data from the ellipses, Linear Photodiode Array and Laser Diffractometer fit together.

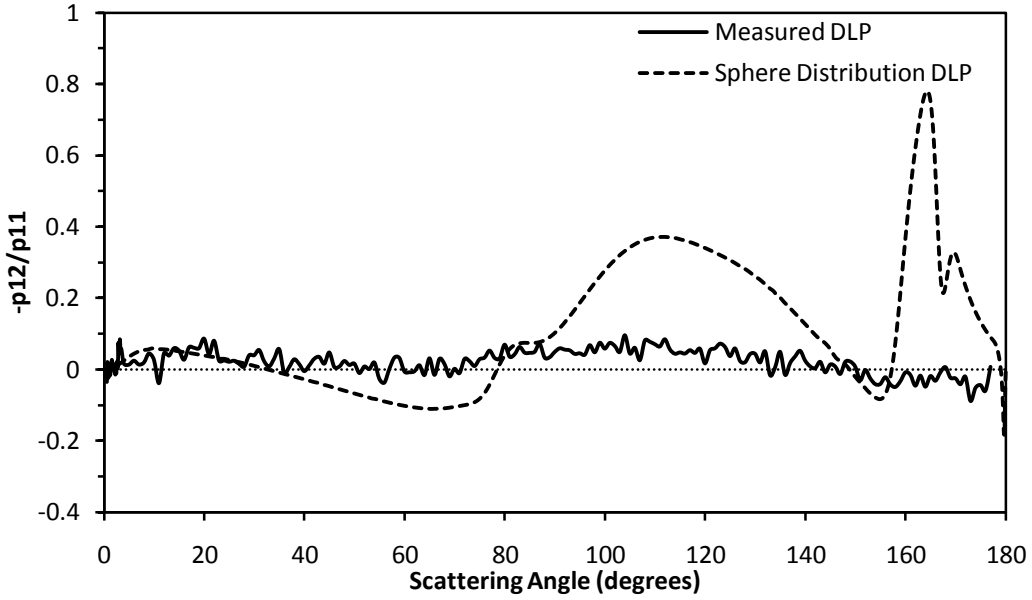

Figure 9-3-4 - The degree of linear polarization for the particle shown in **Figure 9-3-1**. Also shown for comparison is the DLP for a gamma distribution of spheres.

9.3.2 – Modelling the Particle

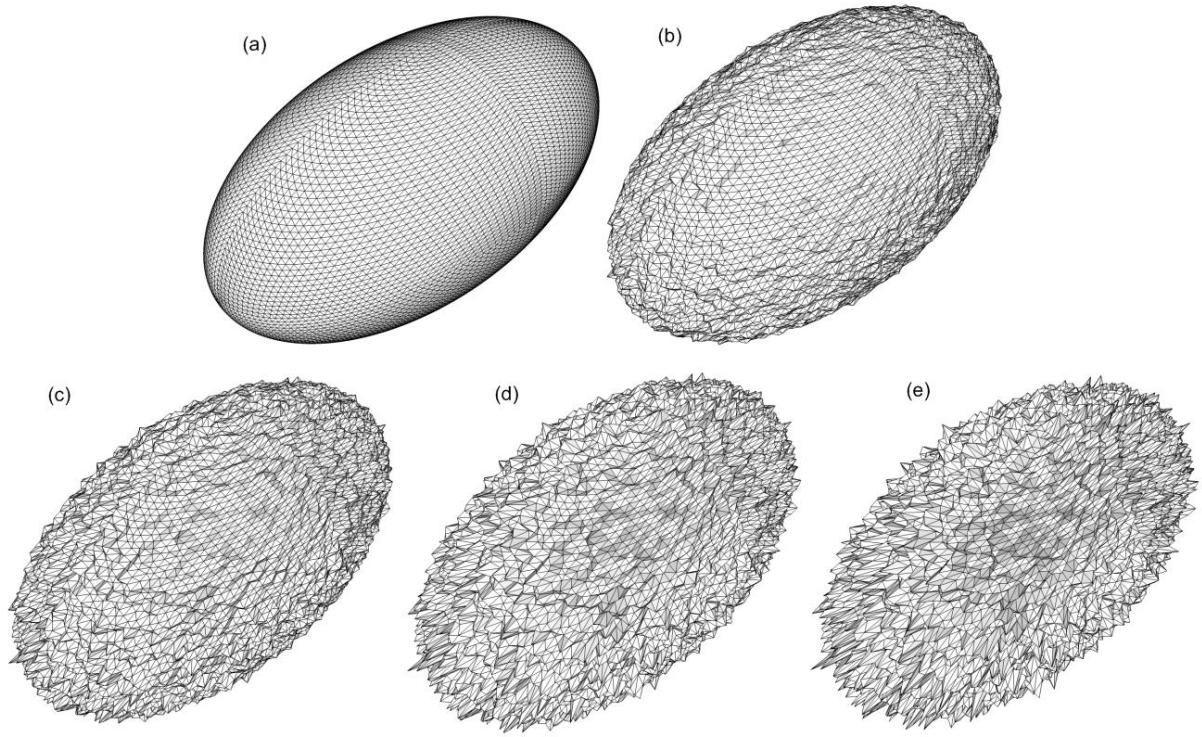

Figure 9-3-5 - Polygonal mesh approximations of the particle shown in **Figure 9-3-1**. All the figures are composed of 20,000 facets. Particle (a) is a perfect prolate spheroid, of aspect ratio ε=0.5. Particles (a) – (d) have surfaces generated using Gaussian Random statistics **[38]** and a correlation angle of 1°. The standard deviation σ for each particle is (a) σ=0.0, (b) σ=0.01, (c) σ=0.02, (d) σ=0.03, (e) σ=0.04

The particle is modelled as a prolate spheroid of equal-volume-sphere size parameter 150, with an aspect ratio of 0.5.

9.3.3 – RTDF and GO Calculations

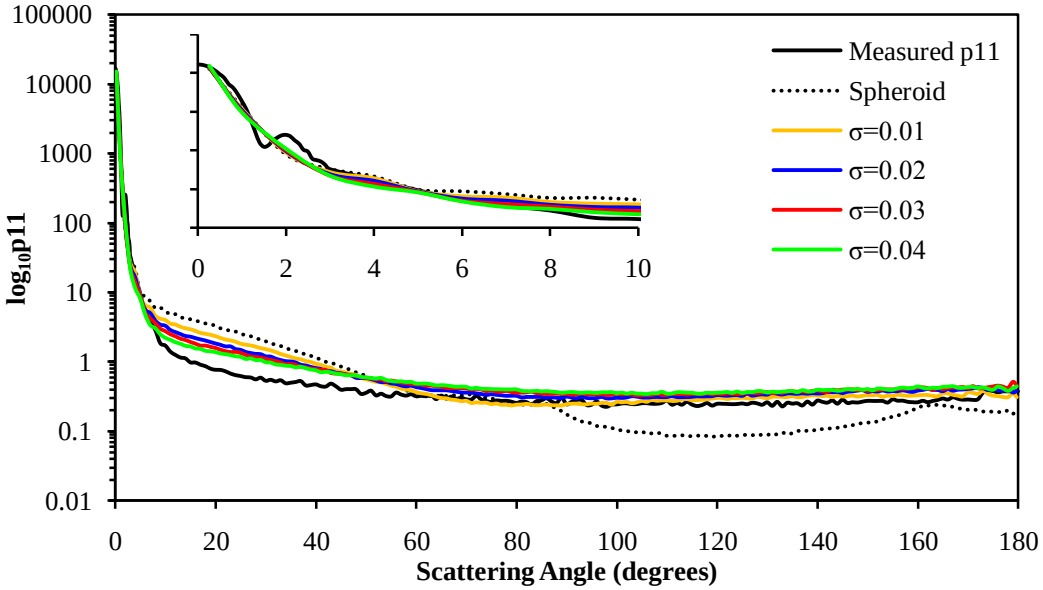

Figure 9-3-6 - The scattering phase functions as calculated using RTDF for a range of modelled particles compared with the measured phase function for particle 3. The modelled particles are those shown in **Figure 9-3-5**, and the refractive index used for these calculations is 1.55 + 0i. In these calculations, the orientation of the particle was limited as described in the text.

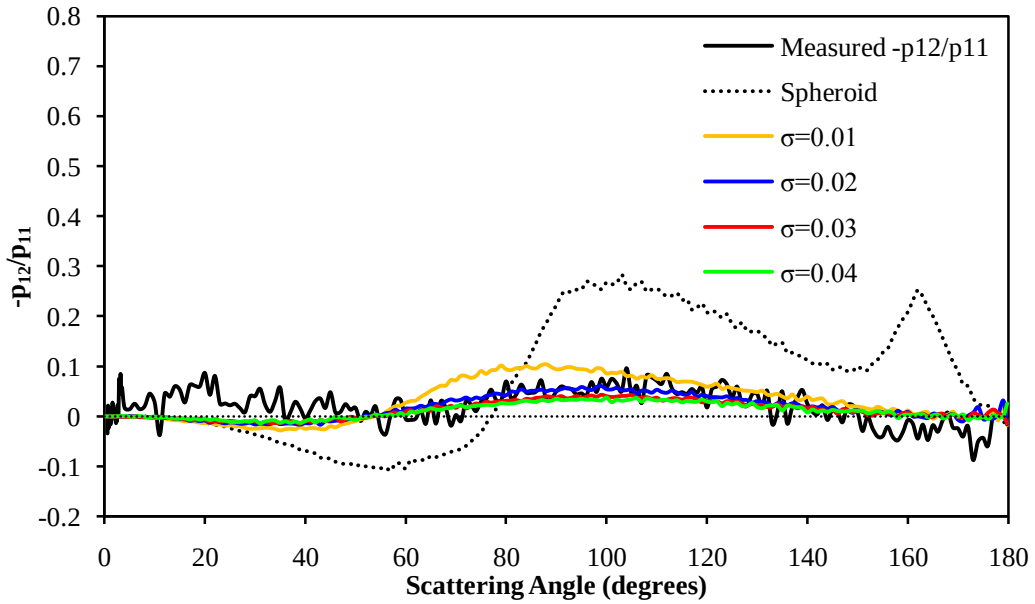

Figure 9-3-7 – As in **Figure 9-3-6** for the Degree of Linear Polarisation

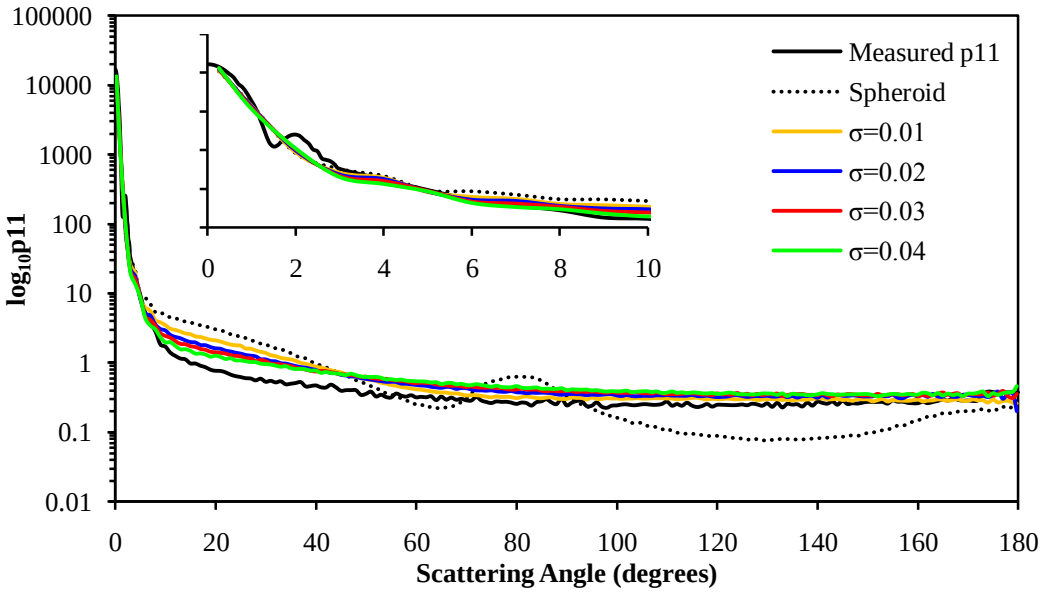

Figure 9-3-8 – As in **Figure 9-3-6** but the particle was free to rotate randomly.

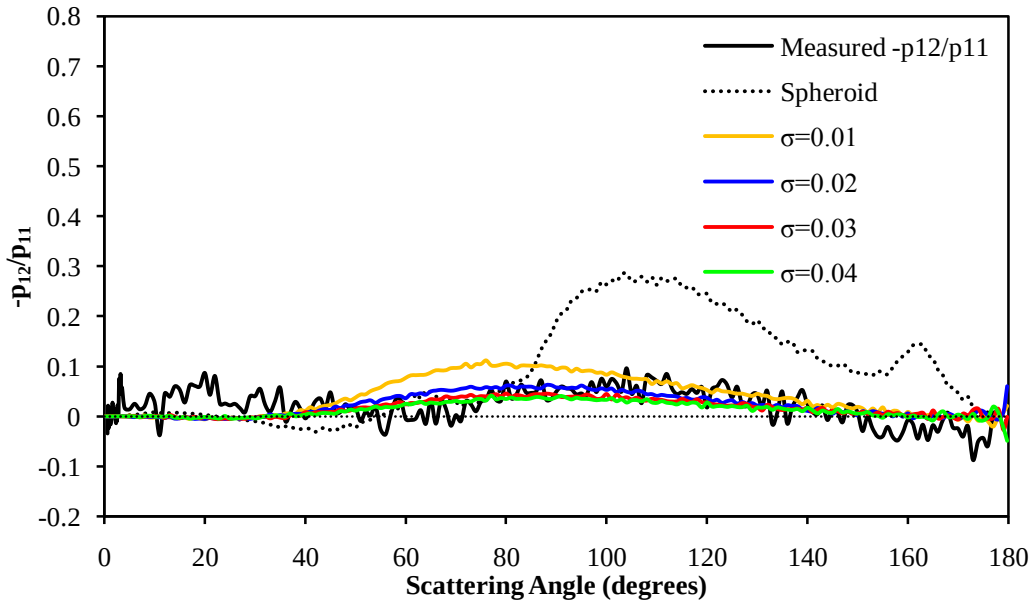

Figure 9-3-9 - As in **Figure 9-3-8** for the Degree of Linear Polarisation.

Figure 9-3-6 – 9-3-9 show RTDF calculations using a refractive index of 1.55 + 0i. Again, there is excellent agreement in the phase function at low scattering angles. Above 8° and below 150° the measured scattering is lower than the calculated scattering, with improved agreement for higher values of σ. For the limited orientation case, the agreement is excellent for all values of σ above a scattering angle of 70°. This is an occasion where limiting the orientation appears to improve the comparison, and we see decreased agreement for much of the scattering angle range. Above 140°, the agreement improves for all values of σ.

The measured DLP shows a polarisation peak at 20° which is not reproduced in the calculations. Between 80° and 140°, there is good agreement for higher values of σ. Above 140°, the measured results demonstrate a small amount of depolarisation, again not reproduced in the calculations.

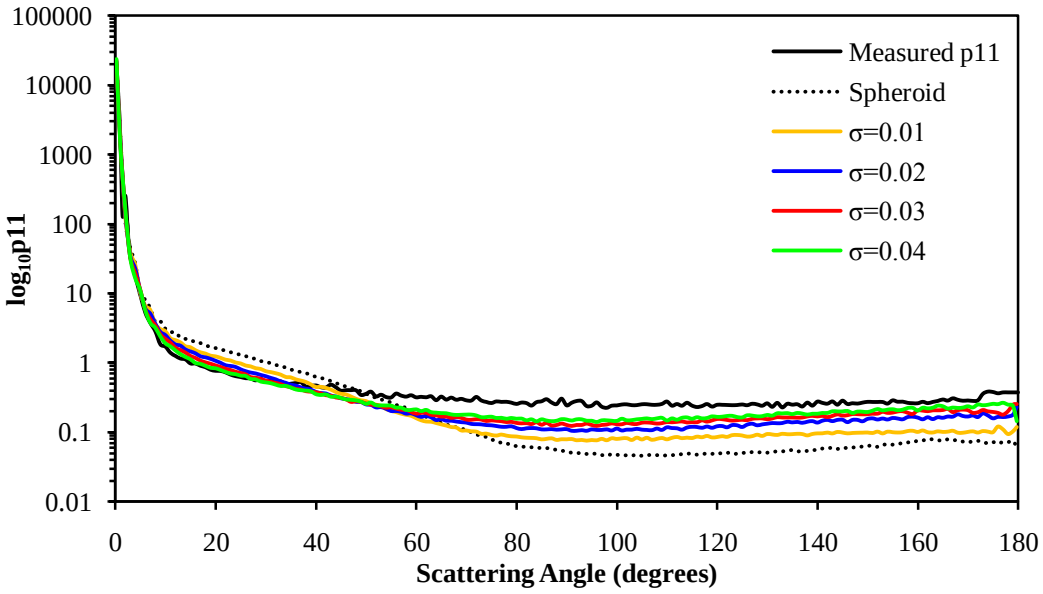

Figure 9-3-10 – As in **Figure 9-3-6** with refractive index 1.55 + 0.003i.

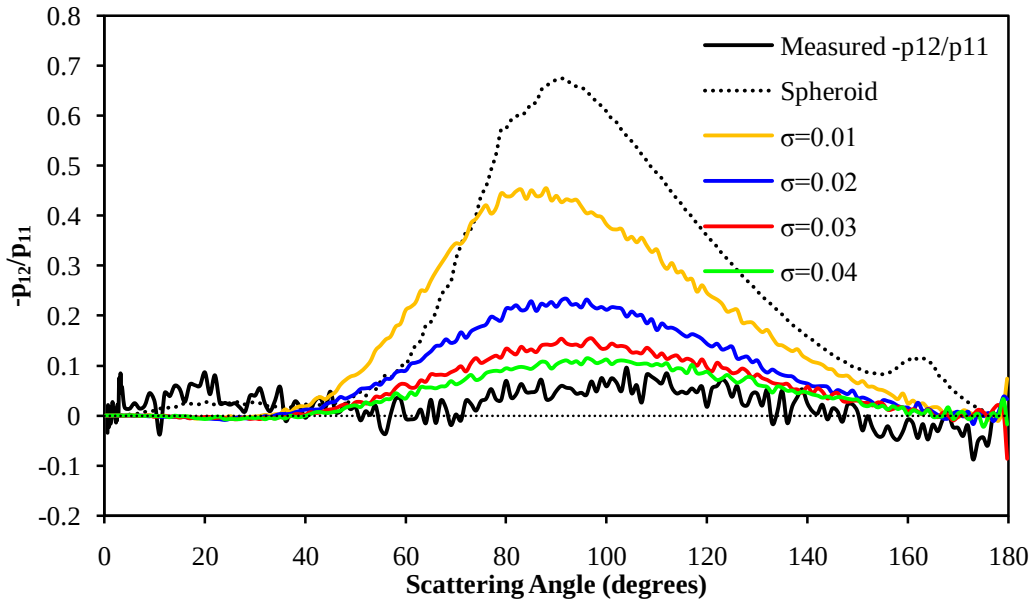

Figure 9-3-11 – As in **Figure 9-3-10** for the Degree of Linear Polarisation.

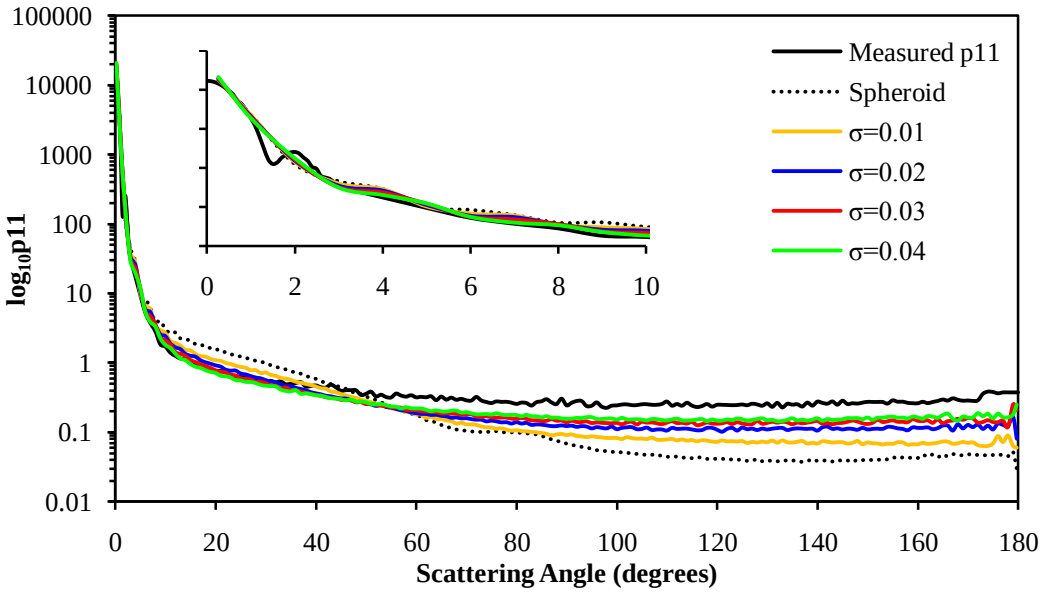

Figure 9-3-12 - As in **Figure 9-3-8** with refractive index 1.55 + 0.003i.

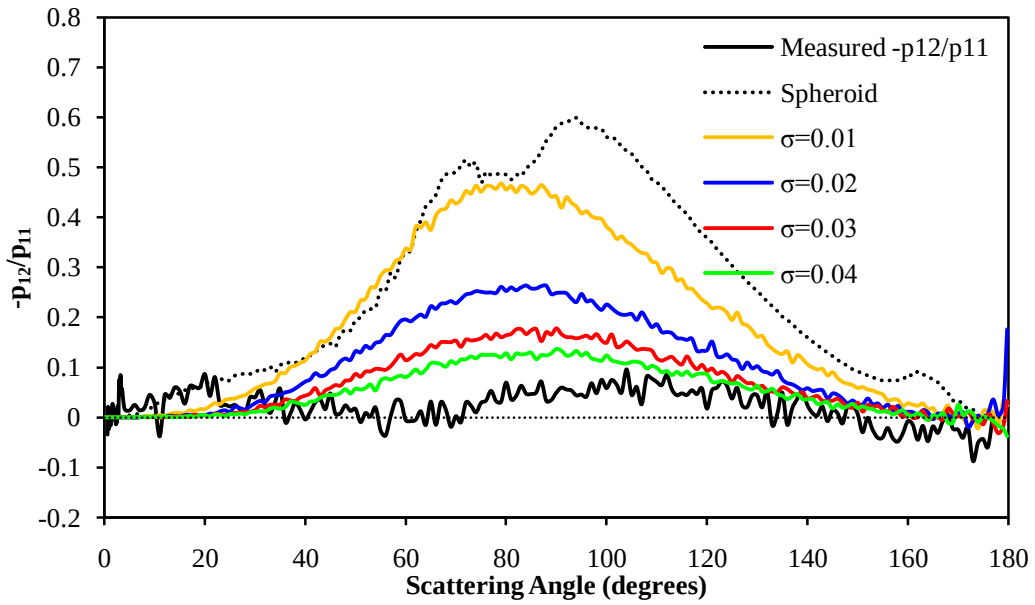

Figure 9-3-13 - As in **Figure 9-3-12** for the Degree of Linear Polarisation.

Figure 9-3-10 – 9-3-13 show RTDF calculations using a refractive index of 1.55 + 0.003i. Here, we see excellent agreement in the forward scattering region between 0° and 40° for higher values of σ. For scattering angles above 50°, the calculated scattering is lower than measured, although the agreement improves for higher values of σ. Again, limiting the orientation appears to produce slightly better agreement – above 100°, the calculated results show an increase in scattered intensity, with the highest values of σ approaching the measured results at 180°.

As we have seen in previous calculations, the degree of linear polarisation produces a pronounced bell curve shape when calculations using a complex refractive index are performed. The calculated results are higher than the measured across the entire angular range, except in the immediate forward scattering region where there is a polarisation peak in the measured results.

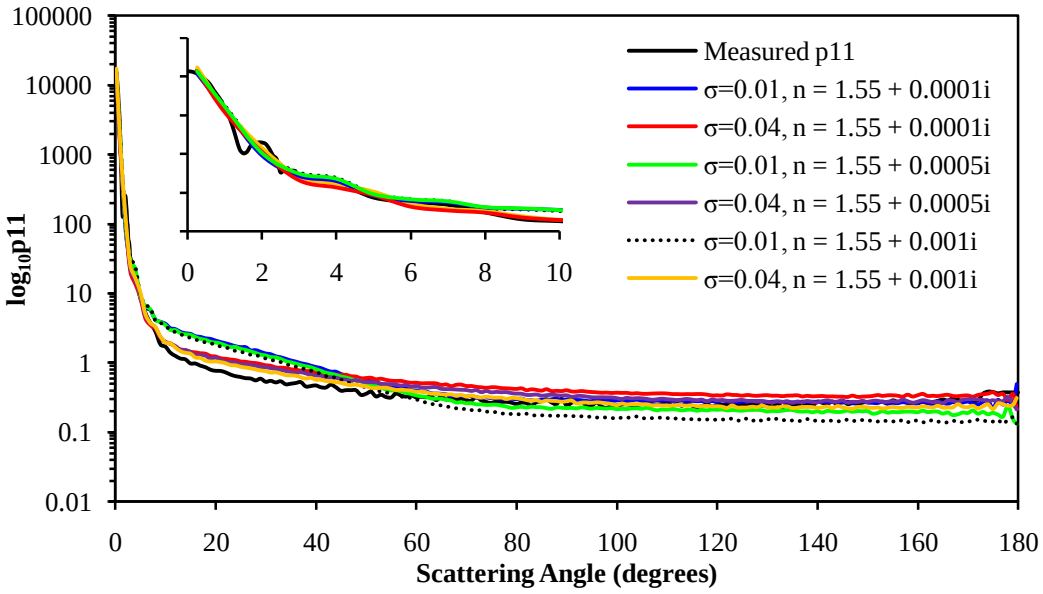

Figure 9-3-14 – The scattering phase functions as calculated using RTDF for a range of modelled particles compared with the measured phase function for particle 3. The modelled particles are those shown in **Figure 9-3-5**. The complex component of the refractive index was varied, and two values of σ were used. Here, the particle was free to orient randomly.

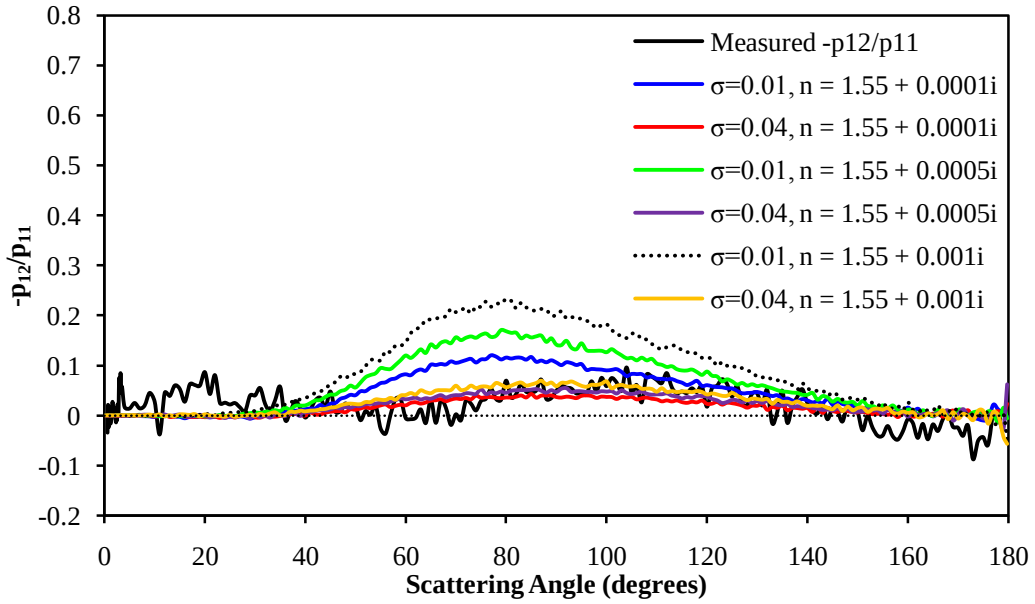

Figure 9-3-15 - As in **Figure 9-3-14** for the Degree of Linear Polarisation

Figure 9-3-14 and **9-3-15** show RTDF calculations for a range of surface roughness values and a range of absorption components. In the phase function we can see that the computed results 'group' together by σ value in the forward scattering region up to approximately 50°. Above 50°, the results spread out – the best fit visually is given by σ = 0.04, n = 1.55 + 0.001i.

The computed DLP results again describe a skewed bell curve – the peak observed at 20° in the levitated particle measurements is not reproduced. Between 80° and 150°, there is good agreement between computed and observed results for computations with a high value of σ. Lower values of σ demonstrate larger DLP across most of the angular range than the levitated particle.

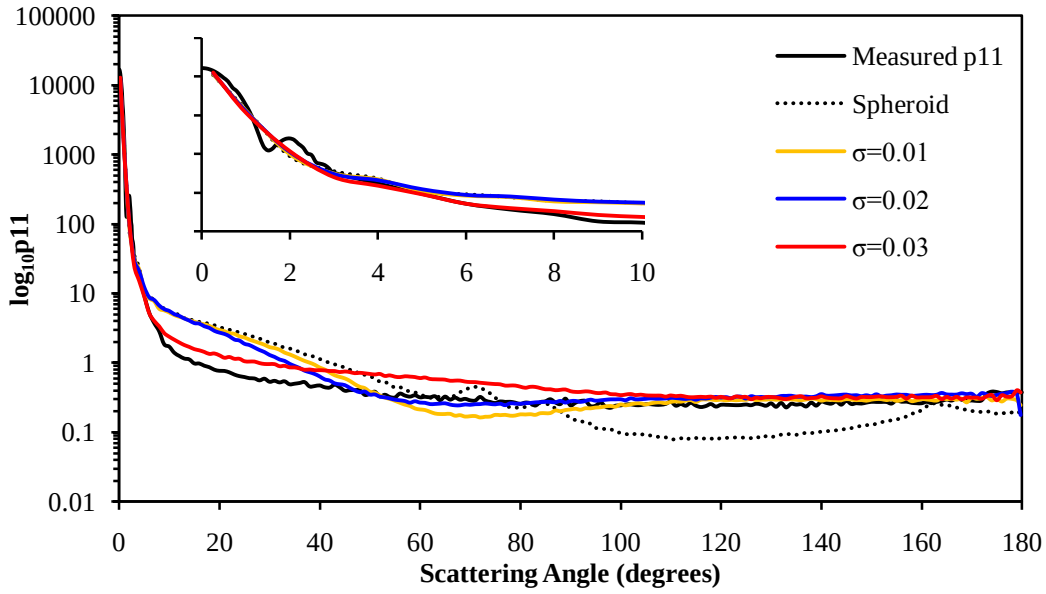

Figure 9-3-16 - The scattering phase functions as calculated using GO for a range of modelled particles compared with the measured phase function for particle 3. The modelled particles are those shown in **Figure 9-3-5**, and the refractive index used for these calculations is 1.55 + 0i. In these calculations, the particle orientation was limited as described in the text.

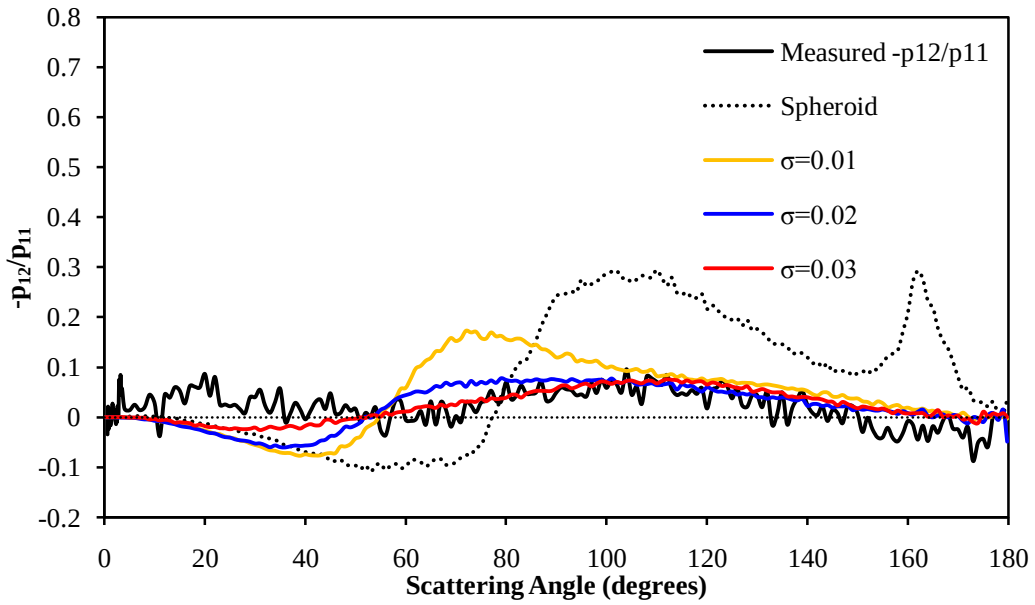

Figure 9-3-17 – As in **Figure 9-3-16** for the Degree of Linear Polarisation.

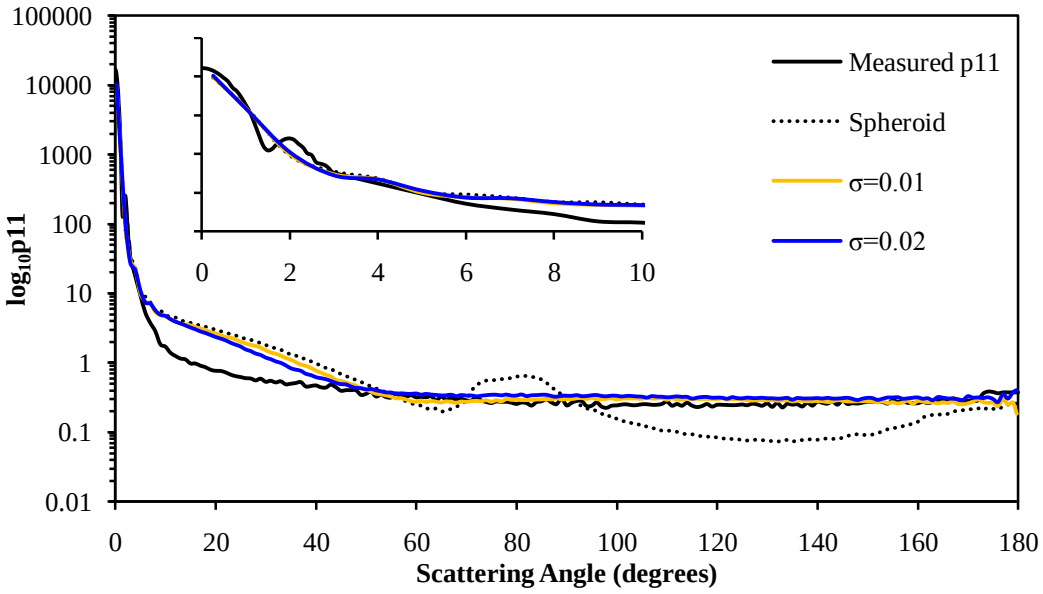

Figure 9-3-18 – As in **Figure 9-3-15** but the particle was free to rotate randomly.

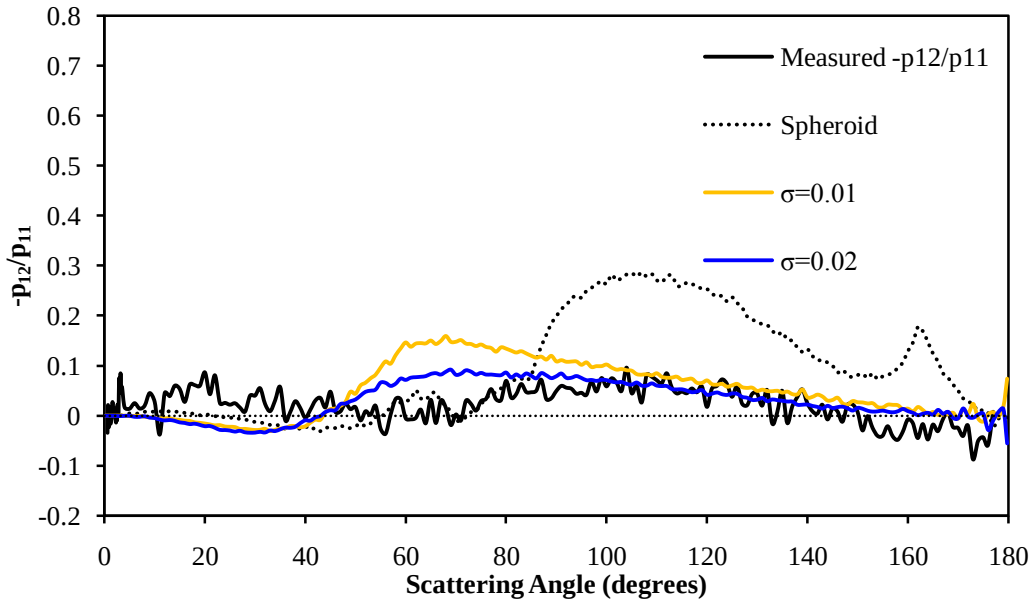

Figure 9-3-19 – As in **Figure 9-3-18** for the Degree of Linear Polarisation.

Figure 9-3-16 – 9-3-19 show GO calculations using a refractive index of 1.55 + 0i. Several of the test case calculations did not complete, and so are omitted. Again, there is good agreement in the immediate forward scattering region – this is followed by a disparity between the results between approximately 5° and 50° (for $\sigma \leq 0.02$) and 10° to 100° ($\sigma = 0.03$). The most appropriate comparison is found for random orientations when $\sigma = 0.02$, where the calculated results compare favourably with the measurements for scattering angles above 50°.. Here, orientation limited calculations show improved agreement with the measured results.

The calculations show a depolarisation peak in the forward scattering region that is not present in the measured results. There is then a polarisation peak at 60°, also not present in the measured results, but there is good

agreement between 100° and 150°. The calculated results do not show the low level of depolarisation observed in the backscattering region.

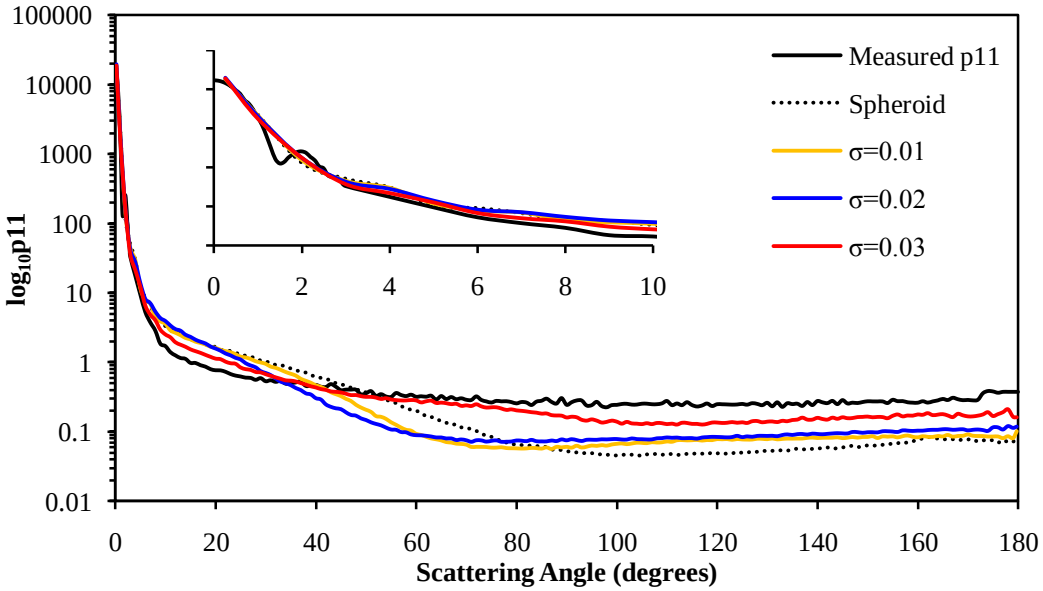

Figure 9-3-20 - As in **Figure 9-3-16** for refractive index 1.55 + 0.003i.

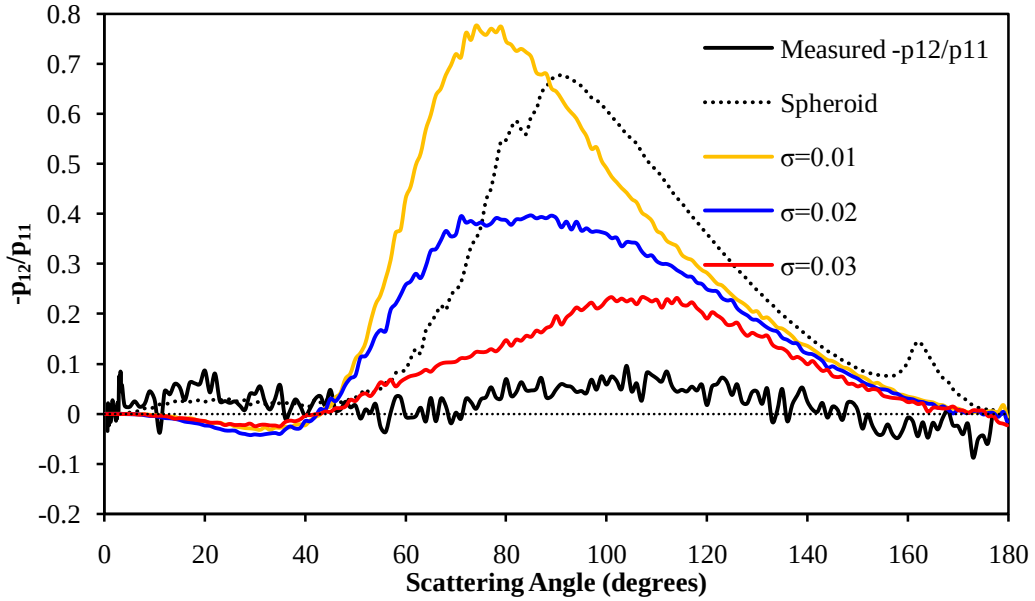

Figure 9-3-21 - As in **Figure 9-3-20** for the Degree of Linear Polarisation.

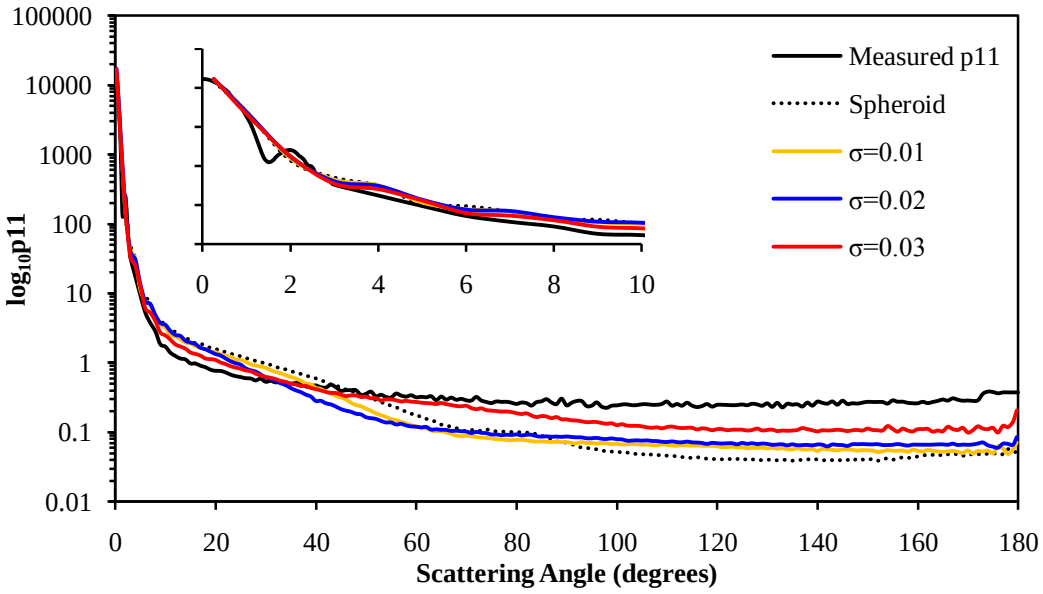

Figure 9-3-22 - As in **Figure 9-3-18** for refractive index 1.55 + 0.003i.

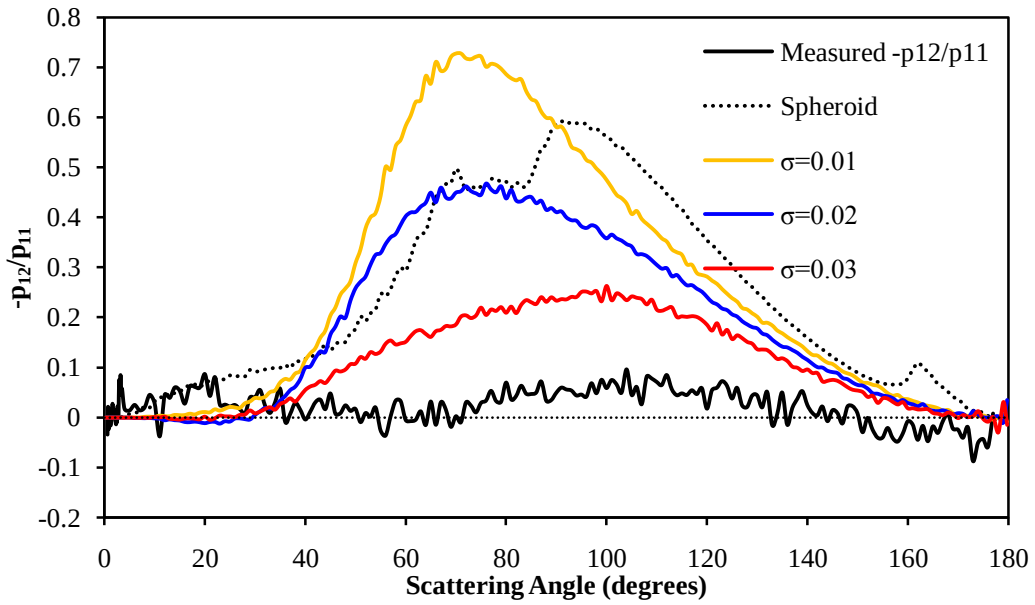

Figure 9-3-23 - As in **Figure 9-3-22** for the Degree of Linear Polarisation.

Figure 9-3-20 – 9-3-23 show GO calculations using a refractive index of 1.55 + 0.003i. There is good agreement in the forward scattering region with a small difference in scattered intensity between 10° and 35°. For angles above that, the calculated scattering intensity is increasingly lower than the measured intensity. The comparison is improved by increasing σ, and the orientation limited case is marginally improved due to a slight increase in backscattered intensity.

The degree of linear polarisation from the calculations again exhibits an exaggerated bell curve, and is significantly larger than the measurements for most of the angular range. The measured polarisation peak is not present, and the polarisation peak for σ = 0.03 is in the same angular position as the measured peak.

9.3.4 – RMS Comparison of phase functions

The RMS differences for the phase functions of the modelled particles are presented as described in **9.1.4**.

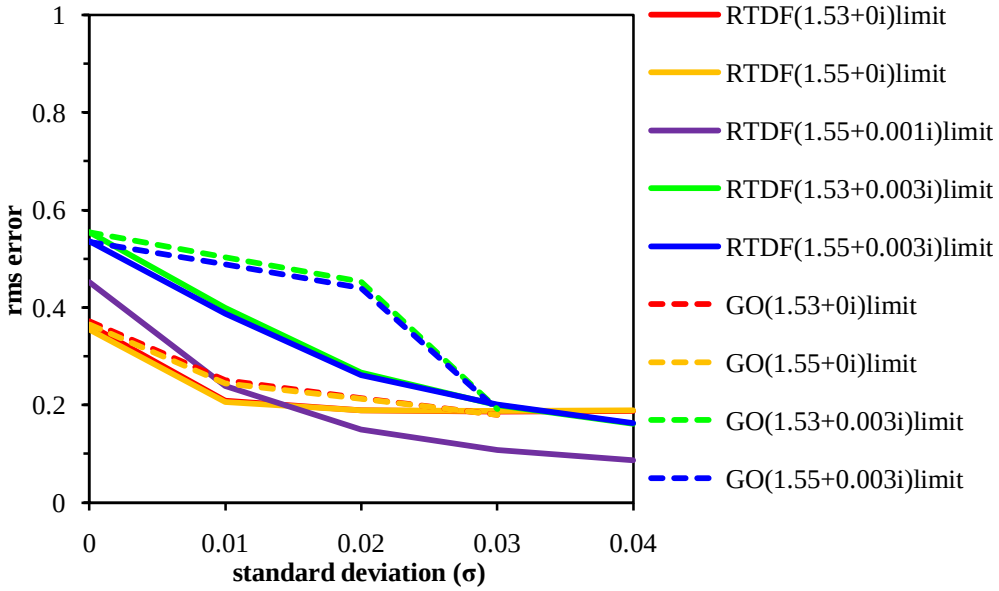

Figure 9-3-24 - RMS errors comparison. For these calculations, the particle orientation was limited as described in the text.

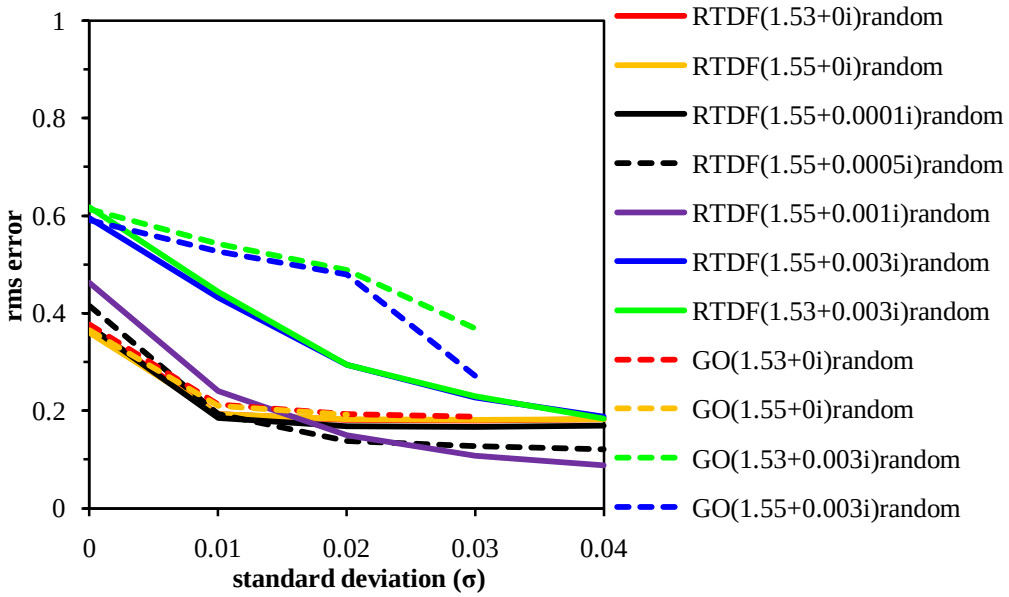

Figure 9-3-25 - RMS errors comparison. For these calculations, the particles were allowed to orient randomly.

Figure 9-3-24 and **9-3-25** show the RMS errors between the measured and computed results.

Here, adding a small complex component to the refractive index for particles with large values of σ gives the lowest errors. For all but the largest values of σ, strongly absorbing (ni = 0.003i) particles give larger errors than are observed elsewhere. As was observed in **Figure 9-3-14**, a very low error is confirmed for σ = 0.04 and n = 1.55 + 0.001i.

9.3.5 – Asymmetry Parameter

The asymmetry parameter for the levitated particle is 0.729, as calculated from the measured phase function.

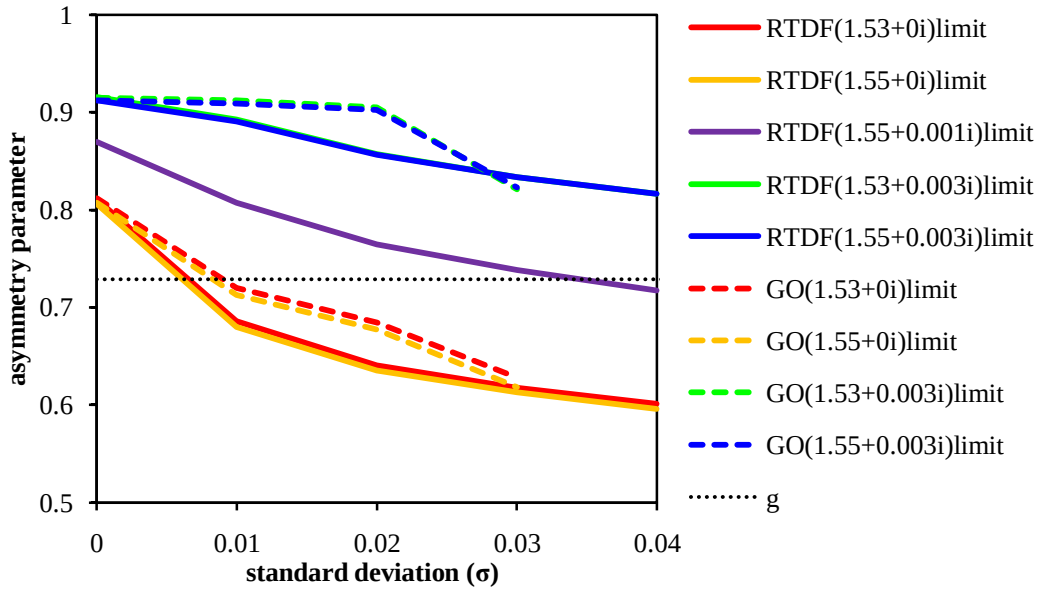

Figure 9-3-26 - Comparison of calculated asymmetry parameters with that of the levitated particle (g). Here, the particle orientation was limited as described in the text.

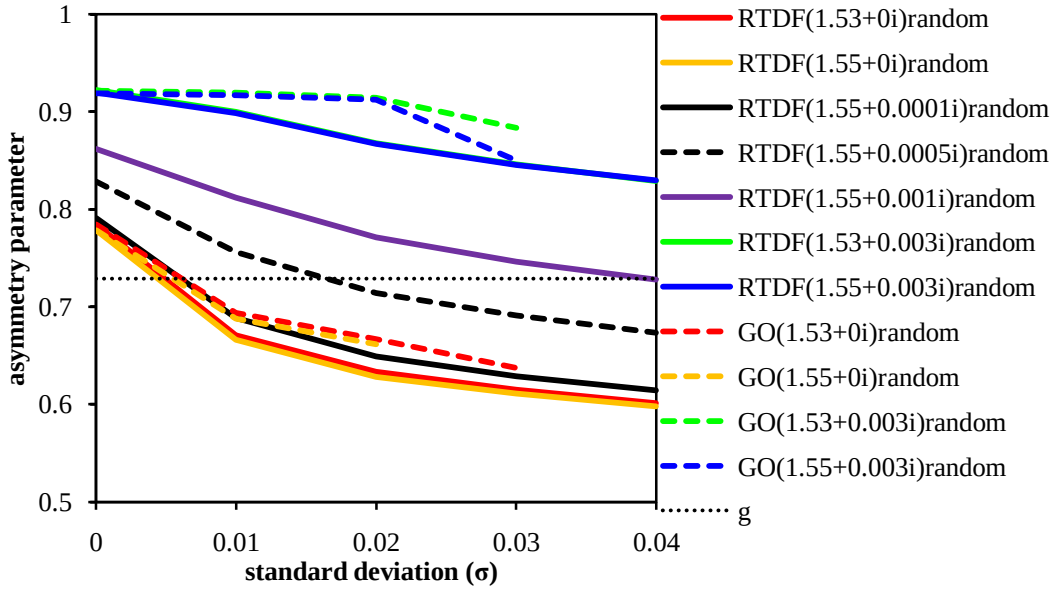

Figure 9-3-27 - Comparison of calculated asymmetry parameters with that of the levitated particle (g). Here, the particles were allowed to orient randomly.

Figure 9-3-26 and **9-3-27** show that the measured asymmetry parameter is best approximated by computations using non-absorbing refractive indices for fairly smooth particles or for very rough lightly absorbing particles. The agreement decreases as σ is increased. We can observe in the phase functions for non-absorbing particles that as σ increases, the side and back scattered intensity is higher than the measured intensity. This will lower the asymmetry parameter.

9.4 – Case Study 4

9.4.1 – Levitation and Scattering Experiments

Dust particle 4 strongly resembles a prolate spheroid with an approximate aspect ratio of 2. The size parameter is in the range 123 – 138 (surface area) or 117 – 133 (volume).

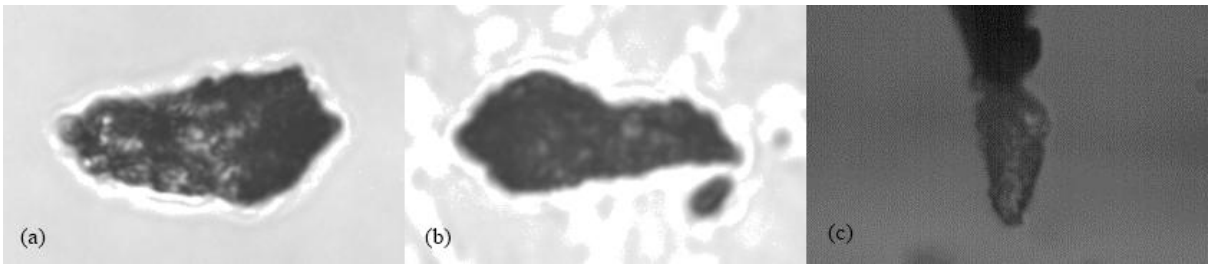

Figure 9-4-1 - Particle 4 as seen under transmission microscopy (a,b) and seen through an optical microscope after being picked up by the needle for injection (c). Assuming that the long axis is along the horizontal, the particle dimensions are: (a) 34.1 x 17.5µm, (b) 33.7 x 14.5µm. The approximate size parameter is between 123 and 138 (surface area) or 117 and 133 (volume).

This particle was levitated with its long axis horizontal, and exhibited rapid and full rotation about the vertical axis. A further small and rapid rotation was observed, with the particle tilting very rapidly along the short axis of the particle parallel to the horizontal. Upon illumination by the laser, the rotation of the particle about the vertical axis increased rapidly.

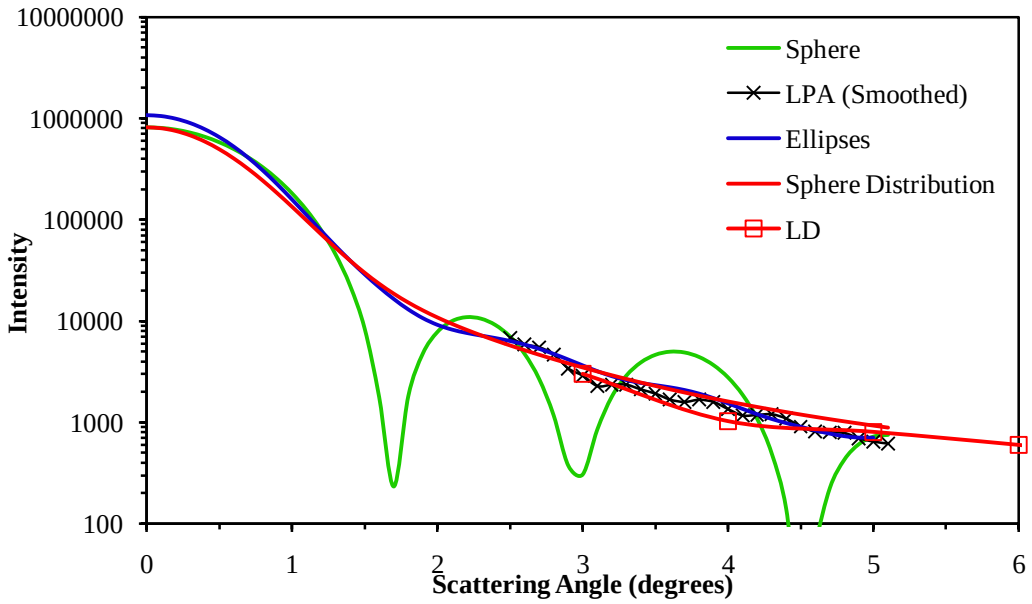

Figure 9-4-2 – Small angles scattering data and fitting patterns for the particle shown in **Figure 9-4-1**. The sphere data for comparison was generated using a single sphere (X_s = 130) and a gamma distribution of spheres (X_s = 130, shape parameter a=130, scale parameter b=0.1, r_{min}=0 and r_{max}=800, all values except b given in terms of size parameter). For the spheres a refractive index of 1.55 + 0.001i was used. For the ellipses, a minimum radius of 4.5 µm, a maximum radius of 8.5 µm and an aspect ratio of 2 was used.

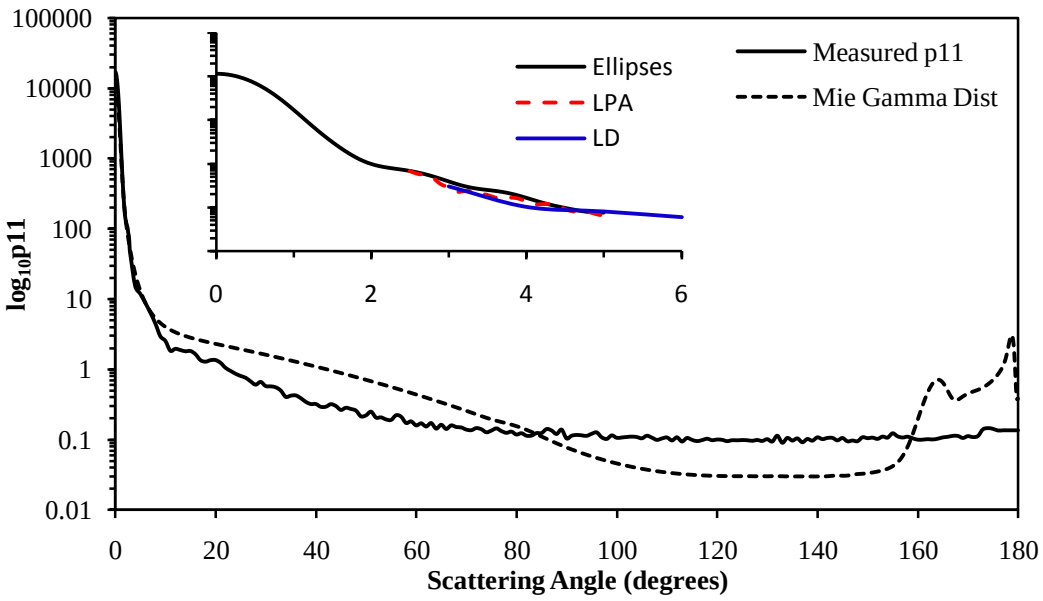

Figure 9-4-3 - The full phase function for the particle shown in **Figure 9-4-1**. The phase function for a gamma distribution of spheres is also shown for comparison. Inset: The small angle scattering data, showing how the 3 readings are joined together. The refractive index used in the sphere distribution calculations is 1.55 + 0.001i.

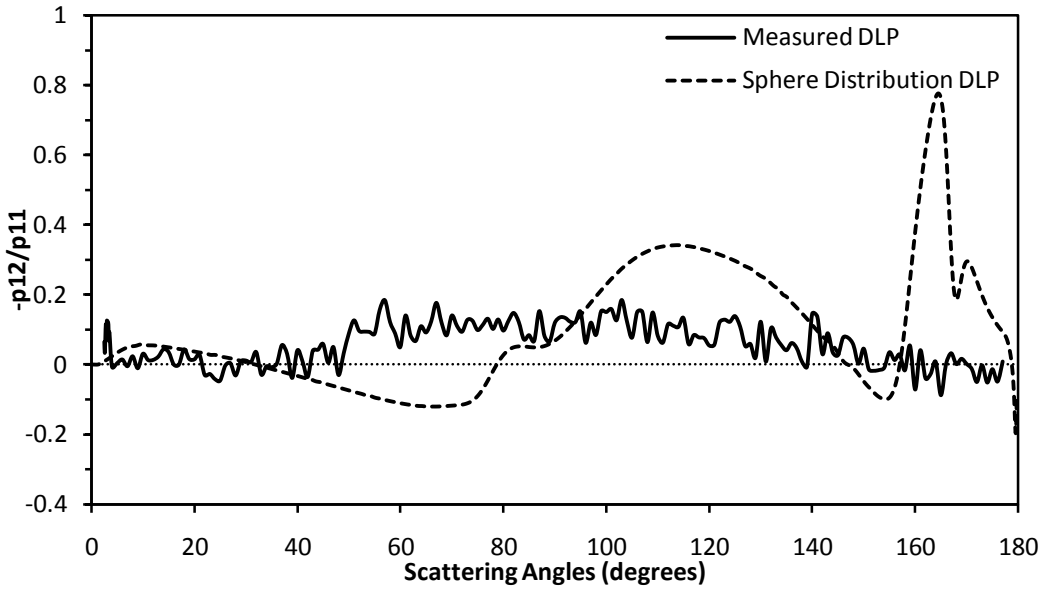

Figure 9-4-4– The degree of linear polarization for the particle shown in **Figure 9-4-1**. Also shown for comparison is the DLP for a gamma distribution of spheres.

9.4.2 – Modelling the Particle

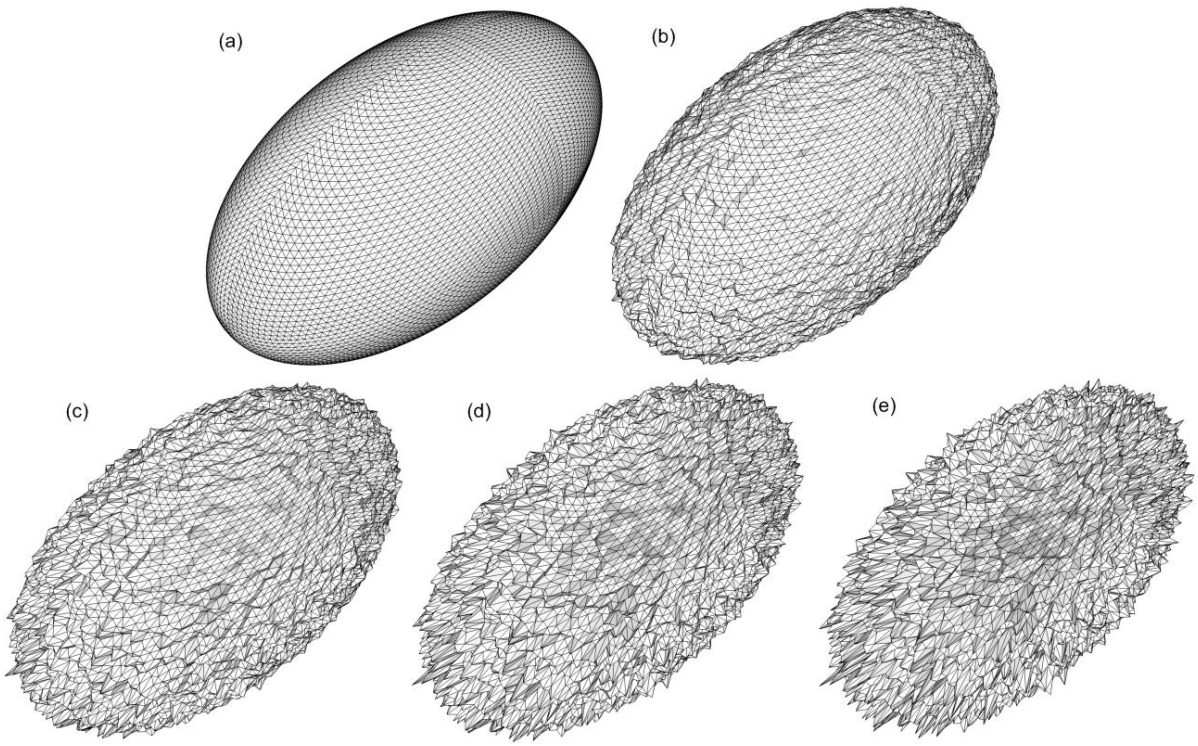

Figure 9-4-5 - Polygonal mesh approximations of the particle shown in **Figure 9-4-1**. All the figures are composed of 20,000 facets. Particle (a) is a perfect prolate spheroid, of aspect ratio ε=0.5. Particles (a) – (d) have surfaces generated using Gaussian Random statistics **[38]** and a correlation angle of 1°. The standard deviation σ for each particle is (a) σ=0.0, (b) σ=0.01, (c) σ=0.02, (d) σ=0.03, (e) σ=0.04

The particle is modelled as a prolate spheroid of equal-volume-sphere size parameter 130, with an aspect ratio of 0.5.

9.4.3 – RTDF and GO calculations

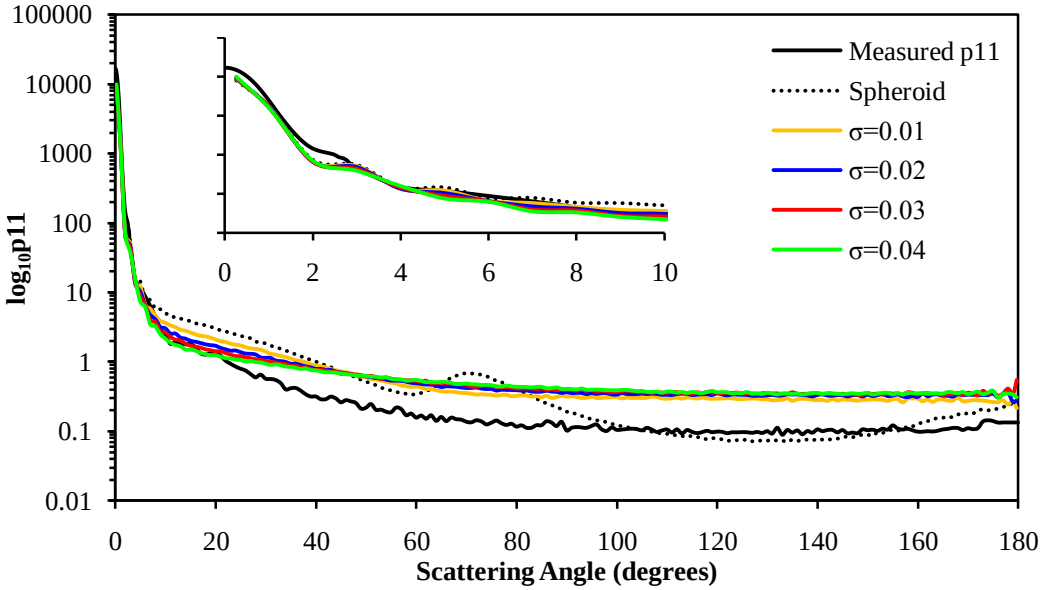

Figure 9-4-6 - The scattering phase functions as calculated using RTDF for a range of modelled particles compared with the measured phase function for particle 4. The modelled particles are those shown in **Figure 9-4-5**, and the refractive index used for these calculations is 1.55 + 0i. In these calculations, the orientation of the particle was limited as described in the text.

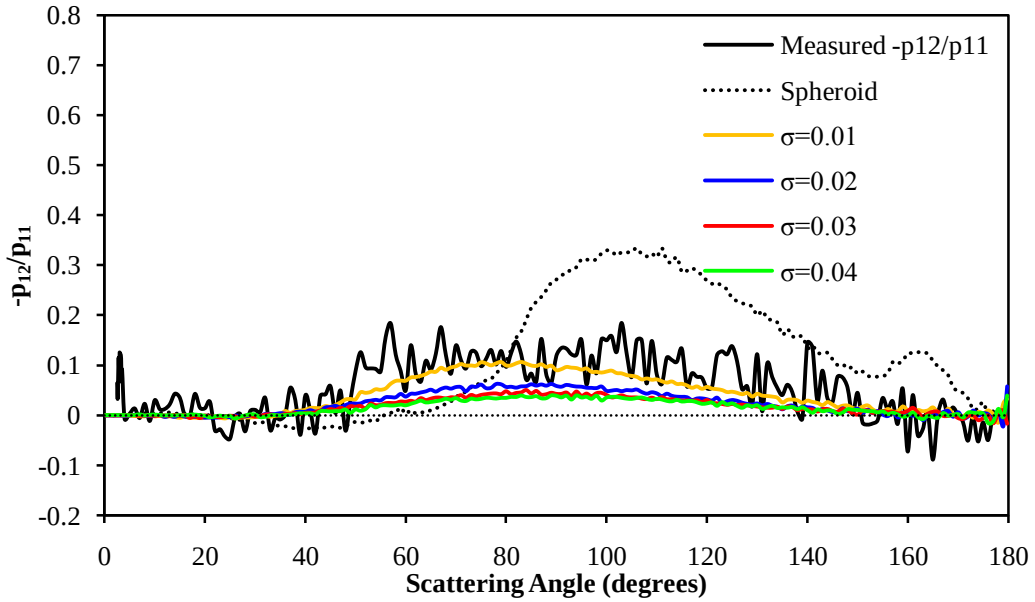

Figure 9-4-7 - As in **Figure 9-4-6** for the Degree of Linear Polarisation.

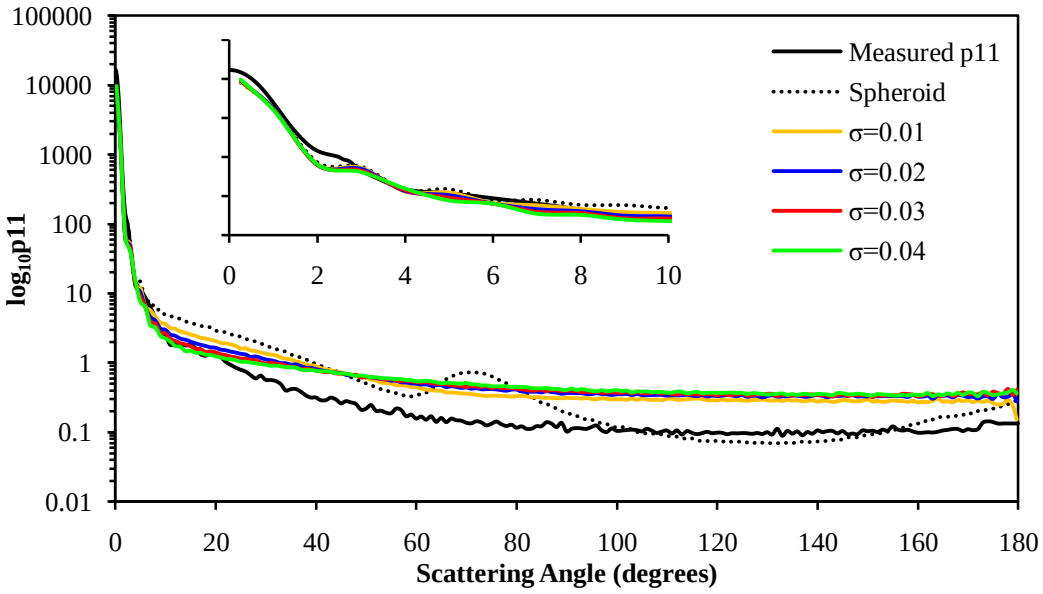

Figure 9-4-8 – As in **Figure 9-4-6** but the particle was free to rotate randomly.

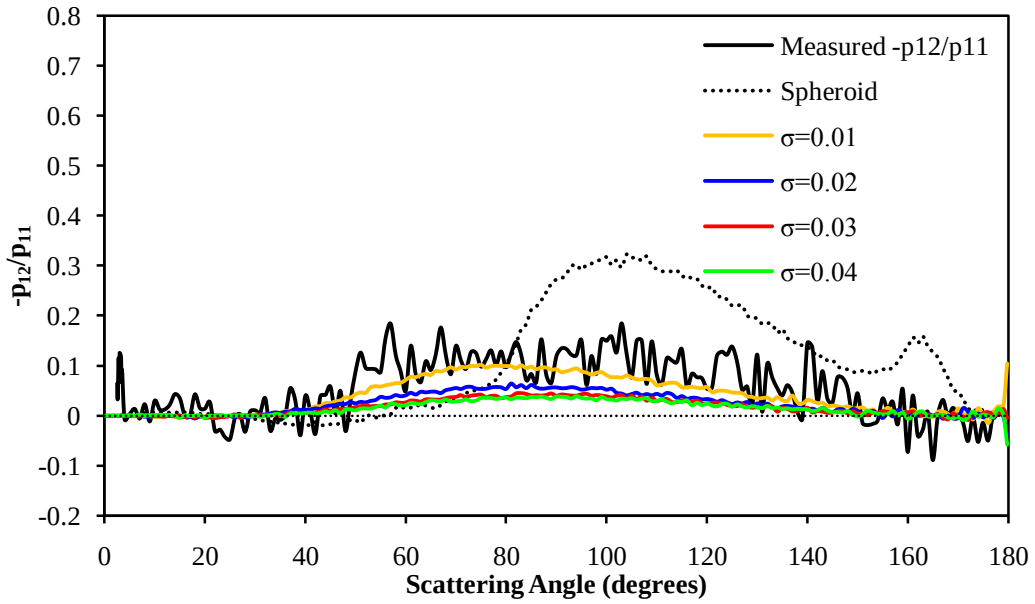

Figure 9-4-9 – As in **Figure 9-4-8** for the Degree of Linear Polarisation.

Figure 9-4-6 – 9-4-9 show RTDF calculations using a refractive index of 1.55 + 0i. The computed and measured functions all agree quite well in the small angle region below 20°, with increasing σ giving increased agreement. The computed phase function for rough spheroids above 20° is considerably higher than the measured phase function. The computed results agree well in the forward scattering region below 10° and for scattering angles above 40°. Between these two angles the intensity decreases as σ increases.

The computed DLP results agree reasonably well with the measured results for σ=0.01. For values of σ higher than this, the computed results are much lower than the measured.

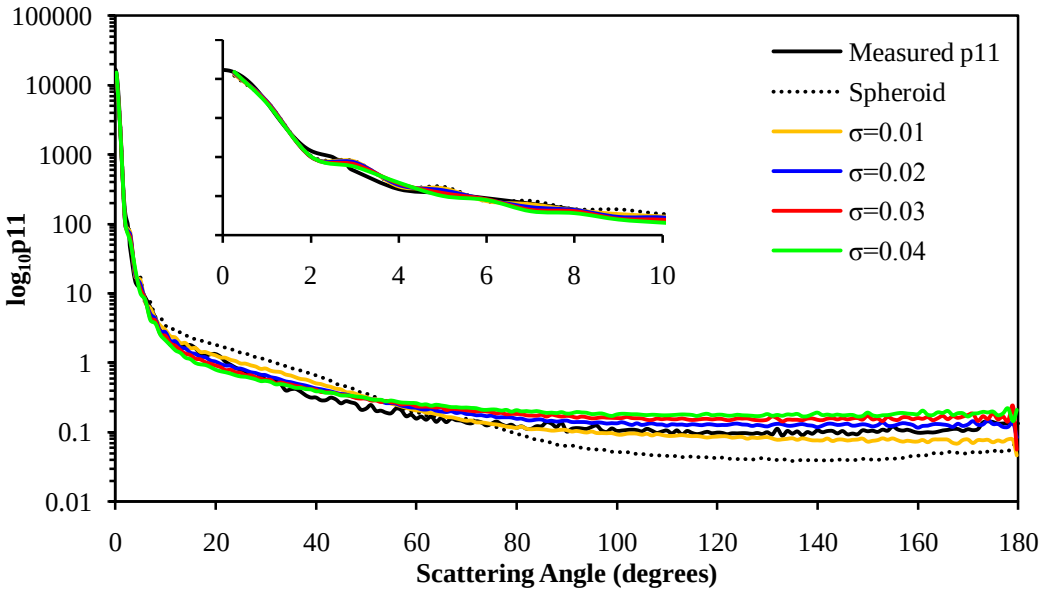

Figure 9-4-10 – As in **Figure 9-4-6** for refractive index 1.55 + 0.003i.

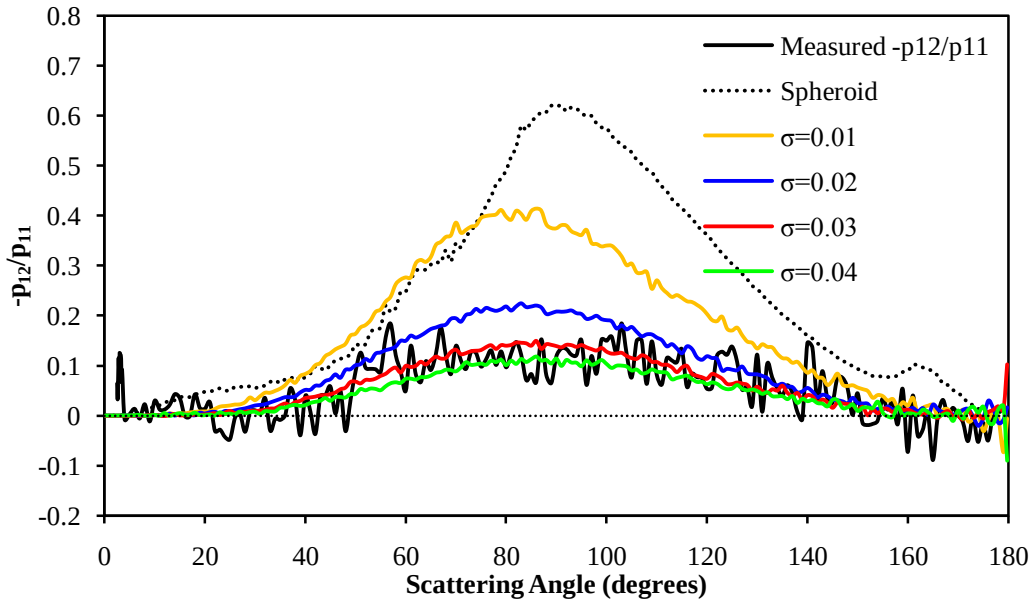

Figure 9-4-11 – As in **Figure 9-4-10** for the Degree of Linear Polarisation.

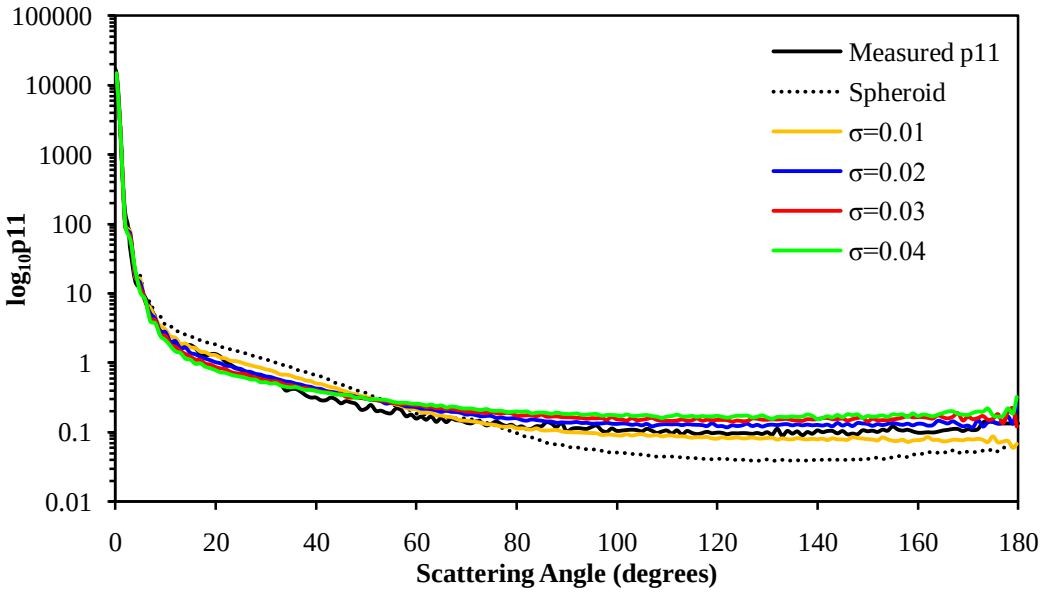

Figure 9-4-12 – As in **Figure 9-4-8** for refractive index 1.55 + 0.003i.

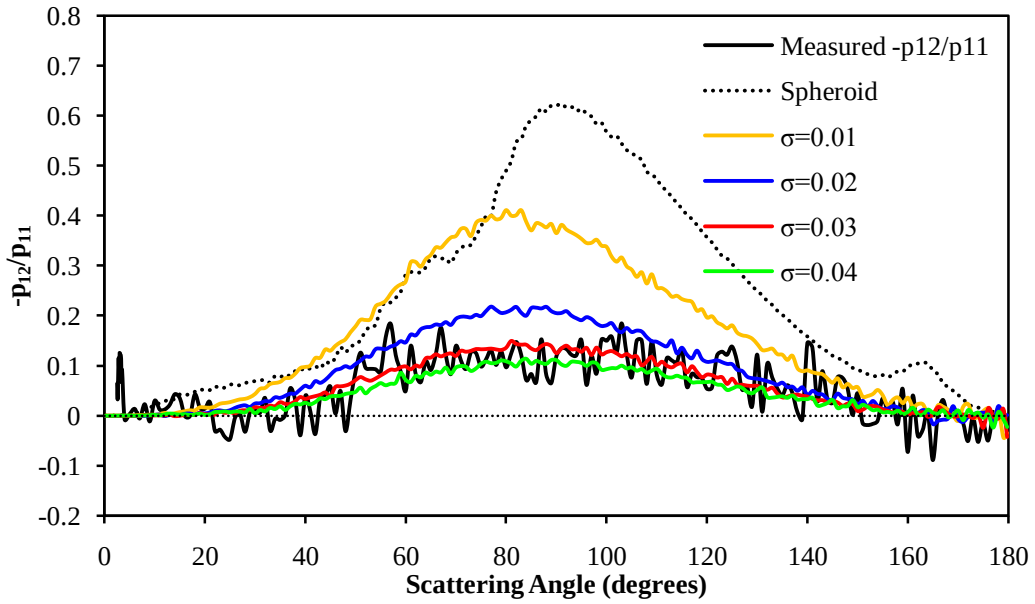

Figure 9-4-13 – As in **Figure 9-4-12** for the Degree of Linear Polarisation.

Figure 9-4-10 – 9-4-13 show RTDF calculations using a refractive index of 1.55 + 0.003i. Immediately we can see that the agreement across the entire angular range is an improvement on computations with no absorption. In the forward scattering region below 35°, very good agreement is seen for all values of σ, with the best agreement observed when σ=0.04. Above this, the intensity for the highest value of σ levels off, and is higher than the measured intensity for the rest of the scattering region. Improved agreement in this region is seen for low-mid values of σ,

The DLP computations are also an improvement on those with no absorption. As σ is increased, the computed DLP approaches the measured result, with calculations where σ=0.03 and σ=0.04 comparing very well.

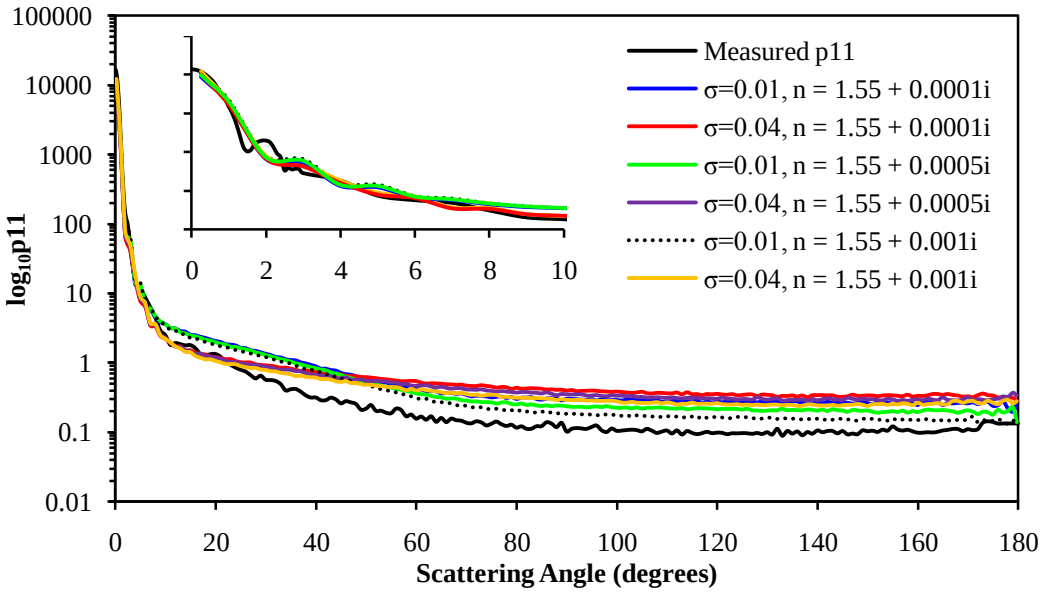

Figure 9-4-14 – The scattering phase functions as calculated using RTDF for a range of modelled particles compared with the measured phase function for particle 4. The modelled particles are those shown in **Figure 9-4-5**. The complex component of the refractive index was varied, and two values of σ were used. Here, the particle was free to orient randomly.

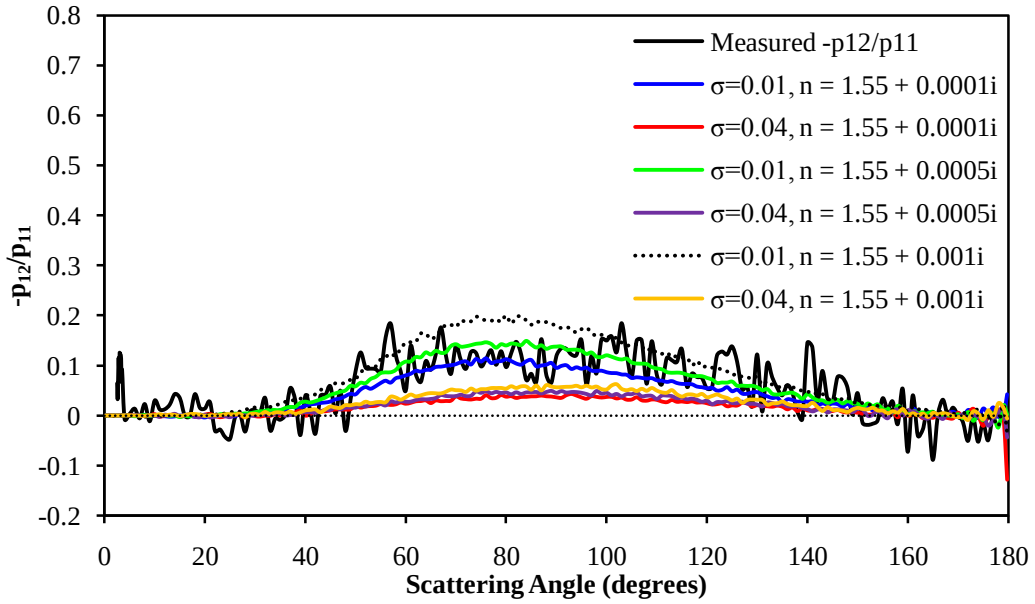

Figure 9-4-15 - As in **Figure 9-4-14** for the Degree of Linear Polarisation

Figure 9-4-14 and **9-4-15** show RTDF calculations for a range of surface roughness values and absorption components. In this case, the intensity measured from the levitated particle is lower than the computed intensity for most of the angular range. There is good agreement in the forward scattering range up to 10° (σ = 0.01) and up to 20° (σ = 0.04).

The computed DLP for low values of σ agrees quite well with that measured from the levitation experiments. The flattened bell curve shape is well reproduced by all of the computations, but high values of σ show a much lower DLP than was measured.

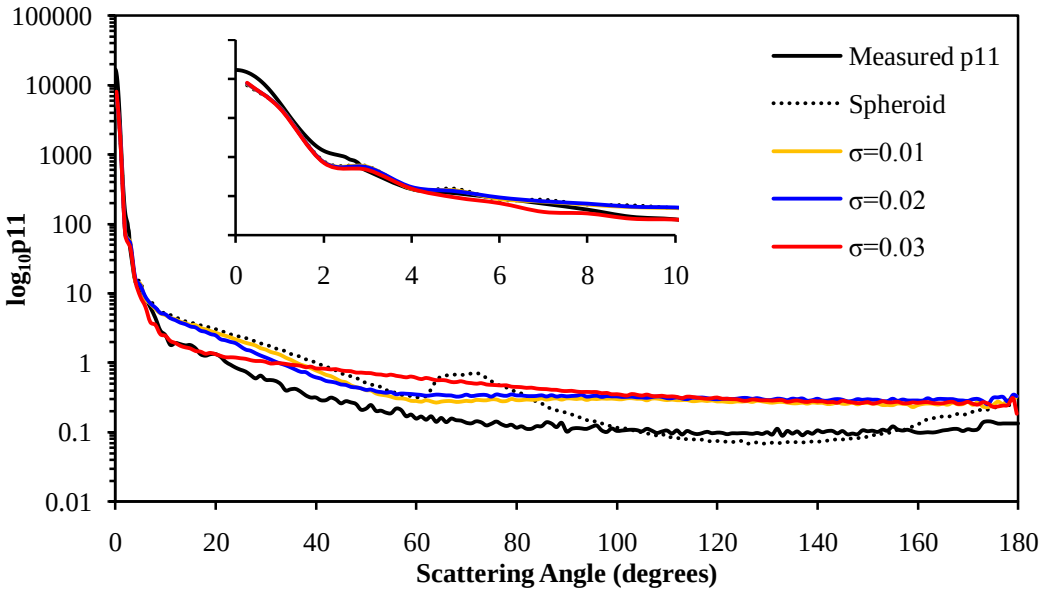

Figure 9-4-16 - The scattering phase functions as calculated using GO for a range of modelled particles compared with the measured phase function for particle 4. The modelled particles are those shown in **Figure 9-4-5**, and the refractive index used for these calculations is 1.55 + 0i. In these calculations, the particle orientation was limited as described in the text.

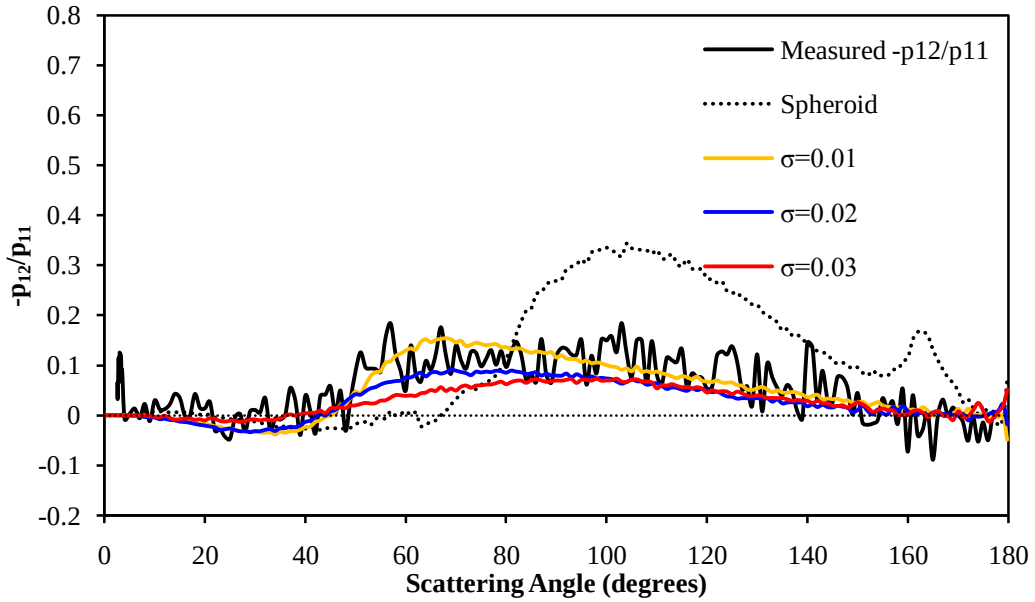

Figure 9-4-17 – As in **Figure 9-4-16** for the Degree of Linear Polarisation.

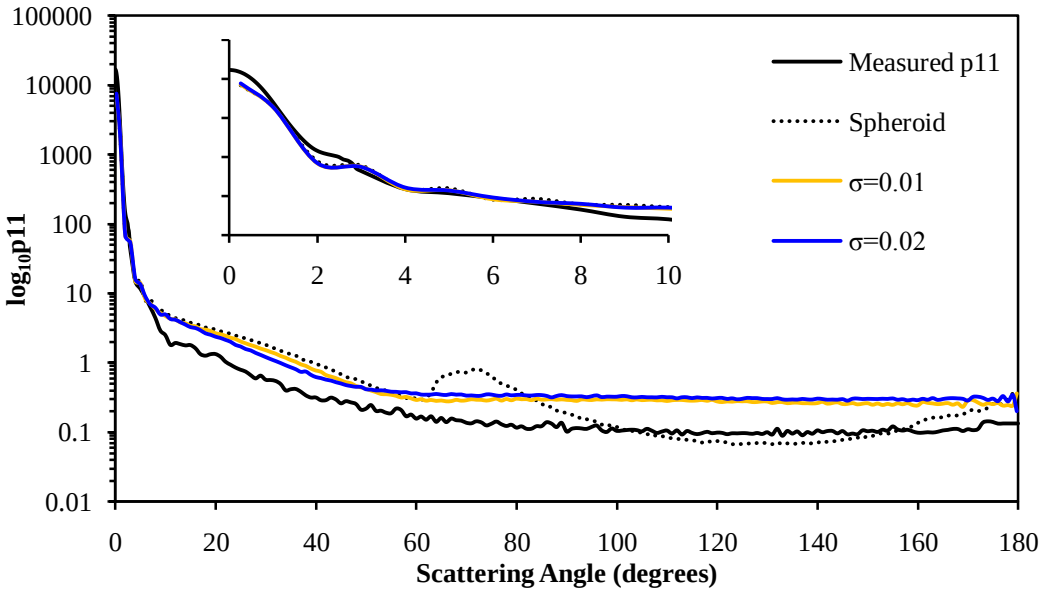

Figure 9-4-18 – As in **Figure 9-4-16** but the particle was free to rotate randomly.

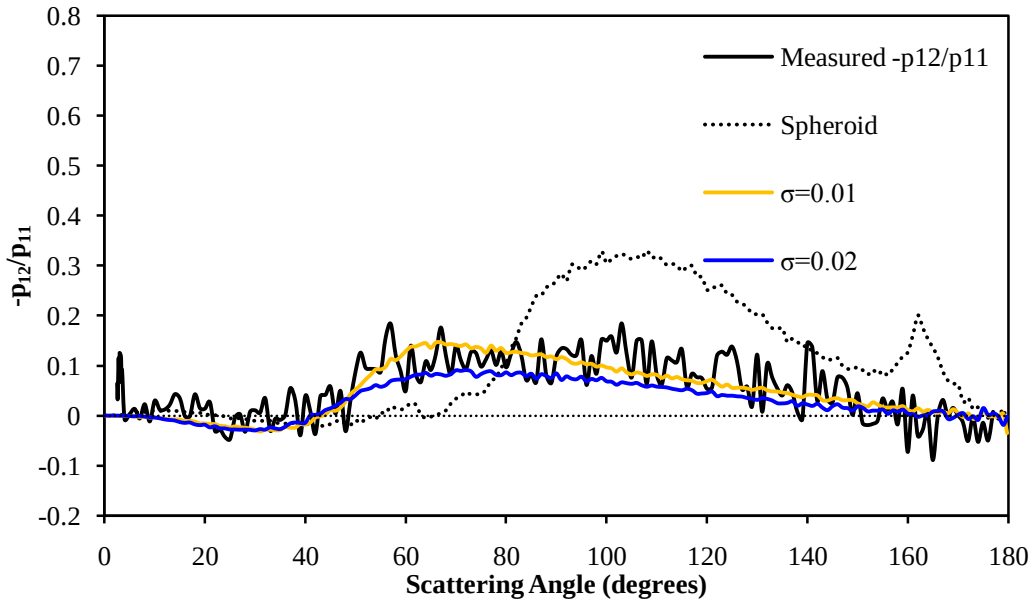

Figure 9-4-19 – As in **Figure 9-4-18** for the Degree of Linear Polarisation.

Figure 9-4-16 – 9-4-19 show GO calculations using a refractive index of 1.55 + 0i. As in the RTDF computations, the scattering for rough particles shows good agreement with the measured results in the forward scattering region, and then deviates for all higher scattering angles. For angles above 100°, all the computations where σ>0 give similar results. Unfortunately, GO computations did not complete for all values of σ.

The DLP computations for the rough spheroids show reasonable agreement across the entire angular range. The computations show a small negative DLP between 5° and 40°, and then a peak at approximately 70°. While the measured DLP demonstrates greater variance not replicated in the computations (due to the imperfect randomisation of the particle in the trap), the results can still be observed to be similar.

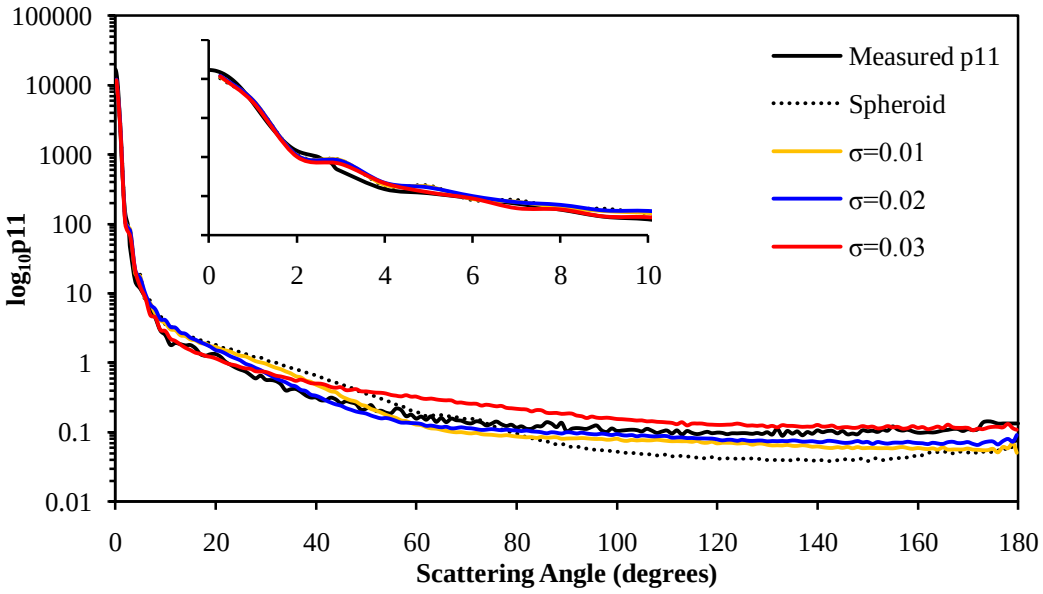

Figure 9-4-20 – As in **Figure 9-4-16** for refractive index 1.55 + 0.003i.

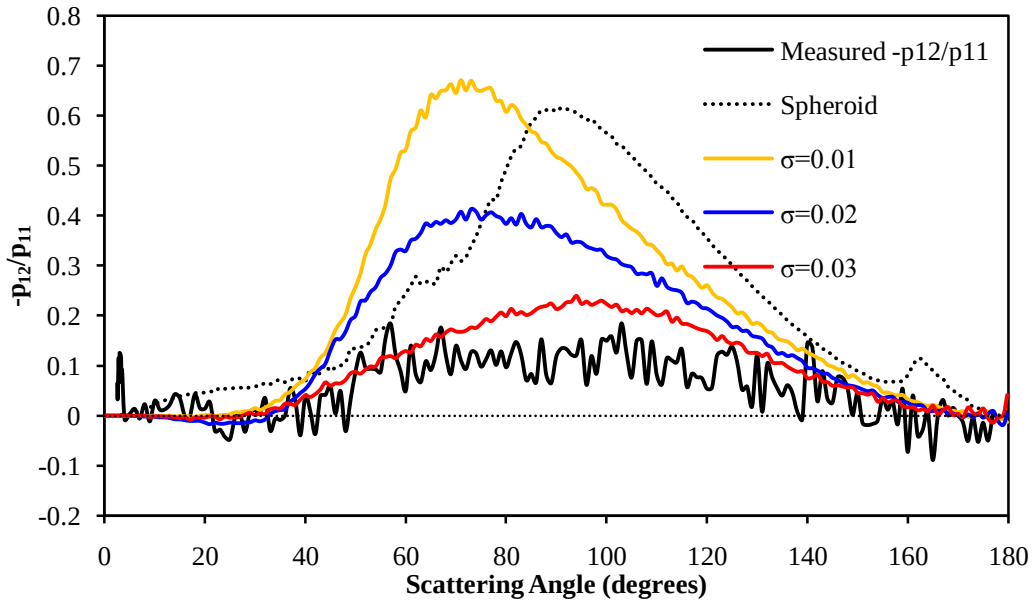

Figure 9-4-21 – As in **Figure 9-4-20** for the Degree of Linear Polarisation.

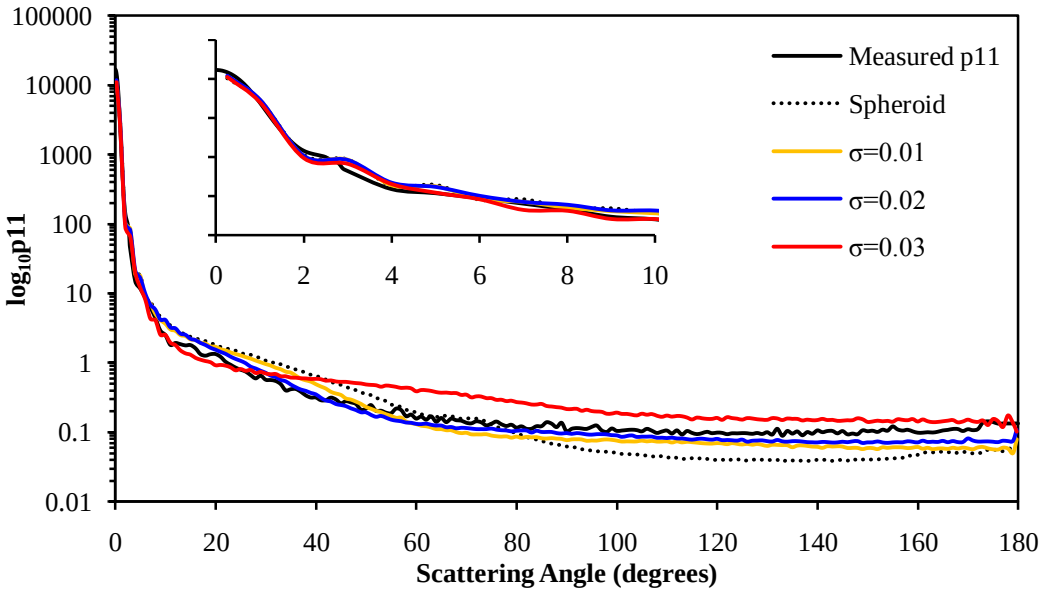

Figure 9-4-22 – As in **Figure 9-4-18** for refractive index 1.55 + 0.003i.

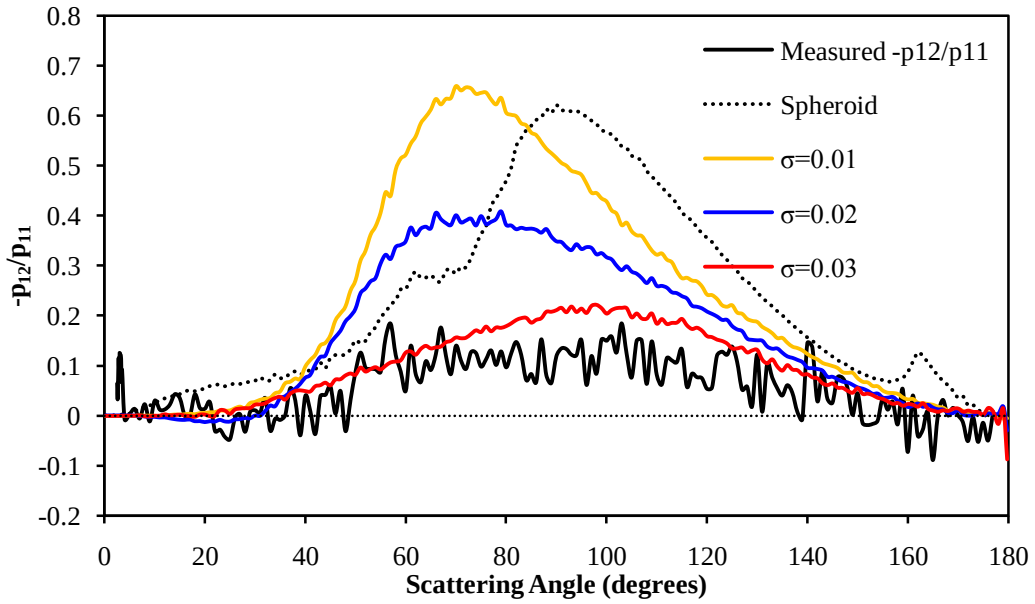

Figure 9-4-23 – As in **Figure 9-4-22** for the Degree of Linear Polarisation.

Figure 9-4-20 – 9-4-23 show GO calculations using a refractive index of 1.55 + 0.003i. As in RTDF, the addition of absorption improves the comparison between computed and measured results considerably. Again, low-mid values of σ give the best agreement across the entire angular range. In the forward scattering region below 30°, the best agreement is for σ=0.03, but for all larger angles, lower values of σ are better approximations.

The DLP results are also improved with the addition of absorption. While low values of σ show DLP that is much higher than the measured results, increasing σ improves the comparison considerably.

9.4.4 – RMS Comparison of phase functions

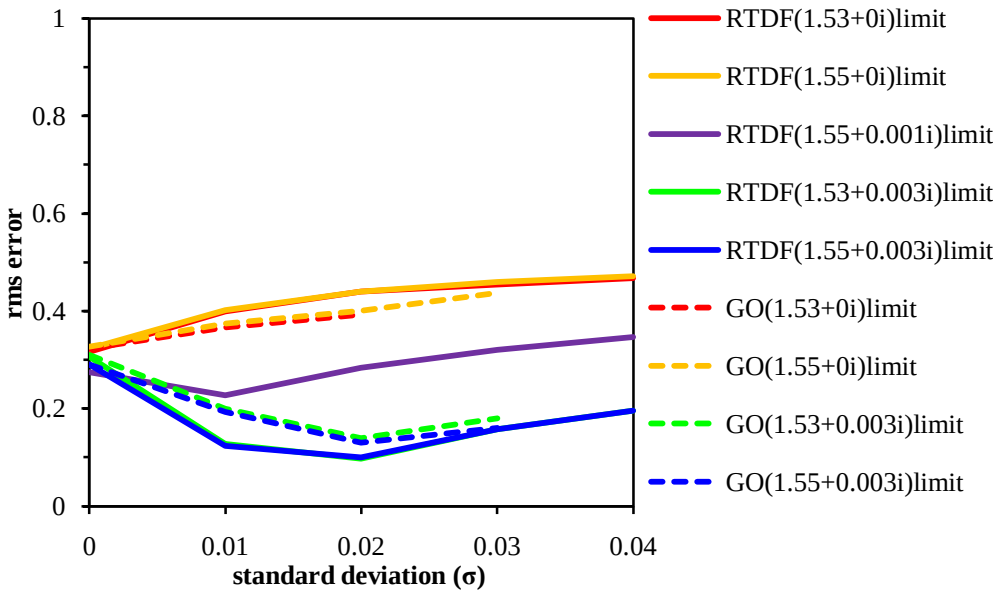

Figure 9-4-24 - RMS errors comparison. For these calculations, the particle orientation was limited as described in the text.

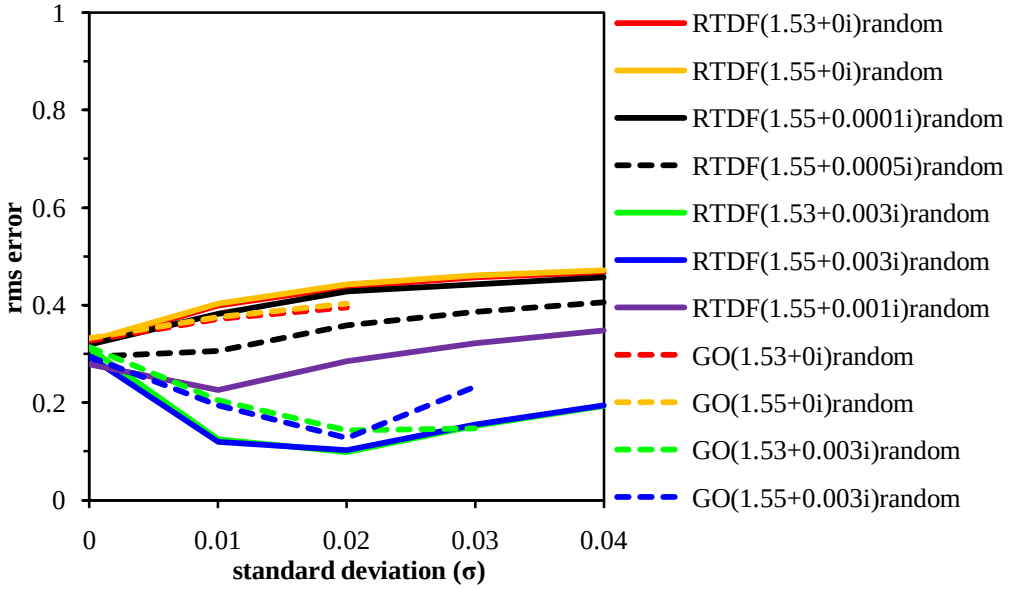

Figure 9-4-25 - RMS errors comparison. For these calculations, the particles were allowed to orient randomly.

Figure 9-4-24 & **9-4-25** again demonstrate the improvement of the comparison when absorption is included in the computations. As noted previously, the best comparison is for absorbing particles with values of σ in the low-mid range, where the errors increase as σ increases. This supports what was observed in the phase functions. The largest errors are for very rough, non-absorbing and lightly-absorbing particles.

9.4.5 – Asymmetry Parameter

The asymmetry parameter for the levitated particle is 0.876, as calculated from the measured phase function.

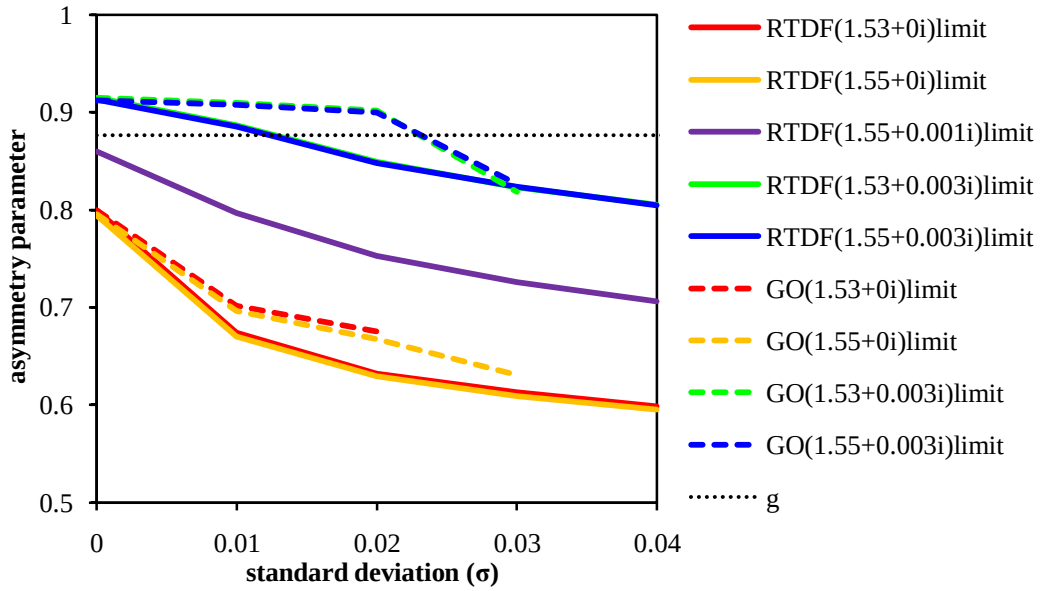

Figure 9-4-26 - Comparison of calculated asymmetry parameters with that of the levitated particle (g). Here, the particle orientation was limited as described in the text.

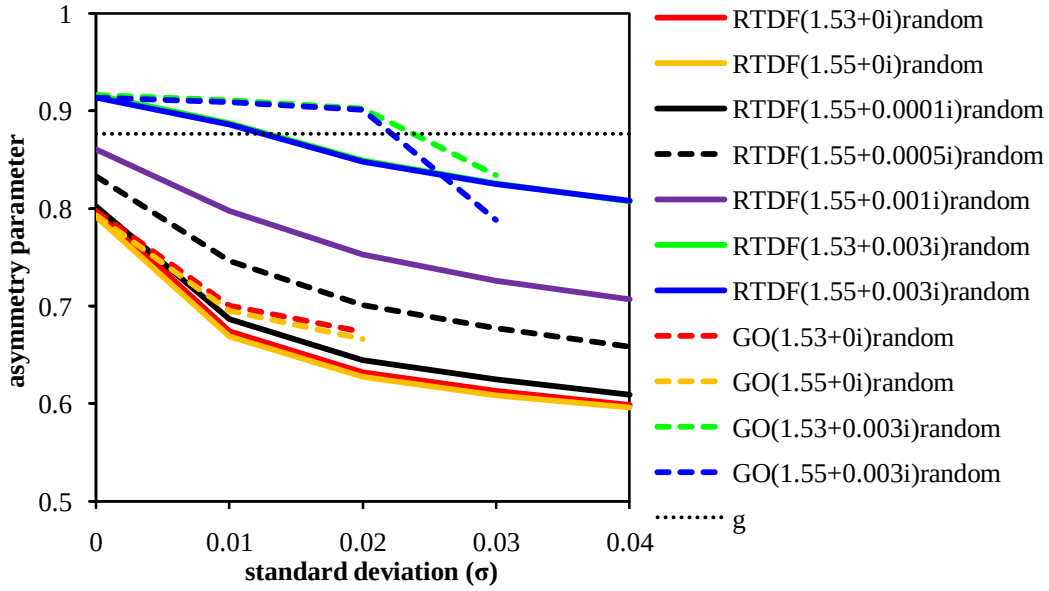

Figure 9-4-27 - Comparison of calculated asymmetry parameters with that of the levitated particle (g). Here, the particles were allowed to orient randomly.

In **Figure 9-4-26** & **9-4-27,** we see that the asymmetry parameter compares well against computations with absorption present. As the lightly-absorbing and non-absorbing cases demonstrated much higher intensity across the angular range, the corresponding asymmetry parameter is much lower than for the levitated particle. The best comparison is observed for low-mid values of σ where ni = 0.003i.

Chapter 10 – Summary and Outlook

The previous chapters have considered electromagnetic scattering by Saharan dust particles. A sample of Saharan dust particles has been characterised through the use of optical microscopy and a scanning electron microscope (SEM). An Electrodynamic Balance (EDB) has been used to levitate several single dust particles in order that scattering experiments could be carried out. When levitated, the trap parameters (ac-voltage frequency and amplitude) were adjusted in order that the particles could be made unstable within the trap, and would therefore rotate randomly about all three axes. It was not possible to make these particles rotate totally randomly, but partial randomisation was induced and recorded to video.

The particles, once levitated, were illuminated by a laser of wavelength 514.5nm, and a rotating half-wave retarder enabled illumination of the particle by either vertically or horizontally polarised light. A laser diffractometer allowed measurement of scattering intensity between scattering angles of 3° and 177°, while a Linear PhotoDiode Array has been used to measure angular intensity between 0.5° and 5°. By calculating Fraunhofer diffraction on a range of elliptical apertures corresponding to the cross-section of the particle as 'seen' by the laser beam, the small-angle scattering intensity has been extrapolated. With the combined measurements, we have normalised across the angular range and produced phase functions and plots of the degree of linear polarisation against scattering angle.

The phase function for each of the particles demonstrated a much smaller variation in intensity at larger scattering angles than is seen for similar size parameter spheres. For the particles presented in case studies 1,2 & 3, the scattering intensity was almost uniform above scattering angles of approximately 20°. This was also similar in case study 4, except here the scattering intensity decreased from 0° until approximately 60°, and then became almost uniform until 180°. Due to the lack of regular features on each of the particles, there are no halo peaks present such as those observed in hexagonal ice columns. The only exception to this is the particle presented in case study 2, where the particle has a noticeably flatter side than the other particles. As this particle was almost stationary in the laser beam, this flat side has produced a halo-like feature in the forward scattering region. This can be seen in the form of an inflection and a ‘bump’ between approximately 10° and 20°. A corresponding negative polarisation peak is also present.

The degree of linear polarisation has also been measured for each particle. In general, this parameter is very low for each example, describing a flattened bell curve with its peak in the 90° scattering region. As already mentioned, this is slightly different for the particle in case study 2.

The lack of flat facets and dominance of random roughness on the surface of the particles give rise to very diffuse scattering - the side scattering is noticeably higher than for similar spheres and spheroids, but the forward scattering region above approximately 10° and below approximately 60° for each of the particles is noticeably lower. As the particle surfaces are very rough, this is understandable - there are very few common paths through the particles.

The challenges regarding the calculation of scattering by such particles have been discussed - the rough surface structure, aspherical nature and large size parameter mean that the use of exact methods is not possible.

Geometric Optics (GO) is an approximate method used for particles of intermediate size parameter, with a particular advantage being its applicability to almost any particle shape. By combining GO with forward area diffraction, reasonably accurate results can be obtained for large size parameter spheres and spheroids. Ray Tracing with Diffraction on Facets (RTDF) is an improved approach to GO that considers diffraction on individual facets - this approach, when applied to hexagonal columns, gives excellent agreement with analytic methods such as Finite Difference Time Domain calculations down to a size parameter of about 20.

In this thesis, Gaussian Random Sphere methods have been used to construct model particles similar to those on which experiments were performed. By modifying the computer code that generates these particles to use quadruple precision calculations, it was possible to produce particle models that had very small scale surface roughness. As the particle models were comprised of flat polygonal facets, many thousands of facets were needed in order that the particle roughness could be captured adequately. Calculation times for the GO model were found to scale quadratically as the number of facets increased, and it was found that a particle with 3000 facets would take over 15 hours to complete. As the modelled particles were comprised of 20000 facets or more, each calculation would take over 23 days. As the RTDF model would take even longer due to the additional calculations it performed, a spatial subdivision technique was implemented into each of the models in order to reduce computation time. Calculation times were reduced to under 8 minutes for GO and under 3 hours for RTDF.

For each of the levitated particles, a range of GO and RTDF calculations were performed on approximate particle reconstructions. Parameters that were varied included the size of the surface roughness (σ, the standard deviation of the radius of a sphere, specified as a percentage of the radius) and the real and imaginary parts of the refractive index of the particle. Calculations were performed for values of σ ranging from 0 - 0.04 (where 0 indicates a smooth surface) and for refractive indexes of 1.53 + 0i, 1.53 + 0.003i 1.55 + 0i and 1.55 + 0.003i. Also taken into account was the range of orientations of the particles when the scattering measurements were taking place. A video taken of each particle during the scattering experiments was used to limit the orientation of the modelled particles within the GO and RTDF calculations. For comparison a further calculation was performed where the particle orientation was free to rotate about all three axes.

The RTDF and GO models take input parameters as described in section 7.3.1:

- Number of orientations of the model particle – 10000
- Incident rays per orientation – 100
- Maximum number of ray reflections and transmissions – 10
- Maximum number of total internal reflections – 100

As the models are Monte Carlo based, each computation was performed 10 times, and then a mean of the results was taken to produce the figures shown in Chapter 9. In all cases, it was demonstrated that a smooth model particle did not give a good representation of scattering by dust particles - the phase function was higher than for the measured particles in the forward scattering region, lower in the side scattering region, and exhibited features not present at all the in the measured particles, such as rainbow peaks and dark bands. However, the addition of surface roughness made a large difference to the calculations, and in all cases offered an improvement. The phase function flatness found in the measurements was replicated in the calculations, with

scattering in the forward region between approximately 10° and 50° decreasing as σ was increased. The RTDF and GO models responded differently to the increase in surface roughness - with lower values of σ, GO maintained the higher forward scattering and low side scattering of the smooth particle. As σ increases, the angles between adjacent facet normals become larger, causing greater deviation in ray paths due to diffraction (in the RTDF model only). This caused RTDF to have increased back and side scattering.

Limiting the orientation of the particles did not appear to affect the phase function results significantly - small differences can be noticed in the degree of linear polarisation, where the results appear slightly smoother when random orientation is used. Altering the real part of the refractive index did not change the results noticeably either. Adding an imaginary component to the refractive index, however, did make a large difference. In all cases, the scattering intensity above 10° decreased rapidly, while increasing at angles below this. For three of the particles, increasing the imaginary part of the refractive index from 0 to 3E-3 gave poorer agreement with the measured scattering. In case study 4, however, the non-absorbing scattering was much higher than measured for most of the angular range: the addition of an imaginary component to the refractive index gave far better comparison across the entire angular range. This particle was from the same sample as the previous case studies, appeared the same colour as the others under optical microscopy, and did not appear noticeably different under optical transmission microscopy.

Quantitative comparisons of phase functions were performed using RMS error and asymmetry parameter comparison. The RMS error comparison supported the results observed in the phase functions, with a trend towards higher errors for low values of σ, decreasing as σ increased. In case studies 1 - 3, the lowest error was always obtained using RTDF, with zero or very low absorption and σ of either 0.03 or 0.04. For case study 4, the lowest error was obtained using RTDF with an imaginary refractive index component of 0.003i and a median value of σ. For the asymmetry parameter, the results were less conclusive, with suitable fits being found at various values of σ and refractive index.

It is observed from the computations that the asymmetry parameter decreases as σ is increased – the particles scatter more light backwards than the equivalently sized smooth particle. This is particularly important here, where the particle facets are comparable in size to the wavelength of the incoming light. The direct radiative effect (DRE) due to dust particles scattering shortwave incident radiation will be a reduction in radiative forcing at the top-of-atmosphere (TOA). For incident light with longer wavelengths, the roughness would not have so large an effect on backscattering, and would be comparable to that for smooth particles. While no investigation was undertaken here into longwave scattering, it is likely that the asymmetry parameter will be lower than for visible wavelengths, due to the reduced effect of minor surface features. This will cause an increase in radiative forcing at the TOA.

This project has begun investigation into the possibility of replicating scattering by Saharan dust particles using Geometric Optics techniques. Work is currently being carried out at the University of Hertfordshire to introduce interference effects into RTDF – this should enable more accurate calculation of scattering by smaller particles. In order to more accurately represent the levitated particles, it would be advantageous to recreate the particle geometries faithfully, rather than approximating by a spheroid. This would be particularly important for aligned particles, a fact highlighted in Case Study 2.

Underpinning all of this, more dust particles should be levitated for experimentation using the Electro Dynamic Balance. Methods of improving the orientation randomisation of the dust particles in the trap would enable the experimental verification of the importance of orientation on scattering. The particles in this thesis were all from the same sample – performing experiments on particles sourced from different regions with differing mineralogy, refractive index, size and surface features will enable a more complete picture of the scattering properties of dust. Radiative transfer modelling using data gathered from the kind of experiments performed here will enable the investigation of the influence of atmospheric dust on the Earth's energy budget.

Bibliography

[1] Baran, A. (2004). On the scattering and absorption properties of cirrus cloud. *Journal of Quantitative Spectroscopy and Radiative Transfer , 89*, 17-36.

[2] Yu, H., Kaufman, Y. J., Chin, M., Feingold, G., Remer, L. A., Anderson, T. L., et al. (2006). A review of measurement-based assessments of the aerosol direct radiative effect and forcing. *Atmos. Chem. Phys. , 6*, 613-666.

[3] Schladitz, A., Muller, T., Kaaden, N., Massling, A., Kandler, K., Ebert, M., et al. (2009). In situ measurements of optical properties at Tinfou (Morocco) during the Saharan Mineral Dust Experiment SAMUM 2006. *Tellus Series B: Chemical and Physical Meteorology , 61B*, 64-78.

[4] Otto, S., de Reus, M., Trautmann, T., Thomas, A., Wendisch, M., & Borrmann, S. (2007). Atmospheric radiative effects of an in situ measured Saharan dust plume and the role of large particles. *Atmos. Chem. Phys. , 7*, 4887-4903.

[5] Heinold, B., Tegen, I., Esselborn, M., Kandler, K., Knippertz, P., Muller, D., et al. (2009). Regional Saharan dust modelling during the SAMUM 2006 campaign. *Tellus Series B: Chemical and Physical Meteorology , 61B*, 307-324.

[6] Perez, C., Nickovic, S., Baldasano, J. M., Sicard, M., & Rocadenbosch, F. (2006). A long Saharan dust event over the western Mediterranean: Lidar, Sun photometer observations, and regional dust modelling. *J. Geophys. Res. , 111* (D15), D15214.

[7] Hesse, E., Ulanowski, Z., & Kaye, P. H. (2002). Stability Characteristics of cylindrical fibres in an electrodynamic balance designed for single particle levitation. *J. Aerosol Science , 33*, 149-163.

[8] Ulanowski, Z., Greenaway, R. S., Kaye, P. H., & Ludlow, I. K. (2002). Laser diffractometer for single particle scattering measurements. *Meas. Sci. Technol. , 13*, 292-296.

[9] Ulanowski, Z., Hesse, E., Kaye, P. H., & Baran, A. (2006). Light scattering by complex ice-analogue crystals. *Journal of Quantitative Spectroscopy and Radiative Transfer , 100*, 382-392.

[10] Kathuria, Y. (1983). Far-field radiation patterns of elliptical apertures and its annuli. *IEEE Trans. Antenna Propag. , 31*, 360-364.

[11] Mishchenko, M. I., Lacis, A. A., Carlson, B. E., & Travis, L. D. (1995). Nonsphericity of dust-like tropospheric aerosols: Implications for aerosol remote sensing and climate modeling. *Geophys. Res. Lett. , 22* (9), 1077-1080.

[12] Mishchenko, M. I., Travis, L. D., Kahn, R. A., & West, R. A. (1997). Modeling phase functions for dustlike tropospheric aerosols using a shape mixture of randomly oriented polydisperse spheroids. *J. Geophys. Res. , 102* (D14), 16,831–16,847.

[13] Mishchenko, M. I., Wiscombe, W. J., Hovenier, J. W., & Travis, L. D. (2000). Overview of scattering by nonspherical particles. In M. I. Mishchenko, W. J. Wiscombe, J. W. Hovenier, & L. D. Travis (Eds.), *Light Scattering by Nonspherical Particles* (pp. 29-60). San Diego, USA.

[14] Hesse, E., & Ulanowski, Z. (2003). Scattering from long prisms computed using ray tracing combined with diffraction on facets. *Journal of Quantitative Spectroscopy and Radiative Transfer , 79-80*, 721-732.

[15] Clarke, A., Hesse, E., Ulanowski, Z., & Kaye, P. (2006). A 3d Implementation of ray-tracing with diffraction on facets: Verification and a potential application. *Journal of Quantitative Spectroscopy and Radiative Transfer , 100*, 103-114.

[16] Hesse, E. (2008). Modelling Diffraction during ray tracing using the concept of energy flow lines. *Journal of Quantitative Spectroscopy and Radiative Transfer , 109*, 1374-1383.

[17] Bohren, C. F., & Huffman, D. R. (1983). *Absorption and Scattering of Light by Small Particles.* United States of America: John Wiley and Sons.

[18] Macke, A., Mueller, J., & Raschke, E. (1996). Single Scattering Properties of Atmospheric Ice Crystals. *Journal of the Atmospheric Sciences , 53* (19), 2813-2825.

[19] Mishchenko, M. I., Hovenier, J. W., & Travis, L. D. (2000). *Light Scattering by Nonspherical Particles.* London, United Kingdom: Academic Press.

[20] Mishchenko, M., Travis, L., & Lacis, A. (2002). Preface. In *Scattering, Absorption, and Emission of Light by Small Particles.* Cambridge, UK: Cambridge University Press.

[21] Bohren, C. F., & Huffman, D. R. (1983). Introduction. In *Absorption and Scattering of Light by Small Particles* (pp. 3-11). USA.

[22] Bohren, C. F., & Huffman, D. R. (1983). Absorption and Scattering by a Sphere. In *Absorption and Scattering of Light by Small Particles* (pp. 82-129). New York, USA.

[23] Mishchenko, M. I., Travis, L. D., & Lacis, A. A. (2002). *Scattering, Absorption and Emission of Light by Small Particles.* Cambridge: Cambridge University Press.

[24] Mishchenko, M. I., Dlugach, J. M., Yanovitskij, E. G., & Zakharova, N. T. (1999). Bidirectional reflectance of flat, optically thick particulate laters: an efficient radiative transfer solution and applications to snow and soil surfaces. *Journal of Quantitative Spectroscopy and Radiative Transfer , 63*, 409-432.

[25] Asano, S., & Yamamoto, G. (1975). Light Scattering by a spheroidal particle. *Applied Optics , 14* (1), 29-49.

[26] Rother, T. (1998). Generalization of the separation of variables method for nonspherical scattering on dielectric objects. *Journal of Quantitative Spectroscopy and Radiative Transfer* (60), 335-353.

[27] Havemann, S., Rother, T., & Schmidt, K. (1998). Light Scattering on hexagonal ice crystals. *Conference on Light Scattering by Nonspherical Particles: Theory, Measurements and Applications* (pp. 253-256). New York: American Meteorological Society.

[28] Waterman, P. (1971). Symmetry, unitarity and geometry in electromagnetic scattering. *Physical Review D , 3* (4), 825-839.

[29] Mishchenko, M., & Travis, L. (1998). Capabilities and limitations of a current FORTRAN implementation of the T-matrix method for randomly oriented, rotationally symmetric scatterers. *Journal of Quantitative Spectroscopy and Radiative Transfer , 60*, 309-324.

[30] Havemann, S., & Baran, A. J. (2001). Extension of T-matrix to scattering of electromagnetic plane waves by non-axisymmetric dielectric particles: Application to hexagonal ice cylinders. *Journal of Quantitative Spectroscopy and Radiative Transfer , 70* (2), 139-158.

[31] Purcell, E. M., & Pennypacker, C. R. (1973). Scattering and absorption of light by non-spherical dielectric grains. *The Astrophysical Journal , 186*, 705-714.

[32] Yurkin, M., & Hoekstra, A. (2007). The Discrete Dipole Approximation: An overview and recent developments. *JQSRT , 106*, 558-589.

[33] Yee, K. (1966). Numerical Solution of Initial Boundary Value Problems Involving Maxwell's Equations in Isotropic Media. *IEEE Transactions on Antennas and Propagation , 14*, 302-307.

[34] Yang, P., Liou, K. N., Mishchenko, M. I., & Gao, B. (2000). Efficient finite-difference time-domain scheme for light scattering by dielectric particles: application to aerosols. *Applied Optics , 39* (21), 3727-3737.

[35] Hansen, J. E., & Travis, L. D. (1996). Light scattering in planetary atmospheres. *Journal of the Atmospheric Sciences , 53* (19), 2813-2825.

[36] Yang, P., & Liou, K. (1996). Geometric-optics-integral-equation method for light scattering by nonspherical ice crystals. *Applied Optics , 35* (33), 6568-6584.

[37] Hesse, E., McCall, D. S., Ulanowski, Z., Stopford, C., & Kaye, P. H. (2009). Application of RTDF to particles with curved surfaces. *Journal of Quantitative Spectroscopy and Radiative Transfer , 110*, 1599-1603.

[38] Muinonen, K., Nousiainen, T., Fast, P., Lumme, K., & Peltoniemi, J. I. (1996). Light Scattering by Gaussian Random Particles: Ray Optics Approximation. *Journal of Quantitative Spectroscopy and Radiative Transfer , 55* (5), 577-601.

[39] Liou, K., & Hansen, J. (1971). Intensity and Polarization for Single Scattering by Polydisperse Spheres : A comparison of Ray Optics and Mie Theory. *Journal of the Atmospheric Sciences , 28*, 995-1004.

[40] Macke, A., & Mishchenko, M. I. (1996). Applicability of regular particle shapes in light scattering calculations for atmospheric ice particles. *Applied Optics , 35*, 4291-4296.

[41] Glassner, A. S. (1984). Space Subdivision for Fast Ray Tracing. *IEEE Computer Graphics & Applications , 4* (10), 15-22.

[42] Glassner, A. S. (1989). *An Introduction to Ray Tracing*. (A. S. Glassner, Ed.) London: Academic Press Limited.

[43] Petzold, A., Rasp, K., Weinzerl, B., Esselborn, M., Hamburger, T., Dornbrack, A., et al. (2009). Saharan dust absorption and refractive index from aircraft-based observation during SAMUM 2006. *Tellus Series B: Chemical and Physical Meteorology* (61B), 64-78.

[44] Kandler, K. (2008). *Private Communication.*

[45] Weiss-Wrana, K. (1983). Optical properties of interplanetary dust: comparison with light scattering by larger meteoritic and terrestrial grains. *Astronomy and Astrophysics* (126), 240-250.